

**Topology optimization for high-resolution designs  
Application in solar cell metallization**

Gupta, Deepak

**DOI**

[10.4233/uuid:51dde3f6-2a38-47a0-b719-420ff74ded5d](https://doi.org/10.4233/uuid:51dde3f6-2a38-47a0-b719-420ff74ded5d)

**Publication date**

2019

**Document Version**

Final published version

**Citation (APA)**

Gupta, D. (2019). *Topology optimization for high-resolution designs: Application in solar cell metallization*. [Dissertation (TU Delft), Delft University of Technology]. <https://doi.org/10.4233/uuid:51dde3f6-2a38-47a0-b719-420ff74ded5d>

**Important note**

To cite this publication, please use the final published version (if applicable).  
Please check the document version above.

**Copyright**

Other than for strictly personal use, it is not permitted to download, forward or distribute the text or part of it, without the consent of the author(s) and/or copyright holder(s), unless the work is under an open content license such as Creative Commons.

**Takedown policy**

Please contact us and provide details if you believe this document breaches copyrights.  
We will remove access to the work immediately and investigate your claim.

# **TOPOLOGY OPTIMIZATION FOR HIGH-RESOLUTION DESIGNS**

APPLICATION IN SOLAR CELL METALLIZATION



# **TOPOLOGY OPTIMIZATION FOR HIGH-RESOLUTION DESIGNS**

APPLICATION IN SOLAR CELL METALLIZATION

## **Dissertation**

for the purpose of obtaining the degree of doctor  
at Delft University of Technology,  
by the authority of the Rector Magnificus Prof. dr. ir. T. H. J. van der Hagen,  
chair of the Board of Doctorates,  
to be defended publicly on  
Tuesday 02, April 2019 at 10:00 o'clock

by

**Deepak K. GUPTA**

Master of Science & Technology  
Indian Institute of Technology (Indian School of Mines), Dhanbad, India,  
born in Basti, India.

This dissertation has been approved by the promotor.

Composition of the doctoral committee:

Rector Magnificus,	chairperson
Prof. dr. ir. F. van Keulen,	Delft University of Technology, promotor
Dr. ir. M. Langelaar,	Delft University of Technology, promotor

*Independent members:*

Prof. dr. A. H. M. Smets,	Delft University of Technology
Prof. Dr.-Ing. habil. M. Ruess,	Hochschule Düsseldorf - University of Applied Sciences
Dr. N. Aage,	Technical University of Denmark
Dr. O. Amir,	Technion - Israel Institute of Technology
Prof. dr. U. Staufer,	Delft University of Technology, reserve member

*Other members:*

Dr. ir. M. Barink,	TNO Holst Centre, Eindhoven
--------------------	-----------------------------

This work is part of the Industrial Partnership Program “Computational sciences for energy research” of the Foundation for Fundamental Research on Matter, which is part of the Netherlands Organization for Scientific Research (NWO). This research programme (12CSER090) was co-financed by Shell Global Solutions International B.V.



*Keywords:* metallization designs, solar cells, topology optimization, freeform, multiresolution, adaptivity

*Printed by:* Gildeprint

*Cover image:* Created with slight modifications applied to a result related to this research.

Copyright © 2019 by D. K. Gupta

ISBN 978-94-6366-152-2

An electronic version of this dissertation is available at  
<http://repository.tudelft.nl/>.

*to my late mother,  
my father and my beloved wife*



# SUMMARY

Due to global population growth and industrial development, there is a rising demand for energy. It is desired that this demand is met in a cleaner and more sustainable way. Among the various renewable energy sources, solar power is experiencing remarkable growth throughout the world. To ensure that solar power can be a sustainable solution for the future energy demands, intensive research is being conducted to make solar cells more efficient and thereby reduce the cost of solar energy.

Solar cells have metallization patterns on the front side to collect current generated in the semiconductor layer. The performance of a solar cell significantly depends on the amount of electrode material used for metallization, and the pattern in which it is deposited. There exist several optimization approaches to optimize the metallization distribution on the front surface of solar cells. However, due to the numerical simplifications associated with these methods, only limited gains in power output are observed. Moreover, the applicability of these methods is historically restricted to rectangular or circular domains. There has recently been a drive towards increased freeform photovoltaic installations. Given that these shapes can be very arbitrary, the optimal metallization patterns for such geometries can be expected to be complex, and the traditional methods cannot be used to design them.

The main aim of this thesis is to explore the potential of topology optimization (TO) to optimize the metallization designs for solar cells with minimal restrictions on electrode and domain shape. Solar cell metallization typically covers only a small area fraction of the cell, and its critical dimensions are much smaller than the cell itself. The computational cost of conventional TO approaches becomes a limiting factor for such design problem characteristics. To address this, a second aim of this thesis is to develop efficient TO formulations. Such methods should be computationally cheap, able to generate high-resolution designs and the results should be accurate.

The two aims of this thesis are addressed in two parts. Part I focuses on building a modeling and optimization strategy based on TO for the metallization patterns in solar cells. The resultant designs obtained using TO are found to resemble the conventionally used H-patterns in terms of performance, but no significant efficiency improvements are found. However, for freeform solar cell geometries (e.g. circular, leaf-shaped, christmas tree-shaped) and for concentrated photovoltaics under nonuniform temperature and illumination profiles, the optimized designs can improve the solar cell performance by over 50% and 26%, respectively.

Part II of this thesis aims at efficiently obtaining high-resolution designs in TO. For this purpose, multiresolution topology optimization (MTO) methods are explored. In MTO schemes, the finite element mesh and the design domain are decoupled allowing high resolution design representations at low analysis costs. We show that for a certain chosen analysis resolution, there is always an upper bound on the number of design variables that can be used to express the design resolution without leading to non-

uniqueness. Further, a detailed investigation is performed into the formation and properties of QR-patterns, which are numerical artefacts comprising artificially stiff regions that can arise in MTO optimized designs.

Based on our results related to conventional MTO, an efficient novel MTO scheme, namely *dp*-adaptive MTO, is proposed which is suited for generating high-resolution designs at reasonable computational costs. Through several numerical examples of 2D test cases, it is found that *dp*-adaptive MTO can obtain equally well performing optimized designs at up to 10 times lower computational cost than the conventional MTO. Although the potential of *dp*-adaptive MTO for solar cell metallization design has briefly been discussed, the real benefits still need to be explored and is a direction of future research work related to this subject.

Overall, based on the results presented in this thesis, it can certainly be concluded that TO can contribute to improving the performance of solar cells. In particular, it is of interest to use TO for designing metallization patterns in concentrated and freeform solar cells, where significant improvements in performance can be obtained over the conventional patterns. The numerical investigations related to high-resolution TO and particularly the *dp*-adaptive MTO scheme provide new directions to generate high-resolution structures that can deliver increased power output at relatively low computational (and energy) cost, and are also expected to be of great use for many applications outside the solar cell field. It is expected that the research output of this thesis contributes towards making renewable energy affordable and making this world greener.

# SAMENVATTING

Door de wereldwijde bevolkingsgroei en industriële ontwikkeling is er een toenemende vraag naar energie. Het is wenselijk dat deze vraag beantwoord wordt met schonere en duurzamere oplossingen. Een van de verschillende beschikbare duurzame energiebronnen, zonne-energie, maakt wereldwijd een enorme groei door. Om te verzekeren dat zonne-energie een duurzame oplossing kan vormen voor de toekomstige energievraag, wordt er intensief onderzocht hoe zonnecellen efficiënter gemaakt kunnen worden, en zodoende de kosten van zonne-energie te drukken.

Zonnecellen hebben aan de voorzijde een metallisatie patroon om de stroom te geleiden die in de halfgeleiderlaag gegenereerd wordt. De prestaties van een zonnecel hangen sterk af van de hoeveelheid elektrodemateriaal dat gebruikt wordt voor deze metallisatie, alsmede van het patroon waarin het wordt aangebracht. Er bestaan verschillende optimalisatieprocedures om het optimale metallisatiepatroon op het oppervlakte van een zonnecel te bepalen. Echter, door de numerieke vereenvoudigingen in deze methodes, is de toename in geproduceerde energie slechts gering. Daarnaast is de toepasbaarheid van deze methodes historisch gezien beperkt gebleven tot rechthoekige of ronde domeinen. Recent staan echter ook vrij gevormde zonnecellen en zonnepanelen sterk in de belangstelling. Aangezien deze vormen heel arbitrair kunnen zijn, zijn de optimale metallisatie patronen voor dergelijke geometrieën naar verwachting zodanig complex dat bestaande methodes niet gebruikt kunnen worden om deze patronen te ontwerpen.

Het hoofddoel van dit proefschrift is om het potentieel van topologie optimalisatie (TO) om metallisatie van zonnecellen te optimaliseren te verkennen, met minimale restricties op zowel de vorm van de cel als de electrode. De metallisatie beslaat normaliter slechts een klein deel van het zonnecel-oppervlak, en de bijbehorende kritieke afmetingen zijn veel kleiner dan die van de cel zelf. Deze karakteristieken van dit ontwerpprobleem maken dat bij klassieke TO benaderingen de rekentijd sterk zal oplopen. Om deze beperking te omzeilen, is een tweede doel van dit onderzoek het ontwikkelen van efficiëntere TO methoden. Deze methoden dienen een geringe rekentijd te hebben, moeten hoge resolutie resultaten kunnen opleveren en moeten daarbij ook numeriek nauwkeurig zijn.

De twee doelen van dit onderzoek zijn in dit proefschrift beschreven in twee delen. Deel I richt zich op het ontwikkelen van een simulatie- en optimalisatie-strategie gebaseerd op TO, voor de metallisatiepatronen van zonnecellen. De hieruit resulterende ontwerpen voor rechthoekige cellen blijken vergelijkbaar te presteren met het conventioneel gebruikte H-patroon, significante verbeteringen in efficiency zijn niet gevonden. Echter, voor vrij gevormde cellen (in de vorm van bijv. cirkels, bladeren of een kerstboom) en voor geconcentreerde fofovoltaïsche cellen onder niet-uniforme temperatuurs- en belichtingssituaties, blijkt dat optimalisatie de energieopbrengst van een zonnecel kan verbeteren met meer dan respectievelijk 50% en 26%.

Deel II van dit proefschrift is gericht op het efficiënt verkrijgen van hoge resolutie TO

resultaten. Hiervoor worden multi-resolutie topologie optimalisatie (MTO) methodes verkend. In MTO worden de eindige elementen mesh en het ontwerpdomein van elkaar losgekoppeld, wat hoge ontwerp-resolutie tegen lage simulatiekosten mogelijk maakt. We tonen aan dat voor een zekere gekozen simulatiereolutie, er altijd een bovengrens is voor het aantal ontwerpvariabelen dat zinvol gebruikt kan worden om het ontwerp te beschrijven, voordat er een niet-unieke beschrijving ontstaat. Verder worden de vorming en de eigenschappen van QR-patronen in detail onderzocht, dit zijn numerieke artifacten bestaande uit delen met een kunstmatig hoge stijfheid welke kunnen ontstaan in ontwerpen gegenereerd via MTO.

Op basis van onze bevindingen betreffende conventionele MTO methoden, wordt een efficiënte nieuwe MTO-benadering voorgesteld genaamd *dp*-adaptieve MTO. Deze benadering is in staat om hoge resolutie ontwerpen te genereren tegen een relatief lage rekentijd. Middels meerdere numerieke voorbeelden van 2D testproblemen blijkt dat *dp*-adaptieve MTO gelijkwaardig presterende ontwerpen kan genereren in slechts een tiende van de rekentijd van conventionele MTO. Hoewel ook het potentieel van *dp*-adaptieve MTO voor zonnecel-metallisatie ontwerp kort wordt besproken, moeten de daadwerkelijke voordelen in die toepassing nog worden verkend, en vormt dit een richting voor verder onderzoek.

Gebaseerd op de resultaten gepresenteerd in dit proefschrift, kan zeker worden geconcludeerd dat TO kan bijdragen aan de prestatieverbetering van zonnecellen. Het is met name interessant om TO te gebruiken voor het ontwerp van metallisatie-patronen van geconcentreerde fotonvoltaïsche cellen en vrij gevormde zonnecellen. Het numerieke onderzoek op het gebied van hoge-resolutie TO en in het bijzonder de voorgestelde *dp*-adaptieve MTO methode biedt nieuwe benaderingen om tegen geringe rekenkosten hoge resolutie zonnecel ontwerpen te genereren met verbeterde energieproductie. De verwachting is dat deze methoden daarbij ook van groot nut kunnen zijn voor andere toepassingen naast zonnecellen. Verder is de verwachting dat de onderzoeksresultaten zoals gepresenteerd in dit proefschrift bijdragen aan het betaalbaarder en haalbaarder maken van hernieuwbare energie en het groener maken van deze wereld.

# CONTENTS

<b>Summary</b>	<b>vii</b>
<b>Samenvatting</b>	<b>ix</b>
<b>1 Introduction</b>	<b>1</b>
1.1 Motivation . . . . .	2
1.1.1 <i>Need</i> for clean energy . . . . .	2
1.1.2 <i>Inspiration</i> from nature . . . . .	4
1.1.3 <i>Challenge</i> of computation . . . . .	5
1.2 Research Objective . . . . .	6
1.3 Outline . . . . .	7
1.3.1 Part I: Optimizing solar cell metallization design. . . . .	7
1.3.2 Part II: High-resolution designs in topology optimization . . . . .	9
1.3.3 Part III: Conclusions and Recommendations. . . . .	9
References . . . . .	9
<b>I Solar cell models and optimization</b>	<b>13</b>
<b>2 A topology optimization framework</b>	<b>15</b>
2.1 Introduction . . . . .	16
2.2 Solar cell architecture and modelling . . . . .	17
2.2.1 Solar cell operation . . . . .	17
2.2.2 Role of front metal electrode . . . . .	19
2.2.3 Finite element model . . . . .	21
2.3 Topology optimization formulation. . . . .	22
2.3.1 Solar cell configurations and parameters. . . . .	22
2.3.2 Element conductivity matrix. . . . .	23
2.3.3 Calculating element current density . . . . .	24
2.3.4 Optimization problem . . . . .	24
2.3.5 Sensitivity analysis . . . . .	25
2.3.6 Filtering . . . . .	26
2.4 Results and discussions . . . . .	26
2.4.1 Effect of mesh resolution. . . . .	27
2.4.2 Effect of solar cell size . . . . .	29
2.4.3 Voltage and current density distribution . . . . .	30
2.4.4 Preliminary comparison with existing designs . . . . .	34
2.4.5 Scope for different types of solar cells . . . . .	35
2.5 Conclusions. . . . .	35
References . . . . .	36

<b>3</b>	<b>Grid optimization of freeform solar cells</b>	<b>39</b>
3.1	Introduction . . . . .	40
3.2	Method . . . . .	42
3.2.1	Topology Optimization . . . . .	42
3.2.2	Mathematical formulation . . . . .	42
3.2.3	Applications . . . . .	46
3.3	Results and Discussions. . . . .	47
3.4	Conclusions. . . . .	52
	References . . . . .	53
<b>4</b>	<b>CPV metallization optimization</b>	<b>57</b>
4.1	Introduction . . . . .	58
4.2	Modeling Approach. . . . .	60
4.2.1	Equivalent Circuit . . . . .	60
4.2.2	Illumination and temperature distribution . . . . .	62
4.2.3	Finite Element Model . . . . .	63
4.3	Modeling results . . . . .	65
4.3.1	Model parameters . . . . .	65
4.3.2	Model validations . . . . .	67
4.3.3	Effect of contact resistance. . . . .	70
4.4	Optimization approach . . . . .	70
4.4.1	Optimization problem . . . . .	70
4.4.2	Sensitivity analysis. . . . .	71
4.5	Optimization results . . . . .	73
4.5.1	Illumination profiles. . . . .	74
4.5.2	Temperature profiles. . . . .	79
4.6	Conclusions. . . . .	81
4.A	Computing $I^e$ . . . . .	81
4.B	Computing $\frac{dI^e}{dV^e}$ . . . . .	82
4.C	IV curves for concentrated illuminations . . . . .	82
4.D	Sensitivity analysis . . . . .	83
4.D.1	Computing $\frac{d\tilde{\mathcal{J}}}{d\rho}$ . . . . .	84
4.D.2	Computing $\frac{d\tilde{\mathcal{J}}}{dV_b}$ . . . . .	84
4.E	Computing $\frac{\partial I^e}{\partial \rho}$ . . . . .	84
	References . . . . .	85
<b>II</b>	<b>High-resolutions designs using topology optimization</b>	<b>89</b>
<b>5</b>	<b>Combined mesh and penalization adaptivity</b>	<b>91</b>
5.1	Introduction . . . . .	92
5.2	Approach . . . . .	95
5.2.1	Mesh refinement indicator. . . . .	95
5.2.2	Adaptive filter radius. . . . .	97
5.2.3	Penalization continuation . . . . .	98

5.3	Results . . . . .	98
5.4	Discussion and Conclusion . . . . .	102
	References . . . . .	104
<b>6</b>	<b>Bounds for decoupled analysis and design discretizations</b>	<b>107</b>
6.1	Introduction . . . . .	108
6.2	A basic example. . . . .	109
6.3	Condition for uniqueness of density distribution . . . . .	111
6.4	Choice of the number of design variables . . . . .	115
6.5	Discussion and Conclusion . . . . .	116
6.A	Appendix A . . . . .	117
6.B	Appendix B . . . . .	118
	References . . . . .	118
<b>7</b>	<b>QR-patterns</b>	<b>121</b>
7.1	Introduction . . . . .	122
7.2	Artificially stiff features in MTO . . . . .	124
	7.2.1 MTO concept . . . . .	124
	7.2.2 Occurrence of QR-patterns. . . . .	125
7.3	Origin of QR-patterns . . . . .	126
	7.3.1 Study of elementary cases . . . . .	126
	7.3.2 Gap modeling with polynomial shape functions . . . . .	128
	7.3.3 Displacement solution accuracy . . . . .	130
	7.3.4 Role of penalization and design-uniqueness. . . . .	133
7.4	Filtering in MTO . . . . .	134
	7.4.1 Role of filtering. . . . .	134
	7.4.2 Effect of filtering and limitations. . . . .	134
	7.4.3 Choosing the filter radius . . . . .	137
7.5	Discussion . . . . .	142
7.6	Conclusions. . . . .	144
	References . . . . .	144
<b>8</b>	<b>Design and analysis adaptivity in MTO</b>	<b>147</b>
8.1	Introduction . . . . .	147
8.2	Multiresolution Topology Optimization. . . . .	151
	8.2.1 Domain and variable definitions. . . . .	151
	8.2.2 Mathematical formulation. . . . .	154
8.3	<i>dp</i> -adaptivity . . . . .	157
	8.3.1 General description of the method. . . . .	157
	8.3.2 Refinement criteria . . . . .	158
	8.3.3 <i>dp</i> -adaptivity algorithm . . . . .	163
8.4	Numerical tests . . . . .	165
	8.4.1 Definition of test problems. . . . .	165
	8.4.2 Results . . . . .	166

---

8.5	Discussions . . . . .	175
8.6	Conclusions. . . . .	178
8.A	<i>k</i> -means clustering . . . . .	179
8.B	Numerical integration scheme . . . . .	180
	References . . . . .	181
<b>III</b>	<b>Conclusions and Future work</b>	<b>185</b>
<b>9</b>	<b>Conclusions and Recommendations</b>	<b>187</b>
9.1	Conclusions. . . . .	187
9.1.1	Optimizing metallization patterns in solar cells . . . . .	187
9.1.2	Design of high-resolution structures using TO . . . . .	188
9.1.3	Overall conclusions . . . . .	189
9.2	Recommendations . . . . .	189
	References . . . . .	191
	<b>Acknowledgements</b>	<b>193</b>
	<b>List of Publications</b>	<b>195</b>
	<b>Curriculum Vitæ</b>	<b>197</b>

# 1

## INTRODUCTION

## 1.1. MOTIVATION

### 1.1.1. *Need* FOR CLEAN ENERGY

With the increasing energy demand and the desire to meet this demand in a cleaner and more sustainable way, renewable energy sources such as wind, sun and water are gaining more and more importance. Among the various renewable energy sources, solar power is considered to be of significant potential impact. More than 140 years ago, Professor Augustine Mouchot stated that the sun could be seen as one of the important sources of energy for the future [1]:

*“The time will arrive when the industry of Europe will cease to find those natural resources, so necessary for it. Petroleum springs and coal mines are not inexhaustible but are rapidly diminishing in many places. Will man, then, return to the power of water and wind? Or will he emigrate where the most powerful source of heat sends its rays to all? History will show what will come.”*

- A. Mouchot, 1873

When Charles Fritt created the first working solar cell from selenium, Werner von Siemens commented [2]:

*“In conclusion, I would say that however great the scientific importance of this discovery may be, its practical value will be no less obvious when we reflect that the supply of solar energy is both without limit and without cost, and that it will continue to pour down upon us for countless ages after all the coal deposits of the earth have been exhausted and forgotten”* - W. von Siemens, 1885

These two quotes clearly highlight the importance of solar energy as well as the future expectations from it.

Solar power is experiencing remarkable growth throughout the world. It is expected that the cumulative global solar photovoltaics (PV) market will triple to around 700 GW in 2020 compared with that in 2015 [3] and anticipations are that by 2050, solar power will become the largest source of electricity with PV capacity growing upto 4600 GW [4]. Looking at the United States alone, the total electrical power sector capacity in 2015 was reported to be around 1045 GW [5] with 27 GW of total solar power capacity, and it is reported that 30% of its all new electricity generation capacity in 2015 came from solar. In 2017, the PV installations are expected to increase by more than 85 GW [6].

To ensure that solar power can be a sustainable solution for the future energy demands, new and innovative ways are being attempted to increase the overall installations. Significant research is being conducted to make solar cells more efficient and thereby reduce the cost per unit of solar energy [7]. At cell level, various ways to improve the cell efficiency include using superior semiconductor material, improving the metallization design, minimizing shading losses and improving light-trapping capability of the solar cell. In this thesis, we focus on improving the metallization design in solar cells.

Solar cells have metallization patterns on the front side to collect current generated in the semiconductor layer. During metallization, electrode material is deposited on the front side, which helps to reduce the overall series resistance, and improves the solar cell

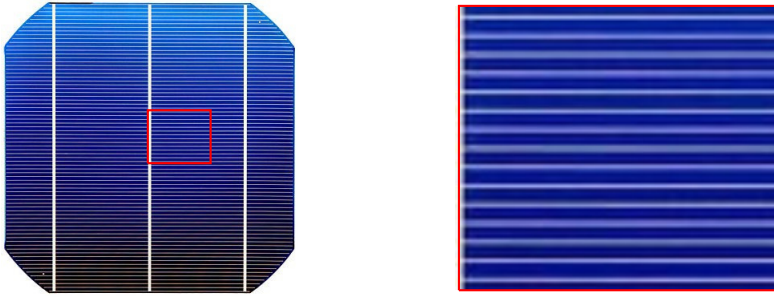


Figure 1.1: Front view of a crystalline silicon solar cell<sup>1</sup> (left), and the magnified view of its bounded region in red (right). The magnified view shows the H-pattern, comprising parallel electrode fingers with uniform line spacing.

performance. In the past, several researchers have looked into developing cost-effective fabrication techniques to obtain desired metallizations. A few examples of fabrication techniques are laser sintering [8], selective aerosol ablation [9], metal aerosol jet printing [10] and screen printing [11]. The performance of a solar cell significantly depends on the amount of electrode material used for metallization, and the pattern in which it is deposited. For example, for a rectangular solar cell, traditionally an H-pattern based metallization design, as shown in Fig. 1.1, is used [12]. Similarly, for a circular cell, a radial pattern is preferred [13]. The important characteristic of these patterns is that they provide maximum power output for the respective solar cell geometries. With tailored metallization designs, the series resistance is reduced, and higher solar cell efficiencies are obtained. The details on how certain metallization designs lead to increased power output will be discussed in Chapter 2 of this thesis.

In the past, various ways to optimize the metallization pattern have been explored. Some of the earliest examples are optimization of the grid line spacing assuming a unidirectional current flow in the collecting grid [15], distributed-diode-based optimization [16], and simultaneous optimization of the grid lines and the main metallic strip (busbar) [17]. However, due to the numerical simplifications involved, most of the existing approaches can lead to limited improvement in the solar cell performance and are applicable to only a few geometrical shapes. For example, the traditional H-pattern shown in Fig. 1.1 consists of only vertical busbars and horizontal metal fingers and is optimized for rectangular solar cells. With the restriction on the geometry of the metal lines, only the finger thickness and line spacing are optimized. Optimization approaches involving such restrictions have reduced flexibility and only limited improvement in performance can be expected.

To cope with the increasing need for solar power, researchers are also investigating possibilities of fabricating non-rectangular solar cells (*e.g.* [18]). The advantage of non-rectangular shapes is that these cells can be installed on objects of daily use without any interference with their visual aesthetics. With added freeform photovoltaic installations, the overall solar power generation can be increased, however, it is important that these

<sup>1</sup>Image of a modern crystalline silicon solar cell by WhistlingBird [14], available under a Creative Commons Attribution-Noncommercial-Share Alike license.

solar cells are efficient as well. Unlike the rectangular shapes, the H-pattern cannot be used as a metallization design for these cells. Also, given that these shapes can be very arbitrary, the optimal metallization patterns for such geometries can be expected to be complex, and it is not easy to choose efficient metallization designs intuitively.

There exist several advanced techniques to fabricate very fine electrode lines [11, 19, 20], which can eventually help in printing complex metallization patterns. Thus, realizing complex metallization patterns is not a problem anymore, however, designing such patterns is still a challenge. Clearly, in this advanced computing era, we are missing a recipe that can find designs with minimal restrictions.

### 1.1.2. *Inspiration* FROM NATURE

The shapes and designs of various objects found in nature are complicated, difficult to understand, yet are aesthetically pleasing. Although these patterns might seem random at first sight, it has been found that they are generally optimized for a certain task or a variety of tasks. The venation network of leaves is one such beautiful example. Fig. 1.2 shows the venation networks for three different leaves. At first sight, no direct correlation can be deduced among these networks. However, research has shown that these networks are optimized by nature so as to adapt to the local geographical conditions such as local precipitation and temperature [21].

There are various physical phenomena that are taken into consideration for designing the optimal venation networks. For example, the carbon assimilation needs to be maximized through effective water transport rates and an optimized balance between the photosynthesis and transpiration processes. Other aspects are minimizing sags or mechanical deformations through optimal mass distribution, maximizing leaf life span through improved mechanical strength and avoiding biotic and abiotic damage [22].

From this example, it can be seen that the complex shapes in nature are not random, but instead maximize certain performance aspects. Similar observations have motivated scientists in the past to use such designs in engineering problems, *e.g.* improving metal carbide synthesis [23], and designing microfluidic networks for perfusable tissue constructs [24]. There exist several other examples of bioinspired applications, where the designs existing in nature have been adopted. However, it is important that the designs are not directly copied from nature, since they are optimized for a certain task. Our goal should be to understand the physics behind these designs, learn from them, and adopt their features to our design problem. From the examples listed here, it is certainly clear that designs that resemble the patterns existing in nature could possibly help in improving the performance of a structure. To obtain such designs, it is important that the design freedom is increased, which means reducing the restrictions on the shapes of the design. Nevertheless, these designs serve as a motivation to investigate whether solar cell performance can be improved with reduced restrictions on metallization design.

Among other possibilities, *Topology Optimization* stands out as the most promising approach to exploit increased design freedom. Without any requirement of the initial concept from the side of the designer, topology optimization (TO) generates well performing designs, taking into account the physics of the problem and without any explicit restriction on geometry, *i.e.* shape and topology. In a more mathematical sense, TO is a computational procedure that optimizes the distribution of a given material in a certain

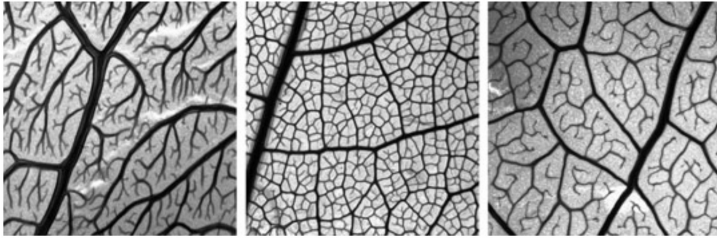


Figure 1.2: Venation network of leaves for three different angiosperm species [22].

domain under a set of given constraints, such that the value of a certain performance functional is maximized [25]. Looking back at the topology of the structures optimized in nature, for certain problems, it has been observed that the TO resultant designs form similar dendritic structures and resemble the patterns existing in nature. Whether or not TO is the exact match to how nature optimizes designs, the patterns obtained using TO generally perform very well. In the past, the potential of TO has been demonstrated by researchers for various problems, and an overview can be found in the review paper by Deaton and Grandhi [26]. Based on this motivation, TO is further used in this thesis.

### 1.1.3. *Challenge* OF COMPUTATION

In a TO regime, it is important that the physics of the problem is correctly modeled. This is generally achieved using the finite element method [27]. For the solar cell metallization design problem, the current flow as well as the voltage distribution on the front surface of the cell need to be accurately modeled. This can be considered a two-dimensional flow problem and has been modeled in the past using finite element modeling (FEM) [28]. For optimizing the metallization pattern, such a model can be employed and a two-dimensional implementation of TO is needed. Since TO is a well-studied approach, its advantages and limitations in the context of solar cell metallization design can be forecasted beforehand. TO in 2D has been used for a wide variety of problems *e.g.* structural, thermal, and efficient computer codes in various programming languages are freely available on the web. The 99-line MATLAB<sup>®</sup> based implementation of TO is one of the finest examples, written to optimize structural designs for maximum stiffness [27].

The solar cell metallization design problem is a computationally challenging problem to solve. Among others, the main challenges are:

- The inherent nonlinearity of the solar cell response due to the behavior of the semiconductor layer, which requires iterative solution procedures.
- The desired metallization feature size requires very fine meshes with high FEM costs.
- Metallization typically covers 5-10% of the solar cell surface. For such low material fractions, solving the optimization problem becomes harder.

Combined, these challenges significantly increase the computational cost and complexity of the TO process. More details related to these challenges follow.

At every iteration of TO, a system of equations, obtained from FEM discretization, is solved. In general, this is the most expensive part of a TO methodology in terms of computational cost. For linear problems, a 2D implementation of TO is not so expensive. For example, a simple 2D structural compliance minimization solved using a sufficiently fine mesh on a personal computer takes only a minute or two [29]. However, the solar cell metallization problem is not so straightforward. The current generated at any point in the solar cell is nonlinearly related to the voltage drop across it. Due to this, the system of equations obtained using FEM discretization need to be solved in an iterative manner. This means that at every iteration step of TO, the FE system needs to be solved several times, thus, leading to an increase in the required computational time.

Compared to the design domain size, *i.e.* the front surface of the cell, the size of the smallest metal feature that can be fabricated is generally several orders lower. For example, for a crystalline silicon solar cell of  $15 \times 15 \text{ cm}^2$  area, the minimum allowed width of the electrode metal can even be  $30 \mu\text{m}$ . If a structured mesh of quadrilateral elements with bilinear shape functions is used, a minimum of 25 million FEs will be needed to model the current flow for such a case. To avoid issues of checkerboards and mesh-dependence, filtering is employed in TO. This requires refining the mesh further and the problem size can easily cross 100 million FEs. This level of computation is far beyond the limits of a personal computer. Thus, advanced TO formulations are needed which can handle such problems.

For most of the problems studied using TO in the past (*e.g.* structural, thermal *etc.*), the material takes up a considerable fraction of the design domain ( $> 30\%$ ). However, for the solar cell problem, the material volume fraction is significantly lower, governed by the compromise between series resistance losses and shading losses. A general observation is that the total area of the front surface that is covered with the electrode metal layer is only 4-6% of the total front surface area of the cell. TO problems with such low volume fractions can be very difficult to solve. It is well known that for low volume fractions, the optimizers used in TO find it hard to efficiently distribute the material. With such limitations, the convergence of traditional TO process can be affected and it might be challenging to obtain efficient metallization patterns that can deliver improved power output.

## 1.2. RESEARCH OBJECTIVE

The main aim of this thesis is to explore the potential of topology optimization (TO) in designing efficient metallization patterns for solar cells. However, based on the reasonings provided earlier, it is quite evident that to be able to fully use the power of TO for improving solar cell performance, efficient TO formulations with proper modeling techniques are needed. Such methods should be computationally cheap, able to generate high-resolution designs and the results should be reliable.

An investigation in the direction of improving the topology optimization methodology, so as to obtain efficient high-resolution designs, is implied. However, this research aspect is applicable to a wide range of other TO application domains and is not necessarily restricted to the solar cells. Thus, in this work, an attempt is made to answer the following two related research questions:

1. *How can topology optimization be used to optimize the metallization patterns in solar cells ?*
2. *How can topology optimization be used to obtain well performing high-resolution designs for a given problem ?*

To the best of our knowledge, the application of TO for designing efficient metallization designs for solar cells has so far been unexplored. Thus, the first research question focuses in this direction. The goal here is to establish a TO framework for the metallization design of solar cells. Due to the enormous flexibility, TO is applicable for cases where the other existing methods cannot be used, e.g., freeform solar cell geometries. The application of TO for such scenarios as well is investigated.

In the second part of the research, investigation is done in the direction of obtaining high-resolution designs from TO. A fundamental study is performed on this aspect and based on the existing approaches, the scientific gaps are identified. Among other possibilities, multiresolution topology optimization (MTO) methods [30, 31] are found to be of potential use. In MTO schemes, the finite element mesh and the design domain are decoupled allowing high resolution design representations for low modeling costs. In this research, a rigorous study is performed on the theoretical foundation and numerical stability of these methods. Based on the results of this study, an efficient TO scheme is proposed which is suited for generating high-resolution designs at reasonable computational costs.

## 1.3. OUTLINE

The majority of the chapters of this thesis are based on published or submitted journal articles and conference papers. Although this has resulted in a certain degree of redundancy, the advantage is that the chapters are self-explanatory and can be read independently. Fig. 1.3 illustrates the structure of this thesis which is divided into three parts and consists of a total of nine chapters. Part I focuses on building a modeling and optimization strategy for the metallization patterns in solar cells. Part II looks at the problem of high-resolution designs in topology optimization from a more general point of view. The conclusions and recommendations form Part III of this thesis. More details on each part follow.

### 1.3.1. PART I: OPTIMIZING SOLAR CELL METALLIZATION DESIGN

Chapter 2 presents a TO formulation for optimizing the metallization designs on the front surface of the solar cells. This chapter also provides the reader a general introduction to solar cell architecture and terminology. For simplicity, the shunt resistance and some components of the series resistance, such as contact resistance, are ignored in the finite element model and uniform illumination of the cell under one sun intensity is assumed. Together with the metallization pattern, the operating voltage of the busbar is also optimized. Several solar cell configurations are considered and the role of cell size as well as the resolution of the finite element mesh are studied.

Chapter 3 extends the application of TO towards simultaneous optimization of the metallization patterns on the front as well as the rear sides of solar cells. The potential

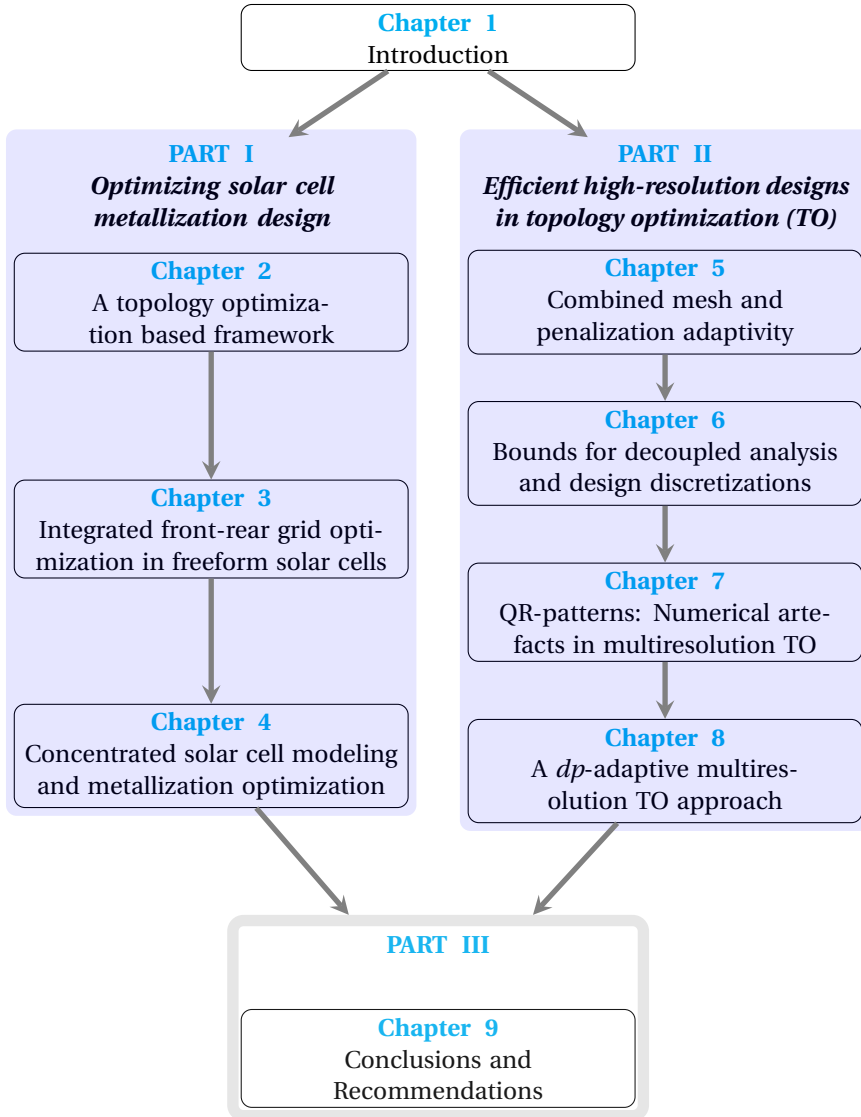


Figure 1.3: Visual outline of this thesis. The thesis comprises a total of 9 chapters and is divided into three parts. Parts I and II focus on the two research questions and can be read independently.

of TO is also investigated for freeform solar cells and the performance of the resultant optimized designs are validated against recently published experimental results.

For more accurate modeling and optimization, Chapter 4 presents an improved version of the numerical model presented in Chapter 2. The shunt and series resistance components are included. The inclusion of contact resistance especially makes this model significantly different from the earlier one. The model is further extended for concentrated photovoltaics (CPV), and non-uniform illumination and temperature profiles are considered. Based on this model, the potential of TO is explored for designing metallization patterns under non-uniform, concentrated illumination and varying temperature conditions.

### 1.3.2. PART II: HIGH-RESOLUTION DESIGNS IN TOPOLOGY OPTIMIZATION

The research towards efficiently obtaining high-resolution designs in TO starts with an investigation of the various existing approaches that could be of potential use and the scientific gaps that exist. Chapter 5 presents an adaptive TO formulation where the finite element mesh resolution and penalization terms are adapted during the course of the optimization. The applicability of this approach is tested on numerical examples of TO.

Chapters 6 and 7 study the multiresolution topology optimization (MTO) approaches and outline the associated issues based on theoretical and numerical investigations. Possible solutions to these issues are identified and an adaptive MTO method is proposed in Chapter 8. The applicability of this method is demonstrated on various numerical examples.

### 1.3.3. PART III: CONCLUSIONS AND RECOMMENDATIONS

Chapter 9 presents the conclusions from this research and recommendations for the future.

## REFERENCES

- [1] P. F. Ploutz, *Global Warming: Handbook of Ecological Issues* (Xlibris Corporation, 2012).
- [2] W. von Siemens, *On the electromotive action of illuminated selenium, discovered by Mr. Fritts, of New York*, Van Nostrands Engineering Magazine **32**, 514 (1885).
- [3] A. James, *Global PV Demand Outlook 2015:2020: Exploring Risk in Downstream Markets*, GTM Research Reports (2015).
- [4] *Technology Roadmap: Solar Photovoltaic Energy*, Energy Technology Perspectives, International Energy Agency (2014).
- [5] US Energy Information Administration, *Annual Energy Outlook 2015*, Table: Electricity Generating Capacity .
- [6] B. Attia, *Global Solar Demand Monitor: Q1 2017*, GTM Research Reports, Tech. Rep. (2017).

- [7] N. Lewis, *Basic Research Needs for Solar Energy Utilization*, Report on the Basic Energy Sciences Workshop on Solar Energy Utilization (2005).
- [8] M. Aleman, A. Streek, P. Regenfuß, A. Mette, R. Ebert, H. Exner, S. W. Glunz, and G. Wileke, *Laser micro-sintering as a new metallization technique for silicon solar cells*, in *European Photovoltaic Solar Energy Conference* (2006).
- [9] A. Knorz, M. Peters, A. Grohe, C. Harmel, and R. Preu, *Selective laser ablation of SiNx layers on textured surfaces for low temperature front side metallizations*, *Progress in Photovoltaics: Research and Applications* **17**, 127 (2009).
- [10] A. Mette, P. L. Richter, M. Hörteis, and S. W. Glunz, *Metal aerosol jet printing for solar cell metallization*, *Progress in Photovoltaics: Research and Applications* **15**, 621 (2007).
- [11] D. Erath, A. Filipović, M. Retzlaff, A. K. Goetz, F. Clement, D. Biro, and R. Preu, *Advanced screen printing technique for high definition front side metallization of crystalline silicon solar cells*, *Solar Energy Materials and Solar Cells* **94**, 57 (2010).
- [12] A. Flat and A. G. Milnes, *Optimization of multi-layer front-contact grid patterns for solar cells*, *Solar Energy* **23**, 289 (1979).
- [13] G. M. M. W. Bissels, M. A. H. Asselbergs, J. J. Schermer, N. J. Haverkemp, and E. Vlieg, *A genuine circular contact grid pattern for solar cells*, *Progress in Photovoltaics: Research and Applications* **19**, 517 (2011).
- [14] WhistlingBrid, *File:silicon solar cell (perc) front and back.jpg*, [https://commons.wikimedia.org/wiki/File:Silicon\\_solar\\_cell\\_\(PERC\)\\_front\\_and\\_back.jpg](https://commons.wikimedia.org/wiki/File:Silicon_solar_cell_(PERC)_front_and_back.jpg), retrieved on August 16, 2017.
- [15] M. Wolf, *Limitations and possibilities for improvement of photovoltaic solar energy converters*, in *Proceedings of the IRE* (1960) pp. 1246–1263.
- [16] W. A. Beckman, *Optimization of Contact Grid Spacing for High Solar Flux Photovoltaic Cells*, *Journal of Engineering for Power* **89**, 415 (1967).
- [17] H. Serreze, *Optimizing SC performance by simultaneous consideration of grid pattern design and interconnect configuration*, in *1978, IEEE Photovoltaic Specialists Conference* (IEEE, 1978) pp. 609–614.
- [18] T. Eggenhuisen, Y. Galagan, A. Biezemans, T. Slaats, P. Voorthuijen, S. Kommeren, S. Shanmugam, J. P. Teunissen, A. Hadipour, W. Verhees, S. C. Veenstra, M. Coenen, J. Gilot, R. Andriessen, and P. Groen, *High efficiency, fully inkjet printed organic solar cells with freedom of design*, *Journal of Materials Chemistry A* **3**, 7255 (2015).
- [19] J. Hoornstra, H. de Moor, A. Weeber, and P. Wyers, *Improved front side metallization on silicon solar cells with stencil printing*, in *16th European Photovoltaic Solar Energy Conference, Glasgow, UK* (2000) pp. 1416–1419.

- [20] Y. Galagan, E. W. Coenen, R. Abbel, T. J. van Lammeren, S. Sabik, M. Barink, E. R. Meinders, R. Andriessen, and P. W. Blom, *Photonic sintering of inkjet printed current collecting grids for organic solar cell applications*, *Organic Electronics* **14**, 38 (2013).
- [21] L. Sack and C. Scoffoni, *Leaf venation: structure, function, development, evolution, ecology and applications in the past, present and future*, *New Phytologist* **198**, 983 (2013).
- [22] B. Blonder, C. Violle, L. P. Bentley, and B. J. Enquist, *Venation networks and the origin of the leaf origin spectrum*, *Ecology Letters* **14**, 91 (2011).
- [23] Z. Schnepf, W. Yang, M. Antonietti, and C. Giordano, *Biotemplating of metal carbide microstructures: The magnetic leaf*, *Angewandte Chemie* **49**, 6564 (2010).
- [24] J. He, M. Mao, Y. Liu, J. Shao, Z. Jin, and D. Li, *Fabrication of Nature-Inspired Microfluidic Network for Perfusable Tissue Constructs*, *Advanced Healthcare Materials* **2**, 1108 (2013).
- [25] M. P. Bendsøe, *Optimal shape design as a material distribution problem*, *Structural Optimization* **1**, 193 (1989).
- [26] J. Deaton and R. Grandhi, *A survey of structural and multidisciplinary continuum topology optimization post 2000*, *Structural and Multidisciplinary Optimization* **49**, 1 (2014).
- [27] O. Sigmund, *A 99 line topology optimization code written in matlab*, *Structural and Multidisciplinary Optimization* **21**, 120 (2001).
- [28] A. Mellor, J. L. Domenech-Garret, D. Cheminasa, and J. I. Rosell, *A two-dimensional finite element model of front surface current flow in cells under non-uniform, concentrated illumination*, *Solar Energy* **89**, 1459 (2009).
- [29] E. Andreassen, A. Clausen, M. Schevenels, B. S. Lazarov, and O. Sigmund, *Efficient topology optimization in MATLAB using 88 lines of code*, *Structural and Multidisciplinary Optimization* **43**, 1 (2011).
- [30] T. H. Nguyen, G. H. Paulino, J. Song, and C. H. Le, *A computational paradigm for multiresolution topology optimization (MTOPT)*, *Structural and Multidisciplinary Optimization* **41**, 525 (2010).
- [31] J. Parvizian, A. Duster, and E. Rank, *Topology optimization using the finite cell method*, *Optimization and Engineering* **13** (2012).



# I

## SOLAR CELL MODELS AND OPTIMIZATION



# 2

## A TOPOLOGY OPTIMIZATION FRAMEWORK FOR SOLAR CELL METALLIZATION DESIGN

*This chapter presents a framework to optimize the front electrode patterns for solar cells. Improving the front electrode design is one of the approaches to improve the performance of the solar cells. It serves to produce the voltage distribution over the front surface such that the current flow through the solar cell is maximized. In this chapter, we develop a TO formulation for designing the front electrode pattern for side-contact and pin-up modules. Specific challenges include the nonlinearity of the physical problem and the design-dependent photocurrent loading. The greater design freedom of TO versus traditional shape optimization generates novel, efficient electrode patterns. In addition, we study the effect of mesh resolution and solar cell size on the final design. The results suggest that TO can probably be an effective method to generate designs that improve the performance of solar cells.*

---

This chapter is based on a journal article published in Structural and Multidisciplinary Optimization journal, **51**, 941-955 (2015) [1].

## 2.1. INTRODUCTION

With the increasing population and the depletion of easily accessible fossil fuel reserves, it has become necessary to find alternate and sustainable energy sources. Solar energy has enormous potential and can be one of the solutions to our search. But, further technological improvements are needed to reduce the net cost per kilowatt-hour (kWh) of power extracted from the solar cells.

A typical solar cell consists mainly of an active semiconductor layer sandwiched between a back electrode and a front metallization pattern (Fig. 2.1). The front and back metal contacts are used to extract the current generated in the semiconductor layer. This helps in reducing the power loss due to the low conductivity of the semiconductor. A considerable amount of research has been conducted in the past to optimize the solar cell designs but the front electrode pattern has received relatively little attention. The challenge of distributing the electrode material over the front surface of the solar cells can be considered as an optimization problem of minimizing the power loss due to shading caused by the electrode material (by reflecting the incident light) and the power dissipated due to the resistance generated by the solar cell components.

Flat and Milnes [2] presented an effective use of multi-level grid metallization which leads to improved performance of the solar cells. Conti [3] proposed a new approach for designing the front metal grid of photovoltaic solar cells for an arbitrary cell geometry. Burgers *et al.* [4] further improved the performance of solar cells by introducing a new metallization pattern design which consisted of a limited number of holes connecting the front side metallization to a foil at the rear side using pins. Antonini *et al.* [5] proposed a tool for comparing the performances of different contact patterns for standard solar cells. This method helped to some extent in moving from conventional to non-conventional layouts. Wen *et al.* [6] performed a detailed analysis of two different top contact grid structures based on the loss mechanisms associated with solar cells. Although some work has been done on optimizing the front metal pattern, most of these methods are based on intuitive notions and are restricted to certain predefined geometries such as the 'H-pattern'. With the advancements in printing technologies, fabrication of complex patterns is no longer a problem [7]. But the real challenge lies in designing these complex patterns such that they can improve the performance of the solar cells. Burgers [8] presented a two step approach that could eliminate the restrictions on topology of the metallization design. However, this approach involved a few heuristic calculations requiring prior information from the side of the designer.

We explore the application of topology optimization (TO) to generate new and potentially superior layouts by optimizing the front metal pattern for maximum power output. In some recent studies, TO has been used to design efficient light trapping structures for solar cells [9–11]. But, to the best of our knowledge, it has not been used to design optimal front electrode patterns for solar cells. The current generated in a small section of the solar cell depends on its local voltage. The design freedom of TO allows the designs to approach optimal local voltage distribution over the front surface, which maximizes the amount of current flowing through the solar cell. TO does not rely on an initial geometric parametrization given by the designer. Rather, it allows material distribution in any possible manner, thereby producing superior layouts which could never be achieved by shape optimization [12].

The current flowing in a solar cell and the voltage across it are nonlinearly related, resulting in a nonlinear physical model. The occurring nonlinearity due to a nonlinear voltage-dependent current source results in a path-independent nonlinear problem. Some of the previous path-independent nonlinear problems considered in topology optimization are non-linear thermoelastic problems [13], structural problems involving geometrical nonlinearity (e.g. [14, 15]) and electrothermomechanical problems [16]. Some of the previous applications of TO which show resemblance to the problem presented in this chapter are steady-state heat conduction problems [17, 18], involving the solution of a similar Poisson equation and steady-state flow of incompressible fluid [19, 20], dealing with a pressure Poisson equation. However, the problem considered here involves a strong nonlinearity. In addition, a particular feature of the solar cell front electrode design problem is that the shading caused by the electrode material distribution reduces the performance. Thus, there needs to be no volume constraint in the problem and the optimum amount of material follows from the balance between shading and resistive losses. Furthermore, the power produced by a solar cell depends on the voltage drop across the connected load. Because this voltage drop is design dependent, it is included as an additional design variable in TO.

This chapter intends to introduce and discuss the TO procedure for solar cell electrode design. A comparative study with existing designs in terms of performance is outside the scope of this work. Further, there are fabrication-related constraints which have not been yet incorporated in the proposed methodology. The results presented in this chapter cannot be directly considered as producible patterns. Additional constraints such as black-white pattern, imposing appropriate restrictions on the minimum possible feature occurring in the pattern, weak sensitivity towards fabrication imperfections *etc.* need to be considered for obtaining producible patterns.

The rest of this chapter is organized in the following manner. Section 2.2 describes the solar cell architecture, role of front electrode and provides a brief description on modelling of a solar cell using the finite element method. Section 2.3 discusses the TO formulation and the sensitivity analysis. Results and related discussions are provided in Section 3.3 with the final conclusions reported in Section 3.4.

## 2.2. SOLAR CELL ARCHITECTURE AND MODELLING

### 2.2.1. SOLAR CELL OPERATION

A solar cell is an electric device based on the photovoltaic effect and it converts the energy of light directly into electricity. Fig. 2.1 shows the configuration of a simple silicon (Si) solar cell. It consists of a semiconductor layer sandwiched between the front and back electrodes. The semiconductor layer consists of a p-doped layer and an n-doped layer joined together to form a p-n junction. The electrode grid transports the generated current to a larger main electrode, commonly called the busbar. From the busbar, electrical connections are made to adjacent cells or an external load. Sometimes, a transparent conductive oxide (TCO) layer might be added over the semiconductor layer. TCO allows most of the sunlight to pass through and helps in the conduction of current [21]. However, it also has some adverse effects, such as, unwanted absorption of a part of solar spectrum [22]. While the conductivity of TCO is very high as compared to the semicon-

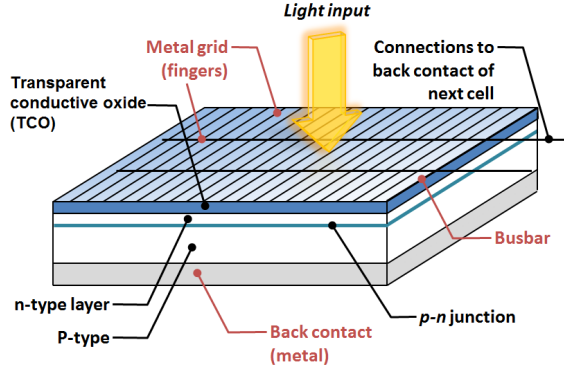


Figure 2.1: Typical Si solar cell configuration as used in this study.

ductor material, it is still several orders less than the conductivity of electrode material.

In the absence of photoillumination, the current generated in a solar cell is termed as dark current ( $I_D$ ) and is given as

$$I_D = I_0 \left( \exp \left( \frac{\tilde{q}V}{k_B T} \right) - 1 \right), \quad (2.1)$$

where  $I_0$  is the reverse bias current,  $\tilde{q}$  is the electric charge,  $V$  is the voltage,  $k_B$  denotes the Boltzmann constant and  $T$  is the temperature of the solar cell. For a detailed introduction on current generation across a p-n junction, see [23]. Under photoillumination, the net current ( $I$ ) is given as

$$I = I_L - I_D = I_L - I_0 \left( \exp \left( \frac{\tilde{q}V}{k_B T} \right) - 1 \right), \quad (2.2)$$

where ( $I_L$ ) is the photoillumination current.  $I_L$  is opposite to  $I_D$ .

In a solar cell model, resistance corresponding to each component of the cell needs to be taken into account. Fig. 2.2 represents the equivalent circuit of a solar cell. As the reverse bias current across a p-n junction is negligible as compared to the forward bias current, it can be represented by a diode. Solar cells have parasitic series and shunt resistances associated with them. Series resistance ( $R_S$ ) can include the series resistance within the semiconductor layers, metallic contacts, contact interface of the semiconductor and electrode layers and the external circuit (connecting the solar cell to the load having resistance  $R_L$ ). Since we model the local current values at every spot of the solar cell surface, the resistance of the metallic contacts and the interconnections are excluded. The series resistance of the interconnections is included as a part of the load and the electrode resistance is taken into account while computing the total current at the busbar. Shunt resistance ( $R_{SH}$ ) can be generated due to the presence of a crack in the semiconductor material. This crack causes for leakage across the p-n junction, thereby providing an alternate path to the flow of current. In this work, we neglect  $R_S$  and  $R_{SH}$  and assume the semiconductor material to have no ohmic series resistance and no sig-

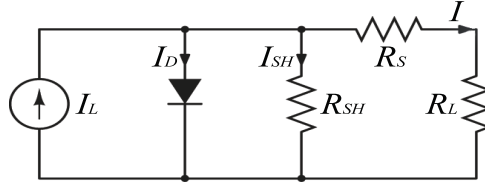


Figure 2.2: Equivalent electrical circuit for a solar cell [23].

nificant defects. In order to understand the effect of  $R_S$  and  $R_{SH}$  on the performance of the solar cell, the reader is suggested to refer [23].

The total current  $I$  generated in a solar cell is the sum of the local current densities on the whole surface area of the solar cell. To model the local phenomena in the cell, instead of the total current, we must consider the local current density ( $j$ ). This current density  $j$  depends on the local voltage distribution of the solar cell. From this point,  $V$  is used to represent the local voltage distribution and the relation between  $j$  and  $V$  is given by:

$$j = j_L - j_D = j_L - j_0 \left( \exp\left(\frac{qV}{k_B T}\right) - 1 \right), \quad (2.3)$$

where  $j$ ,  $j_L$ ,  $j_D$  and  $j_0$  are net, photoilluminated, dark and reverse bias current densities, respectively at a spot of the solar cell. Fig. 2.3 shows the current density-voltage curve for a solar cell. This curve can be defined for a single spot of the solar cell as well as for the complete cell. Here, we discuss the  $j$ - $V$  curve for a single spot of the solar cell. From the  $j$ - $V$  curve, it can be observed that  $j$  and  $j_D$  increase non-linearly with voltage. Under open-circuit condition, there is no net flow of current across the p-n junction and the voltage drop across it is termed as open-circuit voltage ( $V_{OC}$ ). The output power at  $V_{OC}$  is zero. Under short-circuit condition, the net current density across the p-n junction is termed as short-circuit current density ( $j_{SC}$ ). In this condition, the voltage across the cell is zero and the output power is again zero. From the power density curve, it can be seen that there exists a point in between where output power is maximum. The current density and voltage values corresponding to this point are represented by  $j_{mp}$  and  $V_{mp}$ , respectively. For every unique semiconductor material, a new set of values for  $j_{mp}$  and  $V_{mp}$  might exist. Because of the non-linear relation between current and voltage for a solar cell, identifying the maximum power point for a given solar cell is an optimization problem itself. We observe that the performance of the solar cell depends on the local voltages. Thus, it depends on the connected load and therefore, we use the busbar voltage as one of the design variables in the optimization.

### 2.2.2. ROLE OF FRONT METAL ELECTRODE

The net current generated in a solar cell needs to be extracted and passed into the attached load. Due to the very low conductivity of the semiconductor material, connecting the load directly to the semiconductor through point nodes will lead to a high value of  $R_S$  and, consequently, a considerable amount of power will be dissipated. Fig. 2.4 shows two different solar cells, A and B. Cell A consists of only a metal contact at the left side and Cell B has a left metal contact and two fingers extending on the surface of the

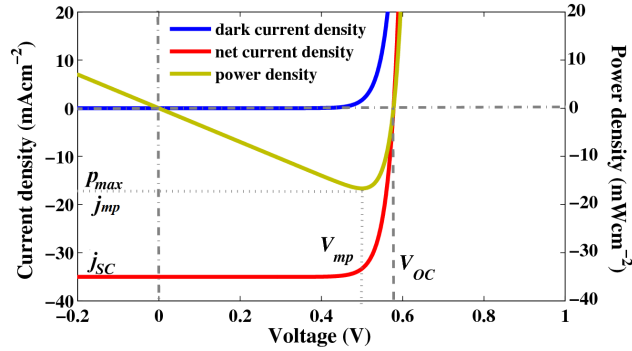


Figure 2.3: Current density-voltage characteristics curves for a solar cell. Also shown is the power density as a function of voltage. Maximum power output is obtained when the cell operates at  $V_{mp}$ .

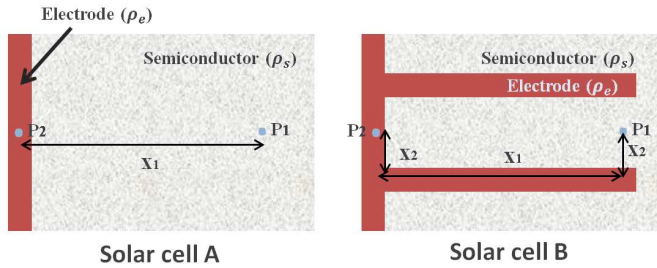


Figure 2.4: Front surface of solar cells A (non-metallized) and B (metallized with two fingers).

semiconductor. The metal contact on the left side is assumed to be directly connected to the external load. Considering the point sources of current,  $P_1$  and  $P_2$ , which have same locations in Cells A and B, the ratio of resistance of path from  $P_1$  to  $P_2$  in A ( $R_A$ ) to that in B ( $R_B$ ) can be written as

$$\frac{R_A}{R_B} = \frac{\rho_s x_1}{\rho_s x_2 + \rho_e (x_1 + x_2)},$$

where  $\rho_s$  and  $\rho_e$  are the resistivities of semiconductor and electrode, respectively, such that  $\rho_s \gg \rho_e$ . Assuming that  $x_1 = 5x_2$ , it is seen that  $R_A \sim 5R_B$ . The addition of a metal electrode pattern over the semiconductor surface provides low resistance path for the flow of current on the front surface. Thus, the amount of power dissipated in the form of resistive losses is reduced.

From Fig. 2.4, we inferred that the metallization of semiconductor surface reduces the series resistance of a solar cell. But, covering a part of semiconductor surface by a metal electrode shades that part of the surface, thereby cutting off a part of the incident solar energy. Because the current is assumed to be perpendicular to the front surface, the photoillumination current is reduced only in the shaded regions. Fig. 2.5 shows power lost in a solar cell as a function of the amount of electrode material used on the front surface. It describes the qualitative effect of series resistance and shading over the power lost in a solar cell. The introduction of a metal pattern over the semiconductor surface

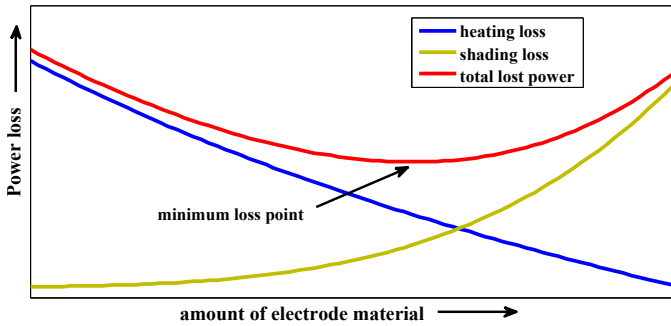


Figure 2.5: Qualitative effect of series resistance and shading on total power lost in a solar cell, in relation to the amount of front electrode material.

decreases the series resistance and the resistive losses are reduced. At the same time, shading increases, blocking more of the incident solar energy and reducing the output power. The red curve shown in Fig. 2.5 denotes the sum total of power losses due to series resistance and shading. It can be seen that there exists a point on the curve, where the total power loss achieves a minimum value. This illustrates that, in an electrode optimization, there is no need to bound the amount of electrode material. The optimum amount will result as a compromise between resistive and shading losses.

### 2.2.3. FINITE ELEMENT MODEL

The performance of a solar cell can be analyzed using the finite element method (FEM). Fig. 2.6 shows the front surface of a solar cell. The presence of a TCO layer on the front surface helps to reduce the resistive losses. The resistivity of the electrode as well as the TCO layer is several orders less as compared to that of the semiconductor layer. Therefore, it is unlikely that there are large side effects along the edges of the electrode and current generated in the semiconductor layer can be assumed to flow perpendicular to the front surface [24]. Once arrived there, the current flows along the surface to reach the electrode. We model this surface using 2D finite elements.

The physics of the conductive layer can be explained using the reformulated version of Ohm's law [25], stated as

$$\mathbf{j} = \sigma \mathbf{E}, \quad (2.4)$$

where  $\mathbf{j}$ ,  $\sigma$  and  $\mathbf{E}$  are the current density, material dependent conductivity and the electric field in a given area, respectively. For a conservative field, the electric field can be expressed as the gradient of potential as

$$\mathbf{E} = -\nabla V, \quad (2.5)$$

where  $V$  denotes the electric potential. Based on Kirchhoff's circuit law, the charge conservation equation can be written as

$$\nabla \cdot \mathbf{j} = -\frac{\partial \bar{\rho}}{\partial t}, \quad (2.6)$$

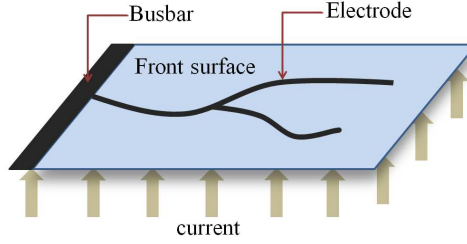


Figure 2.6: Schematic diagram of the front surface of a solar cell.

where  $\bar{\rho}$  is the enclosed charge density. Using Eq. 2.4, 2.5 and 2.6, the Poisson equation for electrical conductivity can be stated as

$$\sigma \nabla^2 V = \frac{\partial \bar{\rho}}{\partial t} . \quad (2.7)$$

This equation is similar to the Poisson equation that describes heat flow problems.

After finite element discretization of Eq. 2.7, the matrix equations for the solar cell problem can be stated as

$$\mathbf{G}\mathbf{V} = \mathbf{I}, \quad (2.8)$$

where  $\mathbf{G}$ ,  $\mathbf{V}$  and  $\mathbf{I}$  are the total conductivity matrix, voltage vector and current vector, respectively. The design area is divided into a finite number of elements. We use quadrilateral elements with bilinear shape functions as described in [26]. Eq. 2.2 shows that there exists a non-linearity between current and voltage of a solar cell. Due to this non-linearity, Eq. 2.8 cannot be solved directly. Thus, we express Eq. 2.8 in the form of a residual equation as

$$\mathbf{R}(\mathbf{V}) = \mathbf{G}\mathbf{V} - \mathbf{I}(\mathbf{V}) = 0, \quad (2.9)$$

where  $\mathbf{R}$  is the residual. This equation is solved using Newton method. The iterations are started with some initial guess for  $\mathbf{V}$  and it is updated at every step as follows,

$$\mathbf{V}_{k+1} = \mathbf{V}_k - \left[ \frac{d\mathbf{R}}{d\mathbf{V}_k} \right]^{-1} \mathbf{R}. \quad (2.10)$$

In the optimization process, we restart the Newton iterations from the solution of the preceding design.

## 2.3. TOPOLOGY OPTIMIZATION FORMULATION

### 2.3.1. SOLAR CELL CONFIGURATIONS AND PARAMETERS

We use TO to determine the optimal front electrode pattern that achieves maximum power output for two different configurations (Fig. 2.7). Both these solar cells are rectangular in shape. The first configuration is a side-contact model (Fig. 2.7a) where the left side boundary is kept at voltage  $V_{bus}$ . We assume that this boundary is directly connected to the busbar, which runs on the left side of the cell. The second configuration is a pin-up module (PUM). In the PUM model presented here (Fig. 2.7b), the centroid is

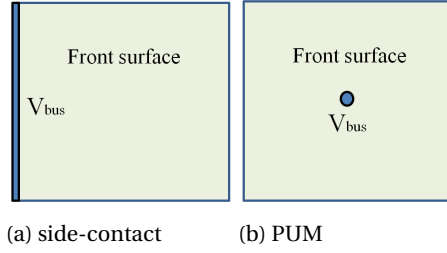


Figure 2.7: Solar cell geometries considered in this study. The external load connects to the cell via the busbar, at voltage  $V_{bus}$ .

kept at voltage  $V_{bus}$ . The electrode, starting from the centroid, runs all the way through the cell towards the rear side [27]. In general, for a PUM solar cell, the panel connections are done on the rear side of the solar cell. Contrary to the first configuration, this configuration does not have a busbar on the left, which accounts for lower shading losses.

In the considered numerical examples, we use the following relation between current and voltage for a solar cell.

$$j = 310 - 0.006(\exp(16.4V)). \quad (2.11)$$

In Eq. 2.11, the units of  $j$  and  $V$  are  $A/m^2$  and volts, respectively. This equation is based on the measurements done at TNO Eindhoven. These values were obtained for an input power density of  $1000W/m^2$  of sunlight intensity under standard conditions. The front surface is considered to be a combination of the TCO layer and metal electrode having thicknesses of  $200nm$  and  $10\mu m$ , respectively. The conductivities for the TCO layer and the metal electrode are  $10^5 S/m$  and  $10^7 S/m$ , respectively.

### 2.3.2. ELEMENT CONDUCTIVITY MATRIX

The element conductivity matrix  $\mathbf{G}_e$  is constructed from  $\mathbf{G}_0$  using the modified simplified isotropic material with penalization (SIMP) interpolation scheme [28, 29]. Thus,  $\mathbf{G}_e$  can be stated as

$$\mathbf{G}_e = \mathbf{G}_e(\rho_e) = (\sigma_s^{TCO} + \rho_e^q(\sigma_s^m - \sigma_s^{TCO}))\mathbf{G}_0, \quad (2.12)$$

where  $\sigma_s^{TCO}$  and  $\sigma_s^m$  are the sheet conductivity values for the TCO layer and metal electrode, respectively.  $\rho_e$  refers to element density describing the volume fraction of element  $e$  occupied by the metal electrode,  $q$  is the SIMP penalization power.  $\mathbf{G}_0$  for this problem is the same as used in thermal problems. For square elements, it can be written as

$$\mathbf{G}_0 = \begin{bmatrix} 2/3 & -1/6 & -1/3 & -1/6 \\ -1/6 & 2/3 & -1/6 & -1/3 \\ -1/3 & -1/6 & 2/3 & -1/6 \\ -1/6 & -1/3 & -1/6 & 2/3 \end{bmatrix}. \quad (2.13)$$

For the electrode design problem presented in this chapter, the value of  $p$  used is 3. The contributions from all the elements are assembled together to form the total conductivity matrix.

### 2.3.3. CALCULATING ELEMENT CURRENT DENSITY

It is assumed that the current in the TCO layer is perpendicular to the surface and the current density is constant over the element. This constant current density is computed by averaging over the element using  $2 \times 2$  Gauss quadrature. The shape function vector ( $\Phi$ ) is expressed as

$$\Phi(x, y)^\top = [ \phi_1 \quad \phi_2 \quad \phi_3 \quad \phi_4 ]. \quad (2.14)$$

The local voltage information  $u(x, y)$  corresponding to an element can be computed as follows

$$v(x, y) = \Phi(x, y) \cdot \mathbf{v}, \quad (2.15)$$

where  $\mathbf{v}$  is the nodal voltage vector expressed as

$$\mathbf{v}^\top = [ v_1 \quad v_2 \quad v_3 \quad v_4 ]. \quad (2.16)$$

The current density at each of the Gauss points can be computed using the following equation

$$j(x, y) = j_L^* + j_0 (\exp(\beta \Phi(x, y) \cdot \mathbf{v}) - 1), \quad (2.17)$$

where  $\beta$  is equal to  $\frac{q}{k_B T}$ . The element current density is the arithmetic mean of the current densities at the 4 nodes. The presence of electrode material over the front surface blocks a part of the sunlight. This leads to reduction in  $j_L$ . The term  $j_0$  depends only on the properties of the semiconductor material and does not get affected by shading. The term  $j_L^*$  is the corrected current density which incorporates the effect of shading and is expressed as:

$$j_L^* = j_L (1 - \rho_e)^r. \quad (2.18)$$

Here,  $\rho_e$  is the volume fraction of an element occupied by the electrode material and  $r$  is the penalization power. We tested the models for several different values of  $r$  and it was observed that  $r$  equal to 3 was a good choice. A lower value of  $r$  led to a gray design, while higher values hindered the convergence process of TO.

### 2.3.4. OPTIMIZATION PROBLEM

The solar cell power maximization problem can be stated as an unconstrained optimization problem. The objective of our problem is to maximize the power output from the solar cell. We use Kirchoff's law according to which all the generated current in the domain must pass through the busbar which has been given potential  $V_{bus}$ . Thus the power output  $P_{out}$  from the solar cell can be expressed as:

$$P_{out} = V_{bus} A_e \sum J_e, \quad (2.19)$$

where  $A_e$  is the area of one element in the design domain and  $J_e$  is the element current density. The objective function  $\mathcal{J}(\mathbf{s})$  is given as:

$$\begin{aligned} \min_{\mathbf{s}} \quad & \mathcal{J}(\mathbf{s}), \\ \text{with} \quad & \mathcal{J}(\mathbf{s}) = -P_{out}, \end{aligned} \quad (2.20)$$

where  $\mathbf{s}$  denotes the set of design variables. To perform the optimization, we use the MATLAB subroutine of method of moving asymptotes [30] provided by Krister Svanberg.

### 2.3.5. SENSITIVITY ANALYSIS

The optimizer requires information regarding sensitivity of the response with respect to each of the design variables. In order to compute these sensitivities, we use the adjoint method (see [31] and references therein). In case of the considered path-independent nonlinear model, adjoint sensitivity analysis of the response  $\mathcal{J}$  requires only a back-substitution. The augmented response  $\hat{\mathcal{J}}$  is expressed as

$$\begin{aligned} \hat{\mathcal{J}}(\mathbf{s}) &= \mathcal{J}(\mathbf{V}_f(\mathbf{s}), \mathbf{V}_p(\mathbf{s}), \mathbf{s}) + \boldsymbol{\lambda}^\top \mathbf{R}(\mathbf{V}_f(\mathbf{s}), \mathbf{V}_p(\mathbf{s}), \mathbf{s}) \\ &= \mathcal{J} + \begin{bmatrix} \lambda_f \\ \lambda_p \end{bmatrix}^\top \left( \begin{bmatrix} \mathbf{G}_{ff} & \mathbf{G}_{fp} \\ \mathbf{G}_{pf} & \mathbf{G}_{pp} \end{bmatrix} \begin{bmatrix} \mathbf{V}_f \\ \mathbf{V}_p \end{bmatrix} - \begin{bmatrix} \mathbf{I}_f(\mathbf{V}_f, \mathbf{V}_p) \\ \mathbf{I}_p(\mathbf{V}_f, \mathbf{V}_p) \end{bmatrix} \right), \end{aligned} \quad (2.21)$$

where the subscript notations  $f$  and  $p$  denote free degrees and prescribed degrees of freedom, respectively. The design vector  $\mathbf{s}$  can be expressed as

$$\mathbf{s} = [\rho_1, \rho_2, \dots, \rho_n, V_{bus}],$$

where  $\rho_n$  is the density of the  $n^{\text{th}}$  element and  $V_{bus}$  is the busbar voltage of the solar cell. Eq. 2.21 holds for any value of  $\boldsymbol{\lambda}$ . Thus, we reduce it by putting  $\lambda_p$  equal to  $\mathbf{0}$  and get

$$\hat{\mathcal{J}} = \mathcal{J} + \lambda_f^\top (\mathbf{G}_{ff} \mathbf{V}_f + \mathbf{G}_{fp} \mathbf{V}_p) - \lambda_f^\top \mathbf{I}_f. \quad (2.22)$$

The derivative of  $\hat{\mathcal{J}}$  with respect to  $\mathbf{s}$  can be expressed as

$$\begin{aligned} \frac{d\hat{\mathcal{J}}}{d\mathbf{s}} &= \frac{\partial \mathcal{J}}{\partial \mathbf{s}} + \lambda_f^\top \left( \frac{\partial \mathbf{G}_{ff}}{\partial \mathbf{s}} \mathbf{V}_f + \frac{\partial \mathbf{G}_{fp}}{\partial \mathbf{s}} \mathbf{V}_p - \frac{\partial \mathbf{I}_f}{\partial \mathbf{s}} \right) + \\ &\quad \left( \lambda_f^\top \mathbf{G}_{ff} + \frac{\partial \mathcal{J}}{\partial \mathbf{V}_f} - \lambda_f^\top \frac{\partial \mathbf{I}_f}{\partial \mathbf{V}_f} \right) \frac{d\mathbf{V}_f}{d\mathbf{s}} + \\ &\quad \left( \lambda_f^\top \mathbf{G}_{fp} + \frac{\partial \mathcal{J}}{\partial \mathbf{V}_p} - \lambda_f^\top \frac{\partial \mathbf{I}_f}{\partial \mathbf{V}_p} \right) \frac{d\mathbf{V}_p}{d\mathbf{s}}. \end{aligned} \quad (2.23)$$

For eliminating  $\frac{d\mathbf{V}_f}{d\mathbf{s}}$ , we define the following adjoint problem:

$$\begin{aligned} \lambda_f^\top \mathbf{G}_{ff} + \frac{\partial \mathcal{J}}{\partial \mathbf{V}_f} - \lambda_f^\top \frac{\partial \mathbf{I}_f}{\partial \mathbf{V}_f} &= \mathbf{0}, \text{ which yields:} \\ \lambda_f^\top &= - \left( \mathbf{G}_{ff} - \frac{\partial \mathbf{I}_f}{\partial \mathbf{V}_f} \right)^{-1} \frac{\partial \mathcal{J}}{\partial \mathbf{V}_f}. \end{aligned} \quad (2.24)$$

This equation involves the same tangent operator as used in the Newton iterations of the nonlinear analysis, so only a back-substitution is required to solve for the adjoint vector. Thus, we obtain:

$$\begin{aligned} \frac{d\hat{\mathcal{J}}}{d\mathbf{s}} &= \frac{\partial \mathcal{J}}{\partial \mathbf{s}} + \lambda_f^\top \left( \frac{\partial \mathbf{G}_{ff}}{\partial \mathbf{s}} \mathbf{V}_f + \frac{\partial \mathbf{G}_{fp}}{\partial \mathbf{s}} \mathbf{V}_p - \frac{\partial \mathbf{I}_f}{\partial \mathbf{s}} \right) + \\ &\quad \left( \lambda_f^\top \mathbf{G}_{fp} + \frac{\partial \mathcal{J}}{\partial \mathbf{V}_p} - \lambda_f^\top \frac{\partial \mathbf{I}_f}{\partial \mathbf{V}_p} \right) \frac{d\mathbf{V}_p}{d\mathbf{s}}. \end{aligned} \quad (2.25)$$

The voltage at the prescribed nodes is independent of the density distribution. Thus, we have

$$\frac{d\mathbf{V}_p}{d\rho} = \mathbf{0}, \quad (2.26)$$

$$\frac{d\mathbf{V}_p}{dV_{bus}} = \mathbf{1}. \quad (2.27)$$

The conductivity matrix depends only on the material properties. Thus, from Eq. 2.12, we have

$$\frac{\partial \mathbf{G}_e}{\partial \rho_e} = q\rho_e^{q-1}(\sigma_s^m - \sigma_s^{TCO})\mathbf{G}_0. \quad (2.28)$$

$$\text{Also, we can write } \frac{\partial \mathbf{G}_e}{\partial V_{bus}} = \mathbf{0}. \quad (2.29)$$

### 2.3.6. FILTERING

To ensure that the optimal design does not have very fine branches and to avoid the formation of checker-board patterns, we use a density filter [15, 32]. The density filter modifies the actual densities as follows:

$$\tilde{\rho}_e = \frac{1}{\sum_{i \in N_e} H_{ei}} \sum_{i \in N_e} H_{ei} \rho_i. \quad (2.30)$$

Here,  $\tilde{\rho}_e$  is the filtered density and  $N_e$  is the set of elements  $i$  whose center-to-center distance from element  $e$  ( $\Delta(e, i)$ ) is smaller than the filter radius  $r_{min}$ .  $H_{ei}$  is a weight factor defined as:

$$H_{ei} = \max(0, r_{min} - \Delta(e, i)). \quad (2.31)$$

The sensitivities with respect to the design variables  $\rho_j$  are obtained from the filtered densities using the following chain rule:

$$\frac{df}{d\rho_j} = \sum_{e \in N_j} \frac{1}{\sum_{i \in N_e} H_{ei}} H_{je} \frac{df}{d\tilde{\rho}_e}. \quad (2.32)$$

## 2.4. RESULTS AND DISCUSSIONS

To demonstrate the effectiveness of TO for front metallization design, we apply it to several different cases for the side-contact model and PUM solar cells. For both the models, we report 4 instances each and their corresponding  $V_{bus}$  and efficiency ( $\eta$ ) values. The efficiency ( $\eta$ ) is calculated as

$$\eta = \frac{P_{out}/A_c}{p_{inp}} \times 100\%, \quad (2.33)$$

where  $P_{out}$  and  $A_c$  are the output power and area of the solar cell and  $p_{inp}$  is the input power density of the sun which is assumed to be  $1000\text{Wm}^{-2}$  under standard conditions. The configurations used in this study are mentioned in Section 2.3.1. The essential boundary condition for these configurations is that the connection points to the

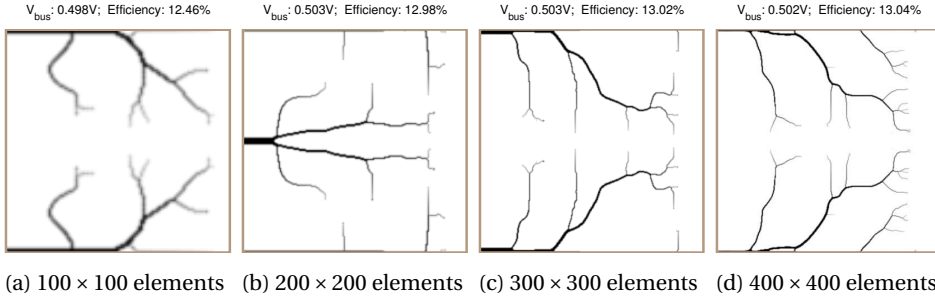


Figure 2.8: Front electrode patterns for side-contact solar cells with different mesh resolutions at constant value of  $r_{min}$  ( $r_{min} = 1.5$  element widths).

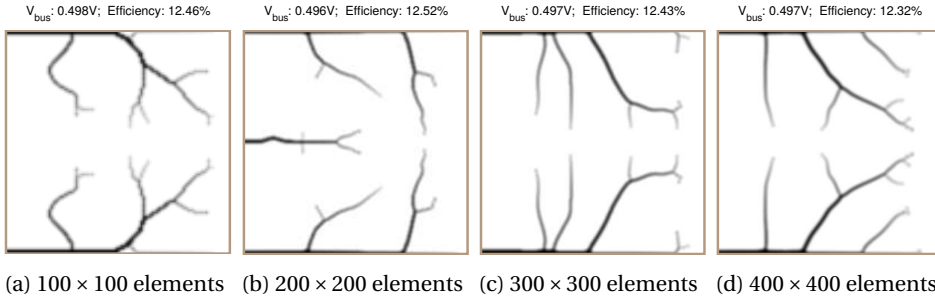


Figure 2.9: Front electrode patterns for side-contact solar cells with different mesh resolutions using mesh-independent density filter.

busbar are kept at voltage  $V_{bus}$ . The natural boundary condition is that the current flow across the other boundaries is zero. For all the cases, we use an initial design where the whole front surface is covered with the electrode material. We analyze the current density and voltage distributions on the front surface of the solar cell for the optimal front designs obtained using TO. Furthermore, the effects of mesh resolution and the solar cell size on the performance are studied for both the configurations and are reported in the subsections below. The obtained designs typically resemble branching sparse electrode networks, which have some similarity to designs resulting from thermal/electrical power dissipation minimization problems (e.g. [17]). However, the problem considered here is of a different nature due to the nonlinear design-dependent current source and the absence of a volume constraint. The obtained volume fractions are typically low (5-10%). For more examples, see [33].

### 2.4.1. EFFECT OF MESH RESOLUTION

To understand the effect of mesh resolution over the final output design, we analyze the side-contact and PUM solar cells at 4 different mesh resolutions. The dimensions of the solar cells are assumed to be  $1.5\text{cm} \times 1.5\text{cm}$  and the number of elements in the design space corresponding to the 4 cases are  $100 \times 100$ ,  $200 \times 200$ ,  $300 \times 300$  and  $400 \times 400$ , respectively. Fig. 2.8 presents the optimized front electrode patterns for the side-contact

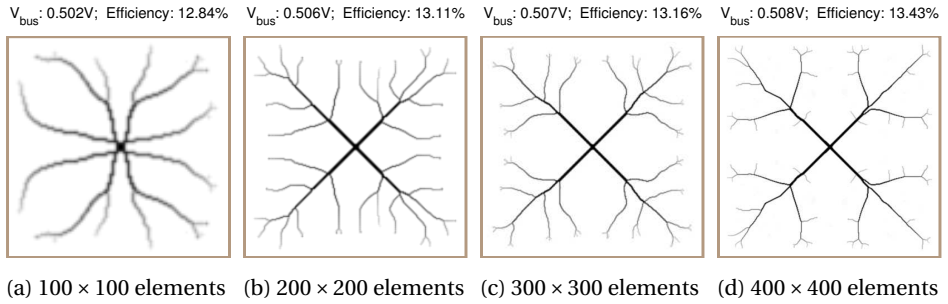


Figure 2.10: Front electrode patterns for PUM solar cells with different mesh resolutions at constant value of  $r_{min}$  ( $r_{min} = 1.5$  element widths).

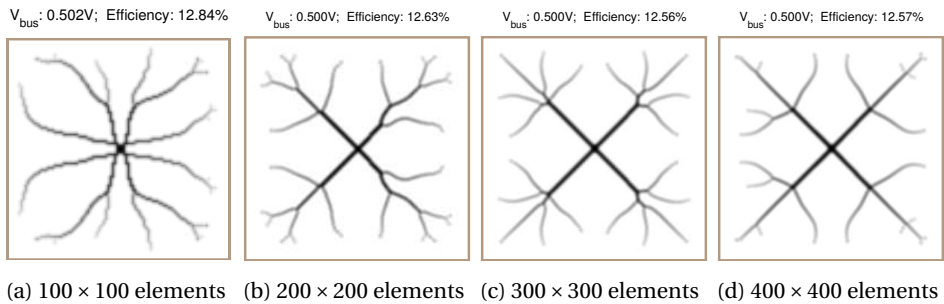


Figure 2.11: Front electrode patterns for PUM solar cells with different mesh resolutions using mesh-independent density filter.

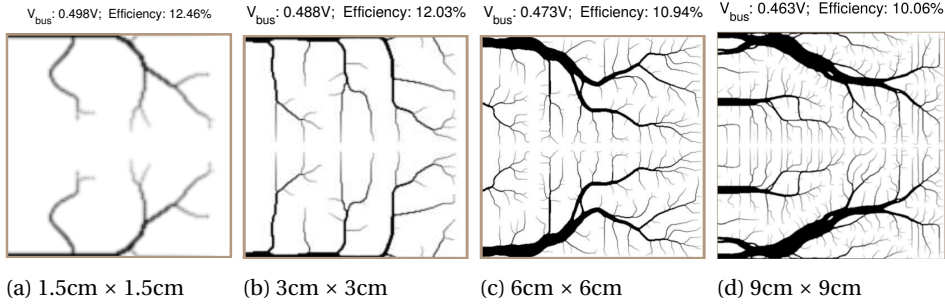


Figure 2.12: Optimized front electrode patterns for side-contact solar cells of different sizes. The mesh resolution for all the cases is same and the size of an element in all the cases is  $0.015\text{cm} \times 0.015\text{cm}$ .

solar cells with  $r_{min}$  equal to 1.5 element widths for all the 4 cases. Fig. 2.8b shows a design which does not look identical to the designs obtained at other mesh resolutions and this can possibly be due to the presence of a large number of local optima in the design domain.

It is observed that with increasing mesh resolution, the performance of the solar cell improves. This is due to the fact that increasing the number of elements in a fixed design space provides increased spatial freedom in the determination of the optimum front electrode design. For high resolution meshes, we observe that the design tends to contain very fine branches which might not be feasible for fabrication. To overcome this problem, we use mesh-independent filtering approach such that  $r_{min}$  remains constant at  $0.225\text{mm}$  (Fig. 2.9). It is observed that the finer branches are removed. Contrary to the expectations that the mesh independent filter should not affect the performance, we observe that the efficiency of the solar cell slightly decreases for designs with higher mesh resolutions. Fig. 2.10 and 2.11 show the optimal front designs for the 4 cases for PUM solar cells for constant filter and mesh-independent filter, respectively. For a constant value of  $r_{min}$  (equal to 1.5 element widths), increasing the mesh resolution improves the solar cell performance but tends to develop very fine unwanted branches. The mesh-independent filter removes these fine branches. But, similar to the observations for the side-contact designs, the performance of the solar cell slightly decreases for increased mesh resolutions (Fig. 2.11). This is because, elimination of the finer branches leads to increased resistive losses in those sections of the front surface, thereby shifting the final design from its optimum.

#### 2.4.2. EFFECT OF SOLAR CELL SIZE

For a given set of parameters, changing the solar cell size largely affects its performance. Fig. 2.12 and 2.13 show 4 solar cells of different sizes for the side-contact and PUM models, respectively. The dimensions of the 4 solar cells for both the models are  $1.5\text{cm} \times 1.5\text{cm}$ ,  $3\text{cm} \times 3\text{cm}$ ,  $6\text{cm} \times 6\text{cm}$  and  $9\text{cm} \times 9\text{cm}$ , respectively. To keep the physical mesh resolution equal for the 4 cases, the number of elements are taken to be  $100 \times 100$ ,  $200 \times 200$ ,  $400 \times 400$  and  $600 \times 600$ , respectively. For both the models, it is observed that the performance of the solar cell reduces with its increasing size. A reason could be that

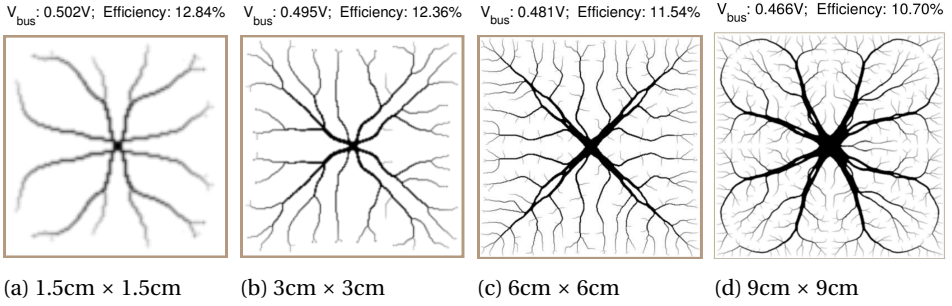


Figure 2.13: Optimized front electrode patterns for PUM solar cells of different sizes. The mesh resolution for all the cases is same and the size of an element in all the cases is  $0.015\text{cm} \times 0.015\text{cm}$ .

the finer topology mesh resolution for the larger cells leads to higher perimeter, thereby a larger area with gray values at the boundaries. Thus, we do another analysis with constant topology mesh resolution. Fig. 2.14 and 2.15 show the cases of Fig. 2.12 and 2.13, respectively, but with constant mesh size of  $600 \times 600$  in all the cases. It is observed that the performance of solar cell still reduces with the increasing size. Also, the front surface of larger cells is found to use a larger volume fraction of electrode material as compared to the smaller cells. One of the possible explanations could be that with increasing solar cell size, the current from the farthest regions to the busbar has to travel a longer distance, leading to increased resistive losses. If we simply scale the design of smaller cells to fit on a larger physical domain, the distance of the farthest elements from the electrode increases. This leads to increased resistive losses for the flow of current from these elements to the busbar and the overall performance of the cell is reduced. To extract maximum current from these elements, TO tries to increase the thickness of the metal electrode fingers and develop more sub-branches. This leads to increased shading, but helps to reduce the resistive losses to some extent.

Though reducing the size of a solar cell improves its performance when considered separately, it will increase the amount of space being occupied by the busbars when constructing a complete solar panel. Thus, for maximum performance of a complete solar panel, there exists an optimum size for each of the constituting solar cells. Given information on the busbar dimensions, the proposed electrode topology optimization can be used to find the optimal cell size and electrode layout.

### 2.4.3. VOLTAGE AND CURRENT DENSITY DISTRIBUTION

Fig. 2.16 shows the front electrode design and current density and voltage distributions for two different solar cell sizes for the side-contact (Fig. 2.16a, b) and PUM (Fig. 2.16c, d) solar cells. In Section 2.4.2, we discussed that for a larger solar cell, more electrode material has to be deposited on the front surface. This leads to increased shading, thereby reducing the solar cell output. From Fig. 2.16, we see that with increased solar cell size, the voltage contrast on the front surface increases. This causes for reduction in the amount of current for the elements whose local voltage value is very high as compared to  $V_{mp}$  (value of  $V_{mp}$  mentioned in Fig. 2.18a). Comparing Fig. 2.16a with Fig. 2.16b and Fig.

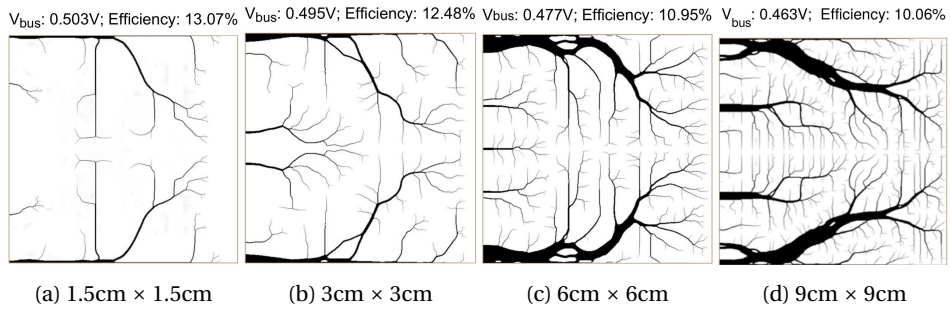


Figure 2.14: Optimized front electrode patterns for side-contact solar cells of different sizes. The topology mesh for all the cases is same and comprises of  $600 \times 600$  elements.

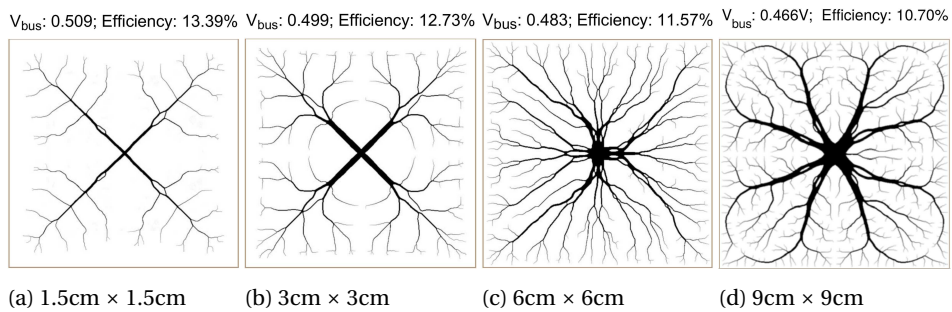


Figure 2.15: Optimized front electrode patterns for PUM solar cells of different sizes. The topology mesh for all the cases is same and comprises of  $600 \times 600$  elements.

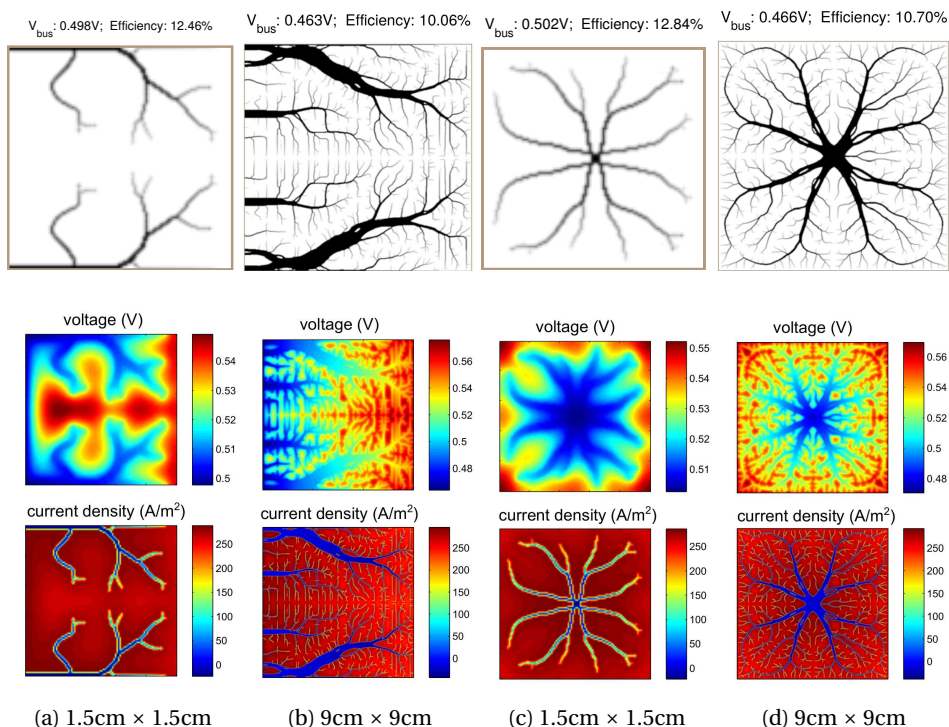


Figure 2.16: Front electrode patterns, out-of-plane current density distributions and voltage distributions for side-contact (a and b) and PUM (c and d) solar cells obtained using topology optimization.

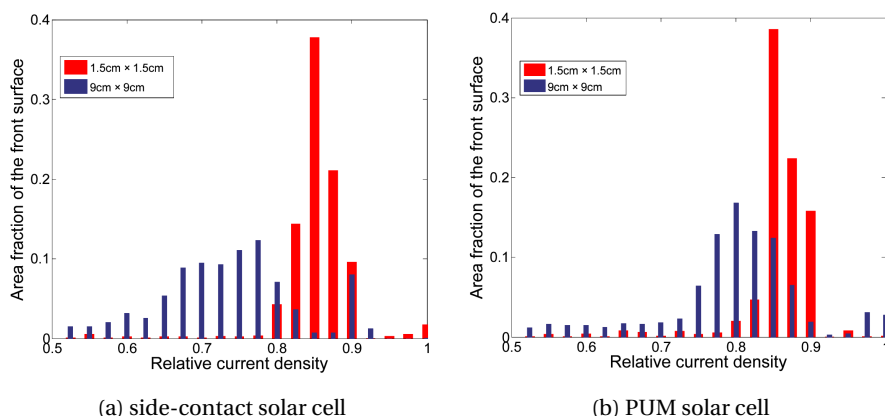


Figure 2.17: Area fractions of the front surface corresponding to different values of relative current density. Relative current density here, is the actual current density value normalized by the maximum current density value on the front surface.

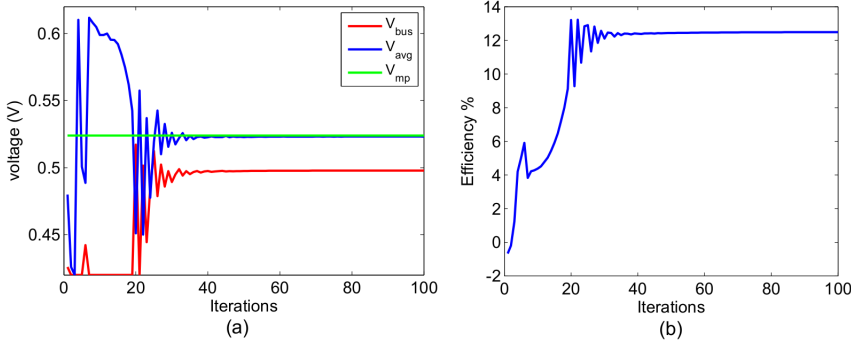


Figure 2.18: Voltage vs. Iterations plot and Efficiency vs. Iterations plot for a side-contact solar cell of dimensions  $1.5\text{cm} \times 1.5\text{cm}$  and mesh size of  $100 \times 100$  elements. Because of the evolving electrode design, the average voltage in the cell ( $V_{avg}$ ) quickly approaches the ideal voltage at which maximum power is produced ( $V_{mp}$ ). The voltage at the busbar ( $V_{bus}$ ) is adjusted accordingly by the optimizer.

2.16c with Fig. 2.16d, we observe that on an average, the current density is higher for smaller solar cells as compared to the larger ones. A better interpretation can be deduced from the bar graphs shown in Fig. 2.17. It shows the area fraction of the front surface corresponding to different values of relative current density (RCD). RCD is obtained by normalizing the current density values with the maximum current density value obtained on the front surface. For small cells ( $1.5\text{ cm} \times 1.5\text{ cm}$ ), a large fraction of the front surface has RCD values greater than 0.8. On the other hand, for larger cells ( $9\text{cm} \times 9\text{cm}$ ), only a small part of the front surface has high RCD values. Thus, for larger solar cells, significant part of the photoillumination current density is lost due to the high voltage contrast on the front surface. A possible way to overcome this problem could be to have a design with uniform voltage difference between the front and the back surface of the solar cell. This requires the optimization of the rear surface electrode as well. Thus, optimizing the front and rear surfaces together could help in achieving a design which could produce a uniform voltage distribution throughout, thereby improving the solar cell performance.

The voltage distribution on the front surface of the solar cell affects the output power. In Section 2.2.1, we discussed that for every p-n junction, there exists a voltage value ( $V_{mp}$ ) for which the power output is maximum. Fig. 2.18a shows the variation of  $V_{bus}$ ,  $V_{avg}$  and  $V_{mp}$  with every iteration during the process of TO. Here,  $V_{avg}$  is the average of the voltages at all the nodes of the front surface of the solar cell. Fig. 2.18 corresponds to a solar cell of dimensions  $1.5\text{ cm} \times 1.5\text{ cm}$  and the design domain consisting of  $100 \times 100$  elements.

During initial iterations, the optimizer tends to assign very low values to  $V_{bus}$ . This is because, initially, due to the lack of sufficient electrode material on the front surface, there are large voltage contrasts. Another possibility could be to start with an initial model which has large amount of electrode material on the front surface. However, in our experience, the optimizer does not favor this design and moves quickly towards zero electrode material, which could possibly be due to the increased shading imposed by

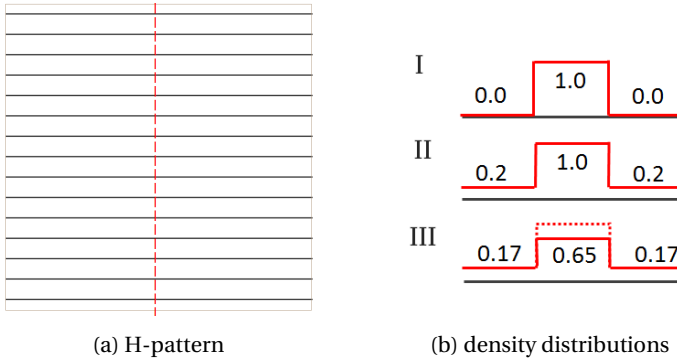


Figure 2.19: H-pattern and the density distribution corresponding to an electrode finger for 3 different cases.

this initial design. Fig. 2.18b shows the efficiency of the solar cell obtained at every iteration. It is observed that the efficiency obtained during first iteration is negative. Because  $V_{bus}$  is positive, this can only be possible if the total current on the front surface is negative. This can happen when the voltage values of some nodes are far higher than the  $V_{mp}$ . Fig. 2.3 shows that for these voltage points, we get high value of negative current which tends to make the overall current as negative. This leads to negative efficiency being reported during that iteration. As the electrode design evolves, the voltage in the cell becomes more evenly distributed and  $V_{avg}$  tends to move closer to  $V_{mp}$  (Fig. 2.18a). At the same time,  $V_{bus}$  achieves an optimal value. This optimal value of  $V_{bus}$  lies below  $V_{mp}$  because the finite conductivity of the front electrode will result in increasing voltages away from the busbar. For the case presented here, we get an optimal design after about 50 iterations as seen from Fig. 2.18b.

#### 2.4.4. PRELIMINARY COMPARISON WITH EXISTING DESIGNS

In this chapter, no detailed comparison is made between our optimized designs and the conventional H-pattern electrodes. In our opinion, such a comparison would be premature and inaccurate at this stage. However, we conducted some preliminary comparisons and the results indicate that the designs currently obtained using TO are not superior to contemporary H-pattern designs. Using the same physical model as applied for the TO studies, we optimized the H-pattern for line position, linewidth and  $V_{bus}$  for a black-white design (Fig. 2.19a). This resulted in 13.52% efficiency for 1.5 by 1.5 cm cells. The designs we obtained using TO on finer grids deliver an efficiency of above 13% (Fig. 2.14, Fig. 2.15) but do not exceed this. The performance of the TO-optimized designs is reduced since the obtained results are not completely black-white designs. The applied consistent density filter results in intermediate densities in transition regions at the edges of the electrodes. Because of the double penalization on conductivity and current density, the output power of the gray designs is expected to be lower as compared to the shape-optimized conventional designs.

Thus, before correctly comparing with existing designs, a black-white design needs to be obtained using the TO methodology. Simply thresholding the gray designs proves a too crude operation. As a reverse approach, we tested the performance of H-patterns

perturbed with gray values. Fig. 2.19b shows the cross-sectional view of an electrode finger (across the dashed red line shown in Fig. 2.19a) for 3 different cases. Case (I) corresponds to a black-white design, where the densities of center element and its neighbours are set to 1 and 0, respectively. Note that this design cannot be obtained using TO with a density filter. Case (II) shows a perturbed design, where the the density of the neighbouring elements is set to 0.2. Due to the gray values, the performance falls from 13.52% to 12.68%. Case (III) shows a H-pattern post-processed using density-filtering ( $r_{min} = 1.5$ ). In this case, the drop in efficiency is even higher and is recorded to be 12.58%. Comparing these with the designs obtained using TO, we observe that for perturbed H-patterns the efficiencies are significantly lower. This provides an insight that the gray values associated with the TO optimized designs are playing a significant role in reducing the cell performance. Our current research therefore involves exploring other techniques, such as advanced filtering methods, to obtain a well performing black-white design. Still, the fact that the high resolution designs already approximate optimized H-pattern cell efficiency, while still containing gray regions, is a promising indication that higher efficiencies are possible.

Besides already closely matching the efficiency of existing designs for rectangular cells, it is clear that the presented approach also holds promise for non-rectangular shapes. Solar cells are expected to become more ubiquitous and designers are likely to find novel ways to integrate them in future products using non-rectangular shapes. In [33], we have discussed an example of a disc-shaped solar cell, for example. As no established electrode design such as the H-pattern exists for arbitrarily shaped domains, the presented TO-based design procedure can be used to generate grids for such cells optimized for efficiency.

#### 2.4.5. SCOPE FOR DIFFERENT TYPES OF SOLAR CELLS

The solar cell parameters used in this chapter correspond to thin film Si solar cells. It does not imply that TO can be used for designing front electrode patterns for thin-film solar cells only. Rather, investigating the application of this approach on other solar cell types is a part of our future research. Our proposed methodology contains certain assumptions and simplifications. As long as these are valid for other solar cells (c-Si cell, CIGS cell *etc.*), the methodology can be used for these solar cells as well. The main assumption of our methodology is that we deal with an active semiconductor layer sandwiched between the front and back contact electrodes. These electrodes have significantly better conductivity than the active layer. Thus, the current in the active layer is assumed to travel perpendicular to the front surface. This assumption is expected to hold valid for all solar cells where a metal electrode is used on the front surface to collect current from the active layer. To the best of our knowledge, most of the solar cells use electrode material on the front surface. Thus, we expect our approach to be generalized and applicable to different types of solar cells.

## 2.5. CONCLUSIONS

One of the possible ways to improve the performance of solar cells is to improve the front electrode design. In this chapter, we explored the capability of TO to come up with com-

plex front metallization patterns for solar cells which could not be designed using conventional shape optimization methods. Some of the characteristic properties of solar cell front electrode design problem are its strong nonlinearity, the design-dependent photocurrent load and the boundary value being included as one of the design variables in optimization. The solar cell performance depends on the connected load due to which the busbar voltage was used as a design variable.

The proposed TO method was tested on side-contact and pin-up module solar cells and proved capable of generating complex electrode designs. While simple geometries can serve as electrode designs for square-shaped or rectangular solar cells, they might not hold good for arbitrarily-shaped solar cells. The design domain of these free-form solar cells can be discretized using finite elements and TO might help in designing the corresponding front electrode patterns. TO tends to find the voltage distribution on the front surface such that the amount of current flowing across the solar cell is maximized. We have found that intermediate densities at boundaries appear in TO results that decrease their efficiency, but nevertheless the optimized designs compare well with idealized conventional designs.

Furthermore, we studied the effects of the mesh resolution, solar cell size and the filter length on the performance of the solar cell. For a filter of constant length (in elements), increasing the mesh resolution gives more freedom for optimal design and the performance of the solar cell increases. In case of mesh-independent filters, increasing the mesh resolution does not help in increasing the power output. Increasing the physical size of the solar cell with constant mesh resolution tends to cover a larger fraction of the front surface with electrode material, thereby reducing the power output of the solar cell. Thus, given the busbar dimensions, TO can be used to find the optimum size of the solar cell for which the power output is maximized.

Our future work involves exploring advanced filtering methods and including sensitivity, fouling, damage and robustness aspects in the TO formulation. This will help us to obtain a black-white design with low sensitivities to fabrication-related imperfections and the results will be compared with the existing designs in terms of performance. Based on the results presented here, we conclude TO could be an effective tool to determine the optimum front electrode designs for the front surface of solar cells.

## REFERENCES

- [1] D. K. Gupta, M. Langelaar, M. Barink, and F. van Keulen, *Topology optimization of front metallization patterns for solar cells*, Structural and Multidisciplinary Optimization **51**, 941 (2015).
- [2] A. Flat and A. G. Milnes, *Optimization of multi-layer front-contact grid patterns for solar cells*, Solar Energy **23**, 289 (1979).
- [3] M. Conti, *Optimal design of front-contact metallization for photovoltaic solar cells*, Solid State Electron. **24** (1981).
- [4] A. R. Burgers, J. H. Bultman, A. C. Tip, and W. C. Sinke, *Metallisation patterns for interconnection through holes*, Sol. Energ. Mat. Sol. C. **65**, 347 (2001).

- [5] A. Antonini, M. Stefancich, D. Vincenzi, C. Malagu, F. Bizzi, A. Ronzoni, and G. Martinelli, *Contact grid optimization methodology for front contact concentration solar cells*, Sol. Energ. Mat. Sol. C. **80**, 155 (2003).
- [6] L. Wen, L. Yueqiang, C. Jianjun, C. Yanling, W. Xiaodong, and Y. Fuhua, *Optimization of grid design for solar cells*, J. Semicond. **31**, 1 (2010).
- [7] Y. Galagan, E. W. Coenen, R. Abbel, T. J. van Lammeren, S. Sabik, M. Barink, E. R. Meinders, R. Andriessen, and P. W. Blom, *Photonic sintering of inkjet printed current collecting grids for organic solar cell applications*, Organic Electronics **14**, 38 (2013).
- [8] A. Burgers, *New metallization patterns and analysis of light trapping for silicon solar cells*, in *PhD Thesis* (2005).
- [9] S. Hyun-Jun and Y. Jeonghoon, *Texturing design for a light trapping system using topology optimization*, IEEE T. Magn. **48**, 227 (2012).
- [10] C. Wang, Y. Shuangcheng, W. Chen, and C. Sun, *Highly efficient light trapping structure design inspired by natural evolution*, Sci. Rep. **3**, 1025 (2013).
- [11] M. Otomori, T. Yamada, K. Izui, S. Nishiwaki, and N. Kogiso, *Level set-based topology optimization for the design of light-trapping structures*, IEEE Transactions on Magnetism **50**, 729 (2014).
- [12] O. Sigmund, *Topology optimization: a tool for the tailoring of structures and materials*, Philos. T. R. Soc. A **358**, 211 (2000).
- [13] C. S. Jog, *Distributed-parameter optimization and topology design for nonlinear thermoelasticity*, Computer Methods in Applied Mechanics and Engineering **132**, 117 (1997).
- [14] T. Buhl, C. B. W. Pedersen, and O. Sigmund, *Stiffness design of geometrically nonlinear structures using topology optimization*, Struct. Multidiscip. O. **19**, 93 (2000).
- [15] T. E. Bruns and D. A. Tortorelli, *Topology optimization of nonlinear elastic structures and compliant mechanisms*, Comput. Method. Appl. M. **190**, 3443 (2001).
- [16] O. Sigmund, *Design of multiphysics actuators using topology optimization - Part I: One-material structures*, Comput. Method. Appl. M. **190**, 6577 (2001).
- [17] A. Gersborg-Hansen, M. P. Bendsoe, and O. Sigmund, *Topology optimization of heat conduction problems using the finite volume method*, Struct. Multidiscip. O. **31**, 251 (2006).
- [18] T. Gao, W. H. Zhang, J. H. Zhu, Y. J. Xu, and D. Bassir, *Topology optimization of heat conduction problem involving design-dependent heat load effect*, Finite Elem. Anal. Des. **44**, 805 (2008).
- [19] J. Petersson and T. Borrvall, *Topology optimization of fluids in Stokes flow*, Int. J. Numer. Meth. Fl. **41**, 77 (2003).

- [20] A. Gersborg-Hansen, O. Sigmund, and R. B. Haber, *Topology optimization of channel flow problems*, Struct. Multidiscip. O. **30**, 181 (2005).
- [21] J. van Deelen, L. A. Klerk, M. Barink, H. Rendering, P. Voorthuijzen, and A. Hovestad, *Improvement of transparent conducting materials by metallic grids on transparent conductive oxides*, Thin Solid Films **555**, 159 (2014).
- [22] P. P. Edwards, A. Porch, M. O. Jones, D. V. Morgan, and R. M. Perks, *Basic material physics of transparent conducting oxides*, Dalton T. **19**, 2995 (2004).
- [23] M. A. Green, *Solar Cells: Oper Princ Tech Sys Appl* (Prentice Hall, 1981).
- [24] J. van Deelen, M. Barink, L. Klerk, P. Voorthuijzen, and A. Hovestad, *Efficiency loss prevention in monolithically integrated thin film solar cells by improved front contact*, Prog. Photovoltaics **23**, 498 (2015).
- [25] O. Darrigol, *Electrodynamics from Ampère to Einstein* (Oxford University Press, 2000).
- [26] T. J. R. Hughes, *The Finite Element Method: Linear static and dynamic finite element* (Dover Publ., 2000).
- [27] A. W. Weeber, R. Kinderman, C. J. J. Tool, F. Granek, and P. C. de Jong, *How to achieve 17 % cell efficiencies on large back-contacted MC-SI solar cells*, in *Proceedings, IEEE 4th World Conf Photovol Ener Conv, Hawaii* (2006) pp. 1–4.
- [28] M. P. Bendsøe, *Optimal shape design as a material distribution problem*, Structural Optimization **1**, 193 (1989).
- [29] G. I. N. Rozvany, M. Zhou, and T. Birker, *Aims, scope, methods, history and unified terminology of computer-aided topology optimization in structural mechanics*, Struct. O. **4**, 250 (1992).
- [30] K. Svanberg, *The method of moving asymptotes - a new method for structural optimization*, International Journal for Numerical Methods in Engineering **24**, 359 (1987).
- [31] F. van Keulen, R. T. Haftka, and N. H. Kim, *Review of options for structural design sensitivity analysis. Part 1: linear systems*, Computer Methods in Applied Mechanics and Engineering **194**, 3213 (2005).
- [32] O. Sigmund, *Morphology-based black and white filters for topology optimization*. Structural and Multidisciplinary Optimization **33**, 401 (2007).
- [33] D. K. Gupta, M. Langelaar, M. Barink, and F. van Keulen, *Topology optimization: An effective method for designing front metallization patterns of solar cells*, in *2014, IEEE 40th Photovoltaic Specialists Conference* (IEEE) pp. 1–6.

# 3

## INTEGRATED FRONT–REAR–GRID OPTIMIZATION OF FREE-FORM SOLAR CELLS

*Free-form solar cells expand solar power beyond traditional rectangular geometries. With possibility of installation on objects of daily use, they allow making better use of available space and are expected to provide new opportunities to generate solar power in the coming future. In addition, their customizable shape can add to the aesthetics of the surroundings. Evidently, free-form solar cells need to be efficient as well. One way to improve their performance is to optimize the metallization patterns for these cells. This chapter introduces an optimization strategy to generate metallization designs of a solar cell such that its performance is maximized. For the purpose of verification, we model an existing transparent free-form solar cell design, including front and rear electrode patterns, to validate it against previously published experimental results. The front and rear metallizations of this transparent free-form solar cell are subsequently redesigned using topology optimization. More than 50% improvement in output power is achieved through topology optimization.*

---

This chapter is based on an article published in IEEE Journal of Photovoltaics, 7, 294-302 (2017) [1].

### 3.1. INTRODUCTION

With the growing energy demand and the need for new and clean energy resources, solar power is experiencing remarkable growth throughout the world. It is expected that the cumulative global solar photovoltaics (PV) market will triple to around 700 GW in 2020 compared to that in 2015 [2] and a long-term global forecast scenario describes worldwide solar PV capacity to reach 4600 GW by 2050 [3]. Looking at the United States alone, the total electrical power sector capacity in 2015 was reported to be around 1045 GW [4] with 27 GW of total solar power capacity and it is reported that 30% of its all new electricity generation capacity in 2015 came from solar [5]. In 2016, the PV installations are expected to increase by around 65 GW.

To ensure that solar power can be a sustainable solution to the growing energy demand for future, innovative ways are being explored to increase the overall PV installations. In some recent works, free-form solar cells have been designed which can be installed on objects of daily use [6–8]. These provide new possibilities of generating solar power, however, the generated energy needs to be affordable as well. Significant research is being conducted to make solar cells more efficient and thereby reduce the cost per unit of solar energy [9].

Among various other possibilities to enhance efficiency is optimization of solar cell metallization patterns. The metallization determines the voltage distribution over the cell, which affects the generated current and power. Significant research has been conducted in the past to improve on this aspect [10–16]. To the best of our knowledge, these standard methods are restricted to predefined geometries such as the H-pattern and in general optimize for the grid width and the spacing between the grid lines. The truly optimal designs might be more complex than the shapes that can be realized from optimization under such restrictions. With the advancements in printing technologies, fabricating more complex patterns is no longer a problem [8, 17], however, the real challenge lies in designing them such that the solar cell performance can be improved. Burgers [18] presented a two step approach that could eliminate the restrictions on topology of the metallization design. However, this approach involved a few heuristic calculations requiring prior information from the side of the designer.

In a paper presented at the 40th IEEE Photovoltaic Specialists Conference [19], it was shown that new and potentially superior layouts can be generated using a topology optimization (TO) approach. TO is a computational paradigm capable of optimizing the distribution of a certain material in a given domain subjected to certain constraints, such that the performance of the system is maximized [20]. Compared to conventional shape and size optimization approaches, TO provides more flexibility and does not even require an initial design concept. For a general overview of the concepts and applications of TO, see [20–22] and references therein. In the context of solar cells, TO has also been used to design efficient light trapping structures [23–25].

The work presented in [19] uses TO to optimize the front metallization patterns for solar cells. The details related to the mathematical formulation of the problem as well as the computational aspects of the methodology are discussed in [26]. It is also shown that the optimized front metal grids obtained using TO are comparable in terms of performance to the H-patterns for standard solar cell shapes.

An important advantage of the TO methodology is demonstrated in [27], where this

method is used to optimize the front metal grids for *free-form, non-rectangular* solar cells. Freeform solar cells are gaining recent attention from an aesthetic point of view since they can easily blend into the architectural makeup of the surroundings. For recent research related to unconventional shapes for the solar cell domain, see [6–8, 27, 28]. In the study reported in [27], front grid patterns for several freeform shapes were optimized *e.g.* circular, hexagonal, leaf-shaped, shapes of motorbike fairings, *etc.* For unconventional shapes, no established efficient grid pattern is known, like the H-pattern for rectangular cells. Grid optimization using the TO approach however applies to any domain shape.

It is important to note here that while TO can design efficient metallization patterns for freeform solar cells, there are various other challenges associated with these freeform shapes. Manufacturing non-rectangular solar cell shapes (*e.g.* circular or semi-circular geometries) and the corresponding grid layouts has been attempted for the past four decades [29]. Manufacturing of free-form silicon solar cells is quite difficult due to technological limitations. Printing and coating techniques utilized in the manufacturing of organic solar cells open a lot of possibilities in the freedom of forms and shapes. These create a new market for PV technologies by combining PV functionality and aesthetics. Therefore, solar cells with artistic shapes attract a lot of attention. However, scaling up the size and their non-rectangular shapes typically lead to efficiency losses. It points on the necessity of optimizing the metallization patterns for these cells.

In conventional solar cells, only the front electrode has been considered for optimization, as the rear electrode usually covers the entire backside. Transparent or semi-transparent solar cells are more aesthetically appealing than the opaque ones. To preserve this transparency, it is important not to cover the whole rear surface with the electrode material. Thus, a limited amount of electrode material can be used on the rear side and it becomes important to use an appropriate pattern. Important to note here is that the optimal grid designs for the front and the rear sides depend on each other, since together they determine the local voltage difference between front and rear side that determines the local current density. To maximize the performance of a solar cell, they should be optimized together. Some preliminary results related to this aspect were reported by us in [30], however that study was restricted to only electrode thickness optimization on the rear side.

This chapter presents for the first time an optimization strategy which can be used to simultaneously optimize the front and rear metallization patterns for solar cells. For the purpose of this optimization, a solar cell model with front and rear metal designs is presented. Based on the available experimental data, the model is tuned so as to match the behavior of the fabricated tree-shaped solar cell example presented in [8]. Further, this model together with the proposed approach are used to optimize the metallization designs for this example.

The rest of this chapter is organized in the following manner. Section 3.2 describes the optimization method and the mathematical model for the integrated front-rear grid optimization in solar cells. This approach is tested on a solar cell with the shape of a Christmas tree. The model validation and optimization results are discussed in Section 3.3 and the final conclusions are presented in Section 3.4.

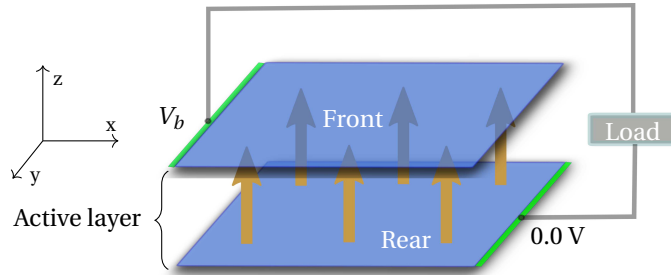


Figure 3.1: Schematic diagram of a solar cell model with front and rear conductive surfaces. The voltage difference between the front and rear sides, combined with the illumination level, controls the current density across any point in the semiconductor layer.

## 3.2. METHOD

### 3.2.1. TOPOLOGY OPTIMIZATION

In this chapter, topology optimization (TO) is used to simultaneously optimize the front and rear metallization patterns for solar cells. As stated above, TO is a computational approach capable of optimizing the material distribution in a given domain without violating some given constraints such that the performance of the system is maximized. In the traditional optimization methods, the electrode pattern is assumed to consist of straight lines and the design is only optimized for metal line width and line spacing. TO abandons such restrictions and can achieve more complex and better performing designs which cannot be obtained with the conventional shape optimization techniques.

TO comprises of a series of design updates, each update being based on the sensitivity responses computed from the design obtained in the previous step. Typically, the design domain at each step is discretized into a set of finite elements and the performance of the design is evaluated using finite element analysis. Within every finite element, the amount of material is allowed to vary from 0 to 1. Here 0 refers to void (no material) and 1 refers to solid (full material). To obtain a manufacturable solution, the intermediate values are penalized and made unfavorable [31, 32]. The optimization process is stopped when changes in objective value or design fall below a certain threshold in consecutive steps.

### 3.2.2. MATHEMATICAL FORMULATION

In this section, the mathematical aspects of the solar cell metallization design optimization problem are discussed. A solar cell model with front and rear electrodes is presented and then the various aspects of the proposed optimization strategy are discussed. These are as follows:

#### SOLAR CELL MODEL

For the purpose of front and rear grid optimization in solar cells, a simplified model is used. This model is an extended version of the front grid optimization model described in [26] and is illustrated in Fig. 3.1. In this figure, the semiconductor layer is sandwiched between the front and rear conductive surfaces. In general, these surfaces might consist

of thin, transparent, moderately conductive layers with a deposition of highly conductive metal grid lines. Since the conductivity of the transparent layers as well as the metal grid is several orders higher than that of the active layer, it is assumed that the current across the active layer in the thin-film solar cell travels in the transverse direction. On the front and rear conductive surfaces, current flows along the surface planes.

The out-of-plane current density at any spot of the solar cell can be described using the following equation:

$$j = j_L - j_0 \left( e^{\frac{\tilde{q}\Delta V}{k_B T}} - 1 \right), \quad (3.1)$$

where  $j$ ,  $j_0$  and  $j_L$  denote net, reverse bias and photoillumination current densities, respectively and  $\tilde{q}$ ,  $k_B$  and  $T$  refer to the electric charge, Boltzmann constant and local temperature, respectively. In general,  $j_L$  does not depend on the voltage difference as in Eq. 3.1. However, for organic solar cells, Eq. 3.1 does not fit very well [33–35]. While modeling, this needs to be taken into account and the behavior of the device needs to be accurately modeled. The illumination can be non-uniform on the solar cell front surface, however, here we consider uniform illumination only. The voltage difference across the active layer denoted by  $\Delta V$  is equal to  $V_f - V_r$ , where  $V_f$  and  $V_r$  denote the voltage values measured on the front and rear conductive surfaces, respectively. For the front side, the busbar voltage is denoted by  $V_b$  and on the rear side, the point at which the load is connected is set to 0 volts. The power output can then be stated as

$$P_{out} = (V_b - 0) \int_{\Omega} j dA = V_b \int_{\Omega} j dA. \quad (3.2)$$

Here,  $dA$  is a differential area of the solar cell and  $j$  is the respective out-of-plane current density. The efficiency  $\eta$  of the solar cell can then be calculated as

$$\eta = \frac{P_{out}/A}{p_{inp}} \times 100\%, \quad (3.3)$$

where  $P_{out}$  and  $A$  refer to the solar cell power output and its front surface area and  $p_{inp}$  is the input power density which is assumed to be  $100 \text{ mWcm}^{-2}$  under standard conditions.

#### FINITE ELEMENT MODELLING

The physics of the front as well as the rear conducting layers can be modeled using a Poisson equation of charge conservation during electrical conductivity, which is as follows:

$$\sigma \nabla^2 V = \frac{\partial \bar{\rho}}{\partial t}, \quad (3.4)$$

where  $\sigma$ ,  $V$  and  $\bar{\rho}$  refer to the conductivity of the material, the electric potential and the enclosed charge density, respectively. When discretised using finite element method, the system of equations for the front and rear sides combined together can be stated as

$$\mathbf{GV} = \mathbf{I}, \quad (3.5)$$

where  $\mathbf{G}$  is the total conductivity matrix and  $\mathbf{V}$  and  $\mathbf{I}$  refer to voltage and current vectors, respectively. From Eq. 3.1, it can be seen that the current and voltage are non-linearly

related. Due to this, the system of equations given in Eq. 3.5 cannot be solved directly. Thus, it is transformed into a set of residual equations and then the system is solved to minimize the overall residual using the Newton method. Changing Eq. 3.5 to a residual form, the following can be stated:

$$\mathbf{R}(\mathbf{V}) = \mathbf{G}\mathbf{V} - \mathbf{I}(\mathbf{V}) = \mathbf{0}, \quad (3.6)$$

where  $\mathbf{R}$  is the residual. For the discretized system, quadrilateral finite elements with bilinear shape functions are used. The total conductivity matrix  $\mathbf{G}$  is constructed from the element conductivity matrix  $\mathbf{G}_e$  using a modified SIMP model [31] as follows:

$$\mathbf{G}_0 = (\sigma_s^{tcl} + \rho^q (\sigma_s^m - \sigma_m^{tcl})) \mathbf{G}_0, \quad (3.7)$$

where  $\sigma_s^{tcl}$  and  $\sigma_s^m$  are linear conductivities of the transparent conductive layer and the metal electrode, respectively and  $\rho$  denotes the fraction of the finite element filled with the electrode material. The term  $q$  refers to penalization power and for this problem it is set to 3. This serves to obtain clearly resolved electrode designs. For more details on this aspect, see [26].

The various components of Eq. 3.6 are constructed as follows:

$$\mathbf{R} = [\mathbf{R}_f \quad \mathbf{R}_r]^\top, \quad (3.8)$$

$$\mathbf{V} = [\mathbf{V}_f \quad \mathbf{V}_r]^\top, \quad (3.9)$$

$$\mathbf{G} = \begin{bmatrix} \mathbf{G}_f & 0 \\ 0 & \mathbf{G}_r \end{bmatrix}, \quad (3.10)$$

where, the subscripts  $f$  and  $r$  correspond to the front and rear surfaces of the solar cell, respectively. The global conductivity matrices  $\mathbf{G}_f$  and  $\mathbf{G}_r$  can be constructed by assembling the contributions from element conductivity matrices for the front and rear grids, respectively. For the consistency of the model, it is important that the magnitude of current entering the active layer at any spot on the rear side is equal to the current exiting the active layer from the corresponding spot on the front side. Thus,  $\mathbf{I}$  is constructed as follows:

$$\mathbf{I} = [\mathbf{I}_0 \quad -\mathbf{I}_0]^\top. \quad (3.11)$$

The model proposed in [26] for the front side metallization assumes that the current flows from the whole front surface to the connection point (busbar). However, for the rear side, current needs to flow from the connection point to the whole rear surface. To take this into account, a minus sign is added to the current vector for the rear side.

#### OPTIMIZATION

The objective of optimizing the metallization patterns is to maximize the solar cell efficiency. The mathematical formulation of the optimization problem can be stated as

$$\begin{aligned} & \max_{\rho, V_b} \eta \\ & \mathbf{R}(\mathbf{V}) = \mathbf{G}\mathbf{V} - \mathbf{I}(\mathbf{V}) = \mathbf{0}, \\ & \frac{1}{N} \sum \rho_r \leq V_r. \end{aligned} \quad (3.12)$$

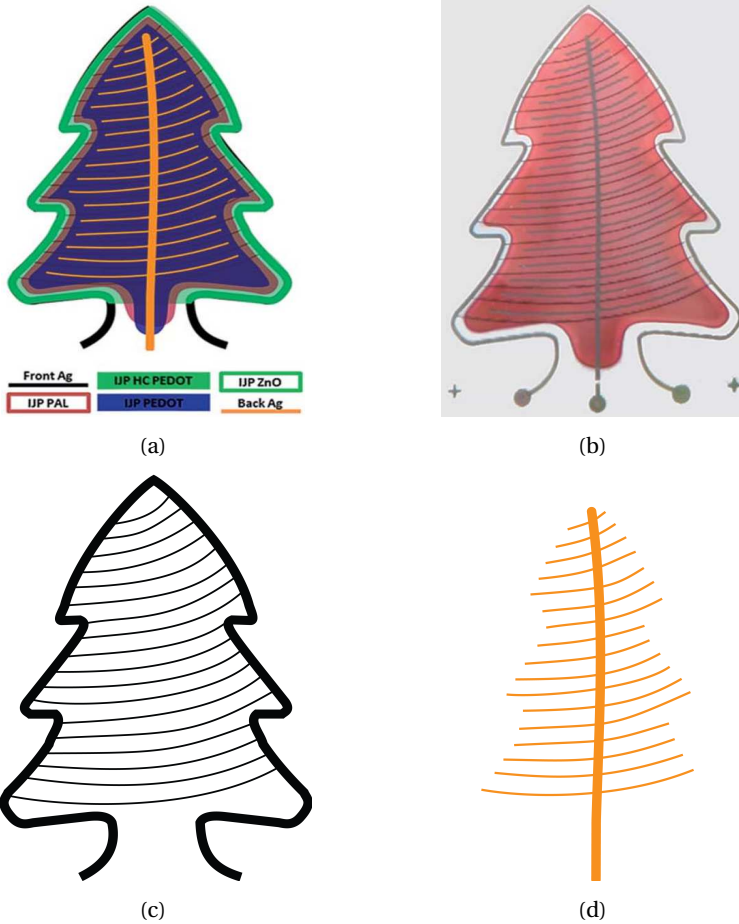


Figure 3.2: Christmas tree shaped free-form solar cell, (a) schematic diagram showing the layout of different printed layers [8] (b) photograph of the solar cell fabricated using inkjet printing [8] (c) modeled front side metallization design and (d) modeled rear side metallization design.

Here,  $\rho$  is given as  $\rho = [\rho_f \ \rho_r]$ , where  $\rho_f$  and  $\rho_r$  are the vectors of design variables for the front side and rear side, respectively and  $V_r$  denotes the material volume fraction for the rear side. Each design variable denotes the volume fraction of the finite element filled with the electrode material. The inequality constraint in Eq. 3.12 represents the restriction on the maximum amount of electrode material that can be used on the rear side of the solar cell. We also let the optimizer find the optimal busbar voltage  $V_b$ , by including it as a design variable in the optimization problem.

For the front side of the solar cell, it is important that an optimum amount of electrode material is chosen. For too less material, the resistive losses will be high due to the increased contrast in voltage distribution on the front side. If too much material is used, although the resistive losses are reduced, a significant part of the incident light gets blocked from entering the active layer leading to increased shading losses. Between the two cases, there exists an optimum amount of material which reduces the sum of the two losses and this can be determined by the optimizer. Thus, unlike the rear side, no restriction needs to be imposed on the maximum allowable amount of front electrode material. The shading effect is taken into consideration by replacing  $j_L$  in Eq. 3.1 by  $j_L^*$  such that

$$j_L^* = j_L(1 - \rho)^r, \quad (3.13)$$

where  $r$  is a penalization power which is set to 2 in this study, to promote well-defined 0/1 solutions.

The optimization problem stated in Eq. 3.12 is a non-convex optimization problem with more than 300,000 design variables and is solved using a gradient based technique. The model generated at each iteration step is updated using method of moving asymptotes [36], a gradient based optimizer capable of handling general non-linear programming problems with large number of design variables. For making a design update, the optimizer needs design sensitivities *i.e.* gradient information denoting the dependence of cell efficiency on the design. Due to the high dimensionality of the problem, an adjoint formulation is adopted for calculating these sensitivities [26, 37].

### 3.2.3. APPLICATIONS

In this work, we use TO to optimize the front and rear metallizations for free-form solar cells. To demonstrate the applicability of TO, a free-form Christmas tree shaped organic photovoltaic (OPV) cell domain is chosen. One of the reasons to choose this test case is the fact that a similar OPV has been fabricated in the past and the results are reported in [8]. Since the goal of the chapter is to present the optimization methodology, the choice of the test case does not limit the application of the methodology. Also, OPV and the inkjet printing technology have a big advantage compared to c-Si due to the possibility of freeforms. These give enormous aesthetical advantage and open possibility for new applications.

Here, we model the electrical behaviour of this test case as it is in [8] using the proposed front-rear electrode model. The model is tuned based on the available experimental data so that it can match the behavior of the fabricated solar cell example. The front and rear metallization patterns are then optimized under two different scenarios assuming that the amount of electrode material that can be used on the rear side is same (12%) as that in [8]. For the first case, the busbar on the front side is assumed to be the

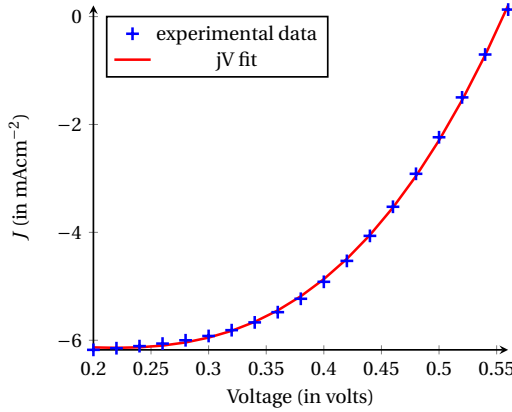


Figure 3.3: J-V data measured for a small device ( $0.04 \text{ cm}^2$ ) and the fitted J-V curve (obtained using a cubic polynomial) for the OPV solar cell used in this study.

Table 3.1: Performance statistics for the ideal device, the fabricated device [8] and various cases for the tree-shaped OPV cell modeled using different metallization patterns.

Parameter	Ideal case	Fabricated [8]	Modeled	Case I	Case II
$J_{sc}$ ( $\text{mAcm}^{-2}$ )	6.14	2.80	2.76	2.92	3.22
$V_{oc}$ (volts)	0.56	0.46	0.47	0.47	0.48
$J_{mp}$ ( $\text{mAcm}^{-2}$ )	5.24	1.45	1.67	1.88	2.31
$V_{mp}$ (volts)	0.38	0.26	0.25	0.3	0.28

same as that in [8] and the electrode distribution is optimized for the rest of the front domain as well as on the rear side. For the second case, no pre-defined busbar configuration is assumed and TO is used to design efficient patterns for both the sides. For both the cases, the busbar connection points on the front and rear sides are assumed to be same as that in [8]. In addition, TO is also used to study the effect of amount of rear electrode material on the performance of the solar cell.

### 3.3. RESULTS AND DISCUSSIONS

In this section, we report the results for different simulation tests performed on the tree-shaped solar cell. Before presenting the application of the proposed methodology, we discuss the details related to this test case.

Fig. 3.2(a) shows the schematic representation of the Christmas tree shaped free-form solar cell and photograph of the finished layout is shown in Fig. 3.2(b). All the functional layers, including the electrodes, were inkjet printed [8]. Inkjet printed devices contained the following layer sequence: glass substrate/front Ag fingers/front PEDOT:PSS/ZnO/ Photoactive layer/rear PEDOT:PSS/rear Ag fingers. The photoactive layer used here is Poly(3-hexylthiophene) - (P3HT) with an optical energy bandgap of around 1.7 eV. Ag fingers and busbars (both front and rear) were inkjet printed using a Fujifilm Dimatix Materials Printer (DMP 2831). Inkjet printing of front PEDOT:PSS, ZnO nanoparti-

Table 3.2: Model parameters for the Christmas tree

Parameter	Value
Device area	6.24 cm <sup>2</sup>
Front PEDOT conductivity	2 × 10 <sup>4</sup> Sm <sup>-1</sup>
Front PEDOT thickness	100 nm
Front metal conductivity	6.3 × 10 <sup>6</sup> Sm <sup>-1</sup>
Front metal thickness	300 nm
Rear PEDOT conductivity	5 × 10 <sup>4</sup> Sm <sup>-1</sup>
Rear PEDOT thickness	200 nm
Rear metal conductivity	6.3 × 10 <sup>6</sup> Sm <sup>-1</sup>
Rear metal thickness	300 nm

cles, the photo-active layer and rear PEDOT:PSS was performed on a LP50 printing platform (Pixdro, OTB) using an industrial printhead (KM512LN, 3.5 cm width, 360 DPI nozzle spacing). The specification of materials, ink formulations and inkjet printing process is described elsewhere [8]. The active area of the cell was 6.24 cm<sup>2</sup>. Fig. 3.2(c) and (d) show the metallization designs for the front and rear side of the free-form solar cell as were used in this study to model the electrical behaviour. These designs were obtained by a best effort based on intuition to maximize performance. Therefore, losses can be expected due to the non-optimal arrangements and thicknesses of the various electrode lines.

In this chapter, we optimize the front and rear metallizations for this free-form solar cell so that its performance can be improved. For modeling purpose, we use experimental J-V data which was measured on a small device (area 0.04 cm<sup>2</sup>). The j-V curve obtained by fitting a cubic polynomial in the experimental data is as follows:

$$j(\text{mAcm}^{-2}) = -6.14 + 4.72V - 43V^2 + 97.88V^3. \quad (3.14)$$

The measured data as well as the fitted j-V curve are shown in Fig. 3.3. The proposed front-rear electrode model uses voltage values between 0.2 and 0.55 volts only. Due to this reason, only this part of the experimental data is used in Fig. 3.3 to derive the j-V curve. This j-V curve is then used in the front-rear electrode model for optimization.

Before optimizing the metallization patterns, we tune the model so that the behavior of the study example can be properly modeled. For the same purpose, the photoillumination component of current density in Eq. 3.14 is reduced by a certain factor. For a OPV, photocurrent is observed to be voltage-dependent [33–35] and this behavior is especially prominent in the reverse regime. Since our model uses the data only for a small range of positive voltage values, we assume that photocurrent is independent of voltage. Thus, the magnitude of  $j_L$  in Eq. 3.14 is 6.14 mAcm<sup>-2</sup>. This assumption does not affect the conclusions of this chapter due to the fact that all performance related comparisons of the optimized designs are done with the modelled version and not directly the fabricated one for the tree-shaped solar cell.

Table 3.2 lists the parameters used for modeling purpose. These parameters are the same as that of the previously fabricated solar cell. The PEDOT and electrode material are used to model the front and rear conductive surfaces. The effective conductivities

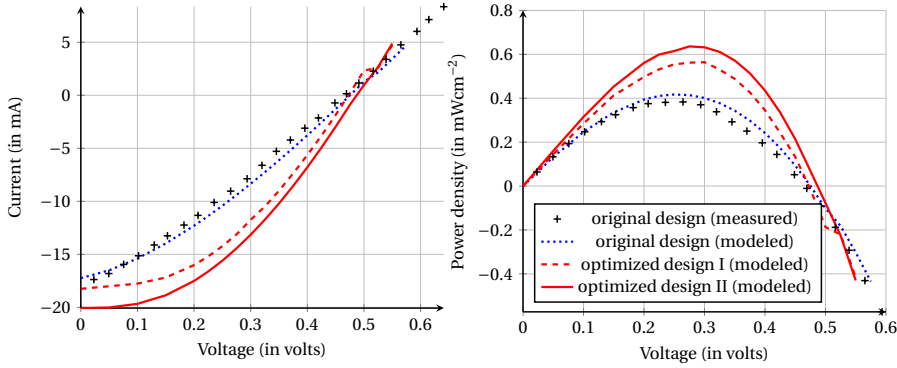


Figure 3.4: I-V and P-V curves for the modeled solar cell with Christmas tree shape.

Table 3.3: Performance statistics for the tree-shaped solar cell model with different metallization patterns.

Model	Power density (in mWcm <sup>-2</sup> )	Relative Improvement
Original	0.416	-
Case I	0.564	35%
Case II	0.632	52%

$G_{min}$  and  $G_0$  for every finite element stated in Eq. 3.7 are calculated using the information stated in Table 3.2 for PEDOT and electrode material, respectively. The electrode finger width is not allowed to be less than  $150 \mu\text{m}$ . Since the main goal of this chapter is to present the potential of the proposed optimized strategy, we preferred to keep the model simple and certain factors have not been taken into account. An example is the transparency of the solar cell. The small device on which the j-V measurements were done consisted of an ITO layer. On the other hand, the tree-shaped solar cell discussed here uses PEDOT layer as the conductive polymer due to which its transparency is significantly lower, thereby lowering its  $j_L$ . Another factor is that the dimensions of the electrode lines in the fabricated design are generally higher than the modeled ones. This is because during inkjet printing, the ink spreads and makes shading larger [38]. Also, additional resistances including the shunt resistance have not been considered here. To include these effects in the model,  $j_L$  has been reduced by 35%. This reduction factor has been chosen ensuring that the I-V and P-V curves obtained from the model for the study device closely match those of the fabricated version.

As a next step, we use TO to optimize the front and rear metal grids for the chosen free-form solar cell. The busbar connection points are chosen to be the same as the ones in [8]. For the first instance of optimization (Case I), a fixed electrode line is defined along the perimeter of the domain for the front side. The thickness of this line is kept roughly the same as the one in the original prototype cell (Fig. 3.2(c)). For the rear side, the amount of electrode material to be used has been set to 12% to match the original design (Fig. 3.2(d)) and no restriction is imposed on the amount of material to be used on the front side. Fig. 5.4 shows the resultant front and rear metallization patterns obtained using TO. The predefined electrodes on the perimeter of the cell already give a relatively

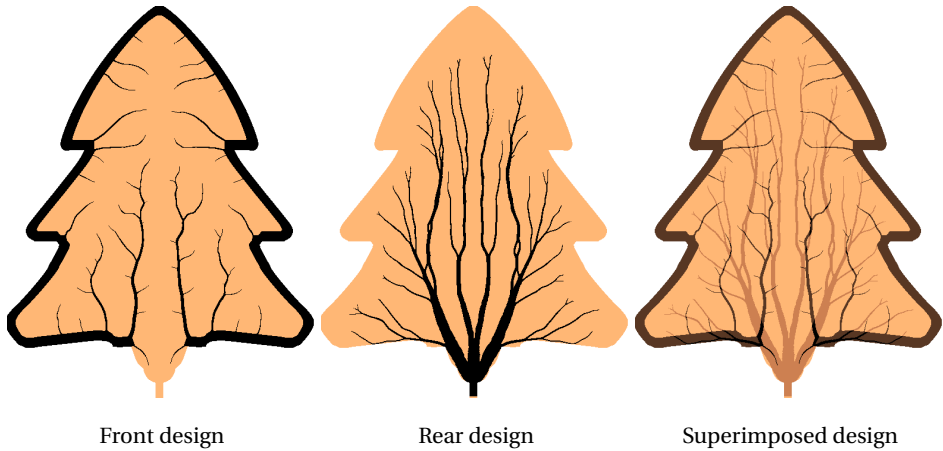


Figure 3.5: Optimized metallization patterns with a pre-defined perimeter electrode for the front side for a solar cell with Christmas tree shape.

low voltage contrast within the domain. The optimization process has only added a few small lines on the front side for further improvement and a total of 16% of the front side is found to be covered with electrode material in the optimized design. The corresponding I-V and P-V curves are shown in Fig. 3.4. The resultant design improves the solar cell performance by around 35% compared to the original design. Interestingly, the dendritic nature of these optimized patterns may be perceived as aesthetically appealing, ‘natural’ features. Other associated parameters such as short-circuit current density  $j_{sc}$ , open-circuit voltage  $V_{oc}$  and current density and voltage at maximum power point,  $j_{mp}$  and  $V_{mp}$ , respectively are reported in Table 3.1. Compared to the ideal case, significant drops are observed in  $j_{sc}$  and  $j_{mp}$  for the tree-shaped solar cell. One of the primary reasons is the shading caused due to electrode deposition on the front side. Also, since the current generated in the active layer depends on the voltage value, considerable reduction can be observed in the total current generated due to the voltage contrast on the front surface eventually leading to reduction in  $j_{sc}$  and  $j_{mp}$  of the device.

In another run of TO (Case II), no pre-defined geometry is assumed for electrode lines on the front and rear sides. Instead, it is left to the optimization process where to place all of the front electrode material. Fig. 5.6 shows the optimized metallization patterns obtained for this case. For this case, only 7% of the front surface is covered with the electrode material. The corresponding I-V and P-V curves are shown in Fig. 3.4 and other related parameters are reported in Table 3.1. With these optimized electrode patterns, a significantly higher amount of current can be collected at the busbar and a relative increase of 52% is observed in the solar cell power output. The optimal value of  $V_b$  for both the cases was around 0.3 volts. Similar to the previous case, a dendritic network of electrode material is obtained for the rear side. However, a very different metallization pattern is obtained for the front side with quite a larger amount of electrode material being added during the optimization process to form the optimized pattern. The relative improvement in the solar cell performance for this case is signifi-

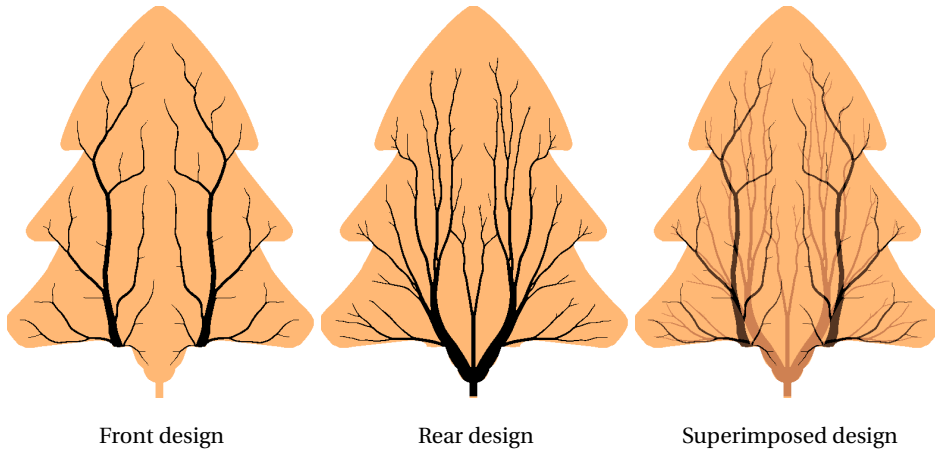


Figure 3.6: Fully optimized metallization patterns for a solar cell with Christmas tree shape.

cantly higher compared to Case I. This is because, with no pre-defined geometry here, the optimization process has more flexibility to distribute the electrode material.

An interesting observation is that the metallization pattern on the front side is not as densely branched as the rear side. For Case I, assuming a pre-defined geometry leaves very less amount of electrode material to be distributed on the front surface. For Case II, the amount of electrode material used on the front side (7%) is still quite low compared to that used on the rear side (12%). Due to this and the fact that a minimum feature-size restriction is imposed, the formation of a dense metallization network is avoided on the front side. Note that the choice of using 12% electrode material on the rear side was made to match the original design. It is of interest to study the influence of this choice on the optimized output power.

Fig. 3.7 shows the output power of different optimized metallization designs for Case II obtained for various electrode material fractions on the rear side ( $V_r$ ). With an increase in  $V_r$ , the overall power output increases. This is because the surface conductivity on the rear side increases thereby leading to a more uniform voltage distribution as well as reduced resistive losses. Thus, ideally the whole rear side should be covered with electrode material to achieve maximum performance. However, from an aesthetic point of view, these cells need to be (partially) transparent. Thus, a restriction is imposed on the value of  $V_r$ . It is interesting to see in Fig. 3.7 that with  $V_r$  set to 12%, the transparent Case II design, at  $0.63 \text{ mWcm}^{-2}$  achieves nearly 82% of the output power density of a fully covered cell.

From the two cases analyzed above, it can be deduced that the proposed modeling and optimization strategies work well with the chosen free-form organic solar cell example. However, the application of this methodology is not restricted to organic solar cells only. Through the use of appropriate parameter values, the proposed solar cell model can be adapted to any kind of solar cells, which allows the optimization methodology to be applied to those technologies as well. An important assumption in the applied model is that the current through the active layer runs in transverse direction. This assump-

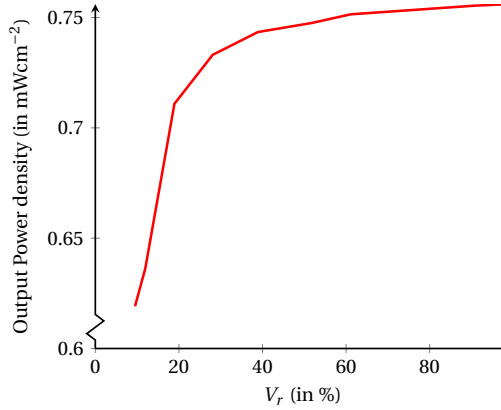


Figure 3.7: Solar cell power outputs for different electrode material volume fractions for the rear side of the cell.

tion is valid for all solar cells where conductivity of front and rear surfaces is significantly higher than that of the active layer. Since this is true for most of the solar cells, our approach can be generalized and is applicable to different types of solar cells.

The goal of this chapter is to demonstrate the application of the proposed optimization methodology and the presented example very well augments it. The advantages of using OPVs and the inkjet printing technique for freeform solar cells are already discussed in [8]. However, to ensure maximum power output from these freeform solar cells, several additional factors need to be considered. The power output of these cells can be affected due to the grid thickness as well as shading degradation [39]. The affect of these parameters has been studied in [40]. In [41], the effect of conductivity on the performance of thin-film solar cells has been studied. It is also important to understand the effect of stress distribution on the delamination of these solar cells and the impact that it would eventually have on their performance. Also, while modeling and optimization of the grids, we ignored the effect of temperature. The local current generated in the active layer also depends on the temperature distribution. Thus, the metallization pattern should ideally be optimized with respect to the temperature as well. In our future research work, we aim to include these aspects to further improve the accuracy of the results.

### 3.4. CONCLUSIONS

In this chapter, a front-rear electrode model is presented which can be used to model the front and rear metallizations in solar cells. The model has been validated through comparisons with previous experimental results. Further, combining topology optimization with this model can generate front and rear metallization designs which perform significantly better than the existing ones. The application on a free-form Christmas tree shaped solar cell domain demonstrates the fact that this approach is not restricted to standard solar cell shapes and can be easily applied to free-forms. As it is nontrivial to design metallization patterns for free-form solar cells by hand, significant improvements

in output power can be achieved: more than 50% for the considered example. It was also found that although efficiency of a semi-transparent cell was less than that of a full coverage rear electrode, through optimization the difference was only 18%. We expect that the proposed methodology can be a significant contribution to the trend towards transparent, free-form solar cell devices.

## REFERENCES

- [1] D. K. Gupta, M. Barink, Y. Galagan, and M. Langelaar, *Integrated front-rear-grid optimization in free-form solar cells*, IEEE Journal of Photovoltaics **7**, 294 (2017).
- [2] A. James, *Global PV Demand Outlook 2015:2020: Exploring Risk in Downstream Markets*, GTM Research Reports (2015).
- [3] *Technology Roadmap: Solar Photovoltaic Energy*, Energy Technology Perspectives, International Energy Agency (2014).
- [4] US Energy Information Administration, *Annual Energy Outlook 2015*, Table: Electricity Generating Capacity .
- [5] A. James, *US Solar Market Insight, Executive summary: 2015 Year-in-Review*, GTM Research Reports (2015).
- [6] V. Shrotriya, *Organic Photovoltaics Polymer power*, Nat. Photonics **3**, 447 (2009).
- [7] W. Cao, Z. Li, Y. Yang, Y. Zheng, W. Yu, R. Afzal, and J. Xue, "Solar tree": *Exploring new form factors of organic solar cells*, Renewable Energy , 134 (2014).
- [8] T. Eggenhuisen, Y. Galagan, A. Biezemans, T. Slaats, P. Voorthuijzen, S. Kommeren, S. Shanmugam, J. P. Teunissen, A. Hadipour, W. Verhees, S. C. Veenstra, M. Coenen, J. Gilot, R. Andriessen, and P. Groen, *High efficiency, fully inkjet printed organic solar cells with freedom of design*, Journal of Materials Chemistry A **3**, 7255 (2015).
- [9] N. Lewis, *Basic Research Needs for Solar Energy Utilization*, Report on the Basic Energy Sciences Workshop on Solar Energy Utilization (2005).
- [10] A. Flat and A. G. Milnes, *Optimization of multi-layer front-contact grid patterns for solar cells*, Solar Energy **23**, 289 (1979).
- [11] M. Conti, *Optimal design of front-contact metallization for photovoltaic solar cells*, Solid State Electron. **24** (1981).
- [12] A. R. Burgers, *How to design optimal metallization patterns for solar cells*, Progress in Photovoltaics: Research and Applications **7**, 457 (1999).
- [13] A. R. Burgers, J. H. Bultman, A. C. Tip, and W. C. Sinke, *Metallisation patterns for interconnection through holes*, Sol. Energ. Mat. Sol. C. **65**, 347 (2001).
- [14] A. Antonini, M. Stefancich, D. Vincenzi, C. Malagu, F. Bizzi, A. Ronzoni, and G. Martinelli, *Contact grid optimization methodology for front contact concentration solar cells*, Sol. Energ. Mat. Sol. C. **80**, 155 (2003).

- [15] A. W. Weeber, R. Kinderman, C. J. J. Tool, F. Granek, and P. C. de Jong, *How to achieve 17 % cell efficiencies on large back-contacted MC-SI solar cells*, in *Proceedings, IEEE 4th World Conf Photovol Ener Conv, Hawaii* (2006) pp. 1–4.
- [16] L. Wen, L. Yueqiang, C. Jianjun, C. Yanling, W. Xiaodong, and Y. Fuhua, *Optimization of grid design for solar cells*, *J. Semicond.* **31**, 1 (2010).
- [17] Y. Galagan, E. W. Coenen, R. Abbel, T. J. van Lammeren, S. Sabik, M. Barink, E. R. Meinders, R. Andriessen, and P. W. Blom, *Photonic sintering of inkjet printed current collecting grids for organic solar cell applications*, *Organic Electronics* **14**, 38 (2013).
- [18] A. Burgers, *New metallization patterns and analysis of light trapping for silicon solar cells*, in *PhD Thesis* (2005).
- [19] D. K. Gupta, M. Langelaar, M. Barink, and F. van Keulen, *Topology optimization: An effective method for designing front metallization patterns of solar cells*, in *2014, IEEE 40th Photovoltaic Specialists Conference (IEEE)* pp. 1–6.
- [20] M. P. Bendsøe and O. Sigmund, *Topology Optimization: Theory, methods and applications* (Springer, 2003).
- [21] O. Sigmund and K. Maute, *Topology optimization approaches: a comparative review*, *Structural and Multidisciplinary Optimization* **48**, 1031 (2013).
- [22] J. Deaton and R. Grandhi, *A survey of structural and multidisciplinary continuum topology optimization post 2000*, *Structural and Multidisciplinary Optimization* **49**, 1 (2014).
- [23] S. Hyun-Jun and Y. Jeonghoon, *Texturing design for a light trapping system using topology optimization*, *IEEE T. Magn.* **48**, 227 (2012).
- [24] C. Wang, Y. Shuangcheng, W. Chen, and C. Sun, *Highly efficient light trapping structure design inspired by natural evolution*, *Sci. Rep.* **3**, 1025 (2013).
- [25] M. Otomori, T. Yamada, K. Izui, S. Nishiwaki, and N. Kogiso, *Level set-based topology optimization for the design of light-trapping structures*, *IEEE Transactions on Magnetics* **50**, 729 (2014).
- [26] D. K. Gupta, M. Langelaar, M. Barink, and F. van Keulen, *Topology optimization of front metallization patterns for solar cells*, *Structural and Multidisciplinary Optimization* **51**, 941 (2015).
- [27] D. K. Gupta, M. Langelaar, M. Barink, and F. van Keulen, *Optimizing front metallization patterns: Efficiency with aesthetics in free-form solar cells*, *Renewable Energy* **86**, 1332 (2016).
- [28] G. M. M. W. Bissels, M. A. H. Asselbergs, J. J. Schermer, N. J. Haverkemp, and E. Vlieg, *A genuine circular contact grid pattern for solar cells*, *Progress in Photovoltaics: Research and Applications* **19**, 517 (2011).

- [29] M. A. Green, *Solar Cells: Oper Princ Tech Sys Appl* (Prentice Hall, 1981).
- [30] D. K. Gupta, M. Langelaar, F. van Keulen, and M. Barink, *Topology Optimization for improving the performance of solar cells*, in *Proceedings, 2014 Eng. Optim Conf* (2014).
- [31] M. P. Bendsøe, *Optimal shape design as a material distribution problem*, *Structural Optimization* **1**, 193 (1989).
- [32] M. Stople and K. Svanberg, *An alternative interpolation scheme for minimum compliance topology optimization*. *Struct. Multidiscip. O.* **22**, 116 (2001).
- [33] L. J. A. Koster, E. C. P. Smits, V. D. Mihailtchi, and P. W. M. Blom, *Device model for the operation of polymer/fullerene bulk heterojunction solar cells*, *Phys. Rev. B* **72**, 085205 (2005).
- [34] L. H. Slooff, S. C. Veenstra, J. M. Kroon, W. Verhees, L. J. A. Koster, and Y. Galagan, *Describing the light intensity dependence of polymer:fullerene solar cells using an adapted Shockley diode model*, *Phys. Chem. Chem. Phys.* **16**, 5732 (2014).
- [35] B. Ray, A. G. Baradwaj, M. R. Khan, B. W. Boudouris, and M. A. Alam, *Collection-limited theory interprets the extraordinary response of single semiconductor organic solar cells*, *Proc. Natl. Acad. Sci. USA* **112**, 11193 (2015).
- [36] K. Svanberg, *The method of moving asymptotes - a new method for structural optimization*, *International Journal for Numerical Methods in Engineering* **24**, 359 (1987).
- [37] F. van Keulen, R. T. Haftka, and N. H. Kim, *Review of options for structural design sensitivity analysis. Part 1: linear systems*, *Computer Methods in Applied Mechanics and Engineering* **194**, 3213 (2005).
- [38] Y. Galagan, R. Andriessen, E. Rubingh, N. Grossiord, P. Blom, S. Veenstra, W. Verhees, and J. Kroon, *Toward fully printed organic photovoltaics: processing and stability*, *Lope-C*, 88–91 (2010).
- [39] S. Dongaonkar and M. A. Alam, *Geometrical design of thin film photovoltaic modules for improved shade tolerance and performance*, *Prog. Photovol: Res. Appl.* **23**, 170 (2015).
- [40] Y. Galagan, E. W. C. Coenen, S. Sabik, H. H. Gortler, M. Barink, S. Veenstra, J. Kroon, R. Andriessen, and P. Blom, *Evaluation of ink-jet printed current collecting grids and busbars for ITO-free organic solar cells*, *Sol. Energ. Mat. Sol. C.* **104**, 32 (2012).
- [41] Y. Galagan, B. Zimmerman, E. W. C. Coenen, M. Jorgensen, D. M. Tanenbaum, F. C. Krebs, H. Gortler, S. Sabik, L. H. Sloff, S. Veenstra, J. Kroon, and R. Andriessen, *Current collecting grids for ITO-free solar cells*, *Adv. Energy Mater.* **2**, 103 (2012).



# 4

## CONCENTRATED SOLAR CELL MODELING AND METALLIZATION OPTIMIZATION

*In the previous chapter, the application of topology optimization (TO) has been demonstrated on freeform solar cells, and a methodology has been presented to simultaneously optimize the metallizations on the front and rear sides of a solar cell. In this chapter, the application of TO is explored for concentrated illumination conditions. In concentrated photovoltaics (CPVs), lenses and mirrors are used to concentrate illumination over a small solar cell, thereby increasing the incident light intensity several folds. This leads to non-uniform illumination and temperature distributions on the front side of the cell, which reduces performance. A way to limit this reduction is to optimize the metallization design of the solar cell for the specific non-uniform illumination and temperature profiles. Most of the existing metallization optimization methods are restricted to the conventional H-pattern, which limits the achievable improvements. We therefore study the use of TO to generate optimized electrodes in this setting. For this purpose, the model presented in the previous chapter is extended with additional resistances, which allows accurate modeling of the current density and voltage distributions. Metallization designs obtained by TO for non-uniform illumination and temperature profiles are found to significantly improve the power output of concentrating solar cells.*

---

This chapter is based on a journal article published in Solar Energy journal, **159**, 868-881 (2018) [1].

## 4.1. INTRODUCTION

Concentrated photovoltaic (CPV) systems allow a large amount of solar power generation at a relatively lower cost, since the required solar cell material is reduced [2]. In CPV systems, lenses and curved mirrors are used to concentrate sunlight on small, but highly efficient solar cells [3]. For further improvement in performance, additional elements such as sun trackers and cooling systems are also used. The use of lenses and mirrors modifies the incident radiation on the solar cells, amplifying it several folds in some parts of the cell [3]. Thus, a concentrated, non-uniform illumination profile and a non-uniform temperature distribution are created on the front side of the cell. Due to illumination being higher in some parts of the cell, the photoillumination current density as well as temperature increase locally, leading to a higher voltage drop and increased ohmic losses. Mitchell [4] showed that under non-uniform illumination, series resistance can lead to significant reductions in power output.

For a CPV system to be efficient, it is important that each of its elements performs well individually as well as collectively. One of the ways to improve the efficiency of CPVs is to improve the design of the metallization patterns of the solar cells. Optimization of metallization has been rigorously studied in the past in the context of uniform illumination and one sun intensity [5–9]. In addition, there exist works on designing efficient metallization patterns for certain solar cell geometries under higher sun concentrations with uniform illumination [10–12]. However, optimizing the metal grids under non-uniform sun intensity has received relatively little attention. Mellor *et al.* [2] optimized a conventional H-pattern metallization for a Gaussian illumination profile and constant temperature, and showed that the solar cell with such metallizations could perform better under non-uniform illumination conditions. Domenech-Garret [13] studied the effect of several illumination and temperature profiles on the performance of solar cells. In these studies, linear concentrators were considered and non-uniformity was only assumed along the finger direction [2, 13]. Shifts in the illumination profile due to tracking misalignment and the non-uniformity in the busbar direction were not considered. Both studies restricted themselves to H-patterns and spacing between the metal finger lines was optimized.

The H-pattern is known to be a very efficient metallization geometry for uniformly illuminated, constant temperature cells. However, for CPV, it is likely that other patterns are superior given the non-uniform illumination and temperature conditions. While simplifying the optimization, geometrical restrictions (*e.g.* assumption of straight metal fingers oriented parallel to each other, as in H-pattern) reduce the flexibility of the optimization process and only limited improvements in performance can be expected. More general metallization geometries have been explored for solar cells under uniform illumination as well. Burgers [8] presented a two-step approach to optimize solar cell front metallizations without any pre-assumptions of topology. In the first step, a smeared version of electrode material distribution is optimized in the whole domain. The second step involves a heuristic procedure to translate the optimized material distribution into a line pattern. During the translation step, some prior information is needed from the side of the designer [14]. The applicability of this approach for non-uniform illumination was briefly discussed. Burgers *et al.* [15] and Weeber *et al.* [16] proposed alternatives using a pin-up module, a configuration where the electrode starts from the center and

runs all the way through the cell towards the rear side. Since all the panels connections are done on the rear side, shading is reduced for such configurations which leads to improved performance.

In an earlier study concerned with uniform illumination and one sun intensity [9], we have presented a topology optimization (TO) formulation that can optimize the metallization patterns without any interference from the side of the user. TO does not impose any restriction on the design of the metal grids and is capable of generating metallization patterns that cannot be obtained with any of the previously existing methods [17]. An application where the advantage of TO has been particularly clear is the design of metallization patterns for freeform solar cells, where the traditional patterns are not suited and intuition based designs are far from optimal [18, 19]. Under higher illumination intensity (more than one sun), the photoillumination current density is increased, which in turn leads to a larger voltage drop on the front side of the cell. Due to increased non-uniformity of the voltage profile, relatively larger power losses occur and the solar cell efficiency is reduced. This effect is more prominent under nonuniform illumination, where it is seen that the efficiency of the solar cells drops dramatically [2, 20, 21]. Thus, it is of interest to optimize the metal grids with minimal restrictions on the design and tailor them for certain illumination and temperature profiles. With TO, it is not required to restrict the non-uniformity only in x-direction. In this study, we optimize the metallization designs for more general illumination and temperature profiles, with non-uniformity in two dimensions, using topology optimization.

During the optimization, it is important that at every iteration, the current and voltage distributions on the front side of the cell are modeled accurately. For this purpose, the finite element method [22] is a very suited approach, and has been used in the past [2, 8, 13, 14, 23]. In [2, 13], COMSOL<sup>®</sup> models have been used for FEM based modeling, however, only limited mathematical details of the numerical model are discussed. A discussion of FEM based implementation is provided in [14], where the numerical model is embedded into a two-step optimization scheme for metallization design. Further, the TO based approach presented by us in [9, 17] uses a two-dimensional finite element scheme for modeling the local current densities and voltage distributions. However, this simplified model did not include the shunt resistance and resistance due to contact of the emitter with the metal electrode material, and is limited to uniform illumination and temperature conditions for a single sun intensity. Although the role of contact resistance can be neglected for good devices, this may not be true in general. More importantly, the allowable contact resistance is inversely proportional to the current density, due to which it becomes important for concentrated illumination conditions [24].

To enable accurate modeling and optimization of concentrating solar cells, this chapter presents an advanced two-dimensional finite element model and a topology optimization strategy. The numerical model can be used to accurately model the current density and voltage distributions on the front surface of the solar cell. Contact and shunt resistances are included in the model and the effect of contact resistance on the solar cell performance is studied. The numerical model is generalized for 1-diode and 2-diode models as well as other empirical I-V relations. Based on this numerical model, a topology optimization formulation and the associated adjoint sensitivity analysis are developed. The proposed topology optimization methodology can optimize the metallization

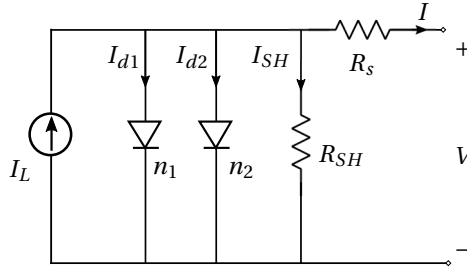


Figure 4.1: Equivalent electrical circuit diagram for a solar cell

patterns for solar cells under concentrating, non-uniform illumination and temperature conditions. While the focus of this chapter is on CPV applications, the presented model as well as the optimization strategy are equally applicable for uniform illumination conditions. The numerical implementations are kept generic for follow up research and a MATLAB<sup>®</sup> implementation of the modeling and optimization procedure is provided<sup>1</sup>. Using the proposed method, metallization patterns are optimized for several cases, and relative performance improvements of up to 26% are observed.

The outline for the rest of the chapter is as follows. Section 4.2 discusses the formulation of the two-layer finite element model. The results obtained from the numerical model for several tests are presented in Section 4.3. This includes numerical tests related to validation of the proposed numerical model against the results reported in [2] (Section 4.3.2), and study of the effect of contact resistance (Section 4.3.3). Section 4.4 presents the optimization strategy and the obtained results for various illumination and temperature profiles are presented in Section 4.5. Finally, the conclusions related to this work are stated in Section 8.6.

## 4.2. MODELING APPROACH

In this section, a detailed numerical model is presented that can efficiently model the current flow and voltage distributions on the front surface of the solar cell. While the discussion is restricted to modeling only the front metallization pattern, the rear side can as well be modeled with slight modifications. To adapt the model for the rear side metallization design, see [19].

### 4.2.1. EQUIVALENT CIRCUIT

Fig. 4.1 shows a simple solar cell circuit diagram applicable to both the 1-diode [25] as well the 2-diode model [26]. Based on this circuit diagram, the characteristic equation for the solar cell can then be stated as

$$I = I_L - I_{d1} - I_{d2} - I_{SH}, \quad (4.1)$$

where,  $I$ ,  $I_L$ ,  $I_{d1}$ ,  $I_{d2}$  and  $I_{SH}$  denote the output current, photoillumination current, the reverse saturation diode currents across diodes 1 and 2 and the shunt current, respec-

<sup>1</sup>A MATLAB<sup>®</sup> implementation is available to download from the repository at <https://github.com/dkgupta90/topsol>.

tively. Let  $V_j$  denote the junction potential, then Eq. 4.1 can be rewritten as

$$I = I_L - I_{01} \left( e^{\frac{\beta V_j}{n_1}} - 1 \right) - I_{02} \left( e^{\frac{\beta V_j}{n_2}} - 1 \right) - \frac{V_j}{R_{SH}}. \quad (4.2)$$

Here,  $n_1$  and  $n_2$  are the ideality factors for diode 1 and 2, respectively and  $\beta = \frac{\bar{q}}{k_B T}$ , where  $\bar{q}$ ,  $k_B$  and  $T$  denote elementary charge, Boltzmann's constant and absolute temperature of the cell, respectively. For a 1-diode model,  $n_1$  and  $n_2$  can be set to 1 and  $\infty$  respectively and for a 2-diode model to 1 and 2, respectively. The shunt resistance  $R_{SH}$  can occur due to defects in the active layer. Due to this, a certain part of the current, termed as shunt current  $I_{SH}$  can take an alternate path [26]. In case there are no defects in the circuit,  $R_{SH}$  can be set to  $\infty$ , and no shunt current is generated.

Next, the junction potential  $V_j$  is further expressed as

$$V_j = V + IR_s, \quad (4.3)$$

where  $V$  is the voltage across the circuit and  $R_s$  denotes the total series resistance. Here,  $R_s$  can consist of contributions from emitter sheet resistance  $R_e$ , ohmic contacts to the emitter  $R_{c,e}$ , metal finger resistance  $R_{fi}$ , busbar resistance  $R_b$ , contributions from the wafer edges  $R_{edge}$ , resistance of the bulk material referred as base resistance  $R_{base}$ , and resistance due to the contact of the metal electrode on the rear side  $R_{c,r}$ . Thus, it can be stated as

$$R_s = R_e + R_{c,e} + R_{fi} + R_b + R_{edge} + R_{base} + R_{c,r}. \quad (4.4)$$

For the sake of simplicity, the resistive components associated with the rear side as well as the edges, *i.e.*,  $R_{c,r}$  and  $R_{edge}$ , are ignored. However, the inclusion of resistive components associated with the rear side should be evident from the model description and from the study presented in [19]. With these simplifications,  $R_s$  can be restated as

$$R_s = R_e + R_{c,e} + R_{fi} + R_b + R_{base}. \quad (4.5)$$

The electrical circuit shown in Fig. 4.1 is a lumped model, however, to correctly model the current and voltage distributions in the emitter and electrode layers, a distributed diode model is required (*e.g.* [27]). In this chapter, a distributed model is used, where the current flow at any point in the active layer is modeled using a diode and the current flow in the emitter and the electrode layers is modeled using a two-layer finite element mesh, as discussed in Section 4.2.3. Let the current entering the emitter layer at any point be denoted by  $I^e$ , then based on Eqs. 4.2 and 4.3,

$$I^e = I_L - I_{01} \left( e^{\frac{\beta(V+I^e\tilde{R}_s)}{n_1}} - 1 \right) - I_{02} \left( e^{\frac{\beta(V+I^e\tilde{R}_s)}{n_2}} - 1 \right) - \frac{V + I^e\tilde{R}_s}{R_{SH}}. \quad (4.6)$$

Note that in Eq. 4.6,  $\tilde{R}_s$  only includes the base resistance and any additional resistances associated with the active layer. The resistances associated with the emitter and electrode layers ( $R_e$ ,  $R_{c,e}$ ,  $R_{fi}$  and  $R_b$ ) are excluded, since they are separately modeled using the finite element mesh.

### 4.2.2. ILLUMINATION AND TEMPERATURE DISTRIBUTION

In this study, solar cells with various illumination and temperature profiles are considered. Illumination profiles for linear concentrators have been identified to be Gaussian [20]. While any profile can be used in our numerical model, following the work presented in [13], we use the Gaussian radiation profiles for this study. The one-dimensional Gaussian profiles used for model validation are same as that used in [2, 13]. However, since we do not restrict the radiation to vary only along the finger direction, two-dimensional illumination non-uniformities are modeled as well. To account for a Gaussian radiation profile, we define the radiation factor as

$$\mathcal{R}(r) = \frac{N_0 A_0}{\zeta} e^{-\frac{r-r_0}{2S^2}}, \quad (4.7)$$

where,  $\mathcal{R}(r)$  denotes the radiation factor at any point  $r = (x, y)$  of the solar cell front surface domain, and  $r_0$  refers to the radiation profile center. Also,  $N_0$  denotes the average number of suns at any point of the solar cell and  $S$  controls the width of the Gaussian curve. For the Gaussian radiation profiles used in this study,  $S = \frac{4r_{max}}{\sqrt{\pi}A_0}$  and  $r_{max} = \sqrt{1 + \frac{L_y}{L_x}}$ , where  $L_y$  and  $L_x$  denote the cell lengths in  $y$ - and  $x$ -directions, respectively. The term  $A_0$  controls the illumination contrast and  $\zeta$  is a normalizing term defined as  $\zeta = \int_{\Omega} e^{-\frac{r-r_0}{2S^2}} d\Omega$ , where  $\Omega$  refers to the solar cell domain. A more complex radiation distribution is an irregular profile (caused due to misalignments, optical aberrations [21]) which is modeled by adding multiple Gaussian and anti-Gaussian profiles.

Under non-uniform temperature distribution, the terms  $I_{01}$  and  $I_{02}$  in Eq. 4.6 are no longer constant in the whole solar cell domain. The reverse saturation diode currents can be expressed as functions of local temperature as [2],

$$I_{01} = I_{001} T^3 e^{-\frac{E_{G0}}{k_B T}}, \quad (4.8)$$

$$I_{02} = I_{002} T^3 e^{-\frac{E_{G0}}{k_B T}}, \quad (4.9)$$

where,  $I_{001}$ ,  $I_{002}$  and  $E_{G0}$  (bandgap energy at 0 K) can be assumed to be constant with respect to temperature.

The temperature profile depends on several factors, *e.g.* the distribution of incident illumination, solar cell properties, cooling device, *etc.*, and simulating it for a certain specific scenario is beyond the scope of this work. The choice of the temperature profile does not affect the proposed modeling and optimization approach, hence we restrict ourselves to some of the popularly used temperature profiles. In [13], it is stated that two of the prominent temperature profiles for concentrators are the Gaussian and anti-Gaussian distributions. For Gaussian radiation profiles, temperature field in silicon solar cells can be described using Gaussian distributions [28]. Temperature profiles can also be considered such that they describe the role of cooling devices. Under such scenarios, the temperature distribution can be described using an inverse Gaussian distribution [13]. Similar to radiation profiles, we do not restrict the temperature to vary only along the finger direction, rather two-dimensional temperature non-uniformities are modeled as well.

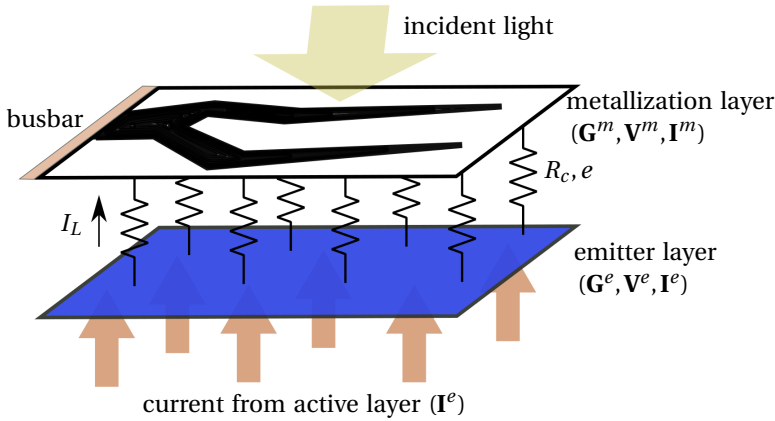


Figure 4.2: A two-layer finite element model of the front surface of a solar cell. Layer 1 comprises the emitter material and layer 2 consists of electrode material parts and void parts. Each node of the emitter layer is connected to the respective node in the metal layer with a resistor (contact resistance  $R_{c,e}$ ).

The Gaussian temperature distribution can be described as

$$T_g(r) = \Delta T e^{-\frac{(r-r_0)^2}{2S_T^2}} + T_0, \quad (4.10)$$

where,  $\Delta T$  denotes the amplitude of temperature with respect to the baseline temperature  $T_0$  and  $S_T$  controls the width of the temperature curve. The anti-Gaussian profile can be described as

$$T_{ag}(r) = \Delta T \left( 1 - e^{-\frac{(r-r_0)^2}{2S_T^2}} \right) + T_0. \quad (4.11)$$

### 4.2.3. FINITE ELEMENT MODEL

We model the solar cell using the finite element method (FEM). Fig. 4.2 shows a two-layer finite element model for the front surface of a solar cell. The lower layer models the voltage and current distributions for the emitter layer and the upper layer similarly models these parameters for the metal electrode. The metallization pattern is defined on the upper layer, and this pattern is optimized using a density-based topology optimization approach [29]. For optimization purposes, the metallization is defined using a set of density design variables  $\rho$  comprising the element densities for each finite element. The term *density* here quantifies the amount of electrode material inside each finite element of the metallization layer. For a density value of 1, the finite element is fully filled with electrode material and for 0, it is empty.

The reason to use a two-layer model is to accurately model the contact resistance  $R_{c,e}$  between the electrode material and the emitter. In general, losses due to the ohmic contact (contact resistance) depend on the current flow between the metal and the emitter layer. Thus, rather than the whole area of metal-emitter contact, only those parts need to be considered where there is a current flow between the two layers. In the proposed

numerical model, this is achieved with two layers of finite element mesh, where every node of the emitter layer is connected to the corresponding node of the metal layer with a resistor of resistance  $R_{c,e}$ . The losses due to local ohmic contact can then take place only if there is a flow of current through the respective resistor  $R_{c,e}$ .

To model the current and voltage distributions, the following partial differential equations need to be solved:

$$\sigma^e \nabla^2 V^e = \frac{\delta \bar{\rho}^e}{\delta t}, \quad (4.12)$$

$$\sigma^m \nabla^2 V^m = \frac{\delta \bar{\rho}^m}{\delta t}. \quad (4.13)$$

Here and henceforth, the superscripts  $e$  and  $m$  refer to the emitter and metal electrode layers, respectively. The material dependent conductivities are represented by  $\sigma$  and  $\bar{\rho}$  refers to enclosed charge density. Based on finite element discretizations (e.g. [22]), the systems of equations for the two layers are

$$\mathbf{G}^e \mathbf{V}^e - \mathbf{I}^e(\boldsymbol{\rho}, \mathbf{V}^e) + \mathbf{I}^m(\mathbf{V}^e, \mathbf{V}^m) = \mathbf{0}, \quad (4.14)$$

$$\mathbf{G}^m(\boldsymbol{\rho}) \mathbf{V}^m - \mathbf{I}^m(\mathbf{V}^e, \mathbf{V}^m) = \mathbf{0}. \quad (4.15)$$

The conductivity matrices are denoted by  $\mathbf{G}$ , and  $\mathbf{V}$  and  $\mathbf{I}$  refer to the column vectors of voltage and current, respectively.

The current  $\mathbf{I}^e$ , coming from active layer and entering the emitter layer, depends on the local shading. Here, local shading refers to the amount of sunlight blocked by the electrode metal in a certain part of the cell, and is dependent on the element density of the respective finite element in the metallization layer. On the other hand,  $\mathbf{I}^m$ , the ohmic current flowing from the emitter layer to the metal electrode, does not depend on the electrode material distribution. This current depends on the contact resistance  $R_{c,e}$  and can be expressed as

$$\mathbf{I}^m = \frac{1}{R_{c,e}} (\mathbf{V}^e - \mathbf{V}^m). \quad (4.16)$$

Using Eqs. 4.14, 4.15 and 4.16, the system of equations can be combined into a residual form as

$$\mathbf{R} = \begin{bmatrix} \mathbf{G}^e & \mathbf{0} \\ \mathbf{0} & \mathbf{G}^m \end{bmatrix} \begin{bmatrix} \mathbf{V}^e \\ \mathbf{V}^m \end{bmatrix} - \begin{bmatrix} \mathbf{I}^e \\ \mathbf{0} \end{bmatrix} + \frac{1}{R_c} \begin{bmatrix} \mathbb{1} & -\mathbb{1} \\ -\mathbb{1} & \mathbb{1} \end{bmatrix} \begin{bmatrix} \mathbf{V}^e \\ \mathbf{V}^m \end{bmatrix} = \mathbf{0}. \quad (4.17)$$

Eq. 4.17 can further be written as

$$\mathbf{R} = \underbrace{\begin{bmatrix} \mathbf{G}^e + \frac{1}{R_c} \mathbb{1} & -\frac{1}{R_c} \mathbb{1} \\ -\frac{1}{R_c} \mathbb{1} & \mathbf{G}^m + \frac{1}{R_c} \mathbb{1} \end{bmatrix}}_{\mathbf{G}} \underbrace{\begin{bmatrix} \mathbf{V}^e \\ \mathbf{V}^m \end{bmatrix}}_{\mathbf{V}} - \underbrace{\begin{bmatrix} \mathbf{I}^e \\ \mathbf{0} \end{bmatrix}}_{\mathbf{I}} = \mathbf{G} \mathbf{V} - \mathbf{I} = \mathbf{0}. \quad (4.18)$$

The conductivity matrix  $\mathbf{G}^e$  is constructed from the global assembly of the element conductivity matrices  $\mathbf{G}_{el}^e$ , where

$$\mathbf{G}_{el}^e = \sigma_s^e \mathbf{G}_0. \quad (4.19)$$

Here,  $\sigma_s^e$  denotes the sheet conductivity of the emitter material and  $\mathbf{G}_0$  denotes the normalized conductivity matrix [17]. The conductivity for layer 2 depends on the electrode

material distribution and can be described using the Solid Isotropic Material with Penalization (SIMP) model [30] as follows:

$$\mathbf{G}_{el}^m = \sigma_s^0 + \rho^q (\sigma_s^m - \sigma_s^0) \mathbf{G}_0, \quad (4.20)$$

where  $\sigma_s^m$  denotes the sheet conductivity of the constant thickness electrode material and  $\sigma_s^0$  is chosen as  $10^{-12} \cdot \sigma_s^m$  to represent physically void areas. A non-zero value is chosen to avoid numerical instabilities. To include the shading effect of the metallization into the model,  $I_L$  in Eq. 4.6 is replaced by  $I_L(1 - \rho)^r$ . Both  $q$  and  $r$  exponents are used to penalize intermediate element densities. This is necessary from a fabrication point of view, since it helps to obtain 0 (electrode material) or 1 (void) values in the final metal layer.

The busbar is assumed to be directly connected to the external load and is therefore set to the cell operating voltage  $V_b$ . For optimal performance of the solar cell, the busbar potential is also considered as an optimization parameter. Next, the nonlinear system of equations (Eq. 4.17) is solved in an iterative manner using the Newton method. An initial guess for  $\mathbf{V}$  is made and at every iteration, it is updated as follows:

$$\mathbf{V}_{i+1} = \mathbf{V}_i - \left( \frac{d\mathbf{R}_i}{d\mathbf{V}_i} \right)^{-1} \mathbf{R}_i, \quad (4.21)$$

where

$$\frac{d\mathbf{R}_i}{d\mathbf{V}_i} = \mathbf{G} - \frac{d\mathbf{I}_i}{d\mathbf{V}_i}, \quad (4.22)$$

$$\frac{d\mathbf{I}_i}{d\mathbf{V}_i} = \begin{bmatrix} \frac{d\mathbf{I}_i^e}{dV_i^e} & \mathbf{0} \\ \mathbf{0} & \mathbf{0} \end{bmatrix}. \quad (4.23)$$

During optimization, the Newton iterations can be started from the solution of  $\mathbf{V}$  obtained in the previous optimization step. At every Newton iteration,  $\mathbf{I}^e$  and  $\frac{d\mathbf{I}^e}{dV^e}$  need to be calculated, details of which are given in Appendices 4.A and 4.B, respectively.

## 4.3. MODELING RESULTS

To validate the proposed numerical model, the numerical solar cell example presented in [2] is modeled and the results are compared. Further, based on our numerical model, the effect of contact resistance on the performance of solar cell is studied for uniform and non-uniform illumination conditions. For model validation as well as for optimization, numerical examples of crystalline silicon solar cell are used in this chapter. However, the proposed approach is general and also applicable to other solar cell types. In the past, variants of the method have been used for other cell types such as thin films [9], organic cells [19].

### 4.3.1. MODEL PARAMETERS

A monocrystalline silicon solar cell of dimensions 4.8 cm  $\times$  10.6 cm is considered with a busbar width of 2 mm and finger width of 35  $\mu\text{m}$ . Additional input parameters used

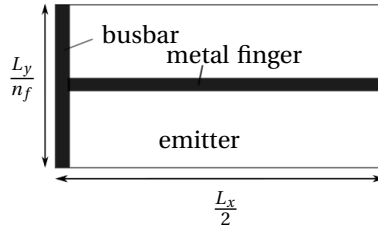


Figure 4.3: The cell element used for modeling purposes. Here,  $L_x$  and  $L_y$  are the cell lengths along x- and y-directions and  $n_f$  denotes the number of metal fingers.

4

Table 4.1: Input parameters for a solar cell under 12 suns illumination (from [2]).

<i>Cell geometry and resistivities</i>	
Cell length ( $L_y$ )	10.6 cm
Cell width ( $L_x$ )	4.8 cm
Busbar width	2mm
Finger width	35 $\mu\text{m}$
Finger sheet resistance	$1.05 \times 10^{-3} \Omega/\text{sq}$
Emitter sheet resistance	100 $\Omega/\text{sq}$
<i>Operation conditions</i>	
Temperature	320 K
Mean illumination intensity	12,000 $\text{Wm}^{-2}$
<i>Diode parameters</i>	
$C_1$	0.39444 $\text{AW}^{-1}$
$C_2$	-11,739 $\text{Am}^{-2}\text{K}^{-3}$
$C_3$	-0.83584 $\text{Am}^{-2}\text{V}^{-1}$
Ideality factor $n_1$	1.0603
$E_g$	1.124 eV

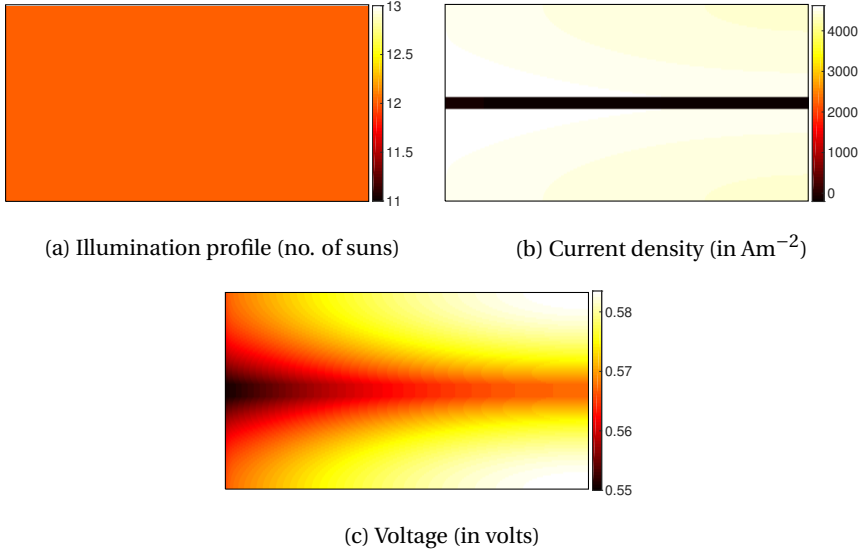


Figure 4.4: Uniform illumination profile for 12 suns and the out-of-plane current density and voltage distributions observed in one cell element (1 sun =  $1000 \text{ Wm}^{-2}$ ).

in our numerical model are the same as that in [2] and are stated in Table 4.1. Note that in [2, 31] as well as several other works related to concentrated illuminations, a different current-voltage characteristic relationship is used. Here, current density and voltage are related as follows:

$$J^e = C_1 G + C_2 T^3 \left( e^{\frac{-E_g}{k_B T}} \right) \left( e^{\frac{qV}{n_1 k_B T}} - 1 \right) + C_3 V, \quad (4.24)$$

where,  $J^e$  and  $G$  denote current density in the emitter layer and illumination, respectively, and  $C_1$ ,  $C_2$  and  $C_3$  are coefficients specific to any given cell [31]. The parameters  $C_1$ ,  $C_2$  and  $C_3$  listed in Table 4.1 are related to this curve. However, for modeling purpose, this is not a problem and it can be transformed into the traditional IV curve listed in Eq. 4.6 (see Appendix 4.C).

For traditional solar cells, where an H-pattern is used for metallization, the size of the modeling domain can be significantly reduced due to the lines of symmetry along the  $x$ - and  $y$ -directions. Thus, we model here only one cell element as shown in Fig. 4.3. For FEM based modeling, the domain of the element is discretized into a structured grid of square elements with bilinear shape functions. The operating voltage of the cell is optimized to achieve maximum performance for the chosen metallization design.

### 4.3.2. MODEL VALIDATIONS

For validation purposes, two different illumination conditions are considered. For the first test, a uniform illumination of 12 suns is assumed on the front side of the solar cell. The optimal metallization design for this scenario consists of 184 parallel metal fingers [2]. The cell element domain is modeled using  $4400 \times 117$  square finite elements. Fig. 4.4

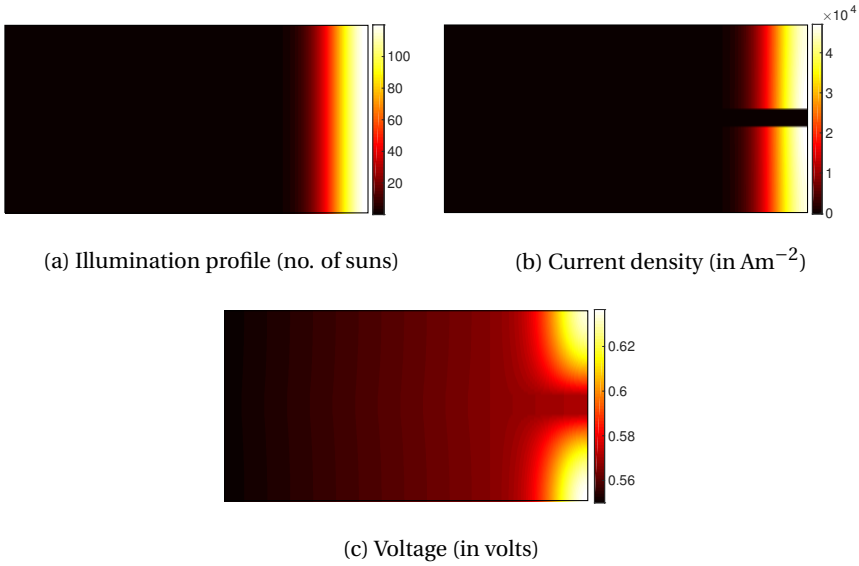


Figure 4.5: Non-uniform illumination profile with an average illumination of 12 suns and peak illumination ratio of 10 and the out-of-plane current density and voltage distributions observed in one cell element (1 sun =  $1000 \text{ Wm}^{-2}$ ).

shows the illumination profile as well as the current and voltage distributions modeled on the front side of one cell element. The fill factor (FF) and efficiency  $\eta$  values obtained using the proposed model are 0.79 and 19.25%. These values match with those obtained in [2], where FF and  $\eta$  are equal to 0.79 and 19.25%, respectively.

In another test, a Gaussian illumination profile with a mean illumination of 12 suns and peak to mean ratio (PIR) of 10 is used. The metallization geometry is assumed to still consist of 184 fingers, which is an optimal geometry of electrode fingers under uniform illumination. With this metallization, the FF and  $\eta$  values drop to 0.73 and 17.49%, respectively. For the non-uniform illumination of PIR = 10, the optimized metallization geometry consists of 287 electrode fingers [2]. For this case, the cell element is modeled using  $4400 \times 84$  electrode fingers. With this metallization, it is observed that the efficiency improves from 17.49% to 18.58% and FF increases from 0.73 to 0.80. The Fig. 4.5 shows the illumination profile, voltage and current distributions for one cell element.

For uniform as well as non-uniform illumination, it is observed that the FF as well as  $\eta$  values obtained using the proposed numerical model match well with the results in [2]. Table 4.2 also reports additional parameters associated with the output IV curves. These values also match well with those stated in [2]. Thus, it is observed that the proposed model can accurately model the published solar cell cases of uniform and non-uniform illumination conditions.

Table 4.2: Number of electrode fingers used and respective output IV characteristics obtained using our model and those reported by Mellor and co-workers.

Parameter	Our results	Mellor <i>et al</i> [2]
<i>Uniform illumination with 12 suns</i> <i>(using 184 metal fingers)</i>		
$I_{sc}$ (in A)	20.69	20.79
$V_{oc}$ (in volts)	0.66	0.65
Fill factor	0.79	0.79
Efficiency (in %)	19.25	19.25
<i>Average illumination of 12 suns with PIR = 10</i> <i>(using 184 metal fingers)</i>		
$I_{sc}$ (in A)	20.69	-
$V_{oc}$ (in volts)	0.65	0.64
Fill factor	0.73	0.73
Efficiency (in %)	17.49	17.50
<i>Average illumination of 12 suns with PIR = 10</i> <i>(using 287 metal fingers)</i>		
$I_{sc}$ (in A)	20.02	-
$V_{oc}$ (in volts)	0.65	0.65
Fill factor	0.80	0.80
Efficiency (in %)	18.58	18.60

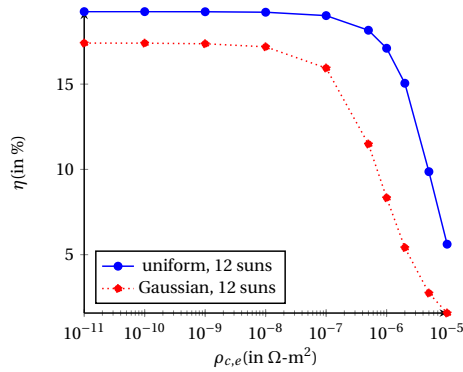


Figure 4.6: Effect of resistivity of the ohmic contact between the emitter and electrode,  $\rho_{c,e}$ , on the efficiency of a solar cell.

### 4.3.3. EFFECT OF CONTACT RESISTANCE

Compared to the effect of other series resistances, generally the effect of contact resistance is very small and can generally be neglected. However, as stated in [24, 32, 33], this holds for good devices and may not be true in general. The effect of contact resistance is more prominent under concentrated conditions. Thus, in the proposed finite element model, the ohmic contact between the emitter layer and the metal electrode is also modeled. Based on the model, here we briefly study the effect of contact resistivity  $\rho_{c,e}$  on the performance of a solar cell. Here, contact resistivity is chosen in place of contact resistance, since it is an area independent parameter. To study its effect, the solar cell example of [2] is studied and the input parameters stated in Table 4.1 are used.

Fig. 4.6 shows efficiency for several values of contact resistivity  $\rho_{c,e}$  for a uniform as well as a non-uniform illumination profile under an intensity of 12 suns. For uniform illumination, it is observed that for a  $\rho_{c,e}$  value close to  $10^{-8} \Omega\text{-m}^2$ , the drop in efficiency is less than 0.04%, which is negligible. This result is in line with [24], where it has been stated that such a value of  $\rho_{c,e}$  should be adequate. However, it is important to note that if the contact resistivity is high, the performance of the cell is significantly affected. For example, for  $\rho_{c,e}$  equal to  $10^{-7} \Omega\text{-m}^2$ , the efficiency drops by 0.23% and for  $10^{-6} \Omega\text{-m}^2$ , an efficiency drop of more than 2% is observed. Clearly, it shows that the contact resistance, if large, can significantly reduce the power output from a solar cell.

Under non-uniform illumination, the role of contact resistance is even more prominent. For a  $\rho_{c,e}$  value of  $10^{-9} \Omega\text{-m}^2$ , the drop in efficiency is close to 0.04%. However, unlike uniform illumination, the efficiency is reduced by more than 0.2% for  $\rho_{c,e}$  equal to  $10^{-8} \Omega\text{-m}^2$ . Thus, under a non-uniform illumination profile, the drop in performance is larger. For  $\rho_{c,e}$  equal to  $10^{-7} \Omega\text{-m}^2$ , an efficiency drop of around 1.5% is observed. Thus, based on these numerical experiments, it can be seen that contact resistance can play an important role in determining the performance of a concentrating solar cell.

## 4.4. OPTIMIZATION APPROACH

### 4.4.1. OPTIMIZATION PROBLEM

The solar cell power maximization problem is an unconstrained optimization problem. To formulate the objective function, Kirchoff's law is used according to which all the generated current in the domain must pass through the busbar which is set to a potential  $V_b$ . Thus, the power output  $P_{out}$  for the solar cell is expressed as

$$P_{out} = V_b \sum_{i=1}^{N_{el}} I_i^m = V_b \sum_{i=1}^{N_{el}} I_i^e, \quad (4.25)$$

where  $I_i^e$  and  $I_i^m$  denote the currents in the  $i^{\text{th}}$  finite element of the emitter and electrode metal layers, respectively, and  $N_{el}$  denotes the number of finite elements in either of the layers.

Traditionally, most of the optimization algorithms require the problem to be posed as a minimization problem. Thus, the objective function  $\mathcal{J}(\boldsymbol{\rho})$  is

$$\begin{aligned} & \min_{\boldsymbol{\rho}} \mathcal{J}(\boldsymbol{\rho}), \\ & \text{with } \mathcal{J}(\boldsymbol{\rho}) = -P_{out}. \end{aligned} \quad (4.26)$$

In this study, gradient-based optimization is applied, using the method of moving asymptotes [34]. In general, it is observed that smaller electrode lines help to improve the solar cell performance. The optimization process would prefer to design very fine electrode features, however, from a fabrication point of view, there is a lower limit on the feature sizes. To take this into account, the optimization process needs to be constrained to not design electrode features smaller than certain minimum size. To impose a restriction on minimum feature size and to avoid any numerical artefacts, we use a density filter [17, 35]. Filtering averages the element densities in a weighted sense within a radius  $r_{min}$ , thereby not allowing electrode features smaller than  $r_{min}$  to occur. In addition, filtering reduces the contrast in density values between the adjacent neighbors, which in turn avoids the formation of checkerboard patterns and other numerical artefacts. For details on density filtering and other alternatives, see [36].

Since the density values are allowed to vary from 0 to 1, it is possible that the converged solution consists of intermediate density values which are not desired from a fabrication point of view. Due to filtering, this effect is more prominent and intermediate density values are seen at the boundaries of the electrode designs. To achieve more crisp solutions, a continuous approximation to the Heaviside function is embedded in the optimization process. The slope of the Heaviside approximation is controlled using a parameter  $\beta_H$ , which is initially chosen to be 1 and its value is doubled at every 50 iterations up to a maximum of 1024. For very high values of  $\beta_H$ , the approximation matches the exact Heaviside function very well. Such a continuation scheme has proven to converge to well performing solutions for several TO problems. The details related to the implementation of continuous Heaviside approximation can be found in [36, 37].

#### 4.4.2. SENSITIVITY ANALYSIS

At every step of the optimization, gradient-based optimization algorithms require information regarding the sensitivity of the objective to each of the design variables. To compute the sensitivities, the adjoint method is used [38]. The adjoint sensitivity analysis of  $\mathcal{J}$  requires an adjoint formulation where the augmented response  $\hat{\mathcal{J}}$  is stated as

$$\hat{\mathcal{J}}(\mathbf{s}) = \mathcal{J}(\mathbf{s}, \mathbf{V}(\mathbf{s})) + \boldsymbol{\lambda}^\top (\mathbf{R}(\mathbf{s}, \mathbf{V}(\mathbf{s}))), \quad (4.27)$$

where,  $\mathbf{s}$  is the set of design variables and can be expressed as  $\mathbf{s} = [\rho_1, \rho_2, \dots, V_b]$ . Using Eq. 4.18 and choosing  $\boldsymbol{\lambda}^\top = [\boldsymbol{\lambda}_e^\top \quad \boldsymbol{\lambda}_m^\top]$ , we obtain

$$\hat{\mathcal{J}} = \mathcal{J} + \begin{bmatrix} \boldsymbol{\lambda}_e \\ \boldsymbol{\lambda}_m \end{bmatrix}^\top \left( \begin{bmatrix} \mathbf{G}^e + \frac{1}{R_c} \mathbb{I} & -\frac{1}{R_c} \mathbb{I} \\ -\frac{1}{R_c} \mathbb{I} & \mathbf{G}^m + \frac{1}{R_c} \mathbb{I} \end{bmatrix} \begin{bmatrix} \mathbf{V}^e \\ \mathbf{V}^m \end{bmatrix} - \begin{bmatrix} \mathbf{I}^e \\ \mathbf{0} \end{bmatrix} \right). \quad (4.28)$$

The sensitivities  $\frac{d\hat{\mathcal{J}}}{d\boldsymbol{\rho}}$  and  $\frac{d\hat{\mathcal{J}}}{dV_b}$  are obtained by taking the derivative of Eq. 4.28 with respect to  $\mathbf{s}$ , details of which are discussed in Appendix 4.D. The total computational cost of the sensitivity analysis for all design variables corresponds to the solution time of a single Newton iteration of the nonlinear solar cell analysis. This efficient approach enables the optimization of detailed metallization topologies.

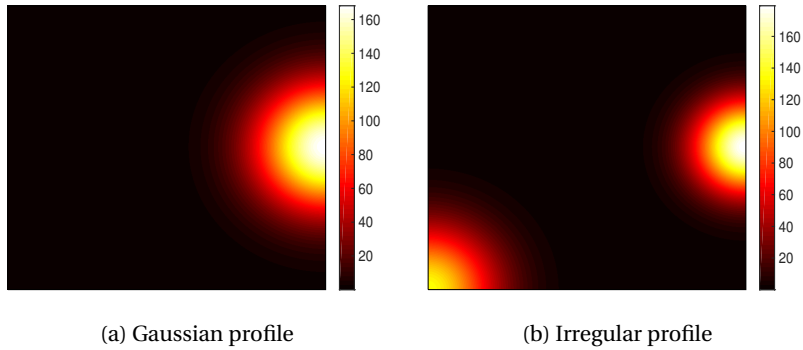


Figure 4.7: Non-uniform illumination profiles with an average illumination of 12 suns (1 sun =  $1000 \text{ Wm}^{-2}$ ). For the Gaussian profile,  $A_0$  is equal to 15 and for the irregular profile  $A_0$  values are 15 and 20 for the two Gaussian distributions.

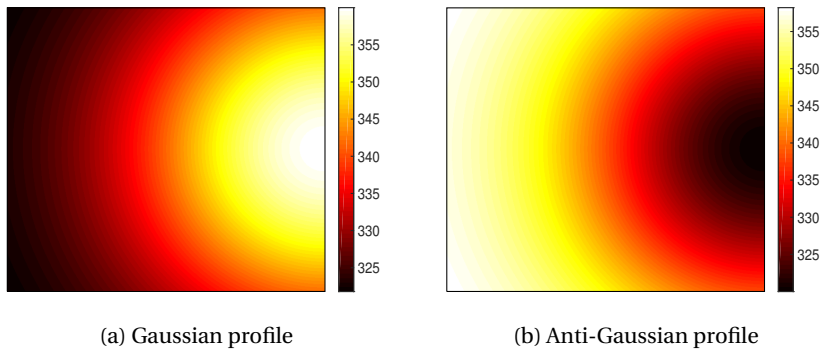


Figure 4.8: Non-uniform temperature profiles with base temperatures equal to 320 K. The temperature amplitude for both cases is set to 40 K deviation from the base temperature.

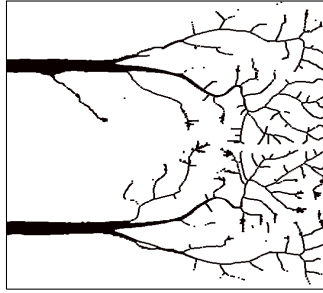
## 4.5. OPTIMIZATION RESULTS

To demonstrate the applicability of the proposed methodology, a number of test cases are considered. Unlike the traditional H-pattern, where due to regularity of the metallization geometry, one cell element (as shown in Fig. 4.3) can be used for optimization, no such regularity is known beforehand for a TO problem. Although it is possible to perform TO on a domain size of one cell element, this would considerably restrict the design freedom of the optimization problem, and limit the performance improvement. For increased flexibility of the optimization problem, considering a larger design domain is preferable. Thus, rather than choosing just one cell element, half of the entire solar cell is used to optimize the metallization design. The input parameters used are same as those stated in Table 4.1. Since typically smaller solar cells are used in CPVs, the physical size of the chosen cell is  $2.42 \text{ cm} \times 1.18 \text{ cm}$ , and the minimum electrode width is restricted to  $60 \text{ }\mu\text{m}$ . The contact resistivity  $\rho_{c,e}$  is set to  $10^{-9} \Omega\text{-m}^2$ .

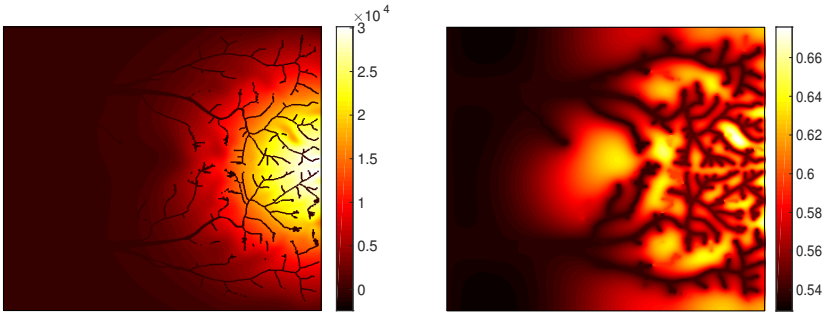
In general, for simple illumination profiles as in [2], well performing H-pattern designs can be easily obtained. We observed that for such illuminations, it is difficult to obtain better performing designs using TO. However, for more complex illumination and temperature profiles, the gain in performance is quite significant using TO, due to which several such non-uniform illumination and temperature profiles are considered here. Three Gaussian profiles (Fig. 4.7a) with  $A_0$  values of 10, 15 and 20, and an irregular profile comprising two Gaussian distributions of  $A_0$  values 15 and 20 (Fig. 4.7b) are considered for defining the illumination field. The average illumination intensity for all the cases is equal to that of 12 suns. Note that these are synthetic profiles for the purpose of illustrating the optimization process. The three temperature profiles used in this work are a uniform field, a Gaussian distribution (Fig. 4.8a) and an anti-Gaussian (Fig. 4.8b) distribution. For all the three temperature profiles, the base temperature was set to 320 K and the temperature amplitude for the non-uniform profiles was set to 40 K.

The design domain of the cell is discretized using a structured mesh of  $600 \times 585$  finite elements, and the filter radius  $r_{min}$  is set to 1.5 elements. This results in a minimum feature size of  $60 \text{ }\mu\text{m}$ . The mesh resolution is chosen such that the desired feature size can be accurately represented. In [17], it has been shown that the optimized designs are not dependent on the choice of mesh, and show only limited variations with change in mesh resolution. A penalty continuation scheme is used, where the exponents  $p$  and  $r$  are both set to 3 initially, and after every 50 iterations of TO, an increment of 0.5 is made to each of them. For a solar cell problem, generally the amount of electrode material to be used is decided by the optimizer based on the compromise between shading and resistive losses [17]. However, in this chapter, numerical cases are considered where the illumination intensity in some regions of the cell is close to zero. In those parts, the optimizer prefers to use electrode material for a marginal gain in conductivity, which can lead to significant parts of the domain being covered with electrode material. To avoid this uneconomic use of material, a constraint is imposed that not more than 10% of the solar cell front surface can be covered with the metallization pattern.

To compare the performance of the designs obtained from TO, a reference H-pattern is used. Parallel electrode fingers of width  $60 \text{ }\mu\text{m}$  are used and the spacing between the fingers is optimized for a uniform illumination intensity of 12 suns and a uniform temperature distribution of 320 K. The efficiency of the reference design under various



(a) Optimized design

(b) Current density (in  $\text{Am}^{-2}$ )

(c) Voltage (in volts)

Figure 4.9: Optimized design and the current density and voltage distributions for the front side of a solar cell under a Gaussian illumination of an average intensity of 12 suns ( $A_0 = 10$ ). A uniform temperature profile is chosen with base temperature set to 320 K. The optimal busbar potential  $V_b$  and efficiency  $\eta$  values are 0.535 volts and 17.075%, respectively.

illumination and temperature conditions is denoted by  $\eta^*$  and the efficiency of the optimized design obtained from TO under similar conditions is denoted by  $\eta$ .

#### 4.5.1. ILLUMINATION PROFILES

Figs. 4.9, 4.10 and 4.11 show the optimized designs and the corresponding current density and voltage distributions for the front side of the solar cell for Gaussian illumination profiles with  $A_0$  equal to 10, 15 and 20, respectively. To reiterate here,  $A_0$  controls the illumination contrast such that for higher values of  $A_0$ , the contrast is higher and the illumination is localized in a smaller region. A uniform temperature distribution with base temperature  $T_0 = 320$  K is chosen. For  $A_0 = 15$  and 20, an intermediate post processing is involved where undesired electrode material from non-illuminated regions of the domain is removed, however, this does not affect the performance of the design. Fig. 4.12 shows the optimized designs before and after processing for  $A_0 = 20$ . During optimization, removing material from the almost non-illuminated parts of the cell does not help in improving its performance. Hence, some ineffective electrode material is left in dark areas in the optimized design, as can be seen in Fig. 4.12a. Table 4.3 states the solar cell

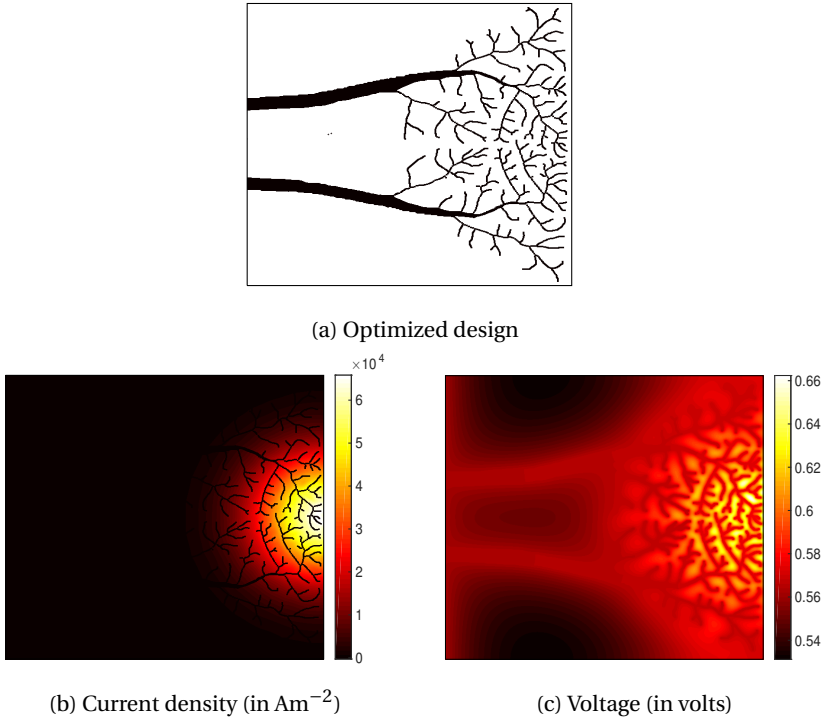
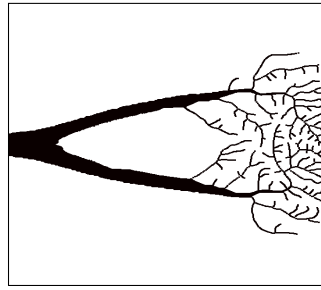


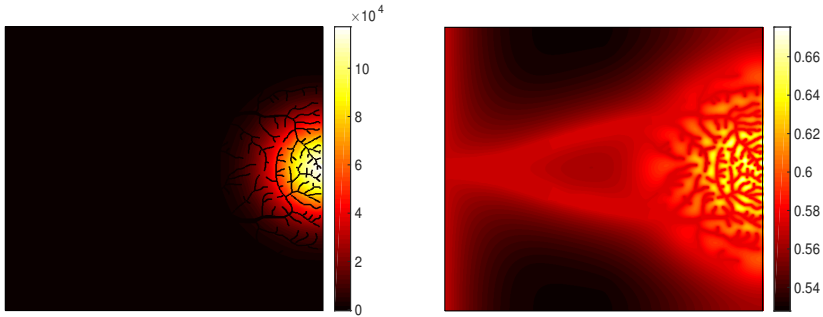
Figure 4.10: Optimized design and the current density and voltage distributions for the front side of a solar cell under a Gaussian illumination of an average intensity of 12 suns ( $A_0 = 15$ ). A uniform temperature profile is chosen with base temperature set to 320 K. The optimal busbar potential  $V_b$  and efficiency  $\eta$  values are 0.562 volts and 17.271%, respectively.

Table 4.3: Solar cell efficiencies obtained for various illumination and temperature profiles using a reference H-pattern design (denoted by  $\eta^*$ ) and topology optimized designs (denoted by  $\eta$ ). Here, the term  $A_0$  is used to control the light intensity contrast for the illumination profiles, and  $T_0$  and  $\Delta T_{max}$  denote the base temperature and amplitude of change in temperature, respectively for the temperature profiles.

Illumination profile	Temperature profile	$\eta^*$ (in %)	$\eta$ (in %)	$\Delta\eta = \eta - \eta^*$
Gaussian ( $A_0 = 10$ )	uniform ( $T_0 = 320$ K)	17.458	17.075	-0.383
Gaussian ( $A_0 = 15$ )	uniform ( $T_0 = 320$ K)	15.511	17.271	1.760
Gaussian ( $A_0 = 20$ )	uniform ( $T_0 = 320$ K)	13.366	16.846	3.480
Irregular (multi-Gaussian with $A_0 = 15$ and 20)	uniform ( $T_0 = 320$ K)	16.035	17.463	1.428
Gaussian ( $A_0 = 15$ )	Gaussian ( $T_0 = 320$ K, $\Delta T_{max} = 40$ K)	13.425	15.043	1.618
Gaussian ( $A_0 = 15$ )	anti-Gaussian ( $T_0 = 320$ K, $\Delta T_{max} = 40$ K)	14.997	16.271	1.274

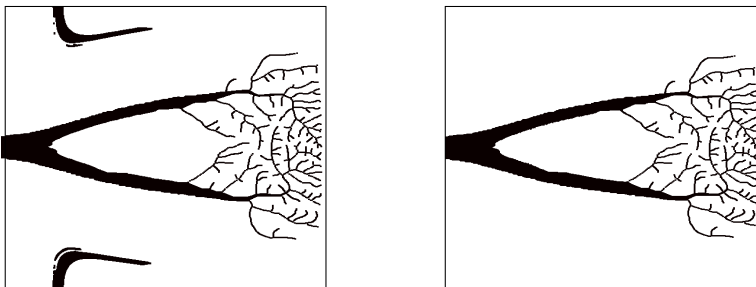


(a) Optimized design

(b) Current density (in  $\text{Am}^{-2}$ )

(c) Voltage (in volts)

Figure 4.11: Optimized design and the current density and voltage distributions for the front side of a solar cell under a Gaussian illumination of an average intensity of 12 suns ( $A_0 = 20$ ). A uniform temperature profile is chosen with base temperature set to 320 K. The optimal busbar potential  $V_b$  and efficiency  $\eta$  values are 0.566 volts and 16.846%, respectively.



(a) Before processing

(b) After processing

Figure 4.12: Optimized design obtained using topology optimization (left), and its post-processed version (right) for the front side of a solar cell under a Gaussian illumination of an average intensity of 12 suns ( $A_0 = 20$ ). The post-processing removed electrode material that remained in dark regions of the cell.

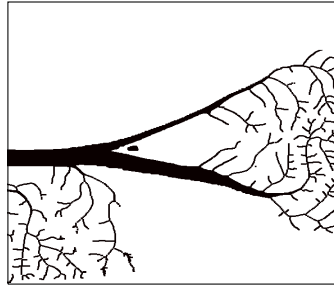
efficiencies obtained using the reference design as well as TO based designs for various illumination and temperature profiles considered in this study. A general observation is that higher values of  $A_0$  result in lower performances of the reference design (denoted by  $\eta^*$ ) as well as the optimized design obtained from TO (denoted by  $\eta$ ).

Among the three Gaussian profiles used, it is observed that for  $A_0 = 15$  and  $20$ , the efficiency of the solar cells increases by  $1.76\%$  and  $3.48\%$ , respectively, for the TO based design compared to the reference design. These imply relative performance improvements of approximately  $11\%$  and  $26\%$ , respectively for the two cases. However, for  $A_0 = 10$ , the TO based design is slightly inferior to the reference design with a reduction of around  $0.38\%$  in efficiency. We believe, it could be a locally optimal solution and with different set of parameters and starting design, it should be possible to obtain a better performing design. In general, given the freedom of design, TO based metallization should be expected to perform better. The solar cell metallization design problem is a highly non-convex problem with many locally optimal solutions in the design domain. At the same time, due to the large number of design variables (*e.g.*  $0.3$  million here), gradient-based optimization methods are used, which can occasionally converge to an inferior locally optimal solution. For the chosen illumination profiles, symmetric metallization designs are expected. However, we use the Newton method to solve Eq. 4.18, and due to even small numerical tolerances at any step of the optimization, the symmetry of the structure can break. For this reason, optimized designs for the solar cell obtained using TO can exhibit asymmetric features.

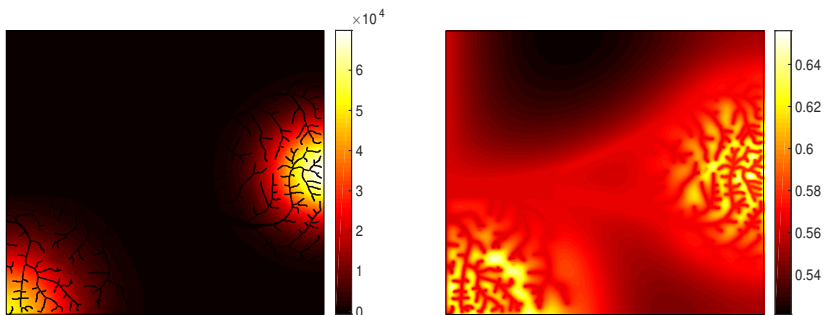
For the choice of  $A_0 = 15$  and  $20$  as well as for various other cases considered in this study, it is observed that there is a voltage drop in the direction away from the busbar (*e.g.* Fig. 4.10c, 4.11c). The reason is that there are some regions in the cell domain where the illumination intensity is close to zero. Due to this, there is no illumination current generated in those areas, which leads to a net current flow in the reverse direction creating local sinks in the cell domain and drop in voltage towards these regions. However, the magnitude of this current is very small compared to the high illumination regions of the cell, and there is no significant impact on the performance of the cell due to the local current absorptions.

Next, an irregular illumination profile is used and the performance of the solar cell is evaluated. The irregular profile is formed by two Gaussian distributions ( $A_0 = 15$  and  $20$ ), with the centres located in two different parts of the design domain as shown in Fig. 4.8b. Fig. 4.13 shows the optimized design and the current density and voltage distributions for the front side of the cell obtained using TO. Compared to the reference design ( $\eta^* = 16.035\%$ ), an increase of  $1.43\%$  is observed in the solar cell efficiency when the TO based design is used ( $\eta = 17.463\%$ ).

For all the four illumination profiles considered here, it is observed that fine features are created in regions with very high illumination intensity. This is because addition of electrode material leads to shading, and in the regions of high illumination intensity, even the addition of a small amount of electrode material leads to large reductions in the illumination, which can significantly affect the performance of the solar cell. We observed that if the restriction on the minimum electrode width is relieved, TO leads to finer electrode features and further improvement in the performance of the solar cell.



(a) Optimized design

(b) Current density (in  $\text{Am}^{-2}$ )

(c) Voltage (in volts)

Figure 4.13: Optimized design and the current density and voltage distributions for the front side of a solar cell under an irregular illumination of an average intensity of 12 suns. The irregular profile is obtained using two Gaussian distributions with  $A_0$  values of 15 and 20. A uniform temperature profile is chosen with base temperature set to 320 K. The optimal busbar potential  $V_b$  and efficiency  $\eta$  values are 0.563 volts and 17.463%, respectively.

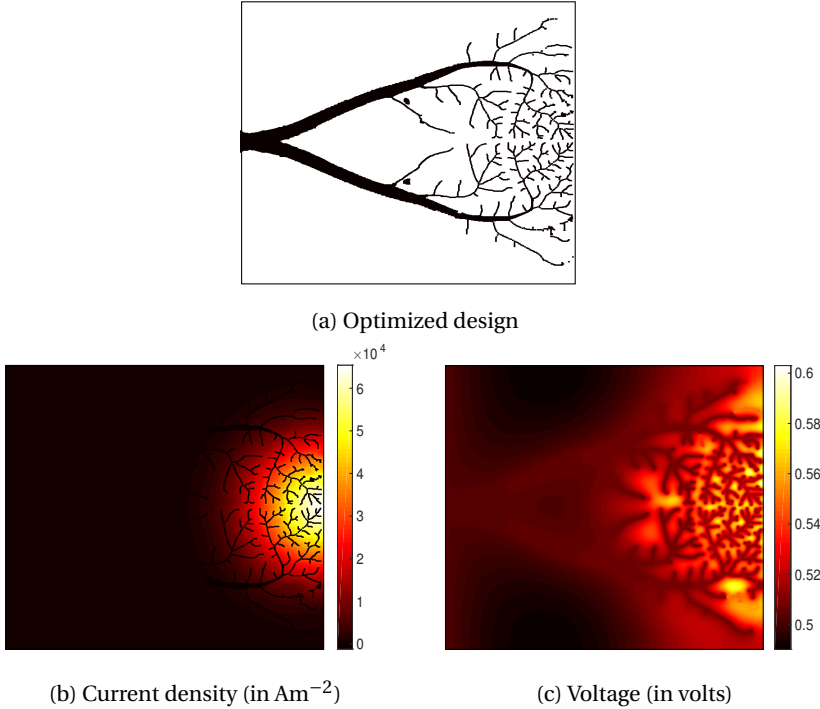
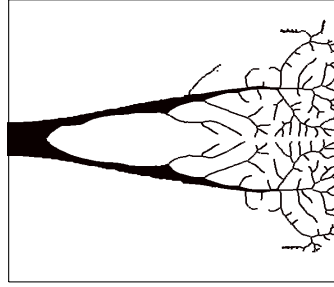


Figure 4.14: Optimized design and the current density and voltage distributions for the front side of a solar cell under a Gaussian illumination of an average intensity of 12 suns ( $A_0 = 15$ ) and a Gaussian temperature profile with base temperature of 320 K and temperature amplitude equal to 40 K. The optimal busbar potential  $V_b$  and efficiency  $\eta$  values are 0.503 volts and 15.033%, respectively.

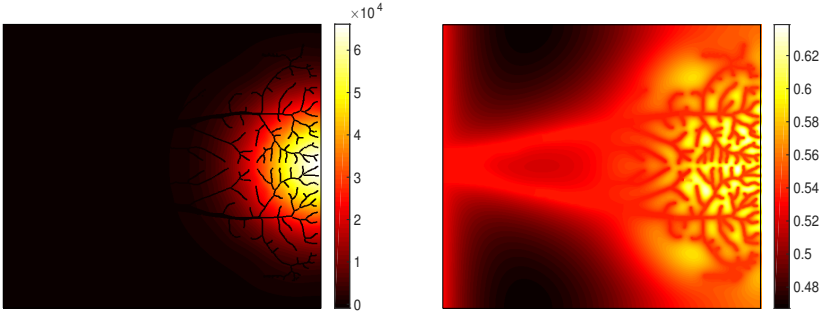
#### 4.5.2. TEMPERATURE PROFILES

The non-uniformity in temperature distribution can also affect the performance of a solar cell. For CPVs, the concentration of sunlight in a small part of the cell leads to a non-uniform temperature profile. Additionally, the cooling systems can also create a non-uniform distribution of temperature. In this chapter, we do not simulate the exact temperature profile for a certain radiation profile and cell properties, as this also requires accurate modeling of all surrounding systems and their thermal properties, which is beyond the scope of this study. Rather, the temperature profile is prescribed (as shown in Fig. 4.8) and the metallization design is optimized, to study its influence on the optimal design. The resulting metallizations and the current density and voltage distributions obtained using TO for the Gaussian and anti-Gaussian temperature distributions are shown in Figs. 4.14 and 4.15, respectively. The efficiency values obtained using these temperature profiles for the reference design as well as for the designs obtained using TO are stated in Table 4.3.

For the reference design itself, it is observed that performance of the solar cell under a non-uniform illumination profile is lower than that of the uniform distribution. The reason is that the local temperature in some parts of the cell for the non-uniform profiles



(a) Optimized design

(b) Current density (in  $\text{Am}^{-2}$ )

(c) Voltage (in volts)

Figure 4.15: Optimized design and the current density and voltage distributions for the front side of a solar cell under a Gaussian illumination of an average intensity of 12 suns ( $A_0 = 15$ ) and an anti-Gaussian temperature profile with base temperature of 320 K and temperature amplitude equal to 40 K. The optimal busbar potential  $V_b$  and efficiency  $\eta$  values are 0.532 volts and 16.271%, respectively.

is higher than the base temperature. Due to increased temperatures, the dark currents are higher in those parts, which leads to an overall reduction in the generated current density and a reduction in performance.

With TO, the performance of the solar cell is improved for both non-uniform temperature profiles (Table 4.3). Compared to the efficiency values of 13.425% and 14.997% obtained for the reference design for the Gaussian and anti-Gaussian temperature profiles, respectively, those obtained using TO are 15.403% and 16.271%, respectively. It is observed that the metallization designs obtained for the two cases are different from that of a uniform temperature distribution (Fig. 4.10). The change in temperature affects the current density and voltage distributions, which in turn affects the electrode material distribution on the front surface. Thus, for the non-uniform temperature distributions, a tailored metallization helps to improve the performance. Similar to the previous cases, small negative currents are observed in some parts of the cell, leading to absorption and a drop in voltage away from the busbar.

## 4.6. CONCLUSIONS

In this chapter, a finite element method based numerical model and a topology optimization strategy have been presented to optimize solar cell metallization patterns under concentrated illumination conditions. All the relevant resistances including the contact and shunt resistance are included in the model. The proposed model is validated through comparisons with previously published modeling results for uniform and non-uniform illumination conditions. Further, from our analysis of solar cells under concentrated conditions, it is observed that contact resistance can significantly affect the performance. Compared to uniform illumination, this effect is more prominent under concentrated conditions. For example, for the case considered in this chapter, it is observed that for the same value of contact resistance, the reduction in solar cell performance under concentrated illumination could be seven times more than that observed under uniform sunlight of equal average illumination. Clearly, this shows that contact resistance can be important for CPVs, and it should therefore be included in the model.

Based on the numerical model, a topology optimization strategy is proposed to design efficient metallization patterns for solar cells under non-uniform illumination and temperature conditions. The applicability of the proposed optimization approach is demonstrated on various synthetic illumination and temperature profiles and for most of the cases, efficient metallization designs are obtained. Using TO, improvement of up to 26% in power output is observed compared to a traditional H-pattern design, optimized for uniform incident sunlight with equivalent average illumination. It is found that a non-uniform temperature distribution can also affect the solar cell performance, and with topology optimization it is possible to design metallization patterns tailored for such profiles. Based on the improvement in performance observed for various cases presented in this study, it can be argued that the proposed approach could serve as an important tool to design solar cell metallizations tailored for concentrated sunlight.

## APPENDICES

### 4.A. COMPUTING $I^e$

Taking the non-uniform illumination and shading effects into account,  $I^e$  for any element can be calculated as

$$I^e = I_L(1 - \rho)^r \mathcal{R} - I_{01} \left( e^{\frac{\beta(V^e + I^e \tilde{R}_s)}{n_1}} - 1 \right) - I_{02} \left( e^{\frac{\beta(V^e + I^e \tilde{R}_s)}{n_2}} - 1 \right) - \frac{V^e + I^e \tilde{R}_s}{R_{SH}}. \quad (4.29)$$

This is a transcendental equation and cannot be solved directly. Thus, we solve it numerically using inner Newton iterations. Eq. 4.29 is rewritten as

$$I^e - I_L(1 - \rho)^r \mathcal{R} + I_{01} \left( e^{\frac{\beta(V + I \tilde{R}_s)}{n_1}} - 1 \right) + I_{02} \left( e^{\frac{\beta(V + I \tilde{R}_s)}{n_2}} - 1 \right) + \frac{V^e + I^e \tilde{R}_s}{R_{SH}} = 0. \quad (4.30)$$

Using 4.30 with some rearrangements, a function  $\psi$  is defined for any element of the emitter layer as

$$\psi(I^e) = I^e \left( 1 + \frac{\tilde{R}_s}{R_{SH}} \right) + I_{01} e^{\frac{\beta(V^e + I^e \tilde{R}_s)}{n_1}} + I_{02} e^{\frac{\beta(V^e + I^e \tilde{R}_s)}{n_2}} - \left( I_L(1 - \rho)^r \mathcal{R} + I_{01} + I_{02} - \frac{V^e}{R_{SH}} \right) = 0. \quad (4.31)$$

To obtain  $\mathbf{I}^e$ ,  $\psi(I^e)$  needs to be assembled for all the finite elements of the domain and the root of equation  $\boldsymbol{\psi}(\mathbf{I}^e) = \mathbf{0}$  needs to be calculated. This is achieved using Newton method, where following is the update scheme:

$$\mathbf{I}_{i+1}^e = \mathbf{I}_i^e - \frac{\boldsymbol{\psi}(\mathbf{I}^e)}{\boldsymbol{\psi}'(\mathbf{I}^e)}, \quad (4.32)$$

where  $\boldsymbol{\psi}'(I^e)$  for any finite element is stated as

$$\boldsymbol{\psi}'(I^e) = \left(1 + \frac{\tilde{R}_s}{R_{SH}}\right) + \frac{\beta \tilde{R}_s I_{01}}{n_1} e^{\frac{\beta(V^e + I^e \tilde{R}_s)}{n_1}} + \frac{\beta \tilde{R}_s I_{02}}{n_2} e^{\frac{\beta(V^e + I^e \tilde{R}_s)}{n_2}}. \quad (4.33)$$

## 4

#### 4.B. COMPUTING $\frac{dI^e}{dV^e}$

From Eq. 4.29, it can be seen that the current at any point of the emitter layer depends only on the local voltage. Thus,  $\frac{dI^e}{dV^e}$  can be obtained by assembling the terms  $\frac{dI^e}{dV^e}$  for the whole finite element domain. For  $\frac{dI^e}{dV^e}$ , the derivative of Eq. 4.30 with respect to  $V^e$  is taken and the following is obtained:

$$\frac{dI^e}{dV^e} + \frac{\beta I_{01}}{n_1} \left(1 + \tilde{R}_s \frac{dI^e}{dV^e}\right) e^{\frac{\beta(V^e + I^e \tilde{R}_s)}{n_1}} + \frac{\beta I_{02}}{n_2} \left(1 + \tilde{R}_s \frac{dI^e}{dV^e}\right) e^{\frac{\beta(V^e + I^e \tilde{R}_s)}{n_2}} + \frac{1}{R_{SH}} + \frac{\tilde{R}_s}{R_{SH}} \frac{dI^e}{dV^e} = 0. \quad (4.34)$$

Rewriting in terms of  $\frac{dI^e}{dV^e}$ ,

$$\frac{dI^e}{dV^e} = - \frac{\frac{\beta I_{01}}{n_1} e^{\beta(V^e + I^e \tilde{R}_s)/n_1} + \frac{\beta I_{02}}{n_2} e^{\beta(V^e + I^e \tilde{R}_s)/n_2} + \frac{1}{R_{SH}}}{\left(1 + \frac{\beta \tilde{R}_s I_{01}}{n_1} e^{\beta(V^e + I^e \tilde{R}_s)/n_1} + \frac{\beta \tilde{R}_s I_{02}}{n_2} e^{\beta(V^e + I^e \tilde{R}_s)/n_2} + \frac{\tilde{R}_s}{R_{SH}}\right)} \quad (4.35)$$

#### 4.C. IV CURVES FOR CONCENTRATED ILLUMINATIONS

The IV curve stated in Eq. 4.6 can be written for 1-diode model ( $n_2 = \infty$ ) and expressed in terms of current density  $j^e$  as

$$j^e = j_L - j_{01} \left( e^{\frac{\beta(V^e + j^e \tilde{R}_s)}{n_1}} - 1 \right) - \frac{V^e \mathcal{A} + j^e \tilde{R}_s}{R_{SH}}, \quad (4.36)$$

where,  $\mathcal{A}$  denotes the local area, and  $j_L$  and  $j_{01}$  refer to photoillumination current density and dark current density in diode 1, respectively. Comparing Eqs. 4.24 and 4.36, following is obtained:

$$j_L = C_1 G, \quad (4.37)$$

$$j_{01} = C_2 T^3 \left( e^{\frac{-E_g}{k_B T}} \right), \quad (4.38)$$

$$\tilde{R}_s = 0, \quad (4.39)$$

$$R_{SH} = \frac{1}{\mathcal{A} C_3}. \quad (4.40)$$

#### 4.D. SENSITIVITY ANALYSIS

For clarity, we assume  $\mathbf{W}_1 = \mathbf{G}^e + \frac{1}{R_c} \mathbb{1}$ ,  $\mathbf{W}_2 = -\frac{1}{R_c} \mathbb{1}$  and  $\mathbf{W}_3 = \mathbf{G}^m + \frac{1}{R_c} \mathbb{1}$  and Eq. 4.28 is rewritten as

$$\hat{\mathcal{J}} = \mathcal{J} + \boldsymbol{\lambda}_e^\top (\mathbf{W}_1 \mathbf{V}^e + \mathbf{W}_2 \mathbf{V}^m - \mathbf{I}^e) + \begin{bmatrix} \boldsymbol{\lambda}_{mf} \\ \boldsymbol{\lambda}_{mp} \end{bmatrix}^\top (\mathbf{W}_2 \mathbf{V}^e + \mathbf{W}_3 \mathbf{V}^m), \quad (4.41)$$

where, the subscripts  $mf$  and  $mp$  refer to the free degrees and fixed degrees of freedom, respectively for the metal electrode layer. Eq. 4.41 should hold for all values of  $\boldsymbol{\lambda}_e$  and  $\boldsymbol{\lambda}_m$ . Thus, we can reduce it by putting  $\boldsymbol{\lambda}_{mp} = \mathbf{0}$ . Thus, we obtain

$$\hat{\mathcal{J}} = \mathcal{J} + \boldsymbol{\lambda}_e^\top (\mathbf{W}_1 \mathbf{V}^e + \mathbf{W}_2 \mathbf{V}^m - \mathbf{I}^e) + \boldsymbol{\lambda}_{mf}^\top ([\mathbf{W}_{2ff} \ \mathbf{W}_{2fp}] \mathbf{V}^e + [\mathbf{W}_{3ff} \ \mathbf{W}_{3fp}] \mathbf{V}^m), \quad (4.42)$$

where,  $\mathbf{W}_2 = \begin{bmatrix} \mathbf{W}_{2ff} & \mathbf{W}_{2fp} \\ \mathbf{W}_{2pf} & \mathbf{W}_{2pp} \end{bmatrix}$  and  $\mathbf{W}_3 = \begin{bmatrix} \mathbf{W}_{3ff} & \mathbf{W}_{3fp} \\ \mathbf{W}_{3pf} & \mathbf{W}_{3pp} \end{bmatrix}$ .

Taking the derivative of Eq. 4.42 with respect to the design variables' set  $\mathbf{s}$ ,

$$\begin{aligned} \frac{d\hat{\mathcal{J}}}{ds} &= \frac{\partial \mathcal{J}}{\partial \mathbf{s}} + \frac{\partial \mathcal{J}}{\partial \mathbf{V}^e} \frac{d\mathbf{V}^e}{ds} + \frac{\partial \mathcal{J}}{\partial \mathbf{V}^m} \frac{d\mathbf{V}^m}{ds} \\ &+ \boldsymbol{\lambda}_e^\top \left( \frac{d\mathbf{W}_1}{ds} \mathbf{V}^e + \mathbf{W}_1 \frac{d\mathbf{V}^e}{ds} + \frac{d\mathbf{W}_2}{ds} \mathbf{V}^m + \mathbf{W}_2 \frac{d\mathbf{V}^m}{ds} - \frac{\partial \mathbf{I}^e}{\partial \mathbf{s}} - \frac{\partial \mathbf{I}^e}{\partial \mathbf{V}^e} \frac{d\mathbf{V}^e}{ds} - \frac{\partial \mathbf{I}^e}{\partial \mathbf{V}^m} \frac{d\mathbf{V}^m}{ds} \right) \\ &+ \boldsymbol{\lambda}_{mf}^\top \left( \left[ \frac{d\mathbf{W}_{2ff}}{ds} \ \frac{d\mathbf{W}_{2fp}}{ds} \right] \mathbf{V}^e + [\mathbf{W}_{2ff} \ \mathbf{W}_{2fp}] \frac{d\mathbf{V}^e}{ds} + \left[ \frac{d\mathbf{W}_{3ff}}{ds} \ \frac{d\mathbf{W}_{3fp}}{ds} \right] \mathbf{V}^m \right) \\ &+ \boldsymbol{\lambda}_{mf}^\top \left( [\mathbf{W}_{3ff} \ \mathbf{W}_{3fp}] \frac{d\mathbf{V}^m}{ds} \right). \end{aligned} \quad (4.43)$$

Since  $\mathbf{W}_1$  and  $\mathbf{W}_2$  are constant matrices, the associated derivative terms with respect to  $\mathbf{s}$  can be set to  $\mathbf{0}$ . In addition, since  $\mathcal{J}$  and  $\mathbf{I}^e$  do not have a direct dependence on  $\mathbf{V}^m$ , the terms  $\frac{\partial \mathcal{J}}{\partial \mathbf{V}^m}$  and  $\frac{\partial \mathbf{I}^e}{\partial \mathbf{V}^m}$  can be set to  $\mathbf{0}$ . Taking these into consideration,

$$\begin{aligned} \frac{d\hat{\mathcal{J}}}{ds} &= \frac{\partial \mathcal{J}}{\partial \mathbf{s}} + \frac{\partial \mathcal{J}}{\partial \mathbf{V}^e} \frac{d\mathbf{V}^e}{ds} + \boldsymbol{\lambda}_e^\top \left( \mathbf{W}_1 \frac{d\mathbf{V}^e}{ds} + \mathbf{W}_2 \frac{d\mathbf{V}^m}{ds} - \frac{\partial \mathbf{I}^e}{\partial \mathbf{s}} - \frac{\partial \mathbf{I}^e}{\partial \mathbf{V}^e} \frac{d\mathbf{V}^e}{ds} \right) \\ &+ \boldsymbol{\lambda}_{mf}^\top \left( [\mathbf{W}_{2ff} \ \mathbf{W}_{2fp}] \frac{d\mathbf{V}^e}{ds} + \left[ \frac{d\mathbf{W}_{3ff}}{ds} \ \frac{d\mathbf{W}_{3fp}}{ds} \right] \mathbf{V}^m + [\mathbf{W}_{3ff} \ \mathbf{W}_{3fp}] \frac{d\mathbf{V}^m}{ds} \right). \end{aligned} \quad (4.44)$$

Rearranging the terms and putting  $\mathbf{V}^m = \begin{bmatrix} \mathbf{V}_f^m \\ \mathbf{V}_p^m \end{bmatrix}$ ,

$$\begin{aligned} \frac{d\hat{\mathcal{J}}}{ds} &= \frac{\partial \mathcal{J}}{\partial \mathbf{s}} + \boldsymbol{\lambda}_e^\top \begin{bmatrix} \mathbf{W}_{2fp} \\ \mathbf{W}_{2pp} \end{bmatrix} \frac{d\mathbf{V}_p^m}{ds} - \boldsymbol{\lambda}_e^\top \frac{\partial \mathbf{I}^e}{\partial \mathbf{s}} + \boldsymbol{\lambda}_{mf}^\top \left[ \frac{d\mathbf{W}_{3ff}}{ds} \ \frac{d\mathbf{W}_{3fp}}{ds} \right] \mathbf{V}^m + \boldsymbol{\lambda}_{mf}^\top \mathbf{W}_{3fp} \frac{d\mathbf{V}_p^m}{ds} \\ &+ \left( \frac{\partial \mathcal{J}}{\partial \mathbf{V}^e} + \boldsymbol{\lambda}_e^\top \mathbf{W}_1 - \boldsymbol{\lambda}_e^\top \frac{\partial \mathbf{I}^e}{\partial \mathbf{V}^e} + \boldsymbol{\lambda}_{mf}^\top [\mathbf{W}_{2ff} \ \mathbf{W}_{2fp}] \right) \frac{d\mathbf{V}^e}{ds} \\ &+ \left( \boldsymbol{\lambda}_e^\top \begin{bmatrix} \mathbf{W}_{2ff} \\ \mathbf{W}_{2pf} \end{bmatrix} + \boldsymbol{\lambda}_{mf}^\top \mathbf{W}_{3ff} \right) \frac{d\mathbf{V}_f^m}{ds}. \end{aligned} \quad (4.45)$$

To eliminate  $\frac{d\mathbf{V}^e}{ds}$  and  $\frac{d\mathbf{V}_f^m}{ds}$ , we define the following adjoint problem:

$$\frac{\partial \mathcal{J}}{\partial \mathbf{V}^e} + \boldsymbol{\lambda}_e^\top \mathbf{W}_1 - \boldsymbol{\lambda}_e^\top \frac{\partial \mathbf{I}^e}{\partial \mathbf{V}^e} + \boldsymbol{\lambda}_{mf}^\top [\mathbf{W}_{2ff} \ \mathbf{W}_{2fp}] = \mathbf{0}, \quad (4.46)$$

$$\boldsymbol{\lambda}_e^\top \begin{bmatrix} \mathbf{W}_{2ff} \\ \mathbf{W}_{2pf} \end{bmatrix} + \boldsymbol{\lambda}_{mf}^\top \mathbf{W}_{3ff} = \mathbf{0}, \quad (4.47)$$

which yields

$$\boldsymbol{\lambda}_e^\top = - \left( \frac{\partial \mathcal{J}}{\partial \mathbf{V}^e} \right) \left( \mathbf{W}_1 - \frac{\partial \mathbf{I}^e}{\partial \mathbf{V}^e} - \begin{bmatrix} \mathbf{W}_{2ff} \\ \mathbf{W}_{2pf} \end{bmatrix} \mathbf{W}_{3ff}^{-1} [\mathbf{W}_{2ff} \ \mathbf{W}_{2fp}] \right)^{-1}, \quad (4.48)$$

$$\boldsymbol{\lambda}_{mf}^\top = \left( \frac{\partial \mathcal{J}}{\partial \mathbf{V}^e} \right) \left( \mathbf{W}_1 - \frac{\partial \mathbf{I}^e}{\partial \mathbf{V}^e} - \begin{bmatrix} \mathbf{W}_{2ff} \\ \mathbf{W}_{2pf} \end{bmatrix} \mathbf{W}_{3ff}^{-1} [\mathbf{W}_{2ff} \ \mathbf{W}_{2fp}] \right)^{-1} \begin{bmatrix} \mathbf{W}_{2ff} \\ \mathbf{W}_{2pf} \end{bmatrix} \mathbf{W}_{3ff}^{-1}. \quad (4.49)$$

Using the values of  $\boldsymbol{\lambda}_e$  and  $\boldsymbol{\lambda}_{mf}$  given in Eqs. 4.48 and 4.49, Eq. 4.45 simplifies to

$$\frac{d\hat{\mathcal{J}}}{ds} = \frac{\partial \mathcal{J}}{\partial \mathbf{s}} + \boldsymbol{\lambda}_e^\top \begin{bmatrix} \mathbf{W}_{2fp} \\ \mathbf{W}_{2pp} \end{bmatrix} \frac{d\mathbf{V}_p^m}{ds} - \boldsymbol{\lambda}_e^\top \frac{\partial \mathbf{I}^e}{\partial \mathbf{s}} + \boldsymbol{\lambda}_{mf}^\top \left[ \frac{d\mathbf{W}_{3ff}}{ds} \ \frac{d\mathbf{W}_{3fp}}{ds} \right] \mathbf{V}^m + \boldsymbol{\lambda}_{mf}^\top \mathbf{W}_{3fp} \frac{d\mathbf{V}_p^m}{ds}. \quad (4.50)$$

#### 4.D.1. COMPUTING $\frac{d\hat{\mathcal{J}}}{d\boldsymbol{\rho}}$

To calculate the sensitivities of the augmented response  $\hat{\mathcal{J}}$  with respect to the design density field  $\boldsymbol{\rho}$ ,  $\mathbf{s}$  is replaced by  $\boldsymbol{\rho}$  in Eq. 4.50. Since  $\mathbf{V}_p^m$  does not depend on material distribution,  $\frac{d\mathbf{V}_p^m}{d\boldsymbol{\rho}} = \mathbf{0}$ . Thus,

$$\frac{d\hat{\mathcal{J}}}{d\boldsymbol{\rho}} = \frac{\partial \mathcal{J}}{\partial \boldsymbol{\rho}} - \boldsymbol{\lambda}_e^\top \frac{\partial \mathbf{I}^e}{\partial \boldsymbol{\rho}} + \boldsymbol{\lambda}_{mf}^\top \left[ \frac{d\mathbf{W}_{3ff}}{d\boldsymbol{\rho}} \ \frac{d\mathbf{W}_{3fp}}{d\boldsymbol{\rho}} \right] \mathbf{V}^m. \quad (4.51)$$

From Eq. 4.26,  $\frac{\partial \mathcal{J}}{\partial \boldsymbol{\rho}} = \frac{\partial}{\partial \boldsymbol{\rho}} \left( V_b \sum_{i=1}^{N_{el}} I_i^e \right) = \frac{\partial}{\partial \boldsymbol{\rho}} (V_b \mathbf{1}^\top \mathbf{I}^e) = V_b \mathbf{1}^\top \left( \frac{\partial \mathbf{I}^e}{\partial \boldsymbol{\rho}} \right)$ , where  $\frac{\partial \mathbf{I}^e}{\partial \boldsymbol{\rho}}$  can be calculated as discussed in Appendix 4.E.

#### 4.D.2. COMPUTING $\frac{d\hat{\mathcal{J}}}{dV_b}$

To calculate the sensitivities of the augmented response  $\hat{\mathcal{J}}$  with respect to the busbar potential  $V_b$ ,  $\mathbf{s}$  is replaced by  $V_b$  in Eq. 4.50. Also,  $\mathbf{W}_3$  and  $\mathbf{I}^e$  do not depend on  $V_b$  and  $\frac{d\mathbf{V}_p^m}{dV_b} = \mathbf{1}$ . Thus,

$$\frac{d\hat{\mathcal{J}}}{dV_b} = \frac{\partial \mathcal{J}}{\partial V_b} + \boldsymbol{\lambda}_e^\top \begin{bmatrix} \mathbf{W}_{2fp} \\ \mathbf{W}_{2pp} \end{bmatrix} \mathbf{1} + \boldsymbol{\lambda}_{mf}^\top \mathbf{W}_{3fp} \mathbf{1}. \quad (4.52)$$

From Eq. 4.26,  $\frac{\partial \mathcal{J}}{\partial V_b} = \frac{\partial}{\partial V_b} \left( V_b \sum_{i=1}^{N_{el}} I_i^e \right) = \sum_{i=1}^{N_{el}} I_i^e$ .

#### 4.E. COMPUTING $\frac{\partial \mathbf{I}^e}{\partial \boldsymbol{\rho}}$

The photoillumination current at any point on the emitter surface is assumed to depend on the shading only at that point. Thus,  $\frac{\partial \mathbf{I}^e}{\partial \boldsymbol{\rho}}$  can be obtained by assembling the terms

$\frac{\partial I^e}{\partial \rho}$  for the whole finite element domain. Thus, Taking the derivative of Eq. 4.30 w.r.t  $\rho$ , following is obtained:

$$\frac{\partial I^e}{\partial \rho} + I_L r (1 - \rho)^{r-1} \mathcal{R} + \frac{I_{01} \beta \tilde{R}_s}{n_1} \frac{\partial I^e}{\partial \rho} e^{\beta(V^e + I^e \tilde{R}_s)/n_1} + \frac{I_{02} \beta \tilde{R}_s}{n_2} \frac{\partial I^e}{\partial \rho} e^{\beta(V^e + I^e \tilde{R}_s)/n_2} + \frac{\tilde{R}_s}{R_{SH}} \frac{\partial I^e}{\partial \rho} = 0. \quad (4.53)$$

Putting together all the terms with  $\frac{dj}{dV}$ ,

$$\frac{\partial I^e}{\partial \rho} \left( 1 + \frac{I_{01} \beta \tilde{R}_s}{n_1} e^{\beta(V^e + I^e \tilde{R}_s)/n_1} + \frac{I_{02} \beta \tilde{R}_s}{n_2} e^{\beta(V^e + I^e \tilde{R}_s)/n_2} + \frac{\tilde{R}_s}{R_{SH}} \right) = -I_L r (1 - \rho)^{r-1} \mathcal{R}. \quad (4.54)$$

This further simplifies to

$$\frac{\partial I^e}{\partial \rho} = \frac{-I_L r (1 - \rho)^{r-1} \mathcal{R}}{1 + \frac{I_{01} \beta \tilde{R}_s}{n_1} e^{\beta(V^e + I^e \tilde{R}_s)/n_1} + \frac{I_{02} \beta \tilde{R}_s}{n_2} e^{\beta(V^e + I^e \tilde{R}_s)/n_2} + \frac{\tilde{R}_s}{R_{SH}}}. \quad (4.55)$$

## REFERENCES

- [1] D. K. Gupta, M. Barink, and M. Langelaar, *CPV solar cell modeling and metallization optimization*, Solar Energy **159**, 868 (2018).
- [2] A. Mellor, J. L. Domenech-Garret, D. Cheminas, and J. I. Rosell, *A two-dimensional finite element model of front surface current flow in cells under non-uniform, concentrated illumination*, Solar Energy **89**, 1459 (2009).
- [3] H. Baig, K. C. Heasman, and T. K. Mallick, *Non-uniform illumination in concentrating solar cells*, Renewable and Sustainable Energy Reviews **12**, 5890 (2012).
- [4] K. W. Mitchell, *Computer analysis of resistance and non-uniform illumination effects on concentrator solar cells*, in *International Electron Devices Meeting* (1977) pp. 229–232.
- [5] W. A. Beckman, *Optimization of Contact Grid Spacing for High Solar Flux Photovoltaic Cells*, Journal of Engineering for Power **89**, 415 (1967).
- [6] A. Flat and A. G. Milnes, *Optimization of multi-layer front-contact grid patterns for solar cells*, Solar Energy **23**, 289 (1979).
- [7] M. Conti, *Optimal design of front-contact metallization for photovoltaic solar cells*, Solid State Electron. **24** (1981).
- [8] A. R. Burgers, *How to design optimal metallization patterns for solar cells*, Progress in Photovoltaics: Research and Applications **7**, 457 (1999).
- [9] D. K. Gupta, M. Langelaar, M. Barink, and F. van Keulen, *Topology optimization: An effective method for designing front metallization patterns of solar cells*, in *2014, IEEE 40th Photovoltaic Specialists Conference (IEEE)* pp. 1–6.
- [10] A. R. Moore, *An optimized grid design for a sun-concentrator solar cell*, RCA Review **40**, 140 (1979).

- [11] C. Algora and V. Díaz, *Influence of series resistance on guide-lines for manufacture of concentrator p-on-n GaAs solar cells*, Progress in Photovoltaics: Research and Applications **8**, 211 (2000).
- [12] G. M. M. W. Bissels, M. A. H. Asselbergs, J. J. Schermer, N. J. Haverkemp, and E. Vlieg, *A genuine circular contact grid pattern for solar cells*, Progress in Photovoltaics: Research and Applications **19**, 517 (2011).
- [13] J. L. Domenech-Garret, *Cell behaviour under different non-uniform temperature and radiation combined profiles using a two dimensional finite element model*, Solar Energy **85**, 256 (2011).
- [14] A. Burgers, *New metallization patterns and analysis of light trapping for silicon solar cells*, in *PhD Thesis* (2005).
- [15] A. R. Burgers, J. H. Bultman, A. C. Tip, and W. C. Sinke, *Metallisation patterns for interconnection through holes*, Sol. Energ. Mat. Sol. C. **65**, 347 (2001).
- [16] A. W. Weeber, R. Kinderman, C. J. J. Tool, F. Granek, and P. C. de Jong, *How to achieve 17 % cell efficiencies on large back-contacted MC-SI solar cells*, in *Proceedings, IEEE 4th World Conf Photovol Ener Conv, Hawaii* (2006) pp. 1–4.
- [17] D. K. Gupta, M. Langelaar, M. Barink, and F. van Keulen, *Topology optimization of front metallization patterns for solar cells*, Structural and Multidisciplinary Optimization **51**, 941 (2015).
- [18] D. K. Gupta, M. Langelaar, M. Barink, and F. van Keulen, *Optimizing front metallization patterns: Efficiency with aesthetics in free-form solar cells*, Renewable Energy **86**, 1332 (2016).
- [19] D. K. Gupta, M. Barink, Y. Galagan, and M. Langelaar, *Integrated front-rear-grid optimization in free-form solar cells*, IEEE Journal of Photovoltaics **7**, 294 (2017).
- [20] G. Johnston, *Focal region measurements of the 20 m<sup>2</sup> tiled dish at the Australian National University*, Solar Energy **63**, 117 (1998).
- [21] A. Luque, G. Sala, and J. Arboiro, *Electric and thermal model for non-uniformly illuminated concentration cells*, Solar Energy Materials and Solar Cells **51**, 269 (1998).
- [22] O. C. Zienkiewicz, R. L. Taylor, and J. Z. Zhu, *Finite Element Method: Its Basis and Fundamentals*, (Elsevier, 2005).
- [23] J. Wong, T. Mueller, R. Sridharan, X. Zhang, Y. Yang, Z. Feng, Q. Huang, P. Verlinden, and A. G. Aberle, *Series resistance modeling of complex metallization geometries of solar cells using conductive line decomposition*, in *2011, IEEE 38th Photovoltaic Specialists Conference (IEEE)* pp. 000501–000504.
- [24] D. Schroder and D. L. Meier, *Solar Cell Contact Resistance - A Review*, IEEE Transactions on Electron Devices **31**, 637 (1984).

- [25] W. Shockley, in *Electrons and Holes in Semiconductors: With Applications to Transistor Electronics* (1950).
- [26] M. Wolf and H. Rauschenbach, *Series resistance effects on solar cell measurements*, *Advanced Energy Conversions* **3**, 455 (1963).
- [27] B. Galiana, C. Algora, I. Rey-Stolle, and I. G. Vara, *A 3-D model for concentrator solar cells based on distributed circuit units*, *IEEE Transactions on Electron Devices* **52**, 2552 (2005).
- [28] E. Franklin and J. S. Coventry, *Effects of highly non-uniform illumination distribution on electrical performance of solar cells*, in *Proceedings of Solar* (Australian and New Zealand Solar Society, 2003).
- [29] M. P. Bendsøe and O. Sigmund, *Topology Optimization: Theory, methods and applications* (Springer, 2003).
- [30] M. P. Bendsøe, *Optimal shape design as a material distribution problem*, *Structural Optimization* **1**, 193 (1989).
- [31] J. I. Rosell and M. Ibañez, *Modelling power output in photovoltaic modules for outdoor operating conditions*, *Energy Conversion and Management* **47**, 2424 (2006).
- [32] D. L. Meier and D. K. Schroder, *Contact Resistance: Its measurement and relative importance to power loss in a solar cell*, *IEEE Transactions on Electron Devices* **31**, 647 (1984).
- [33] J. van Deelen, Y. Tezsevin, and M. Barink, *Multi-material front contact for 19% thin film solar cells*, *Materials* **9**, 96 (2016).
- [34] K. Svanberg, *The method of moving asymptotes - a new method for structural optimization*, *International Journal for Numerical Methods in Engineering* **24**, 359 (1987).
- [35] T. E. Bruns and D. A. Tortorelli, *Topology optimization of nonlinear elastic structures and compliant mechanisms*, *Comput. Method. Appl. M.* **190**, 3443 (2001).
- [36] O. Sigmund, *Morphology-based black and white filters for topology optimization*. *Structural and Multidisciplinary Optimization* **33**, 401 (2007).
- [37] J. Guest, J. Prevost, and T. Belytschko, *Achieving minimum length scale in topology optimization using nodal design variables and projection functions*, *International Journal for Numerical Methods in Engineering* **61**, 238 (2004).
- [38] F. van Keulen, R. T. Haftka, and N. H. Kim, *Review of options for structural design sensitivity analysis. Part 1: linear systems*, *Computer Methods in Applied Mechanics and Engineering* **194**, 3213 (2005).



# II

## HIGH-RESOLUTIONS DESIGNS USING TOPOLOGY OPTIMIZATION



# 5

## COMBINED MESH AND PENALIZATION ADAPTIVITY BASED TOPOLOGY OPTIMIZATION

*In Part II of this thesis, the goal is to develop methodologies for obtaining high-resolution structural designs using topology optimization (TO). For high-resolution designs, it is important that the material boundary descriptions are clear and the design is black-white in nature. A black-white design consists of only solids and voids with no intermediate density (gray) values. Low computational costs are desired for the overall TO process. For fixed discretizations, the requirements of high resolution and low cost are conflicting.*

*This chapter introduces a novel adaptivity scheme for TO that can be used to produce optimal structures with high resolution and reduced gray areas at relatively low computational costs. A new mesh refinement indicator is introduced which efficiently selects the finite elements to be refined/coarsened during the course of the optimization. The filter radius is also adapted and the proposed method is coupled with penalization continuation to generate well-performing designs. The proposed approach is used to optimize the design of a cantilever beam for compliance minimization. The results show that the mesh refinement indicator helps to generate high resolution areas in appropriate locations and suppresses the intermediate densities at low computational costs. Also, the designs obtained using penalization adaptivity are found to resemble the analytical solution of the problem.*

---

This chapter is based on an article published in the conference proceedings of AIAA Scitech 2016 event held in San Diego, California, USA [1].

## 5.1. INTRODUCTION

The goal of structural design problems in aircraft and aerospace related disciplines is to generate designs that can deliver maximum performance for least possible mass. Sizing and shape optimization are the two traditional techniques that have been widely used for such problems [2, 3]. However, due to imposed restrictions on the topology, these methods are not capable of exploiting all possible designs. Topology optimization (TO) extends shape optimization and no or limited restrictions are imposed on the topology of the structure to be optimized. TO is a mathematical approach that allows to efficiently distribute a certain material in a given space, subjected to a set of constraints, such that the performance of the structure is maximized [4]. For the past two decades, this method has been applied to a wide variety of fields in academic and industrial disciplines. For a survey on some current developments in this field, please see the review papers by Sigmund and Maute [5] and Deaton and Grandhi [6]. TO has also gained the interest of aeronautics and aerospace engineering communities and an overview of applications of TO in these fields can be found in the review paper by Zhu *et al.* [7].

Conventionally, in the density-based TO approach, the domain is discretized into a finite set of cells, typically corresponding to the finite elements used for analysis. Each cell is assigned a density value that indicates the volume fraction of the cell filled with the given material and can vary from 0 (void) to 1 (solid) [4]. Note that this density is different from the material density which is an intrinsic property of the material used during TO. These densities are considered as design variables for the optimization purposes.

The designs obtained from TO generally comprise of complex geometries as well as intermediate density values which were not easy to fabricate in the past. Recent advancements in the field of additive manufacturing (AM) have helped to overcome these problems and the complex geometries can now be realized using AM [8]. In some cases, the intermediate densities may be replaced by customized meso-structures to obtain black-white designs [9]. However, in this chapter, we focus on applications where fully solid designs are preferred and it is important that these designs are free from intermediate density (gray) values with fine features clearly represented.

Generally, the density is assumed to be constant inside an element. Thus, a relatively large number of finite elements and design variables are needed for problems which require a high resolution representation of the density field. The naive approach to obtain a high resolution density representation would be to globally refine the mesh. However, starting the optimization with very fine meshes is prohibited in terms of computational cost. Also, if the mesh is globally refined during the intermediate cycles, there would be a significant part of the domain where no improvement is achieved in terms of performance. Thus, refinement in such regions is of no use and makes the refinement process computationally inefficient. Therefore, adaptive approaches, which significantly reduce the required computational costs, are gaining interest.

The term ‘adaptivity’ in general means to modify something in a way such that it functions better or is better suited for a purpose. In the context of TO, it refers to modifying certain part of the computational implementation of TO such that the cost associated with achieving certain performance is lowered. An adaptive approach should be capable of avoiding early convergence to a local minima and should be able to decide a right balance between the analysis accuracy and the design resolution. There can be several

different components of TO where adaptivity can be introduced. A few examples are the finite element discretization (e.g. adaptive mesh refinement (AMR)), the material interpolation (e.g. penalization continuation), or the design representation (e.g. adaptive filter radius, Heaviside projection continuation). In the AMR approach, the mesh might be locally refined ( $h$ -refinement) or the polynomial order of the shape functions might be enriched locally ( $p$ -refinement) based on an error indicator function [10]. Penalization continuation involves slowly increasing the penalty power on the densities which helps to initially reduce the nonconvexity of the optimization problem and find a solution close to the optimum [11]. Adapting the filter radius during the course of TO allows to have a fine representation of the boundaries in the design with reduced intermediate densities.

Other than the adaptive approaches stated above, there can be several other ways to reduce the computational resources needed to optimize the topology of a certain structure. For the sake of completeness, we provide a brief overview of these methods. Wang *et al.* [12] presented fast iterative solvers to reduce the computational costs associated with the finite element analysis step. Amir *et al.* [13] proposed an approximate reanalysis procedure for continuum structural problems which uses the analysis results of one step to predict the displacement field over a number of iterations based on some approximations. Some other approaches that exist in literature comprise of decoupling the analysis and density meshes. In the study by de Ruiter and van Keulen [14], topology definition functions were used to define the density field over the domain. Also, wavelets have been used in a similar manner to reduce the number of design variables [15]. Guest and Genut [16] reduced the computational cost of TO by using the Heaviside projection scheme to project every density value over a certain number of finite elements. This helped to reduce the number of design variables required to represent the density field. With the availability of efficient optimizers such as method of moving asymptotes (MMA) [17], the computational costs in TO are mainly controlled by the finite element analysis costs. In some recent work, authors have attempted to decouple the analysis and design meshes in a way that allows to have several design points inside a single finite element [18–22]. This allows to have a higher resolution density representation at lower finite element analysis costs compared to the conventional approach. In the present chapter, we restrict our discussion to mesh adaptivity and penalization continuation based adaptive approaches.

The AMR approaches can bring significant reduction in the overall computational time as compared to a uniformly fine mesh. These help to increase the resolution of both the analysis as well as the design domain. The objective of introducing adaptivity in TO is to improve the resolution of the design as well as reduce the intermediate density areas. Since the conventional AMR criteria are typically based on the error associated with the finite element analysis and do not consider the distribution of material, they may not be the best choices for TO. Maute and Ramm [23] proposed an adaptive technique which involved optimizing the topology of the design, followed by approximating the boundaries using cubic or Bezier splines. Then shape optimization was performed and the mesh was accordingly remeshed. This was looped over a series of cycles and the new mesh generated at the end of each cycle was used for TO in the subsequent cycle. This approach leads to finer mesh in the material regions. van Keulen and Hinton [24] combined topol-

ogy design approach with a finite element (FE) error based refinement strategy. In this approach, the recovery of material is controlled by the stress level in the adjacent elements and the mesh densities are determined by (a) the standard Zienkiewicz-Zhu error estimator and (b) the shortest distance to the boundary separating material and void region. To the best of our knowledge, this is one of the earliest approaches that combines FE error with a density-based indicator to refine the mesh during the course of TO. Costa and Alves [25] presented an alternative refinement criterion which involved refining the region around the solid material phase. Stainko [26] proposed to refine the mesh only around the boundary regions near the solid-void interface. Bruggi and Verani [27] proposed an AMR strategy based on a goal-oriented error approach which properly guides the progression of refinement and coarsening actions. It considered the FE error through a dual-weighted residual technique as well as included a heuristic density-based indicator which used the gradient of the density at the boundaries to choose the elements for refinement.

While most of the methods stated above help to achieve the adaptivity in mesh refinement, the density-based indicators do not provide sufficient control over the choice of the range of density values to be considered for refinement/coarsening. The available density-based indicators tend to require a common definition of which density values should be considered for refinement/coarsening. By a common definition, we mean that at the start of TO, the user needs to specify a single range of density values which need to be considered for refinement/coarsening. The elements whose density values do not fall in this range are unaffected. However, keeping the density ranges same for refinement/coarsening at every refinement step might not be an efficient way. This aspect will be discussed in more detail in Section 5.2.

Other than having an efficient AMR strategy, adapting the penalization power is important to obtain good solutions in TO. A popular approach is to slowly increase the penalization power over the TO iterations [11]. This approach is often referred to in the literature as ‘penalization continuation’. Due to the penalization, the optimization problems become highly non-convex and therefore, it is theoretically possible to end up at an inferior local minima. However, if the penalization is gradually increased, the optimization problem during the initial iterations might still be close to convex which implies that there are good chances that the final solution might lie close to the global optimum. Various studies indicate that the degree of non-convexity of TO problems is related to the amount of penalization [28–30]. Note that at every step where the penalization power is incremented during penalization continuation, the optimization problem is modified and a new optimization problem needs to be solved. In a recent paper by Rojas-Labanda and Stolpe [31], the penalization power has been included as a design variable and is slowly increased during the course of optimization with the help of an additional constraint. This approach is referred to as ‘automatic penalty continuation (APC)’. The advantage of APC approach is that since the penalty factor is not adjusted manually, only one optimization problem needs to be solved.

The contribution of this chapter is twofold: firstly, a novel density-based AMR strategy for TO is proposed which allows convenient control over the range of density values to be considered for refinement/coarsening at every refinement step. Secondly, this method is coupled with the existing penalization continuation approach. Since ad-

vanced FE error based refinement indicators are already available, we do not touch on this aspect in this chapter. Also, since at every refinement step, we solve a new optimization problem, we preferred to use the conventional penalization continuation over the APC method to keep our approach as simple as possible. An AMR strategy cannot reduce the gray region at the boundaries if the filter radius is kept constant in size. Thus, in the proposed AMR strategy, the filter size is adapted as well. Section 5.2 discusses the proposed approach in detail. To demonstrate the applicability of our method, it is used to optimize the topology of a cantilever beam for compliance minimization. The optimization problem is solved for two different instances (i) with penalization continuation and (ii) without penalization continuation and the results are reported in Section 5.3. The gain in terms of computation is also reported.

## 5.2. APPROACH

This section provides the detailed formulation of the proposed adaptivity scheme. First, a novel density-based mesh refinement indicator is presented which allows to efficiently select the finite elements for refinement/coarsening over a sequence of refinement steps. Note that a refinement step might be occasionally referred to as a refinement cycle as well. Next, the formulation for adaptivity in the filter radius is introduced. Finally, the penalization continuation approach is discussed and it is coupled with our refinement indicator. Each of these aspects is discussed in detail in the following sub-sections.

### 5.2.1. MESH REFINEMENT INDICATOR

To discuss the proposed  $h$ -refinement criterion for TO, we would like to recall the term ‘gray value’ which will be eventually used at several instances in the chapter. With regard to the conventional approaches, a gray value would simply mean any intermediate value of density ( $\rho$ ) between the two bounds  $\rho_{min}$  and  $\rho_{max}$ . Generally, these bounds are taken to be 0 and 1. However, in the proposed approach, gray values correspond to the density values lying between  $\check{\rho}$  and  $\hat{\rho}$ , where  $[\check{\rho}, \hat{\rho}]$  is a sub-range within  $[\rho_{min}, \rho_{max}]$ . This can be better understood from Figure 5.1. The blue region in Figure 5.1 corresponds to the gray values as per the proposed approach. This region will be referred as the ‘refinement zone’ and all the density values lying within this range will be chosen for refinement in the subsequent refinement cycle. Clearly, the span of the refinement zone changes at every refinement cycle. During the initial refinement cycles, a significant part of the design is expected to be gray and as shown in Figure 5.1, the refinement range consists a small set of gray values. However, the extent of grayness depends on how much the design has been allowed to converge. For the cases presented here, the designs have been allowed to converge sufficiently. After several refinement cycles, the design will be close to a black-white design and even the slightest gray regions need to be considered for refinement in the next refinement step. This is the reason the refinement range is allowed to be larger for later refinement cycles. A similar explanation holds true for the coarsening zones shown in Figure 5.1. A coarsening zone basically corresponds to a black or a white density region. During the initial refinement cycles, densities close to 0 and 1 might be categorized under white and black, respectively. However, as the refinement cycles increase, coarsening ranges should reduce (Figure 5.1).

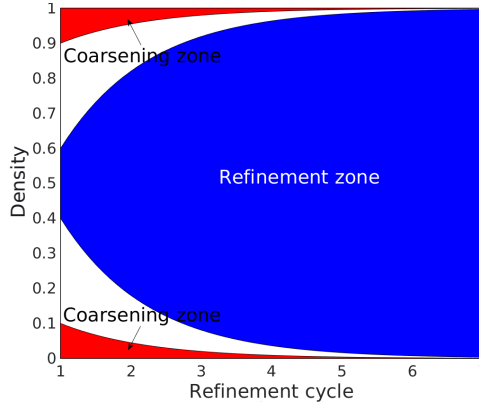


Figure 5.1: Bounds for the mesh refinement indicator as a function of the refinement cycle

5

Consider a density mesh which needs to be adaptively refined/coarsened. Let  $k$  denote the refinement cycle number,  $i$  be the index used to refer the elements of the domain and  $P$  be a refinement indicator. For the  $k$ th refinement cycle, the  $i$ th finite element will be refined or coarsened if the values of the refinement indicator ( $P_i$ ) are 1 and -1, respectively. An element with value of  $P_i$  equal to 0 is neither refined nor coarsened. The value of  $P_i$  can be calculated as follows:

$$P_i = \begin{cases} 1, & \text{if } r_l \leq \rho_i \leq r_u \\ -1, & \text{if } \rho_{min} \leq \rho_i \leq c_l \\ -1, & \text{if } c_u \leq \rho_i \leq \rho_{max} \\ \text{else, } & 0. \end{cases} \quad (5.1)$$

Here,  $r_l$  and  $r_u$  are the lower and upper bounds that characterize the refinement zone. The terms  $c_l$  and  $c_u$  here are used to define the two coarsening zones shown in Figure 5.1. The lower and upper bounds of the refinement and coarsening zone are calculated using the following set of expressions:

$$r_l = \rho_{min} + (1 - \alpha)\rho_{avg}e^{-\beta k}, \quad (5.2)$$

$$r_u = \rho_{max} - (1 - \alpha)\rho_{avg}e^{-\beta k}, \quad (5.3)$$

$$c_l = \rho_{min} + \alpha\rho_{avg}e^{-\beta k}, \quad (5.4)$$

$$c_u = \rho_{max} - \alpha\rho_{avg}e^{-\beta k}. \quad (5.5)$$

Here,  $\alpha$  and  $\beta$  are tuning parameters. The average density ( $\rho_{avg}$ ) is defined using the expression  $\rho_{avg} = (\rho_{max} + \rho_{min})/2$ . For the cases presented here, these values are chosen to be 0.2 and 0.8, respectively. The tuning parameters  $\alpha$  and  $\beta$  are independent of the index of the refinement cycle. However,  $\beta$  is sensitive to the rate at which the design converges. As stated earlier, our method assumes that the design has sufficiently converged. For different problems as well as different FE mesh resolutions, the amount of

gray region may vary at this point. For problems where the designs of initial refinement cycles are significantly gray, lower values of  $\beta$  are recommended. This allows the density range for refinement to expand slowly over a span of refinement cycles. Similarly, for rapidly converging designs, a larger value of  $\beta$  should be helpful.

### 5.2.2. ADAPTIVE FILTER RADIUS

Filters in TO help to prevent the occurrence of checkerboard patterns as well as the fine features in TO. For details on various filters used in TO, see the review paper by Sigmund and Petersson [32]. In simple terms, a filter can be considered as a weighted averaging operator which ensures that the size of a certain feature is not less than a certain limit. A commonly used filter in TO is the density filter [33]. The density filter transforms the original density  $\rho_i$  as follows:

$$\tilde{\rho}_i = \frac{1}{\sum_{j \in N_e} H_{ij}} \sum_{j \in N_e} H_{ij} \rho_j, \quad (5.6)$$

where  $N_e$  is a set of elements  $j$  for which the center-to-center distance  $d(j, i)$  to the  $i$ th element is less than the filter radius  $r_{min}$ . The weight factor  $H_{ij}$  is defined as

$$H_{ij} = \max(0, r_{min} - d(j, i)). \quad (5.7)$$

In the conventional TO approach, the size of  $r_{min}$  is fixed and the value of  $r_{min}$  is decided based on the size of smallest allowable design feature in the domain. For example, a value of  $1.5 r_{min}$  means that the density of an element will be projected over all the neighbouring elements whose centroid to centroid distance with this element is less than or equal to 1.5 times the size of this element. Due to this averaging, the minimum feature size of the design gets restricted.

Here, we define the size of the filter in terms of the physical length. The reason for such an approach can be understood from a simple example. Let us consider two square elements  $e_1$  and  $e_2$  such that the length of any side of  $e_1$  is 2 times that of  $e_2$ . If  $r_1$  and  $r_2$  denote the filter lengths for the two elements, an intuitive guess would be that  $r_1 = 2r_2$ . Using a factor of 2 for such a case would actually be equivalent to using the conventional filtering approach where the filter length is specified in terms of the element length. However, as per our experience, this led to unexpected results. In general, we observed that the size of the filter should be reduced at a slower rate than the size of the element during refinement. The filter length was adapted using the following heuristic method:

$$R_{min}^{(i)} = \gamma^{g(i)} r_{min}. \quad (5.8)$$

Here,  $R_{min}^{(i)}$  is the adapted filter radius for the  $i$ th element and  $g(i)$  denotes the refinement level of the  $i$ th element. ‘Refinement level’ of an element is a number that denotes how many times the original element (level = 0) is refined to reach the current element. The value of the parameter  $\gamma$  should be chosen between above 0.5 and less than 1. As stated earlier, for  $g(i) = 0.5$ , this adaptive filter would be equivalent to the conventional filter. In general, 0.6 proves to be a good choice.

### 5.2.3. PENALIZATION CONTINUATION

In the continuum density based TO, a continuous optimization problem is solved and the value of density is allowed to vary between 0 and 1. This allows us to use the gradient based optimization techniques and solve the problem at affordable costs. However, the intermediate density values are unwanted and one of the best ways to get rid of them is to penalize them [4]. Though this works well, penalization comes with certain drawbacks. Though the original problem might be convex, the new problem after penalization is most likely not convex and new local minima may be introduced [28, 29]. When the penalization is increased, the global minimum might get shifted. However, if the rate of increase is small and the design is allowed to sufficiently converge, the new global minimum may not be far from the actual one. In order to increase the chance of convergence to a well-performing (local) optimum, a gradual increase of the penalization during the optimization process is often effective.

In our approach, penalization continuation is coupled with the refinement steps of the proposed AMR strategy. At every refinement step, parts of the mesh are adapted. At the same time, the penalty factor is incremented and a new optimization problem is solved. For the penalization continuation based results reported here, the starting value of the penalty factor was 1.5 and it was incremented by 0.5 at every refinement step upto a maximum of 3.

5

## 5.3. RESULTS

In this section, we present some results obtained using the proposed adaptivity scheme. For demonstration purposes, a 2D cantilever example is used throughout this chapter (Figure 5.2). Using TO, we solve a problem of compliance minimization. The objective here is to use TO to obtain similar solutions. The basic problem can be expressed in the discrete form as follows:

$$\begin{aligned}
 \min_{\boldsymbol{\rho}} C(\boldsymbol{\rho}, \mathbf{u}) &= \mathbf{f}^\top \mathbf{u} \\
 \text{s.t. : } \mathbf{K}(\boldsymbol{\rho}) \mathbf{u} &= \mathbf{f} \\
 V(\boldsymbol{\rho}) &= \int_{\Omega} \rho dV \leq V_s \\
 \mathbf{0} < \boldsymbol{\rho}_{min} &\leq \boldsymbol{\rho} \leq \mathbf{1}.
 \end{aligned} \tag{5.9}$$

Here, the compliance objective function is denoted by  $C$ . The variables  $\boldsymbol{\rho}$ ,  $\mathbf{f}$ ,  $\mathbf{u}$ ,  $\mathbf{K}$  and  $V_s$  correspond to the density vector, global load vector, displacement vector, global stiffness matrix and prescribed volume fraction of the material, respectively. Also, the term  $\boldsymbol{\rho}_{min}$  is obtained from multiplication of all elements of unit vector  $\mathbf{1}$  by  $\rho_{min}$ . This problem has been chosen because it is a well known benchmark in TO, and because an analytically optimal design has been derived by Rozvany [34]. Figure 5.3 shows the computer-plotted representation of the analytical solution for such problems [34]. The design domain is discretized using a structured grid of Q4 elements and the density distribution within an element is assumed to be uniform. Unless stated otherwise, the filter radius is adapted ( $\gamma = 0.6$ ). For the mesh refinement indicator, the values of  $\alpha$  and  $\beta$  are chosen to be 0.8 and 0.2, respectively.

Figure 5.4 shows the adapted mesh and the design at several refinement levels. For



Figure 5.2: A cantilever example

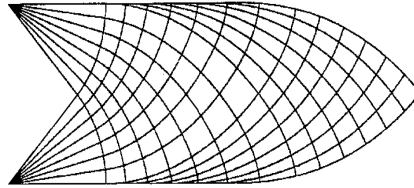


Figure 5.3: Computer-plotted representation of the analytical solution for a cantilever [34].

these results, the penalization is assumed to be constant throughout the TO process. Before going further, we would like to introduce another term ‘Level’ which is basically used as an index to refer to the various analysis meshes and designs obtained during the adaptive refinement approach. The initial mesh is referred as ‘Level 1’ mesh and accordingly the optimized design on this mesh is the ‘Level 1’ design. With every refinement step/cycle, the level increases by 1. Thus, after 4 refinement steps, the ‘Level 5’ mesh is obtained.

The initial mesh (Level 1) is chosen to be very coarse and the design is allowed to converge sufficiently but not fully. For every level, a maximum of 50 iterations are allowed and a coarse tolerance is set on the minimum allowed change in the objective function between two iterations. Using the design of Level 1 and the mesh of Level 2, it can be seen that there are non 0-1 areas in the design for which the mesh has not been refined. With increasing levels, the elements at the boundaries get finer and finer and are thus associated with smaller filter radii. Due to the adapted filter radius, the gray areas get suppressed with increasing refinement levels. Thus, we observe that the proposed adaptive technique is capable of eliminating the gray areas and producing efficient high resolution designs.

The applicability of the proposed technique can be judged from the plots shown in Figure 5.5. Figure 5.5(a) shows the computational time required for TO for different element sizes. It can be observed that for a globally fine mesh, a significantly large computational time is needed and for further refinement it increases rapidly. However, for the proposed adaptive scheme, even a high resolution design can be obtained at relatively low computational costs.

From Figure 5.5(b), it can be observed that with a globally fine mesh, a large number of finite elements are needed to achieve a certain analysis resolution. Analysis resolution can be interpreted as  $1/h_{min}$ , where  $h_{min}$  is the size of the smallest finite element. The proposed adaptive refinement scheme is capable of efficiently representing such high resolutions with less number of degrees of freedom (dofs). Since finite element mod-

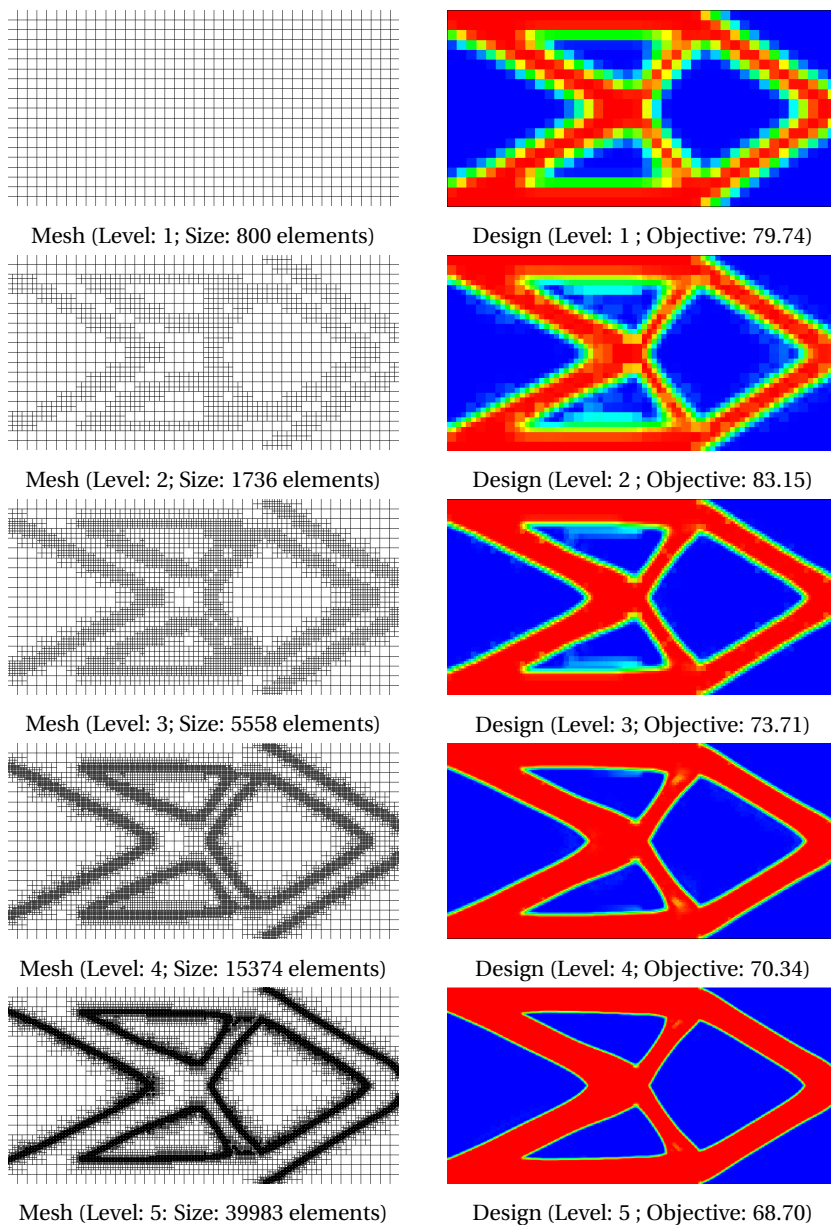


Figure 5.4: Cantilever example considering the adaptive mesh refinement and filter radius.

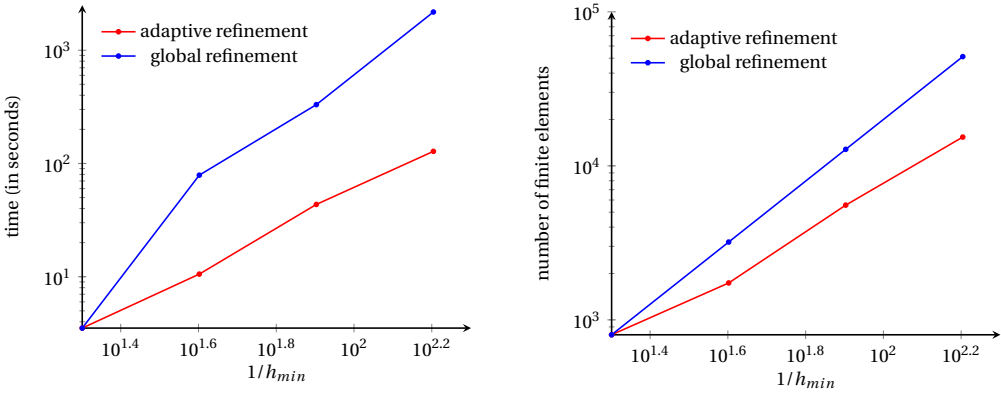


Figure 5.5: (a) Computational time (in seconds) and (b) number of elements needed to achieve a desired design resolution. The design resolution is characterized by the inverse of the minimum element size ( $1/h_{min}$ ).

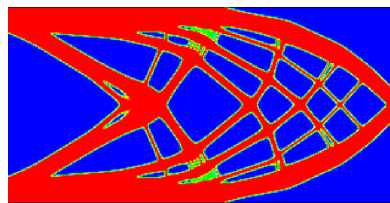
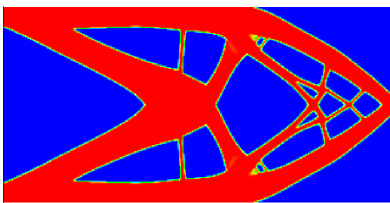


Figure 5.6: Cantilever examples demonstrating the effect of penalization continuation

elling is responsible for the major part of the computational costs associated with TO, reducing the number of elements is beneficial. Based on these, it can be deduced that the proposed refinement scheme is efficient in terms of time as well as memory requirements.

Further, to exclusively study the effect of the penalization, we used the cantilever example to solve the compliance minimization problem for two cases: with a constant penalization (Figure 5.6a) and with a penalization continuation (Figure 5.6b). For both these cases, a fine mesh ( $320 \times 160$ ) is used. Neither the mesh is adaptively refined, nor is the filter radius adapted. For the two cases, we observe that the final designs are very different. Though the design in Figure 5.6b is slightly more gray, it approximates the analytical solutions far better compared to the design obtained with constant penalization [34]. Thus, the penalization continuation helps to obtain better designs. However, to be noted here, the filter radii used for the two cases is small. A larger value would have added gray areas. With smaller radius, we see very fine features which might need to be avoided from a fabrication point of view.

Next, we combine the mesh adaptivity approach with the penalization continuation and demonstrate that it helps to obtain better designs. Figure 5.7 shows the design obtained at every refinement level. During the initial stages, the penalization on the density values is very low. Thus, we see a significant amount of gray region in the design. With increasing penalization, we see that the gray areas disappear. Since the filter radius is larger for the larger elements, we do not see very fine features evolving. The final design for this case is very different from the one obtained in Figure 5.7. This design resembles very closely to the analytical solution for the chosen problem. Thus, we observe that the proposed refinement approach is capable of finding well-performing designs which are close to the optimal solution. In addition, it prevents the occurrence of fine design features and the gray areas in the design. To be noted here, the final designs obtained with and without penalization continuation do not differ too much in terms of performance. This is due to the problem chosen here. For the cantilever problem, there are several designs which can deliver performance close to the optimal value. However, for other problems this might not be the case and the design obtained using penalization continuation should be expected to perform better.

## 5.4. DISCUSSION AND CONCLUSION

In this chapter, we presented an adaptive technique for TO which is capable of obtaining well-performing designs close to the optimum. The proposed heuristic technique comprises of two parts: a density-based mesh refinement strategy and penalization continuation. To comply with our refinement strategy, the filter is adapted as well. The applicability of the proposed approach is demonstrated on a cantilever example and the obtained results look promising. Note that the refinement indicator is only based on density values and does not take the FE error into consideration. Several advanced FE error based indicators already exist in the literature and a future direction of research would be to efficiently couple such indicators with the proposed one. Other than the density values, the gradient of density across the boundaries can also be a useful information for defining the refinement/coarsening regions and this would be another direction to further look into.

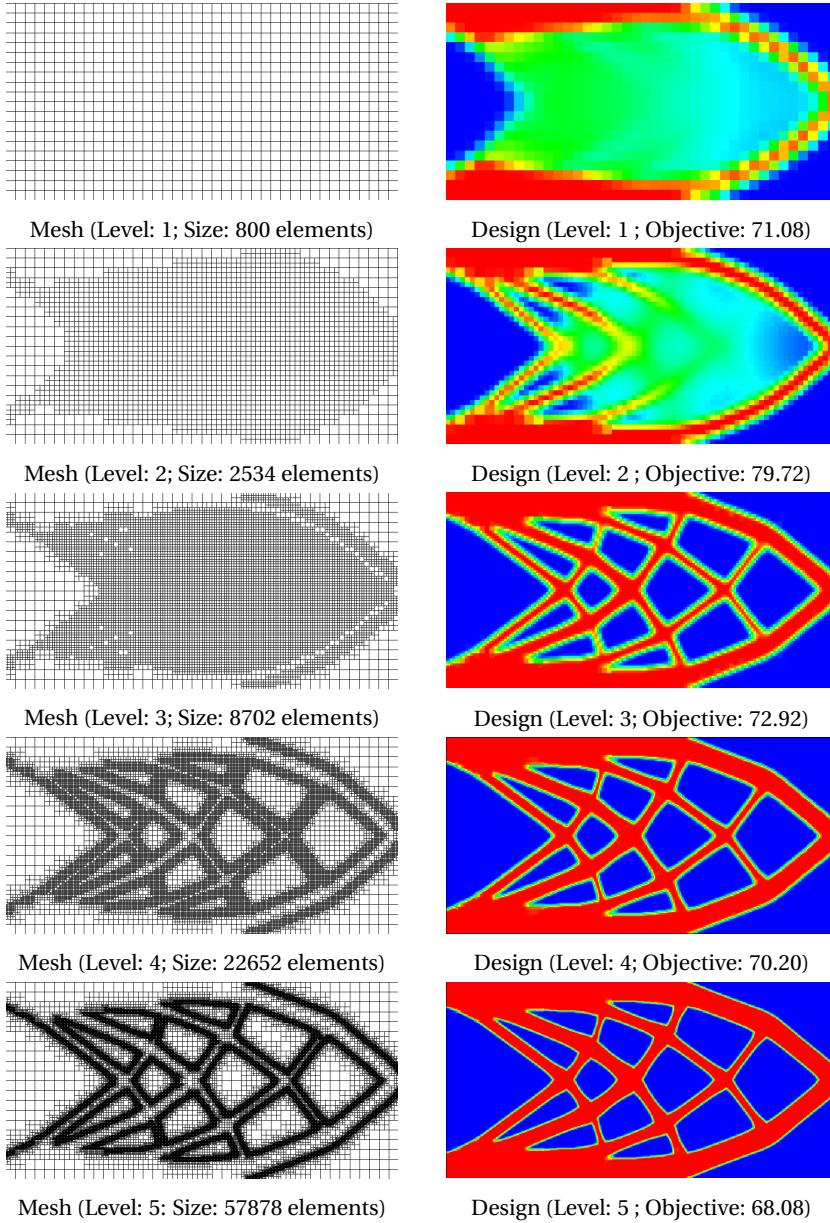


Figure 5.7: Cantilever example considering the proposed adaptive topology optimization scheme. It includes the adaptivity on the mesh and the filter radius and continuation of the penalization.

The proposed refinement indicator is a heuristic indicator with two tuning parameters  $\alpha$  and  $\beta$ . While the value of  $\alpha$  does not affect the approach the value of  $\beta$  needs to be chosen with proper caution. The value of  $\beta$  depends on the convergence speed of the problem as well the extent to which the design has been allowed to converge before every refinement step. A possibility might be that adding more information from the design *e.g.* density gradient might help to get rid of these tuning parameters. For now, based on the current results it can be concluded that the proposed approach is capable of improving the resolution of the designs as well as reduce the gray areas at low computational costs.

## REFERENCES

- [1] D. K. Gupta, M. Langelaar, and F. van Keulen, *Combined mesh and penalization adaptivity based topology optimization*, in *Proc. 57th AIAA/ASCE/AHS/ASC Structures, Structural Dynamics, and Materials Conference*, (AIAA SciTech Forum, (AIAA 2016-0943), 2016).
- [2] L. U. Hansen and P. Horst, *Multilevel optimization in aircraft structural design evaluation*, *Computers and Structures* **86**, 104 (2008).
- [3] S. Chintapalli, M. S. Elsayed, R. Sedaghati, and M. Abdo, *The development of a preliminary structural design optimization method of an aircraft wing-box skin-stringer panels*, *Aerospace Science and Technology* **14**, 188 (2010).
- [4] M. P. Bendsøe, *Optimal shape design as a material distribution problem*, *Structural Optimization* **1**, 193 (1989).
- [5] O. Sigmund and K. Maute, *Topology optimization approaches: a comparative review*, *Structural and Multidisciplinary Optimization* **48**, 1031 (2013).
- [6] J. Deaton and R. Grandhi, *A survey of structural and multidisciplinary continuum topology optimization post 2000*, *Structural and Multidisciplinary Optimization* **49**, 1 (2014).
- [7] J. H. Zhu, W. H. Zhang, and L. Xia, *Topology Optimization in Aircraft and Aerospace Structures Design*, *Archives of Computational Methods in Engineering* (2015).
- [8] D. Brackett, I. Ashcroft, and R. Hague, *Topology optimization for additive manufacturing*, in *Twenty Second Annual International Solid Freeform Fabrication Symposium, Austin, Texas* (2011) pp. 348–362.
- [9] V. G. Sundararajan, *Topology Optimization for Additive Manufacturing of Customized Meso-Structures using Homogenization and Parametric Smoothing Functions*, M.Sc. Thesis (2010).
- [10] I. Babuska, B. A. Szabo, and I. N. Katz, *The p-version of the Finite Element Method*, *SIAM Journal on Numerical Analysis* **18**, 515 (1989).
- [11] G. I. N. Rozvany, *A critical review of established methods of structural topology optimization*, *Structural and Multidisciplinary Optimization* **37**, 217 (2009).

- [12] S. Wang, E. Sturler, and G. H. Paulino, *Large-scale topology optimization using pre-conditioned Krylov subspace methods with recycling*, International Journal for Numerical Methods in Engineering **69**, 2441 (2007).
- [13] O. Amir, M. P. Bendsøe, and O. Sigmund, *Approximate reanalysis in topology optimization*, International Journal for Numerical Methods in Engineering **78**, 1474 (2009).
- [14] M. J. de Ruiter and F. van Keulen, *Topology optimization using a topology description function*, Structural and Multidisciplinary Optimization **26**, 406 (2004).
- [15] T. a. Poulsen, *Topology optimization in wavelet space*, International Journal for Numerical Methods in Engineering **53**, 567 (2002).
- [16] J. K. Guest and L. C. S. Genut, *Reducing dimensionality in topology optimization using adaptive design variable fields*, International Journal for Numerical Methods in Engineering **81**, 1019 (2010).
- [17] K. Svanberg, *The method of moving asymptotes - a new method for structural optimization*, International Journal for Numerical Methods in Engineering **24**, 359 (1987).
- [18] T. H. Nguyen, G. H. Paulino, J. Song, and C. H. Le, *A computational paradigm for multiresolution topology optimization (MTOPT)*, Structural and Multidisciplinary Optimization **41**, 525 (2010).
- [19] T. H. Nguyen, G. H. Paulino, J. Song, and C. H. Le, *Improving multiresolution topology optimization via multiple discretizations*, International Journal for Numerical Methods in Engineering **92**, 507 (2012).
- [20] Y. Wang, J. He, Z. Luo, and Z. Kang, *An adaptive method for high-resolution topology design*, Acta Mechanica Sinica **29**, 840 (2013).
- [21] Y. Wang, J. He, and Z. Kang, *An adaptive refinement approach for topology optimization based on separated density field description*, Computers and Structures **117**, 10 (2013).
- [22] J. Park and A. Sutradhar, *A multi-resolution method for 3D multi-material topology optimization*, Computer Methods in Applied Mechanics and Engineering **285**, 571 (2015).
- [23] K. Maute and E. Ramm, *Adaptive topology optimization*, Structural Optimization **10**, 100 (1995).
- [24] F. van Keulen and E. Hinton, *Topology design of plate and shell structures using the hard kill method*, in *Advances in structural Engineering Optimization*, edited by B. Topping (Civil Comp. Press, Edinburgh, 1996) pp. 177–188, presented at the Third International Conference in Computational Structural Technology in Budapest, 21-23 August, 1996.

- [25] J. C. Arantes Costa and M. K. Alves, *Layout optimization with h-adaptivity of structures*, International Journal for Numerical Methods in Engineering **58**, 83 (2003).
- [26] R. Stainko, *An adaptive multilevel approach to the minimal compliance problem in topology optimization*, Communications in Numerical Methods in Engineering **22**, 109 (2006).
- [27] M. Bruggi and M. Verani, *A fully adaptive topology optimization algorithm with goal-oriented error control*, Computers and Structures **89**, 1481 (2011).
- [28] M. Stolpe and K. Svanberg, *On the trajectories of penalization methods for topology optimization*, Structural and Multidisciplinary Optimization **21**, 128 (2001).
- [29] N. van Dijk, M. Langelaar, and F. van Keulen, *Critical Study of Design Parametrization in Topology Optimization: the influence of design parametrization on local minima*, in *2nd International Conference on Engineering Optimization* (2010) pp. 1–11.
- [30] A. Verbart, N. V. Dijk, L. D. Tin, M. Langelaar, and F. van Keulen, *Effect of design parameterization and relaxation on model responses in topology optimization with stress constraints*, in *9th World Congress on Structural and Multidisciplinary Optimization* (2011) pp. 1–14.
- [31] S. Rojas-Labanda and M. Stolpe, *Automatic penalty continuation in structural topology optimization*, Structural and Multidisciplinary Optimization **52**, 1205 (2015).
- [32] O. Sigmund and J. Petersson, *Numerical instabilities in topology optimization: a survey on procedures dealing with checkerboards, mesh-independencies and local minima*, Structural Optimization **16**, 68 (1998).
- [33] T. E. Bruns and D. A. Tortorelli, *Topology optimization of nonlinear elastic structures and compliant mechanisms*, Comput. Method. Appl. M. **190**, 3443 (2001).
- [34] G. I. N. Rozvany, *Exact analytical solutions for some popular benchmark problems in topology optimization*, Structural Optimization **15**, 42 (1998).

# 6

## BOUNDS FOR DECOUPLED DESIGN AND ANALYSIS DISCRETIZATIONS IN TOPOLOGY OPTIMIZATION

*In the previous chapter, an  $h$ -adaptive variant of the traditional topology optimization method was presented. In this chapter as well as the later chapters, we consider multi-resolution topology optimization (MTO) methods. These formulations involve decoupled design and analysis discretizations, enabling a high-resolution design field at relatively low analysis costs. In the context of MTO, this chapter studies the relation between the number of design variables per element and the polynomial order of the shape functions used in the finite element analysis. We derive that beyond a maximum number of design variables, certain sets of material distributions cannot be discriminated based on the corresponding analysis results. This makes the design description inefficient and the solution of the optimization problem non-unique. To prevent this, we establish bounds for the maximum number of design variables that can be used to describe the material distribution without introducing non-uniqueness for a given finite element scheme.*

---

This chapter is based on an article published in International Journal for Numerical Methods in Engineering, **111**, 1, 88-100 (2017) [1].

## 6.1. INTRODUCTION

Topology optimization (TO) is a numerical procedure that allows obtaining the optimal distribution of a given material within a domain, subject to certain constraints, such that the performance of the resulting structure is maximized. Since its introduction three decades ago [2], this approach has been used to solve a wide variety of problems in various academic and industrial fields. For the recent advancements in TO, please see [3–5]. The so-called density-based formulation is the most popular both in academia and in commercial applications. Conventionally, a single density design variable is associated with each finite element, typically of low order, in the analysis mesh.

Computational costs limit the application of TO in complex, high-resolution 3D problems. The largest part of these costs is associated with finite element analysis (FEA) and the associated sensitivity analysis. By increasing the resolution of the design field relative to the analysis mesh, attempts have been made to reduce this cost [6–10]. In these studies, the design field is characterized by the distribution of design variables in the domain. Based on these design variables, the material density distribution is obtained for the whole domain using some interpolation scheme. While the design variables are used for the optimization, the interpolated density values are used for analysis purposes. For example, consider the ‘Q4/n4/d9’ element shown in Figure 6.1, that corresponds to a 4-node quadrilateral element containing 9 design points within the element. A design variable is associated to each design point. The values of these design variables are used to obtain the density values at 4 integration points where the stiffness matrix contributions are evaluated. Another example, a ‘T3/n6/d3’ element (Figure 6.1), refers to a 3-node triangle with 3 design points and 9 integration points. These elements are based on the conventions denoted in [6, 7] where similar examples such as Q4/n25/d25 and Q4/n25/d9 are presented.

Increasing the number of design points within an element surely increases the resolution of the material distribution without introducing additional DOFs in the analysis. However, since analysis is an integral part of the TO process, one should make sure that the difference between the different high resolution designs obtained using such schemes can be observed in the FEA results. In other words, the question is whether the additional design freedom can be properly exploited in a particular FEA setting. If not, different designs may show similar performance, resulting in non-unique optima and unexpected convergence behaviour. Numerical results related to a similar aspect have been reported in [11], where it is shown that varying the density resolution beyond a certain threshold can lead to unacceptable solutions. Moreover, introducing more design freedom than can be observed from the model only adds to the computational burden.

Note that for the examples mentioned above, design variables are characterized as points in the element domain. However, these may not necessarily be spatial points within an element, *e.g.*, for a material density field expressed using polynomials, design variables can refer to the coefficients of such polynomials (as in Section 6.2). The study in this chapter is not tailored towards a certain choice of design variables. Rather, the focus is on the number of design variables used for optimization.

In this chapter, we study the relation between the number of design variables and the resolution of the analysis mesh used in TO. In this chapter, linear elastostatic problems are considered and the following aspects are covered:

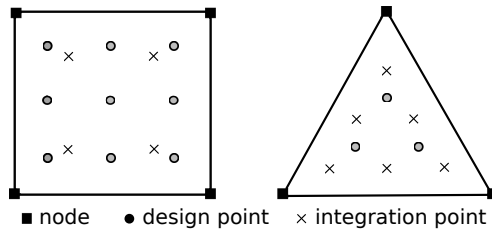


Figure 6.1: Q4 element (left) with 9 design points and 4 integration points ( $Q4/n4/d9$ ) and a T3 element (right) with 3 design points and 6 integration points ( $T3/n6/d3$ ).

- We first illustrate using a basic example that the number of useful design variables is bounded by a certain maximum value (Section 6.2).
- We show mathematically that the permissible number of design variables inside a finite element is bounded by the rank of the element matrix obtained from the discretization of the design domain (Section 6.3). The argument is further extended to the system level as well.
- We present a discussion on the choice of the number of design variables for some popular finite elements (Section 6.4). A brief discussion is provided in Section 6.5 on the issues related to examples that violate the conditions proposed in the present chapter.

## 6.2. A BASIC EXAMPLE

Consider a structural optimization problem involving a simple rod of length  $l$  and area of cross-section  $A$ . This rod is fixed at one end and loaded in axial tension by a force  $F$  acting at the other end. It is assumed that the Young's modulus  $E$  can be varied at any position along the rod. In line with classical density-based topology optimization, we define  $E(x) = E_0 \rho(x)$ , where  $E_0$  is a constant and  $\rho(x)$  represents the material density distribution in the domain. Suppose the bar is modeled using a single finite element and linear shape functions are used to interpolate the displacement field within the element. When using analytical integration, the stiffness matrix  $\mathbf{K}$  can be expressed as

$$\mathbf{K} = \frac{A}{l^2} \begin{bmatrix} 1 & -1 \\ -1 & 1 \end{bmatrix} \int_0^l E(x) dx = \frac{E_0 A}{l^2} \begin{bmatrix} 1 & -1 \\ -1 & 1 \end{bmatrix} \underbrace{\int_0^l \rho(x) dx}_{\rho_{avg}}. \quad (6.1)$$

In Eq. 6.1,  $\mathbf{K}$  depends on the material density distribution only in an average sense. For all choices of  $\rho(x)$  that yield the same average density  $\rho_{avg}$ , the same stiffness matrix is obtained. As a result, the response of the structure for all those choices will be identical. In other words, the modeling of the physics shows independence to certain specific changes in  $\rho(x)$ . Next, we may choose a certain discretization to define  $\rho(x)$  in terms of a finite number of design variables. For the simplest representation by a constant function  $\rho(x) = \hat{\rho}$ , a unique relation between  $\mathbf{K}$  and  $\hat{\rho}$  exists. However, for all higher-order representations, infinite combinations of design variable values exist that result in the same

average density  $\rho_{avg}$ . This leads to loss of uniqueness of the optimal solution. A similar situation can arise in more complex, multidimensional topology optimization problems.

For a better understanding of the issue stated above, we analyze the system of linear equations obtained from the finite element discretization. Using Gaussian quadrature points  $x_i$  for integrating  $\mathbf{K}$  in an isoparametric setting, the discretized system of equations for the bar can be expressed as

$$\mathbf{K}\mathbf{u} = \mathbf{f} \implies \frac{E_0 A}{l} \begin{bmatrix} 1 & -1 \\ -1 & 1 \end{bmatrix} \sum_{i=1}^g w_i \rho(x_i) \begin{bmatrix} u_1 \\ u_2 \end{bmatrix} = \begin{bmatrix} f_1 \\ f_2 \end{bmatrix}. \quad (6.2)$$

Here,  $\mathbf{u}$  and  $\mathbf{f}$  correspond to nodal degrees of freedom (DOFs) and nodal loads, respectively. Suppose that  $\mathbf{u}$  corresponding to a certain optimal design is known, then we would like to establish whether that design is unique.

Let us assume that we integrate the  $\mathbf{K}$  matrix using a 2-point Gaussian quadrature scheme. With the given boundary conditions ( $u_1 = 0$ ), the applied force ( $f_2 = F$ ) and the Gaussian weights ( $w_1 = w_2 = 0.5$ ), there exists only one linearly independent equation:

$$\frac{E_0 A}{2l} [\rho(x_1) + \rho(x_2)] u_2 = F, \quad (6.3)$$

where the two integration points  $x_1$  and  $x_2$  are  $\left(1 \pm \frac{1}{\sqrt{3}}\right) \frac{l}{2}$ . Now, assuming that  $F$  and  $u_2$  are known,  $\rho(x)$  is described by polynomials of different order (zeroth order, first order, etc.), where the coefficients of the polynomial terms are the design variables.

*CASE I:*  $\rho(x) = a$ , i.e., a constant density field. From Eq. 6.3, we obtain

$$\frac{E_0 A}{2l} (a + a) u_2 = F \implies a = \frac{Fl}{E_0 A u_2}. \quad (6.4)$$

*CASE II:*  $\rho(x) = ax + b$ , i.e., a linearly varying density field. For this case, Eq. 6.3 can be written as

$$\frac{E_0 A}{2l} [(ax_1 + b) + (ax_2 + b)] u_2 = F \implies (x_1 + x_2)a + 2b = \frac{2Fl}{E_0 A u_2}. \quad (6.5)$$

The order of the shape functions for both cases leads to a single equation, implying that not more than one design variable can be uniquely determined if  $u_2$  and  $F$  are known. From the example presented above, we see that for *CASE I*, only 1 design variable is used and the solution is unique. However, for *CASE II*, it can be observed from Eq. 6.5 that there can be infinitely many combinations of  $a$  and  $b$  which can produce the same displacement at the end of the bar. Thus, for *CASE II*, the assumed  $\rho(x)$  function cannot be solved uniquely. This still holds when restrictions are imposed on the design ( $0 < \rho(x) \leq 1$ ). Similarly, it can be shown that for an even higher order representation of  $\rho(x)$ , the solution will always be non-unique. The reason is that the finite element discretization is unable to reflect the design changes.

This simple example illustrates that there is an upper bound on the number of design variables that can be used for a given body discretized using finite elements above which the design is no longer unique. More design variables can be included, however, then the effect of certain changes in the design cannot be distinguished. Here, a single

finite element with linear shape functions was used and the strain-displacement matrix was constant. In the following section, we generalize this concept of choosing the appropriate number of design variables to the case of shape functions of arbitrary order and systems of many elements. This will allow us to determine suitable combinations of design and analysis resolutions for use in topology optimization procedures.

### 6.3. CONDITION FOR UNIQUENESS OF DENSITY DISTRIBUTION

Optimization of a structural design in general can refer to finding the optimal distribution of material in a given domain as well as optimizing the material properties themselves at every point  $\mathbf{x}$  in the domain. Assuming that the system is governed by generalized Hooke's law,  $\boldsymbol{\sigma} = \mathbf{D}\boldsymbol{\epsilon}$ . Here,  $\mathbf{D}$ ,  $\boldsymbol{\sigma}$  and  $\boldsymbol{\epsilon}$  denote the constitutive matrix and stress and strain column vectors, respectively. The dependence of all these parameters on the position  $\mathbf{x}$  is implied.

For a design representation in two (three) dimensions, the most general choices of design variables are six (twenty one) entries of the  $\mathbf{D}$  matrix and their pointwise variation throughout the domain. However, our discretized system allows only the representation of a limited number of deformation modes, the combinations of which can represent all possible deformation states of the system. When choosing the number of design variables, a unique design representation should be obtained from these deformation modes. Depending on the type of optimization problem, a certain choice of design variables is made. For instance, in free material optimization of structures for stiffness maximization, the problem is reduced to solving only one design variable per point, namely the norm or the trace of the elasticity tensor [12]. It is shown analytically in [13] that the elements of the elasticity tensor can then be fully recovered from the optimal norm and the related displacements.

Traditionally, in TO one design variable per point is also assumed. However, the approach is different from the free material optimization discussed above. In TO, certain restrictions are typically imposed on the material properties throughout the domain and  $\mathbf{D}$  is expressed as  $\mathbf{D} = \rho(\mathbf{x})\mathbf{D}_0$ , where  $\mathbf{D}_0$  is assumed to be constant for the whole material domain and  $\rho$  denotes the material density. Thus, at any point in the domain only the material volume fraction (material density) is allowed to vary. The focus of this chapter is on TO and thus we tailor the foregoing discussion accordingly. Our objective is to mathematically relate the number of design variables to the number and type of elements used in the analysis. Further, the aim is to establish a threshold condition on the appropriate number of design variables that can be associated with any finite element as well as a system of elements in TO.

Assuming that the design variables represent the coefficients of a polynomial function, the density field inside an element can be defined as

$$\rho(\mathbf{x}) = s_1 + s_2x + s_3y + \dots m \text{ terms} = \bar{\mathbf{x}}^T \mathbf{s}, \quad (6.6)$$

where,  $\mathbf{s} = [s_1, s_2, \dots, s_m]^T$  represents the set of design variables and  $m$  the number of design variables used in the optimization problem. To determine the upper bound on  $m$ , here a linear elastostatic problem is considered. For any finite element, equilibrium can then be expressed as

$$\mathbf{K}^{(e)} \mathbf{u}^{(e)} = \mathbf{f}^{(e)}, \quad (6.7)$$

where,

$$\mathbf{K}^{(e)} = \int_{\Omega_e} \mathbf{B}^\top \rho(\mathbf{x}) \mathbf{D}_0 \mathbf{B} d\Omega = \left( \int_{\Omega_e} \mathbf{B}^\top \mathbf{D}_0 \mathbf{B} \bar{\mathbf{x}}^\top d\Omega \right) \mathbf{s}. \quad (6.8)$$

Here,  $\mathbf{u}^{(e)}$  and  $\mathbf{f}^{(e)}$  represent the kinematic nodal degrees of freedom and corresponding energetically conjugate nodal loads, respectively. The polynomial order of  $\mathbf{K}^{(e)}$  depends on the choice of the density field. For a certain choice of  $\rho(\mathbf{x})$  in Eq. 6.6, the polynomial order of the corresponding  $\mathbf{K}^{(e)}$  can be determined from Eq. 6.8. Accordingly, an appropriate number of integration points can be chosen based on standard Gaussian quadrature.

Assume that  $\mathbf{K}^{(e)}$  is now numerically integrated using  $g$  integration points, then  $\mathbf{K}^{(e)} = \sum_{i=1}^g \rho(\mathbf{x}_i) \mathbf{K}_i = \sum_{i=1}^g \rho(\mathbf{x}_i) \mathbf{B}_i^\top \mathbf{D}_0 \mathbf{B}_i w_i$ . It can further be expressed as

$$\mathbf{K}^{(e)} = \underbrace{\begin{bmatrix} \mathbf{B}_1^\top & \mathbf{B}_2^\top & \dots & \mathbf{B}_g^\top \\ (n \times cg) \end{bmatrix}}_{\Theta_1} \underbrace{\begin{bmatrix} \rho(\mathbf{x}_1) w_1 \mathbf{D}_0 & & & \\ & \rho(\mathbf{x}_2) w_2 \mathbf{D}_0 & & \\ & & \ddots & \\ & & & \rho(\mathbf{x}_g) w_g \mathbf{D}_0 \end{bmatrix}}_{(cg \times cg)} \underbrace{\begin{bmatrix} \mathbf{B}_1 \\ \mathbf{B}_2 \\ \vdots \\ \mathbf{B}_g \end{bmatrix}}_{(cg \times n)}. \quad (6.9)$$

Here,  $n$  represents the number of DOFs per element and  $\mathbf{K}^{(e)}$  is thus an  $n \times n$  matrix. Due to the presence of rigid body modes,  $\mathbf{K}^{(e)}$  is not a full-rank matrix. Let the rank of  $\mathbf{K}^{(e)}$  be denoted by  $r$ . For a linear-elastic material, the stress components can be expressed as linear combinations of the strain components through the constitutive matrix. Since this constitutive relation is invertible and the strain energy density should be positive,  $\mathbf{D}_0$  in Eq. 6.9 is a full-rank and positive-definite matrix. The dimensions of  $\mathbf{D}_0$  are assumed to be  $c \times c$ , where  $c$  is the number of independent stress components in the stress tensor. Since the rank of  $\mathbf{D}_0$  is  $c$ ,  $\Theta_1$  in Eq. 6.9 is a positive-definite block-diagonal matrix with rank  $cg$ . Given that the rank of  $\mathbf{K}^{(e)}$  is  $r$ , we obtain (proof in Appendix A)

$$\text{rank}([\mathbf{B}_1^\top \ \mathbf{B}_2^\top \ \dots \ \mathbf{B}_g^\top]) = \text{rank}(\mathbf{K}^{(e)}) = r. \quad (6.10)$$

Based on numerical integration and rearrangement of terms, the system of linear equations in Eq. 6.7 can be expressed in terms of  $\mathbf{s}$  as

$$\underbrace{\left[ \left( \sum_{i=1}^g \mathbf{K}_i \right) \mathbf{u}^{(e)} \quad \left( \sum_{i=1}^g x_i \mathbf{K}_i \right) \mathbf{u}^{(e)} \quad \left( \sum_{i=1}^g y_i \mathbf{K}_i \right) \mathbf{u}^{(e)} \quad \dots \quad m^{\text{th}} \text{ term} \right]}_{\mathbf{A}^{(e)}} \mathbf{s} = \mathbf{f}^{(e)}. \quad (6.11)$$

For a choice of  $\mathbf{u}^{(e)}$  and  $\mathbf{f}^{(e)}$  such that  $\mathbf{u}^{(e)}$  does not correspond to a rigid body mode, our goal is to determine the maximum possible value of  $m$  such that  $\mathbf{s}$  has a unique solution. From Eq. 6.11, it can be observed that  $m$  cannot be greater than the rank of  $\mathbf{A}^{(e)}$ , which we will determine next:

$$\mathbf{A}^{(e)} = \mathbf{PQ}, \quad (6.12)$$

where,

$$\mathbf{P} = \underbrace{\begin{bmatrix} \mathbf{B}_1^\top & \mathbf{B}_2^\top & \dots & \mathbf{B}_g^\top \\ (n \times cg) \end{bmatrix}}_{\Theta_2} \begin{bmatrix} w_1 \mathbf{D}_0 \mathbf{B}_1 \mathbf{u}^{(e)} & & & \\ & w_2 \mathbf{D}_0 \mathbf{B}_2 \mathbf{u}^{(e)} & & \\ & & \ddots & \\ & & & w_g \mathbf{D}_0 \mathbf{B}_g \mathbf{u}^{(e)} \end{bmatrix}, \quad (6.13)$$

$(cg \times g)$

$$\mathbf{Q} = \begin{bmatrix} 1 & x_1 & \dots & (m^{\text{th}})_1 \\ 1 & x_2 & \ddots & \vdots \\ \vdots & \vdots & & \vdots \\ 1 & x_g & \dots & (m^{\text{th}})_g \end{bmatrix}. \quad (6.14)$$

To determine the rank of  $\mathbf{A}^{(e)}$ , the ranks of  $\mathbf{P}$  and  $\mathbf{Q}$  should be known.

Since  $\Theta_2$  is a block-diagonal matrix,  $\text{rank}(\Theta_2) = g$ . Using the fact that the rank of the product of two matrices cannot exceed the rank of the either factor (proof in [14]), the upper bound on the rank of  $\mathbf{P}$  is given by the minimum of the number of deformation modes  $r$  and the number of integration points  $g$ , *i.e.*,

$$\text{rank}(\mathbf{P}) \leq \min(r, g). \quad (6.15)$$

To gain further insight into the rank of  $\mathbf{P}$ , it can be written as

$$\mathbf{P} = [\mathbf{K}_1 \mathbf{u}^{(e)} \quad \mathbf{K}_2 \mathbf{u}^{(e)} \quad \dots \quad \mathbf{K}_g \mathbf{u}^{(e)}] \quad (6.16)$$

For  $g \geq r$ , we now look into the different possibilities where  $\text{rank}(\mathbf{P}) < r$ . Such instances need to be identified because for any such scenario, the maximum number of design variables that can be used without encountering non-uniqueness would be less than  $r$ .

*CASE I:* One of the possibilities is if  $\mathbf{u}^{(e)}$  is such that no deformation is observed at one of the integration points, *i.e.*, the respective product  $\mathbf{B}_i \mathbf{u}^{(e)}$  is zero. Then, the respective column of the  $\mathbf{P}$  matrix will become zero, decreasing its rank by 1. This scenario can even occur for more than one integration point at the same time. Suppose for certain  $\mathbf{u}^{(e)}$ , two columns of  $\mathbf{P}$  matrix are equal to zero. This would imply that  $\text{rank}(\mathbf{P})$  has to be strictly less than or equal to  $g - 2$ . This can lead to a situation where  $\text{rank}(\mathbf{P})$  becomes less than  $r$ . Such a scenario is restricted to certain choices of  $\mathbf{u}^{(e)}$  and this problem is alleviated if an appropriate integration scheme is used. The number of integration points needed to accurately integrate  $\mathbf{K}^{(e)}$  is generally higher compared to the number of design variables that can be used in a finite element. Thus, even if no deformation is observed at one of the integration points, it can still be observed on at least  $r$  other integration points ensuring that  $\text{rank}(\mathbf{P}) = r$ .

*CASE II:* Another possibility where  $\text{rank}(\mathbf{P}) < r$  is when one or more columns of  $\mathbf{P}$  can be expressed as linear combinations of other columns and the total number of linearly

independent columns becomes less than  $r$ . This would mean that there exist an  $\alpha \neq \mathbf{0}$  such that

$$\sum_{i=1}^g \alpha_i \mathbf{K}_i \mathbf{u}^{(e)} = \mathbf{0}. \quad (6.17)$$

Here, the  $\mathbf{K}_i$  matrices differ only by their respective  $\mathbf{B}$  matrices. In general, every element of  $\mathbf{B}$  is a polynomial function expressed in terms of the spatial coordinates, thereby it depends on the location of the point within the element at which  $\mathbf{K}_i$  is evaluated. Thus, in general, no  $\mathbf{K}_i$  matrix can be expressed as a linear combination of other such matrices which are evaluated at other sampling points in the element domain. This implies that Eq. 6.17 can only be satisfied if  $\mathbf{u}^{(e)}$  belongs to the nullspace of  $\sum_{i=1}^g \alpha_i \mathbf{K}_i$ . This can happen only for some specific cases, *e.g.*, when it is a rigid body mode. However, for the vast majority of cases, it follows that the columns of  $\mathbf{P}$  are linearly independent.

A case where linear dependence occurs for any deformation is encountered when linear functions are used to interpolate the state field within the element. Then the  $\mathbf{B}$  matrix is constant and does not depend on the spatial variables. Due to this, all columns of  $\mathbf{P}$  are equal, reducing its rank to 1. Some examples where this happens are 3-node triangles (T3) and 4-node tetrahedra (TET4). Thus, for the T3 and TET4 elements, not more than 1 unique design variable can be used per element. However, for cases where  $\mathbf{D}_0$  varies throughout the element (*e.g.*, material which is functionally graded in Poisson ratio), the respective  $\mathbf{K}_i$  matrices would differ. This will increase the number of linearly independent columns in  $\mathbf{P}$ .

In a generalized sense then,  $\text{rank}(\mathbf{P}) = \min(r, g)$ . Based on Eqs. 6.12 and the fact that  $\text{rank}(\mathbf{A}^{(e)}) \leq \min(\text{rank}(P), \text{rank}(Q))$ , we obtain that  $m \not\asymp r$ . Thus,  $m$  in Eq. 6.14 is substituted by  $r$ . Next, the structure of the  $\mathbf{Q}$  matrix is studied and based on the discussion provided in Appendix B,

$$\text{rank}(\mathbf{A}^{(e)}) = r \quad \forall \quad g \geq r. \quad (6.18)$$

In general, if  $r$  design variables are used, then the number of integration points required in a Gaussian quadrature scheme to accurately integrate  $\mathbf{K}^{(e)}$  is greater than or equal to  $r$ . The condition  $g \geq r$  does not need to be explicitly imposed and can be ignored. This implies that for a finite element with  $r$  deformation modes, a maximum of  $r$  design variables should be used to represent the density field inside the element and going beyond this limit will lead to non-uniqueness.

Note that unlike the nodal state variables which are defined at the nodal points, design variables here characterize the density distribution within the element and do not possess any direct relationship with the immediate neighboring elements. Thus, even for a group of elements, the number of design variables allowed inside every element of the system cannot be greater than the rank of that element's coefficient matrix. Based on this, the following element-level upper bound can be stated:

*“For any finite element, the number of design variables used to define the element's internal material distribution that can be uniquely optimized by means of finite element analysis, cannot be greater than the rank of the element coefficient matrix.”*

The condition derived here needs to be satisfied for every element. In addition to this, a similar is proposed at the system level as well. A system of elements can itself be con-

sidered as a superelement with a larger number of DOFs. For such an element, a system level condition can be derived using a similar approach. At the system level, the following rule can be formulated:

*“For any structure discretized using finite elements, the total number of design variables used to define the material distribution in the whole domain that can be optimized to a unique solution based on the results of finite element analysis, cannot be greater than the rank of the global coefficient matrix obtained from the discretization of the structure.”*

Important to note here is that the DOFs at the vertices as well as on the faces (edges for 2D) of the element are shared with those of the adjacent elements. Due to this, the system level bound on average will be stricter compared to the element level bound. This aspect is further discussed in the next section using a simple example.

#### 6.4. CHOICE OF THE NUMBER OF DESIGN VARIABLES

The allowed number of design points is element-dependent (Section 6.3). Table 6.1 shows the upper bound on the number of design points for various finite elements. In general, the upper bound  $m$  can be stated as

$$m = d_{el} - r_{el}, \quad (6.19)$$

where  $d_{el}$  and  $r_{el}$  are the total DOFs and the number of rigid body modes for the element, respectively. For example, for a Q4 element in 2D with 2 DOFs per node,  $m = 2 \cdot 4 - 3 = 5$ . However, as pointed out in Table 6.1, for elements such as T3 and TET4, only one design variable should be used per element (as in Section 6.3). This is because these elements use linear shape functions which result into constant strain-displacement matrices for isotropic materials.

Other than the element-level bound, the number of design density points should be lower than the bound at system level as well. For example, let us assume a rectangular grid of  $N \times N$  Q4 elements. In an average sense, the number of density points per element ( $\tilde{m}$ ) for this system needs to satisfy the following criterion:

$$\tilde{m} \leq \frac{(N+1)^2 d - r_{sys}}{N^2}, \quad (6.20)$$

where  $d$  is the DOFs per node and  $r_{sys}$  is the number of zero energy modes for the system. For example, for a rectangular mesh of  $3 \times 3$  Q4 elements with 2 DOFs per node,  $\tilde{m}$  is approximately equal to 3, which means  $\tilde{m}$  is less than  $m$ . For large values of  $N$ , however, the maximum value of  $\tilde{m}$  is approximately equal to  $d$ . Thus, in an average sense, there should not be more design points per element than the DOFs per node. We observe that the system level bound here imposes a stricter limit over the possible design resolution than the element level criterion. Note that Eq. 6.20 is valid only for 2D rectangular meshes with certain choice of elements. For other mesh geometries and element types, this bound needs to be reformulated accordingly. Besides the number of DOFs, the choice of the number of design variables also depends on the number of integration points. In other words, while choosing a high order material distribution, one

Table 6.1: Maximum number of design points for some commonly used finite elements.

Element	DOFs per node	No. of design points
3-node triangle (T3)	2	1
6-node triangle (T6)	2	9
4-node quadrilateral (Q4)	2	5
8-node quadrilateral (Q8)	2	13
9-node quadrilateral (Q9)	2	15
4-node tetrahedron (TET4)	3	1
10-node tetrahedron (TET10)	3	24
8-node hexahedron (H8)	3	18
20-node hexahedron (H20)	3	54

should make sure that the stiffness matrix  $\mathbf{K}^{(e)}$  can be accurately integrated. For example, for a Q4 element, conventionally, a  $2 \times 2$  Gauss quadrature rule is used to integrate  $\mathbf{K}^{(e)}$ . This scheme can integrate exactly up to a cubic polynomial in two variables. For an elementwise constant material density, the polynomial order of the integrand in Eq. 6.8 is 2. Thus, the  $2 \times 2$  scheme is sufficient to exactly integrate it. From Table 6.1, it can be seen that for a Q4 element, up to 5 design variables can be used. With 5 design variables, a second order polynomial-based material distribution can be represented in two dimensions. With such a distribution, the order of the integrand in Eq. 6.8 will be 4 and for such a case, a minimum of  $3 \times 3$  quadrature points is needed. Similarly, it can be shown for a Q9 element, at least a  $4 \times 4$  integration scheme is needed. A similar approach can be followed to determine the appropriate integration schemes for other elements as well. When the number of integration points  $g$  is chosen too low, not only is the solution likely to be inaccurate, but also the number of unique design variables can be affected (as determined by Eq. 6.15).

6

## 6.5. DISCUSSION AND CONCLUSION

The main drive behind using a large number of density points is to obtain a better representation of the material distribution while keeping the computational cost as low as possible. Let us take the case of the Q4/n25/d25 element [6]. Any deformed state obtained using 25 design variables for this element can also be obtained using just 5 design variables. Similarly, for a T6 element, 9 design variables are sufficient to describe all deformation states (Table 6.1). An interesting inference is that for elements with constant strain-displacement matrix (e.g. T3, TET4), elementwise constant density needs to be assumed. For more design variables, a high-dimensional nullspace is introduced which may hinder the convergence of topology optimization. Also, the desire to add more design density points will lead to building the stiffness matrix contributions at significantly more number of points (Table 6.1), which will eventually lead to an unnecessary increase in the computational costs. Significant burden on sensitivity analysis will also be noticed for such cases.

The discussions throughout the chapter have been tailored towards structural topology optimization problems. However, the condition stated in Section 6.3 holds for other

topology optimization problems as well, *e.g.*, thermal, electrical, thermomechanical, *etc.* The argument in Section 6.3 is based on the fact that the design domain is discretized using finite elements. Thus, it would still be valid except that the size of the element as well as the system coefficient matrices may differ based on the number of DOFs per node for the chosen problem. In addition, for problems involving other physics than structural mechanics, deformation modes and rigid body modes may not be the suited terms. For such problems, the proposed condition can be interpreted in terms of the ranks of the element and system coefficient matrices.

In some recent studies [6–9], high resolution designs are obtained for cases where the design resolution is allowed to be very high compared to the analysis resolution. The reason for the apparent quality of these designs can be attributed to the use of smoothing operations such as projection filters [6, 7], Shephard interpolation schemes [8, 9], *etc.* Though smoothing can suppress the non-uniqueness to some extent, the possibility of non-uniqueness still exists. While the proposed condition needs to be satisfied at element level as well as system level, a possibility exists to increase the density resolution inside the element. One could choose to use higher order shape functions which introduce extra DOFs providing more flexibility for the state field representation [15, 16]. However, this only shifts the upper bound on the order of density representation and going beyond this new threshold will bring back the issues of non-uniqueness.

To conclude, the number of design variables for a TO problem depends on the applied finite element and should not be chosen arbitrarily. Rather, a choice of the number of design points should be made in a way such that it satisfies the proposed element level as well as the system level conditions. As shown in this chapter, going beyond the proposed threshold is neither computationally more efficient, nor does it contribute to any improvement in the performance of the structure.

## 6.A. APPENDIX A

*Theorem:* Given that  $\mathbf{B}$  is a  $p \times q$  matrix and  $\mathbf{D}$  is a  $p \times p$  positive definite matrix of full rank  $p$ ,

$$\text{rank}(\mathbf{B}^T \mathbf{D} \mathbf{B}) = \text{rank}(\mathbf{B}).$$

*Proof:* Based on the rank-nullity theorem, following can be stated:

$$\text{rank}(\mathbf{B}) + \text{nullity}(\mathbf{B}) = q = \text{rank}(\mathbf{B}^T \mathbf{D} \mathbf{B}) + \text{nullity}(\mathbf{B}^T \mathbf{D} \mathbf{B}). \quad (6.21)$$

Let  $\mathbf{x}$  denote any vector in the nullspace of  $\mathbf{B}$ . Then,

$$\mathbf{B}\mathbf{x} = \mathbf{0} \implies \mathbf{B}^T \mathbf{D} \mathbf{B} \mathbf{x} = \mathbf{0} \implies \mathbf{x} \in \text{nul}(\mathbf{B}^T \mathbf{D} \mathbf{B}) \implies \text{nul}(\mathbf{B}) \subseteq \text{nul}(\mathbf{B}^T \mathbf{D} \mathbf{B}). \quad (6.22)$$

Similarly, let  $\mathbf{y}$  denote any vector in the nullspace of  $\mathbf{B}^T \mathbf{D} \mathbf{B}$ . Then,

$$\begin{aligned} \mathbf{B}^T \mathbf{D} \mathbf{B} \mathbf{y} = \mathbf{0} &\implies \mathbf{y}^T \mathbf{B}^T \mathbf{D} \mathbf{B} \mathbf{y} = \mathbf{0} \implies (\mathbf{B} \mathbf{y})^T \mathbf{D} \mathbf{B} \mathbf{y} = \mathbf{0} \\ &\implies \mathbf{B} \mathbf{y} = \mathbf{0} \implies \mathbf{y} \in \text{nul}(\mathbf{B}) \implies \text{nul}(\mathbf{B}^T \mathbf{D} \mathbf{B}) \subseteq \text{nul}(\mathbf{B}). \end{aligned} \quad (6.23)$$

From Eq. 6.22 and 6.23,

$$\text{nul}(\mathbf{B}) = \text{nul}(\mathbf{B}^T \mathbf{D} \mathbf{B}) \implies \text{nullity}(\mathbf{B}) = \text{nullity}(\mathbf{B}^T \mathbf{D} \mathbf{B}). \quad (6.24)$$

Substituting Eq. 6.24 in 6.21, following is obtained:

$$\text{rank}(\mathbf{B}^\top \mathbf{D} \mathbf{B}) = \text{rank}(\mathbf{B}). \quad (6.25)$$

## 6.B. APPENDIX B

Let  $\mathcal{N}$  be a set of all vectors that lie in the nullspace of  $\mathbf{P}$  and  $\boldsymbol{\psi} = [\psi_1 \ \psi_2 \ \dots \ \psi_g]^\top$  denote a vector such that

$$\mathbf{P}\boldsymbol{\psi} = \mathbf{0} \quad \forall \boldsymbol{\psi} \in \mathcal{N}. \quad (6.26)$$

Next, let  $\boldsymbol{\gamma} = [\gamma_1 \ \gamma_2 \ \dots \ \gamma_r]^\top$  be a vector in the nullspace of  $\mathbf{A}^{(e)}$ . Then

$$\mathbf{A}^{(e)}\boldsymbol{\gamma} = \mathbf{0} \implies \mathbf{P}\mathbf{Q}\boldsymbol{\gamma} = \mathbf{0}. \quad (6.27)$$

Comparing Eqs. 6.26 and 6.27,

$$\mathbf{Q}\boldsymbol{\gamma} = \boldsymbol{\psi} \quad \forall \boldsymbol{\psi} \in \mathcal{N}, \quad (6.28)$$

where,

$$\mathbf{Q} = \begin{bmatrix} 1 & x_1 & \dots & (r^{\text{th}})_1 \\ 1 & x_2 & \dots & \vdots \\ \vdots & \vdots & \ddots & \vdots \\ 1 & x_g & \dots & (r^{\text{th}})_g \end{bmatrix}. \quad (6.29)$$

As per the matrix structure,  $\mathbf{Q}$  is an alternant matrix similar to a Vandermonde matrix [17] expressed in two variables. If  $x$  and  $y$  are independent variables and no two points coincide, the rows and columns of this matrix are linearly independent and  $\text{rank}(\mathbf{Q}) = \min(r, g)$ . Based on this, we have the following cases:

- For  $g < r$ : The vector  $\boldsymbol{\gamma}$  has more than one solution which implies that in Eq. 6.27, there exists a nullspace of  $\mathbf{A}^{(e)}$  and the design set  $\mathbf{s}$  cannot be solved uniquely.
- For  $g = r$ :  $\text{rank}(\mathbf{P}) = g$  which means that the vector set  $\mathcal{N} = \emptyset$ . Thus,  $\mathbf{A}^{(e)}$  does not have a nullspace and  $\text{rank}(\mathbf{A}^{(e)}) = r$ .
- For  $g > r$ : Eq. 6.28 is an overdetermined but inconsistent system of linear equations, thus  $\boldsymbol{\gamma}$  has no solution. This again implies that  $\mathbf{A}^{(e)}$  does not have a nullspace and  $\text{rank}(\mathbf{A}^{(e)}) = r$ .

## REFERENCES

- [1] D. K. Gupta, G. J. van der Veen, A. M. Aragón, M. Langelaar, and F. van Keulen, *Bounds for decoupled design and analysis discretizations in topology optimization*, International Journal for Numerical Methods in Engineering **111**, 88 (2017).
- [2] M. P. Bendsøe and N. Kikuchi, *Generating optimal topologies in structural design using a homogenization method*, Computer Methods in Applied Mechanics and Engineering **71**, 197 (1988).

- [3] O. Sigmund and K. Maute, *Topology optimization approaches: a comparative review*, Structural and Multidisciplinary Optimization **48**, 1031 (2013).
- [4] N. P. van Dijk, K. Maute, M. Langelaar, and F. van Keulen, *Level-set methods for structural topology optimization: a review*, Structural and Multidisciplinary Optimization **48**, 437 (2013).
- [5] J. Deaton and R. Grandhi, *A survey of structural and multidisciplinary continuum topology optimization post 2000*, Structural and Multidisciplinary Optimization **49**, 1 (2014).
- [6] T. H. Nguyen, G. H. Paulino, J. Song, and C. H. Le, *A computational paradigm for multiresolution topology optimization (MTOPT)*, Structural and Multidisciplinary Optimization **41**, 525 (2010).
- [7] T. H. Nguyen, G. H. Paulino, J. Song, and C. H. Le, *Improving multiresolution topology optimization via multiple discretizations*, International Journal for Numerical Methods in Engineering **92**, 507 (2012).
- [8] Y. Wang, J. He, Z. Luo, and Z. Kang, *An adaptive method for high-resolution topology design*, Acta Mechanica Sinica **29**, 840 (2013).
- [9] Y. Wang, J. He, and Z. Kang, *An adaptive refinement approach for topology optimization based on separated density field description*, Computers and Structures **117**, 10 (2013).
- [10] J. Park and A. Sutradhar, *A multi-resolution method for 3D multi-material topology optimization*, Computer Methods in Applied Mechanics and Engineering **285**, 571 (2015).
- [11] J. P. Groen, M. Langelaar, O. Sigmund, and M. Ruess, *Higher-order multi-resolution topology optimization using the finite cell method*, International Journal for Numerical Methods in Engineering **110**, 903 (2017).
- [12] J. Zowe, M. Kocvara, and M. P. Bendsøe, *Free material optimization via mathematical programming*, Mathematical Programming **79**, 445 (1997).
- [13] M. P. Bendsøe, J. M. Guades, R. B. Haber, P. Pederson, and J. E. Taylor, *An optimal model to predict optimal material properties in the context of optimal structural design*, Journal of Applied Mechanics **61**, 930 (1994).
- [14] M. Marcus and H. Minc, *Introduction to Linear Algebra* (Dover Publications, 1988).
- [15] I. Babuska, B. A. Szabo, and I. N. Katz, *The p-version of the Finite Element Method*, SIAM Journal on Numerical Analysis **18**, 515 (1989).
- [16] T. Strouboulis, K. Copps, and I. Babuska, *The generalized finite element method*, Computer Methods in Applied Mechanics and Engineering **190**, 4081 (2001).
- [17] N. Macon and A. Spitzbart, *Inverses of Vandermonde Matrices*, American Mathematical Monthly **65**, 95 (1958).



# 7

## QR-PATTERNS: NUMERICAL ARTEFACTS IN MULTIREOLUTION TOPOLOGY OPTIMIZATION

*Recent multiresolution topology optimization (MTO) approaches involve dividing finite elements into several density cells (voxels), thereby allowing a finer design description compared to a traditional FE-mesh-based design field. However, such formulations can generate discontinuous intra-element material distributions resembling QR-patterns. The stiffness of these disconnected features is highly overestimated due to limitations of the polynomial FE shape functions. While this modeling deficiency has been observed before, to be able to use MTO at its full potential, it is important that the occurrence of QR-patterns is understood.*

*This chapter investigates the formation and properties of these QR-patterns, which provides the groundwork for the definition of effective countermeasures. We study in detail the fact that the continuous shape functions used in MTO are incapable of modeling the discontinuous displacement fields needed to describe the separation of disconnected material patches within elements. Stiffness overestimation reduces with  $p$ -refinement, but this also increases the computational cost. We also study the influence of design filtering on the formation of QR-patterns and present a low-cost method to determine a minimum filter radius to avoid these artefacts.*

---

This chapter is based on an article published in Structural Optimization and Multidisciplinary Optimization journal, **58**, 4, 1335-1350 (2018) [1].

## 7.1. INTRODUCTION

In the traditional density-based topology optimization (TO) approaches, an element-wise constant density distribution is assumed. Some authors have explored decoupled design and analysis discretizations with the aim of reducing the number of design variables used to describe the material distribution in the domain (e.g. [2, 3]).

Since the computational cost associated with TO is mainly controlled by the finite element analysis (FEA), Nguyen *et al.* [4] proposed to use the strategy of decoupled design and analysis discretizations to obtain high-resolution designs at low analysis costs. A coarse analysis mesh is used and each finite element is divided into several density cells (voxels), which allows a finer density representation. This approach also allows to have material boundaries which are not necessarily aligned with the finite elements. Since different density resolutions are permitted for the same analysis mesh, Nguyen *et al.* [4] referred to the approach as *multiresolution topology optimization* (MTO). Since then, various variants have been proposed (e.g. [5–8]), and these have been used on several TO problems, e.g. for 3D TO in interactive hand-held devices [9], and designing thermo-electric generators [10], phononic materials [11], patient-specific 3D printed craniofacial implants [12], *etc.* In this chapter, we use the term MTO to refer to all those approaches which involve decoupling of the analysis and design discretizations with the goal of reducing the modeling related computational costs.

The MTO-based optimized designs are visually appealing, but it is also important to determine whether the coarse analysis used in MTO approaches is capable of accurately modeling the high resolution material distributions. The methods proposed by [4, 5] used linear shape functions ( $p = 1$ ) to interpolate the displacement field within the analysis elements. Here and henceforth,  $p$  denotes the polynomial order of the shape functions used for analysis. Filtering (density projection) is used in these methods to impose a restriction on minimum feature size and avoid checkerboard patterns. With large filter radii  $r_{\min}$ , designs which were visually appealing and comprised of smooth (but gray) boundaries were obtained. However, it is important to note that the use of large filter radii restricts the design field from expressing a high order material distribution. As a downside, fine structural features and crisp boundaries cannot appear in the solution. Methods such as Heaviside projection [13] can help to improve the crispness of the design [14]. However, the added computational cost associated with such schemes is not preferable for MTO, and it would be of great interest if smaller filter sizes can be used.

Wang *et al.* [7] adaptively reduced the filter-size in their MTO approach. However, some of the optimized structures reported in that study consisted of artificially stiff regions, resembling the QR-patterns. Based on numerical experiments, Groen *et al.* [14] hypothesized that these numerical artefacts observed in MTO schemes are caused due to inappropriate modeling scheme choices. Our investigation results (presented later in this chapter) are aligned with the observations of Groen *et al.* [14], and we show that these QR-patterns are indeed formed due to the limitations of the modeling scheme used.

Besides the formation of QR-patterns, MTO approaches can suffer from nonuniqueness in the solution of the design field [15]. For a high resolution design representation, it is important that the difference in optimized designs is also reflected in the analysis

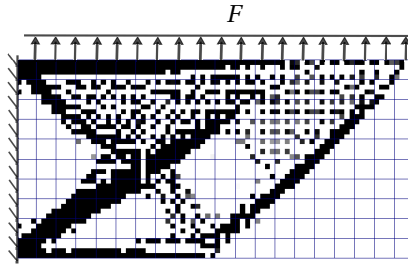


Figure 7.1: Design obtained in MTO compliance minimization of a cantilever beam subjected to a distributed load. The domain is discretized using  $20 \times 10$  finite elements with shape functions of polynomial degree 3 and  $4 \times 4$  design voxels per element. A composite integration scheme with 4<sup>th</sup> order Gauss quadrature rule is used in each voxel.

results. If not, different designs may show similar performance resulting in non-unique optima and instability issues [15, 16]. In [15], a rigorous study of this issue in the context of MTO is provided and mathematical bounds are presented to prevent non-uniqueness.

Parvizian *et al.* [6] proposed a finite-cell method (FCM) based MTO approach. In FCM, higher-order shape functions and numerical integration schemes are used and a high-resolution design field is permitted. The design field is used to describe the material distribution in the domain. Studies related to FCM-based modeling have shown that shape functions of low polynomial order are incapable of accurately modeling material discontinuities [17, 18]. A computationally effective solution to overcome such limitations is the local enrichment strategy in FCM. Joulaian and Düster [18] presented the *hp-d* local enrichment strategy, which could very accurately model the solution field at the material discontinuities with the addition of only a few degrees of freedom. It has been shown that the *hp-d* version of the FCM can model the material discontinuities for non-matching discretizations [19, 20]. Contrary to the extended finite element scheme [21] where new degrees of freedom need to be introduced in all finite elements requiring enrichment, their approach used an overlay mesh with higher-order enrichments to improve the solution of the base mesh. Nevertheless, the extended finite element method as well as enrichment-based FCM require knowledge of the location of material discontinuities in the domain. However, this is not generally available in TO, where the design changes at every iteration, and the boundary descriptions are not known beforehand.

For TO, the simplest solution is to use shape functions of higher polynomial order. With the use of high polynomial degree shape functions (*e.g.*  $p = 10$ ) in TO, the QR-patterns as well as the non-uniqueness related issues can be avoided to a certain extent and physically reasonable structures can be obtained [6, 14, 15]. However, with configurations using very high  $p$  values, the computational advantage over traditional TO could be lost. Based on numerical experiments, Groen *et al.* [14] inferred that by density filtering [22], even relatively low values of  $p$  could be used. However, this solution comes with the same disadvantages as discussed previously for low-order MTO. Application of a minimal filter radius is often preferred, and values have been suggested based on full-scale numerical tests by previous studies [8, 14].

As per our investigations, the filter radii choices for various MTO configurations, as

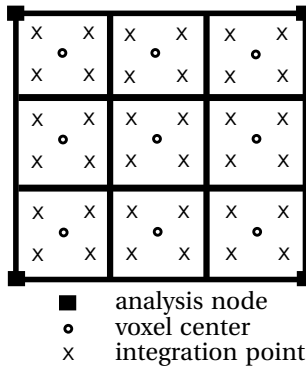


Figure 7.2: MTO element with 4 analysis nodes and 9 design voxels using a composite numerical integration scheme of  $2 \times 2$  Gauss quadrature rule for every design voxel.

described in [8], seem to result in reasonably correct designs. However, it is of considerable interest to explore the full potential of MTO, which motivates us to investigate whether filter radii smaller than those proposed in [8] can also be used. As mentioned earlier, a limiting factor is the occurrence of QR-patterns, which leads us to study the QR-patterns in a more detailed manner. The minimum cost MTO configuration that can achieve a certain desired design resolution and is capable of avoiding these artefacts would be the one where the full capability of MTO is efficiently utilized. In general, the QR-patterns have been observed in several previous studies, however, a systematic study focused on the formation of QR-patterns as well as measures to suppress them is still missing.

The aim of this chapter is to study the QR-patterns, and explain their formation in an MTO context. This can subsequently help to define suitable countermeasures. For this, we investigate whether for a given design resolution, there exists a certain minimum value of  $p$  for which the formation of QR-patterns can be avoided. The capability of the continuous shape functions in modeling the discontinuous displacement fields, that should arise at disconnected material patches within elements, is assessed. Also, an understanding of the applicability and limitations of filtering in MTO is presented.

The structure of the remainder of this chapter is as follows. First, the MTO concept is explained and a numerical MTO example is presented for which the QR-patterns are prominent (Section 7.2). Next, through several elementary test cases, an understanding of these artefacts is presented (Section 7.3). Parameter studies on the influence of both polynomial degree and filter radius, on various test geometries and loadcases, are performed and an explanation on the formation of QR-patterns is presented in Sections 7.3 and 7.4. Discussions related to MTO and conclusions are presented in Section 8.5 and Section 8.6, respectively.

## 7.2. ARTIFICIALLY STIFF FEATURES IN MTO

### 7.2.1. MTO CONCEPT

In MTO approaches, the design and analysis discretizations are decoupled, such that a finer density field can be expressed on a coarse analysis mesh [4, 6, 8]. Fig. 7.2 shows an MTO element that uses 4 analysis nodes and 9 design voxels. In this example, bilinear

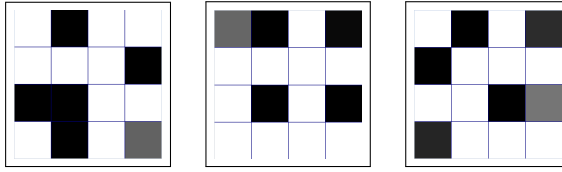


Figure 7.3: Magnified view of 3 finite elements from the optimized cantilever design shown in Fig. 7.1. These elements have been chosen arbitrarily from among finite elements with disconnected material features in the non-void regions of the domain.

shape functions are used for the interpolation of the displacement field within the element. Unlike traditional TO, where only one design voxel would be used, here the finite element is divided into 9 voxels. A density variable is associated with every design voxel and the density is assumed to be constant inside the voxel. Similar to traditional TO, this density represents the volume fraction of the voxel filled with certain material and can vary from 0 to 1.

Based on the density distribution inside the element, the corresponding element stiffness matrix  $\mathbf{K}_e$  is constructed as

$$\mathbf{K}_e = \sum_{i=1}^{n_v} \left( \rho_i^q \sum_{j=1}^{n_g} \mathbf{K}_{ij} w_{ij} \right), \quad (7.1)$$

where  $\mathbf{K}_{ij}$  and  $w_{ij}$  are the stiffness matrix contribution evaluated at the  $j^{\text{th}}$  integration point and the associated Gaussian weight, respectively of the  $i^{\text{th}}$  design voxel and  $\rho_i$  is its density value. The parameters  $n_v$  and  $n_g$  refer to the number of voxels and Gauss integration points, respectively and  $q$  is the penalization power used for material interpolation [23]. The order of the integration rule is chosen in a way that the voxel stiffness matrix can be accurately integrated. For the example shown in Fig. 7.2,  $n_v$  is set to 9, and a  $2 \times 2$  Gaussian quadrature rule ( $n_g = 4$ ) is used for numerical integration inside every design voxel.

### 7.2.2. OCCURRENCE OF QR-PATTERNS

QR-patterns are artificially stiff regions in the design which can lead to erroneous compliance values for the structure. For example, the compliance accuracy  $\mathcal{J}/\mathcal{J}^*$  for the design shown in Fig. 7.1 is  $3.6 \times 10^{-7}$ . Here  $\mathcal{J}$  is the calculated compliance value and  $\mathcal{J}^*$  is the compliance obtained on a finer reference mesh. Such a low value of  $\mathcal{J}/\mathcal{J}^*$  implies that the compliance of the structure has been tremendously underestimated by the employed modeling scheme. During the optimization process, this modeling flaw has been exploited by the formation of the QR-pattern, with characteristic disconnected material patches.

The design shown in Fig. 7.1 has been optimized for minimum compliance subjected to a distributed load and the domain is discretized using  $20 \times 10$  finite elements with  $4 \times 4$  design voxels per element. Shape functions of polynomial degree 3 are used and  $4^{\text{th}}$  order Gaussian quadrature rule is used for numerical integration in each voxel. The order of the design field is chosen to satisfy the element- as well as system-level bounds stated

in [15]. No filtering is employed here, a value of 3 is used for the penalization power  $q$  and a volume constraint of 30% is used. The reference mesh consists of  $80 \times 40$  elements with elementwise constant density field and polynomial degree  $p = 3$ .

Fig. 7.3 shows magnified versions of 3 elements from the optimized design shown in Fig. 7.1. All the 3 elements consist of disconnected or almost disconnected material parts along the horizontal as well as vertical directions. Such disconnected features can be seen in various regions of the design (Fig. 7.1). Note that unlike the infamous checkerboard patterns observed in traditional TO, these artefacts occur *within* the elements. In the presence of such disconnected features, the design appears far from optimal. However, since the QR-patterns obtained using MTO approaches are artificially stiff, erroneous compliance is reported by the used model and a low value of the error indicator  $\mathcal{J} / \mathcal{J}^*$  is obtained.

From the example presented above, it is clear that there are certain limitations of MTO, and to be able to fully harness the capabilities of this method, the limitations need to be known. The erroneous patterns may not always be so apparent as in this example. This can lead to deceptive results, where erroneous objective values are obtained and the structure may incorrectly be interpreted as a well performing one. As has been shown in [14] and [8], filtering may help to reduce this error. In both these studies, minimum filter sizes have been recommended for various shape function orders and design resolutions, and the authors have shown that acceptable designs are obtained. It is observed that the filter sizes proposed by [8] are more conservative than those mentioned in [14].

As stated earlier, it is of interest to see whether even smaller filter sizes can be used which can produce well performing artefact-free-designs. The first step in this direction would be to gain a better understanding of the QR-patterns, and identify the possible reason for their formation. Thus, through several small-scale studies, first we investigate the origin of QR-patterns more closely in the next section.

## 7.3. ORIGIN OF QR-PATTERNS

### 7.3.1. STUDY OF ELEMENTARY CASES

For a better insight in QR-patterns, we examine elementary cases where the material distribution inside a single element is optimized for minimum compliance. Fig. 7.4 shows three plane stress test cases consisting of one square finite element of unit size subjected to axial, biaxial and shear loading. A volume constraint of 30% is chosen for all the cases. Each finite element is divided into  $8 \times 8$  voxels, Lagrange polynomials based shape functions of  $p = 6$  are used and no filtering is applied. A 5<sup>th</sup> order Gaussian quadrature rule is used for numerical integration of the voxel stiffness matrices. Here and throughout this chapter, unless otherwise mentioned, the Young's moduli of the material and the void are chosen to be 1 and  $10^{-9} \text{ Nm}^{-2}$ , respectively, and the Poisson ratio is set to 0.3. A modified SIMP formulation [23] with penalization power  $q = 3$  is used for material interpolation for intermediate density values. As an initial design for optimization purposes, we used a uniform density distribution with slight perturbation in the density of the voxel at the top-rightmost corner. The perturbation was needed because a uniform density distribution leads to equal sensitivities for all the design variables which was not suited for optimization.

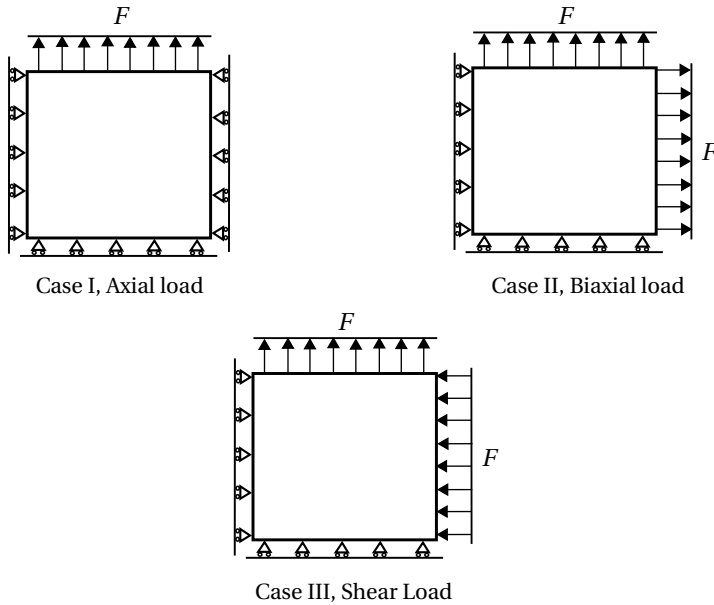


Figure 7.4: Numerical test cases with different loading conditions ( $F = 1\text{Nm}^{-1}$ ). For modeling, the design domain for each case is discretized using a single finite element with shape functions of polynomial order 6, and  $8 \times 8$  design voxels are used.

The optimized designs as well as the deformed shapes for the three cases are shown in Fig. 7.5. For all the three cases, the compliance accuracy  $\mathcal{J}/\mathcal{J}^*$  values are extremely low, which means that the chosen model strongly underestimates the compliance of the optimized designs. Here, the reference compliance  $\mathcal{J}^*$  is calculated on an elementwise constant density based mesh with  $8 \times 8$  finite elements with shape functions of polynomial order 3. Similar to Fig. 7.3, it can be seen that all the optimized designs consist of QR-patterns and possess material parts which are completely disconnected. There are structural features subjected to the distributed load that can freely float along the vertical or horizontal directions, which implies that with accurate modeling, large displacements should be anticipated. This in turn should lead to high compliance objective values for all the cases.

However, the low values of  $\mathcal{J}/\mathcal{J}^*$  imply that these designs are erroneously interpreted as stiff ones. In fact, their stiffness is overestimated by a factor of  $10^8$ . The artificial stiffness is evident from the deformed shapes of these structures for the corresponding exerted loads (Fig. 7.5). We see that the freely floating solid features also get deformed, which means that considerable load is transferred through the voids. Also, contrary to the fact that the voids should be significantly deformed due to their negligible stiffness, we see that the deformations in the void areas are quite comparable to those of the solid parts. This means that as per the employed modeling scheme, the voids possess certain artificial stiffness, making them less compliant.

From these test cases, it is evident that the reason for the formation of these QR-

patterns is linked to the limitations of the finite element model used here. From our numerical experiments with various shape functions, we observed that by using higher values of  $p$ , these artificially stiff regions could be reduced. These observations are aligned with the previous studies related to FCM-based modeling, where it has been shown that the material discontinuities cannot be accurately mapped using low-order elements in an FCM setting [17, 18]. One approach to reduce the modeling error is to use higher-order elements, however, such an approach is not advantageous in terms of the added computational cost. Joulaian and Düster [18] and Kollmannsberger *et al.* [19] used an  $hp$ - $d$  variant of FCM, where local enrichments are introduced through an overlay mesh to improve the modeling accuracy in heterogeneous parts of the domain.

In the context of TO, artefacts arising due to the limitations of low order shape functions in an MTO setting have been reported in [6], [14] and [8]. In line with these studies, the link between the polynomial functions and the QR-patterns are studied in the following sections. Shape functions of higher polynomial degree can better represent the displacement solution. Thus, in Section 7.3.3, we investigate whether the QR-patterns arise due to misrepresentation of the displacement field. Also, we explore whether there exist certain polynomial orders of the shape functions for which these QR-patterns can be eliminated at a reasonable computational cost.

### 7.3.2. GAP MODELING WITH POLYNOMIAL SHAPE FUNCTIONS

To investigate the role of polynomial order of the shape functions in the formation of QR-patterns, we employ a simple elementary test where thin strips of void are modeled. The choice of this test is motivated from the patterns seen in Fig. 7.5, where the void appears to bear load. For problems only related to modeling, the loads are applied on the solid parts of the domain, thus the void does not need to be modeled correctly. However, in the context of TO, it is possible that during the course of optimization, thin strips of void arise in the domain. For such scenarios, either the applied load needs to become zero, or the chosen shape function should be able to correctly model the gap.

For the test problem chosen here (Fig. 7.6), the load is fixed, and the modeling accuracy is investigated. A single square finite element of unit dimensions is constrained from three sides and loaded in tension by a uniform distributed load. The element is filled with two material phases, *i.e.* solid and void. The domain is divided into  $10 \times 10$  design voxels and a composite integration scheme (as stated in Eq. 7.1) is used to integrate the element stiffness matrix. The order of the integration scheme is chosen based on the polynomial order of the shape functions used to model the displacement solution.

Several values of  $p$  are used and the compliance  $\mathcal{J}$  of the structure is calculated. Since we seek the values of  $p$  for which the QR-patterns can be eliminated in general, it is important that the chosen  $p$  works for various feature resolutions. To take this into account, the height of the void layer ( $h_v$ ) is varied. To assess the correctness of  $\mathcal{J}$ , the analytical solution  $\mathcal{J}_0$  is also calculated. The ratio  $\mathcal{J}/\mathcal{J}_0$  indicates the compliance accuracy, with an ideal value of 1.

Fig. 7.7 shows  $\mathcal{J}/\mathcal{J}_0$  for different values of  $p$  and  $h_v$ . A general observation is that for low  $p$  values, *e.g.* 2 or 3, accuracy is poor for all feature sizes. This means that the shape functions of lower polynomial order are not able to represent the displacement

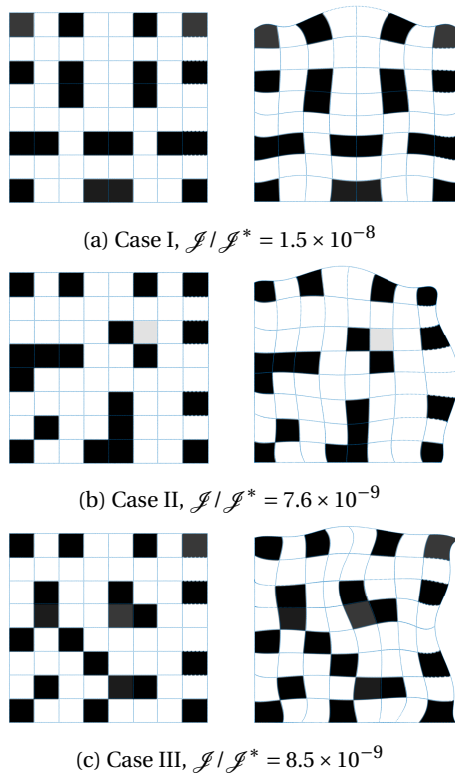


Figure 7.5: Optimized designs (left) and respective deformed shapes (right, scaled for visualization) under various loading conditions obtained for a single finite element obtained using an MTO scheme with  $p = 6$  and  $8 \times 8$  voxels.

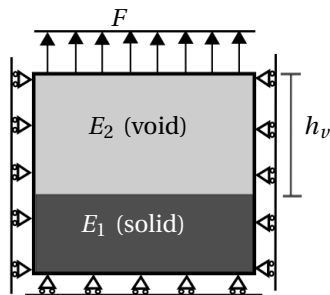


Figure 7.6: An axially loaded finite element ( $F = 1\text{Nm}^{-1}$ ) filled with solid and void parts.

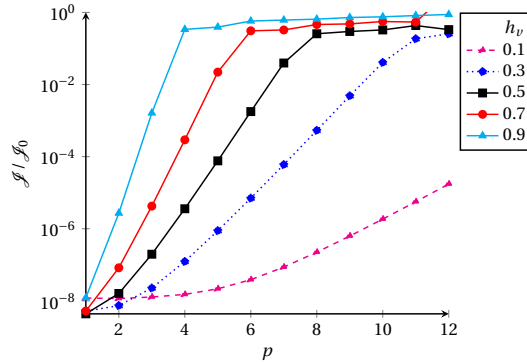


Figure 7.7: Compliance accuracy ( $\mathcal{J}/\mathcal{J}_0$ ) versus the shape function order ( $p$ ) for different void-feature resolutions obtained using a single finite element (as shown in Fig. 7.6) comprising  $10 \times 10$  density voxels. Here,  $\mathcal{J}$  is the compliance obtained using the MTO setting, and  $\mathcal{J}_0$  denotes the analytical solution.

solution arising from such discontinuous material fields. With increasing  $p$ , the accuracy of the model improves, however, the feature resolution  $h_v$  plays a significant role here. For a large gap of  $h_v = 0.9$ , a shape function order of 4 proves sufficient to model the large compliance of the structure. However, for smaller gaps, increasingly high values of  $p$  are needed to properly represent the displacement field and prevent artificial stiffness. The case with  $h_v = 0.1$  is still not adequately modeled with  $p = 12$ . This observation is investigated further in the next section.

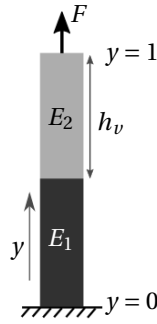
7

In general, it is observed that the feature-size plays an important role in choosing the correct value of  $p$ . Thus, for full-scale multiresolution topology optimization problems, very high-order polynomials are needed to ensure that even the finest features are modeled correctly. However, the use of very high order polynomials comes at significantly increased computational costs, which limits the efficiency of such an MTO setting.

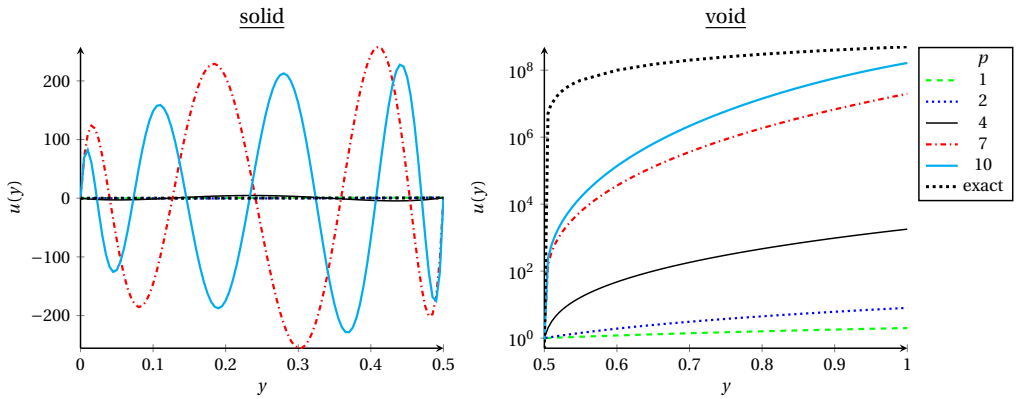
### 7.3.3. DISPLACEMENT SOLUTION ACCURACY

In Section 7.3.2, it has been shown that higher  $p$  values can help to eliminate the QR-patterns. As stated earlier, the reason is that with higher-order polynomials, the displacement solution for a discontinuous material distribution can be more accurately represented. To study this in more detail, we use a simple 1D example where a bar is axially loaded at one end and fixed at the other (Fig. 7.8a). The bar consists of solid and void material phases in equal proportions ( $h_v = 0.5$ ). Fig. 7.8b shows the calculated displacement solutions along the length of the bar for the two phases calculated for several values of  $p$ . As a reference to measure the correctness of the solution, the exact piecewise linear displacement solution has been calculated analytically and is shown in Fig. 7.8b (on log scale).

The first observation is that even shape functions of polynomial order 10 are incapable of accurately representing the displacement field. The continuous polynomials cannot represent a nonsmooth displacement field arising for the chosen material distribution. For lower values of  $p$ , the displacements in the void part of the domain are



(a) 1D bar example



(b) Displacement fields in the solid (left) and void (right) parts. Note that the right-hand graph uses a log scale because of the large displacement differences.

Figure 7.8: Displacement fields obtained for shape functions of various polynomial orders and the analytical solution for a 1D bar example. The Young's moduli of the solid and the void are denoted by  $E_1$  and  $E_2$ , respectively, and  $h_v$  denotes the width of the void.

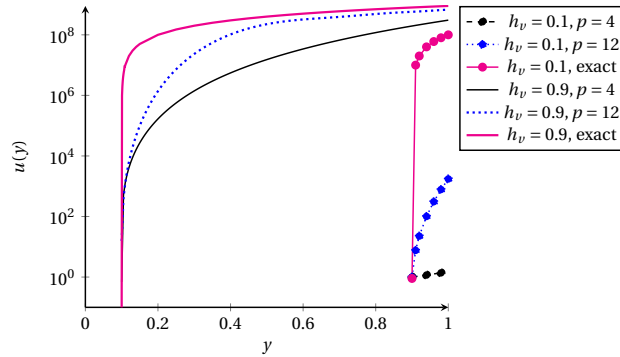


Figure 7.9: Displacement field  $u(y)$  (on a log scale) in the void region for the 1D bar example shown in Fig. 7.8a. The log scale has been used due to large differences in the displacements for different values of  $p$ .

severely underestimated. Similar to the results shown in Fig. 7.7, the design tends to be artificially stiff. With increasing  $p$  values, a better representation of the displacement field can be obtained in the void part, however, large oscillations are generated in the solid part. Although this is incorrect, the deviation from the exact solution in the solid phase is negligible compared to that in the void part. Thus, although the displacement solution in the solid part does not match well with the exact solution, the nodal displacement predicted by higher order polynomials matches well.

Another important thing to note is that although the error in the displacement solution at the top end of the bar reduces significantly with high-order polynomials, the mismatch in the rest of the domain is quite high. The displacement field can become negative in the solid region, and resulting stresses and strains will be highly incorrect. For certain problems, *e.g.* compliance minimization with nodal loads, using high-order polynomials would be fine in an MTO setting. However, for other objective functionals, involving also response quantities within the elements, *e.g.* stress minimization, even the solution obtained with high values of  $p$  could lead to incorrect results.

In Section 7.3.2, it was found that the required shape function order depends on the feature resolution. Larger voids allow lower polynomial order of the shape functions for accurate analysis. Fig. 7.9 provides a better insight into this aspect. In this figure, the displacement fields calculated in the void areas are provided for void widths ( $h_v$ ) equal to 0.1 and 0.9 and shape functions of polynomial orders 4 and 12 are used. These parameters are chosen based on the observations in Fig. 7.7 that for  $h_v = 0.9$ ,  $p = 4$  is sufficient, while for  $h_v = 0.1$ , even  $p = 12$  may not be accurate. We see that for  $h_v = 0.9$ , the displacement curve with even  $p = 4$  reaches close to the analytical solution and with  $p = 12$ , it improves further. However, for  $h_v = 0.1$ , even with  $p = 12$ , the displacements are poorly predicted compared to the analytical solution. This is due to the limitation of polynomial shape functions in representing the drastic change in displacement close to the material discontinuity. The polynomial shape functions increase gradually over an interval of  $y$  to represent such a jump. This behavior is more prominent for lower order shape functions. Thus, for  $h_v = 0.9$ , the displacement at the end of the bar is sig-

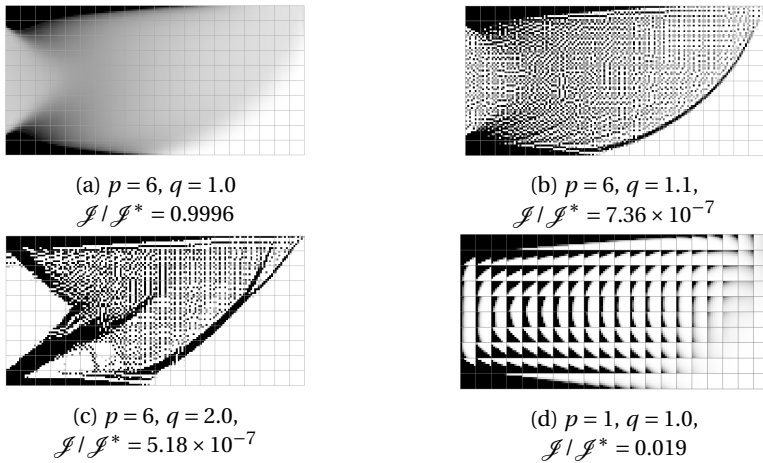


Figure 7.10: Optimized designs for a cantilever beam subjected to a distributed load obtained using various penalization powers  $q$  in the modified SIMP formulation. The domain consists of  $20 \times 10$  finite elements with  $8 \times 8$  voxels per element.

nificantly higher than that for  $h_v = 0.1$ . Consequently, for larger gaps, even lower order polynomials are acceptable. Based on this, controlling feature sizes presents a mechanism to prevent configurations that yield analysis inaccuracy. This aspect is explored further in Section 7.4.

#### 7.3.4. ROLE OF PENALIZATION AND DESIGN-UNIQUENESS

The numerical tests presented in this chapter thus far demonstrated the role of shape functions in the formation of QR-patterns. Due to the weakness of the analysis model, the optimizer prefers to exploit designs consisting of artificially stiff-regions. However, it has been observed that shape function order is not the only factor driving the formation of QR-patterns. Penalization of intermediate density values, as introduced conventionally by, e.g., the SIMP approach, turns out to promote the formation of QR-patterns. In addition to the artificial stiffness caused by the continuous shape functions, penalization gives the black-white QR-patterns an additional advantage over more continuous intermediate density material distributions.

This hypothesis has been numerically validated on the cantilever beam design problem presented in Fig. 7.1. Fig. 7.10a, 7.10b and 7.10c show 3 optimized designs obtained using penalization powers  $q = 1, 1.1$  and  $2.0$ , respectively in the modified SIMP formulation and the corresponding compliance accuracies are reported. A finite element domain of  $20 \times 10$  elements is used with  $8 \times 8$  voxels in each element and shape functions of polynomial degree 6 are used. For  $q = 1$ , the intermediate densities are not penalized due to which the optimized design consists of gray areas throughout the domain and is free from QR-patterns. From the value of  $\mathcal{J} / \mathcal{J}^*$ , it can be inferred that the model is very accurate. However, for  $q = 1.1$  or  $2.0$ , the smooth design is unfavorable and the optimizer creates more solid-void design. Designs largely consisting of QR-patterns are obtained, with even void voxels on the upper edge where the distributed load is applied. Clearly

these parts would be very compliant in reality. However, the chosen MTO scheme cannot model the response properly and extremely low compliance accuracy is obtained.

An interesting result is obtained with shape functions of polynomial degree 1. For this case, even with no penalization, the design consists of QR-patterns and low compliance accuracy is obtained (Fig. 7.10d). Similar to the checkerboard patterns, it is possible that these patterns always perform better than the ones with intermediate densities [24], due to which they appear in the final design. A remedy to remove them would be to employ filtering that bans these patterns from the design space. Alternatively, it is possible that the optimizer converges to this solution due to the non-uniqueness of the design field [15]. Thus, it is important that the shape function orders are chosen in a way that the uniqueness bounds proposed in [15] are satisfied.

## 7.4. FILTERING IN MTO

### 7.4.1. ROLE OF FILTERING

Existing MTO approaches use filtering of voxel densities, which prevents the formation of QR-patterns. Filtering was originally employed in traditional TO to avoid the formation of checkerboard patterns and impose a minimum feature size. Some of the frequently used filtering methods are sensitivity filtering [25], density filtering [22], density filtering with projection [13], *etc.*

Density filters can be understood as regularization functions that smoothen the density field by taking weighted contributions from the neighboring density values located within a certain radius. Thus, in a filtered density field, the density gradients are reduced. In traditional TO, where the density is constant inside every element, the use of filters prohibits large contrasts in densities between two adjacent elements. Since checkerboard patterns feature large density contrasts between adjacent elements, they are eliminated by the use of filters.

Unlike checkerboard patterns, QR-patterns obtained in MTO are *intra-element* artefacts. In traditional TO, a filter radius slightly larger than the minimal element size is sufficient to eliminate the checkerboard patterns. In line with this observation, in MTO approaches, the smallest effective filter size should be slightly larger than the size of a density voxel. However, QR-patterns in MTO require stronger regularization of the density field, hence the smallest filter size to eliminate QR-patterns needs to be considerably larger than the voxel width. Although QR patterns differ on these aspects from checkerboard patterns, Nguyen *et al.* [8] and Groen *et al.* [14] have shown that with the use of filters, acceptable designs could be obtained.

### 7.4.2. EFFECT OF FILTERING AND LIMITATIONS

Here, we investigate using an elementary example the extent to which the use of filters can help to suppress the QR-patterns in MTO. As stated earlier, filters reduce the density contrast between the adjacent elements, which consequently reduces the extent of non-smoothness of the displacement solution. In this section, we study the role of density filters by varying the filter radius  $r_{\min}$  and observing the effect on the accuracy of the calculated compliance solution. The tensile test problem shown in Fig. 7.6 is used and the domain is assumed to consist of solid and void parts in equal proportions prior

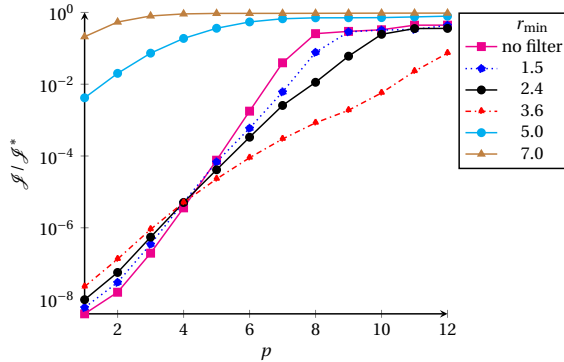


Figure 7.11: Compliance accuracy  $\mathcal{J}/\mathcal{J}^*$  versus the shape function order  $p$  for various filter radii  $r_{\min}$  (in terms of voxel-length) obtained using a single finite element comprising  $8 \times 8$  design voxels. The unfiltered density field consists of solid and void parts in equal proportions.

to filtering. The original density field is smoothed using density filters to obtain the filtered design. The domain is discretized using one finite element consisting of  $8 \times 8$  design voxels.

Fig. 7.11 shows compliance accuracy  $\mathcal{J}/\mathcal{J}^*$  for various filter radii, as a function of polynomial degree  $p$ . The filter radius  $r_{\min}$  is expressed in terms of voxel length. The reference compliance  $\mathcal{J}^*$  is calculated on a domain of  $8 \times 8$  finite elements of elementwise constant density and shape functions of polynomial order 3 are used. For the case without filter, the design is free from intermediate density values, and a solid-void boundary is modeled. From Fig. 7.11, it is seen that for such a configuration, polynomial degree of 8 or higher will be needed to model the displacement field. For shape functions of low polynomial degree  $p$ , the non-smooth displacement field at the solid-void boundary cannot be accurately modeled and poor compliance accuracy is obtained.

For high values of  $p$ , the displacement field can be better approximated and the compliance accuracy improves. At the same time, increasing the filter radius smoothens the density field, due to which the displacement solution becomes smoother and it should be possible to approximate it with shape functions of lower polynomial order ( $p$ ). However, from Fig. 7.11 we observe that under the influence of density filtering, contrary to expectation, higher values of  $p$  are needed. For  $r_{\min}$  equal to 2.4 voxels, a value of 10 or higher is required for  $p$ . Moreover, it is seen that even  $p = 12$  is not sufficient if the design is filtered using  $r_{\min}$  equal to 3.6 voxels. This happens because although under the influence of filtering, the displacement solution becomes smoother, the size of the gap reduces as well (Fig. 7.12b). As seen in Section 7.3.2, smaller void regions cannot be modeled with low values of  $p$ . Thus, for the case presented here, filtering does not have the desired effect, rather it raises the need for higher-order polynomials and is counter-productive in terms of required computational costs.

However, for  $r_{\min}$  values of 5.0 and 7.0 voxels, low values of  $p$  are already sufficient and the error is significantly reduced. This is because with such filter sizes, there is no void part left in the filtered design and the element becomes stiffer. For a better under-

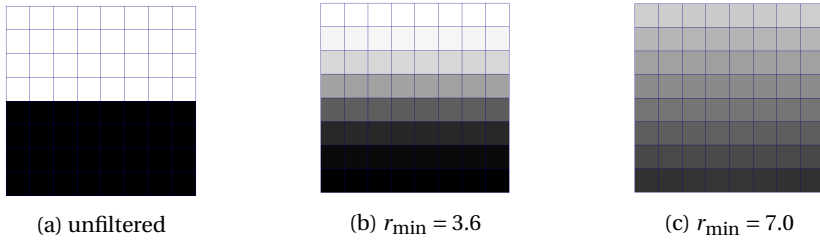


Figure 7.12: Unfiltered density field and its filtered versions obtained using density filters with  $r_{\min}$  equal to 3.6 and 7.0 voxels. The domain consists of 1 finite element with  $8 \times 8$  voxels.

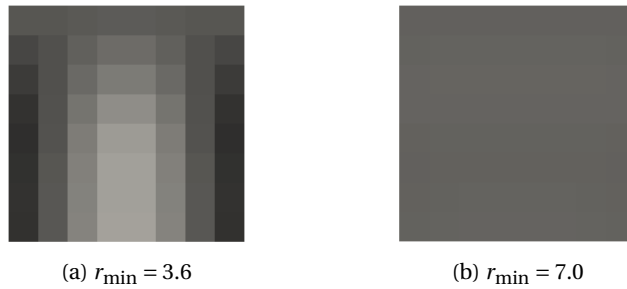


Figure 7.13: Optimized designs obtained for Case I shown in Fig. 7.4 using the density distributions shown in Figs. 7.12b and 7.12c.

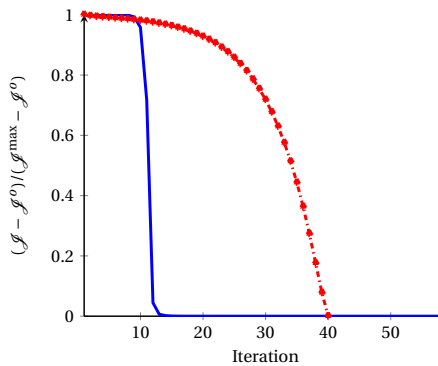


Figure 7.14: Normalized convergence plots of compliance objective values obtained for the axial load case shown in Fig. 7.4 using a homogeneous density field (red) and the density field shown in Fig. 7.12a (blue). For both the cases,  $r_{\min}$  is set to 3.6 voxels and material volume fraction is limited to 0.5. The domain is discretized using one finite element with  $p = 6$  and comprises  $8 \times 8$  density voxels.

standing, consider Fig. 7.13 where the unfiltered design and its two filtered versions are shown which are obtained using density filtering with  $r_{\min}$  equal to 3.6 and 7.0 voxels. Since the density is constant in the horizontal direction, each row of voxels can be considered as an elastic layer of certain stiffness. The design, along the vertical direction, can be interpreted as multiple elastic layers connected in series, with different Young's moduli reflected by the respective density values. The equivalent stiffness of the whole structure along the vertical direction is controlled mainly by the weakest layer.

For  $r_{\min}$  equal to 3.6 voxels, there exists a void of size 1.0 voxel in the filtered design (Fig. 7.12b) due to which the design is highly compliant. For such a scenario, a nonsmooth displacement solution arises which cannot be correctly modeled by low values of  $p$ . However, with  $r_{\min}$  set to 7.0 voxels (Fig. 7.12c) or even 5.0 voxels, no void region exists. This means the equivalent stiffness of the element is higher and the extent of nonsmoothness in the displacement solution is significantly lower.

This example shows that for cases where void features exist in the filtered design and play an important role in an element's response, increasing the filter radius can increase the analysis error. Once the filter radius is large enough to remove such void regions from the filtered field, the opposite is observed and the required value of  $p$  decreases significantly. Thus, even in the presence of filters, it is possible that the displacement field cannot be modeled correctly in an MTO setting. In an optimization process, whether or not an optimizer will exploit these configurations is hard to predict and problem dependent. However, the possibility cannot be ruled out. Additionally, since the filters impose a minimum feature restriction, the desired high resolution of the design is also reduced.

From these observations it can be argued whether density filters are really the solution to eliminate QR-patterns. As a matter of fact, the choice of correct filter radius depends on the material distribution in the unfiltered design as well as the loading condition and chosen shape function order. As per our present understanding, the optimal filter radius can only be determined by computationally expensive trial and error. Fortunately, for various linear structural problems, use of filters has helped to design reasonably optimal MTO designs [14]. In the next section, we study one of these problems and present a numerical approach towards efficiently finding a suitable filter radius.

### 7.4.3. CHOOSING THE FILTER RADIUS

From the tests presented in the preceding section, it is clear that the choice of filter radius  $r_{\min}$  can significantly affect the accuracy of the optimized solution. However, a general theory to determine the minimum filter radius that gives reasonably correct solutions is not yet available. Here, we examine the possibility of finding an appropriate value of  $r_{\min}$  based on numerical experiments conducted for the 3 test cases shown in Fig. 7.4. These 3 cases represent elementary loading conditions that may occur at element level in a full-scale topology optimization mesh. Since the optimization problems for the 3 test cases are computationally very cheap compared to the actual design problem, these tests can be run a priori to choose  $r_{\min}$  for a given set of associated parameters.

The choice of an optimal filter size depends on the fact that small filter radii lead to inaccurate modeling and QR-patterns, while large filter size leads to undesirable loss of resolution and crispness. For several values of  $r_{\min}$ , the error indicator  $\mathcal{J} / \mathcal{J}^*$  is examined on a domain of  $8 \times 8$  voxels with shape functions of polynomial degree 6 and the

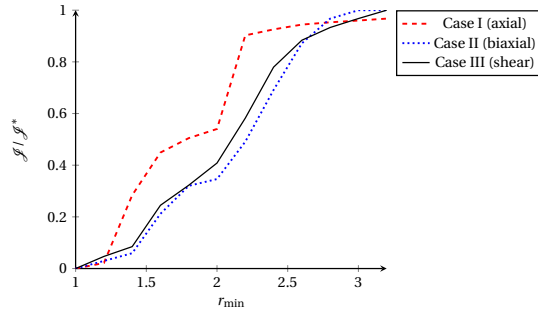


Figure 7.15: Compliance accuracy  $\mathcal{J}/\mathcal{J}^*$  for various filter radii  $r_{\min}$  obtained for the three test cases presented in Fig. 7.4. For all the cases, a single finite element is used with shape functions of polynomial order 6 and  $8 \times 8$  design voxels.

## 7

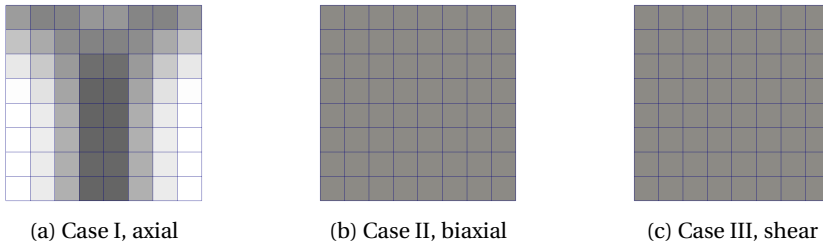


Figure 7.16: Optimized designs for the three elementary test cases shown in Fig. 7.6 obtained using a filter radius of 2.6 voxels. The domain consists of 1 finite element with  $8 \times 8$  voxels and shape functions of polynomial degree 6.



Figure 7.17: Optimized designs for cantilever beam subjected to distributed load (as in Fig. 7.1) for two different filter radii. The domain is discretized using  $20 \times 10$  finite elements with shape functions of polynomial degree 6 and  $8 \times 8$  design voxels per element.

results are shown in Fig. 7.15. To calculate the reference solution  $\mathcal{J}^*$ , an analysis mesh of  $8 \times 8$  finite elements is used and the polynomial order of the shape functions is set to 3.

An interesting observation here is that for all values of  $r_{\min}$ , the compliance accuracy is higher for axial loading compared to the biaxial and shear loading conditions. One of the possible reasons is that for the axial load, there is only one direction along which the material discontinuities affect the accuracy of the model. For choosing optimal  $r_{\min}$ , we assume that a compliance accuracy of close to 90% or even higher is acceptable and from Fig. 7.15, it is seen that this holds true for  $r_{\min}$  equal to 2.6 voxels for all the 3 cases. Fig. 7.16 shows the optimized designs for the 3 cases obtained using  $r_{\min} = 2.6$  voxels. Due to the use of large filters, designs are significantly gray, however, it is clearly evident that they are free from QR-patterns.

Table 7.1: Choice of filter radius (in terms of element size  $h$ ) for various choices of polynomial degree of the shape functions  $p$  and number of design voxels along the x- or y-direction (denoted by  $d$ ), to obtain compliance accuracies  $\mathcal{J}/\mathcal{J}^*$  of around 90% or higher for the three element test cases shown in Fig. 7.4. Here,  $\times$  denotes that one element discretization is not sufficient, and the dark empty cells denote combinations of  $p$  and  $d$  that violate the uniqueness bounds proposed in [15].

$p \backslash d$	2	3	4	5	6	7	8	9	10
1	$\times$								
2	$\times$	0.8							
3	$\times$	0.6	0.7	0.7					
4	$\times$	$\times$	0.5	0.45	0.45				
5	$\times$	$\times$	0.45	0.45	0.4	0.4	0.4		
6	$\times$	$\times$	0.4	0.4	0.35	0.35	0.35	0.3	
7	$\times$	$\times$	0.4	0.4	0.35	0.35	0.3	0.3	0.3
8	$\times$	$\times$	0.35	0.35	0.3	0.3	0.3	0.25	0.25
9	$\times$	$\times$	0.35	0.35	0.3	0.3	0.25	0.2	0.2
10	$\times$	$\times$	0.35	0.35	0.3	0.3	0.25	0.2	0.2

Next, the value of 2.6 is used for  $r_{\min}$  during the optimization of material distribution for the problem shown in Fig. 7.1. The domain is discretized using  $20 \times 10$  finite elements,

Table 7.2: Choice of filter radius (in terms of element size  $h$ ) for various choices of polynomial degree of the shape functions  $p$  and number of design voxels along the x- or y-direction (denoted by  $d$ ), to obtain compliance accuracies  $\mathcal{J} / \mathcal{J}^*$  of around 90% or higher for the three element test cases shown in Fig. 7.4. The domain has been discretized using a patch of  $2 \times 2$  finite elements. For the values marked using \*,  $3 \times 3$  finite elements have been used. The dark empty cells denote combinations of  $p$  and  $d$  that violate the uniqueness bounds proposed in [15].

$p \backslash d$	2	3	4	5	6	7	8	9	10
1	0.8*								
2	0.8*	0.75							
3	0.75*	0.7	0.65	0.7					
4	0.65*	0.5	0.45	0.45	0.45				
5	0.65	0.45	0.45	0.45	0.4	0.4	0.4		
6	0.65	0.45	0.45	0.4	0.35	0.35	0.35	0.3	
7	0.65	0.4	0.4	0.35	0.35	0.35	0.3	0.3	0.3
8	0.6	0.4	0.35	0.3	0.3	0.3	0.3	0.25	0.25
9	0.6	0.35	0.35	0.3	0.3	0.3	0.25	0.2	0.2
10	0.6	0.35	0.35	0.3	0.3	0.3	0.25	0.2	0.2

each comprising  $8 \times 8$  voxels and shape functions of polynomial order 6. Fig. 7.17a shows the optimized design obtained for  $r_{\min} = 2.6$  voxels. With this filter radius, the compliance accuracy of the design is 0.98, which means the model meets the chosen accuracy level and the design is free from artificially stiff regions. Here also, the reference compliance  $\mathcal{J}^*$  is calculated on an elementwise constant density mesh of  $160 \times 80$  finite elements with  $p = 3$ . For comparison, Fig. 7.17b shows the optimized cantilever design obtained with  $r_{\min} = 1.4$  voxels. QR-patterns are very prominent in this design and the compliance accuracy of the design is low. For both the designs, intermediate density areas are seen in some parts of the domain, which could not be resolved using the MTO scheme.

Thus, we find that the  $r_{\min}$  value obtained from Fig. 7.15 works well for this problem. We observe that the compliance accuracy for the cantilever problem is higher compared to the 3 test cases from which the optimal value of  $r_{\min}$  was derived. In terms of closeness, the compliance accuracy values for this design are closest to that of Case I, *i.e.* axial loading. This is indeed as expected since for a single load case compliance minimization, the optimized design tends to form members loaded in tension/compression.

It is important to note that this choice of  $r_{\min} = 2.6$  voxels cannot be generalized. There are several parameters that can affect the appropriate choice of filter radius, *e.g.*, polynomial degree of shape functions, number of voxels, material volume fraction, loading conditions, *etc.* Among these, we study the effect of various shape functions and number of voxels on the optimal filter radius obtained using the 3 element test cases (Fig. 7.4). For ease of comparison, the filter radius for the further study will be defined in terms of element length ( $h$ ). For example, for a square finite element comprising  $5 \times 5$  voxels, a filter radius of 2 voxels will be referred as  $0.4h$ . In addition, the number of voxels

Table 7.3: Choice of filter radius (in terms of element size  $h$ ) for various choices of polynomial degree of the shape functions  $p$  and number of design voxels along the  $x$ - or  $y$ -direction (denoted by  $d$ ), to obtain compliance accuracies  $\mathcal{J}/\mathcal{J}^*$  of around 90% or higher for the three element test cases shown in Fig. 7.4. For the cells marked with \*, one element discretization was insufficient, hence for these cases, a  $2 \times 2 \times 2$  patch of finite elements was used. The dark empty cells denote combinations of  $p$  and  $d$  that violate the uniqueness bounds proposed in [15].

$p \backslash d$	2	3	4	5	6	7
1	0.75*					
2	0.75*	0.6*	0.6			
3	0.75*	0.5	0.5	0.5		
4	0.6*	0.4	0.35	0.4	0.35	0.35
5	0.6*	0.4	0.35	0.35	0.3	0.3
6	0.55	0.4	0.35	0.3	0.3	0.25

along the  $x$ - or  $y$ -direction will be denoted by  $d$ .

Table 7.1 shows the optimal filter radii found for various choices of  $p$  and  $d$  when compliance accuracy of around 90% or higher is assumed to be acceptable. The value 90% is chosen based on the fact that with the resultant filter radii, compliance accuracies of 98% or higher were obtained for several full-scale TO problems of compliance minimization. Clearly with the same method, filter radii limits can be found for other target accuracies. For this study, filter radii of  $0.05h$  to  $1.0h$  are tested at an interval of  $0.05h$ . The dark gray region refers to the infeasible combinations of  $p$  and  $d$  as per the uniqueness bounds proposed in [15]. The symbol  $\times$  denotes that a discretization using only one finite element is not sufficient for the respective combinations of  $p$  and  $d$ , as far as QR-patterns are concerned. When the design is optimized without filtering for single element test cases comprising  $2 \times 2$  voxels and  $3 \times 3$  voxels, very inaccurate solutions are obtained. Clearly, for a very low design resolution, the single element test cases do not seem to work. This happens because with a very low design resolution, the optimization problem is quite restricted. Starting from a uniform distribution, it is observed that designs hardly change during the course of optimization. The unfiltered design itself is well connected and no filtering is needed.

Table 7.2 presents the optimal filter radii for various choices of  $p$  and  $d$  obtained on a mesh of  $2 \times 2$  finite elements. Only values related to the tensile case are reported, since for the one element tests, this case was found to be controlling the choice of minimum filter radii. With an increase in the number of elements, the design freedom is increased, and optimal filter radii values can be obtained for low values of  $d$  as well.

A general observation is that for obtaining very fine features, the filter radius needs to be very small. From Table 7.1, it is observed that for a filter radius of  $0.2h$ , very high values of  $p$  and  $d$  are needed. Lowering  $p$  leads to the need for a larger filter radius. Lower values of  $d$  restrict the design resolution and also require a large filter radius. It is observed that these values of filter radius are slightly higher compared to the results reported in [14], and the reason could be that the element test cases used in this study

are more restrictive. Comparing the values of Table 7.1 and 7.2, we observe that with a finer discretization, the optimal filter radii values decrease slightly for low values of  $p$  and  $d$ . However, for higher values, the minimum required filter radii to achieve the desired solution accuracy are equal.

To investigate how this method of determining an optimal filter radius extends to 3D, a preliminary study has been performed using only the tensile test. Similar to Case I shown in Fig. 7.4, a 3D cube of unit dimensions is considered and the top surface is subjected to a distributed load of  $1 \text{ Nm}^{-3}$ . Apart from vertical displacements, motion is restricted along the other two spatial dimensions for the vertical surfaces of the cube, and the bottom surface is entirely fixed. The optimal filter radii for different values of  $p$  and  $d$  for this case are shown in Table 7.3. The observations are similar to those obtained in Tables 7.1 and 7.2. An interesting observation is that for 3D cases, the required filter radii are slightly lower than those obtained for 2D cases.

A general observation in Tables 7.1, 7.2 and 7.3 is that the required filter radius to guarantee reasonably accurate results only decreases slowly with  $p$ . For example, from Table 7.1, we see that with  $d = 4$  and elements with cubic shape functions ( $p = 3$ ), a filter radius of  $0.7h$  is required, resulting in a feature size of  $2r_{\min} = 1.4h$ . To decrease this feature size by a factor 2 (i.e. allow  $r_{\min} = 0.35h$ ), polynomial shape functions of order 6 or higher are needed with  $d = 6$ . It is questionable whether this is advantageous in terms of computational cost compared to realizing a similar feature size reduction in conventional TO, which would give a similar increase in DOFs but a sparser stiffness matrix contribution. This finding indicates that in the present MTO scheme, increased level of detail is associated with a considerable increase in computational cost, due to which the advantage of MTO could be lost over the traditional TO approach.

## 7.5. DISCUSSION

In this chapter, the disconnected material distributions observed in MTO formulations, denoted as QR-patterns, are investigated using several numerical experiments. From the presented results, it can be inferred that these patterns cannot be correctly modeled by the employed modeling scheme. They form as artefacts in compliance minimization as their stiffness is strongly overestimated. In general, the use of large numbers of design voxels allows the representation of high resolution designs which in turn leads to material features that require shape functions of very high polynomial degree to be correctly modeled.

Density filtering has been used to eliminate the QR-patterns and has been successful for various instances, however, as shown in this work, the use of density filters can have a negative impact and can raise the polynomial order of the shape functions desired for accurate modeling, thereby leading to even higher computational costs. Filtering imposes a restriction on the minimum feature size. The native design resolution given by the voxel size is lost, and without additional measures, blurred design boundaries are formed.

The single-element tests presented in Section 7.4.2 show that void strips give strongly overestimated stiffness. However, these do not always appear during optimization, and seem to be fully suppressed when a sufficiently large filter radius is used. One of the reasons that these thin strips of void are not formed could be that the optimization process

converges to different local optima, and these thin strips are not easily encountered. Moreover, the QR-patterns observed in unfiltered designs consist of quickly spatially-varying material patterns, and filtering removes such design patterns from the solution space. Although the thin strips of void can still be formed, the gradual density transition zone caused by density filtering make them less favorable in term of absolute stiffness compared to the connected designs. Nevertheless, the relative stiffness overestimation is still observed. When filtering is combined with Heaviside projection, the artefacts reappear [14]. This issue can be overcome for most of the cases using the modified Heaviside projection method [26], however, this approach cannot be guaranteed to work and should be used with caution [14].

Although with suitable filtering, the thin strips of void are not observed in the designs optimized for minimal compliance, it cannot be guaranteed that such issues will not be encountered for other more complex TO problems. In this study, as well as most other studies, the application of MTO has focused on compliance minimization problems. Groen *et al.* [14] also studied the application of MTO in a compliant mechanism optimization. Currently an incomplete understanding exists of the applicability of MTO to different optimization problems, and further research is required to support the generalization of MTO approaches. Of interest are for example problems involving eigenfrequencies or stress constraints, where it is yet unknown what interaction the multiresolution modeling will have with the optimization process. As a protective measure, such scenarios should be avoided in general. In this chapter, the MTO approach has been studied from a more conservative point of view. The extreme limitations of MTO are explored, so that the highest permissible design resolution can be achieved without encountering any artefacts.

There are additional aspects that need to be investigated further so as to assess the full capability of the MTO concept. A measure of benefit-versus-cost for increasing the polynomial order of the shape functions can be defined to determine whether the use of high  $p$  values for certain MTO configurations is beneficial or not. Groen *et al.* [14] have presented an empirical measure based on several numerical experiments. It would be of interest to explore further in this direction on a wider variety of MTO problems, and also look into theoretical aspects of the problem to establish more rigorous measure criteria. Another possible solution to look into could be to investigate the role of adaptive  $p$ -refinement in MTO. Locally increasing the value of  $p$  can reduce the artefacts while limiting the additional computational burden. For such methods, well defined refinement indicators are needed which can easily locate the regions at risk of developing QR-patterns.

In this chapter, we have studied in detail the fact that the QR-patterns in MTO originate from the known incapability of the polynomial shape functions in modeling the displacement field that accompanies a discontinuous material distribution. Methods such as XFEM, GFEM, *etc.* are well-established techniques that use enrichment functions to accurately model such nonsmooth or discontinuous displacement fields [21, 27]. XFEM has successfully been used in the context of TO (*e.g.*, [28]). However, the significantly high complexity of this approach restricts its attractiveness, and how to combine XFEM with MTO is an open research question. It may nevertheless present a way to rigorously prevent QR-patterns without sacrificing design resolution.

## 7.6. CONCLUSIONS

In this chapter, numerical artefacts arising in multiresolution topology optimization (MTO), denoted as QR-patterns, have been thoroughly studied and an explanation on their formation has been presented. Through several numerical tests, we observed that elements with discontinuous internal material distributions can show artificially low compliance when shape functions of insufficient polynomial degree are used. This deficiency of the finite element model has been observed before in higher-order multiresolution methods. It can be exploited during optimization, leading to unrealistic QR-patterns. While shape functions of very high polynomial degree can eliminate these artefacts, it is observed that the computational advantage of MTO over traditional TO could be lost due to the additional DOFs introduced. Further, the role of density filtering in MTO is investigated. It is shown that although filtering can reduce the QR-patterns for certain cases, it may not always be the solution to eliminate these artefacts and can sometimes be counterproductive.

Based on the investigations presented in this work, it can be questioned whether the methods based on decoupled design and analysis, in their current state, are suited for TO. Dedicated studies into particular problem types and other responses are needed to gain a fuller understanding on whether the filtering presents a universal remedy. It is expected that our findings will serve as the groundwork to define effective countermeasures to eliminate QR-patterns and help to achieve the goal of obtaining high resolution designs at low computational cost.

## REFERENCES

- [1] D. K. Gupta, M. Langelaar, and F. van Keulen, *QR-patterns: Numerical artefacts in multiresolution topology optimization*, Structural and Multidisciplinary Optimization **58**, 1335 (2018).
- [2] M. J. de Ruiter and F. van Keulen, *Topology optimization using a topology description function*, Structural and Multidisciplinary Optimization **26**, 406 (2004).
- [3] J. K. Guest and L. C. S. Genut, *Reducing dimensionality in topology optimization using adaptive design variable fields*, International Journal for Numerical Methods in Engineering **81**, 1019 (2010).
- [4] T. H. Nguyen, G. H. Paulino, J. Song, and C. H. Le, *A computational paradigm for multiresolution topology optimization (MTO)*, Structural and Multidisciplinary Optimization **41**, 525 (2010).
- [5] T. H. Nguyen, G. H. Paulino, J. Song, and C. H. Le, *Improving multiresolution topology optimization via multiple discretizations*, International Journal for Numerical Methods in Engineering **92**, 507 (2012).
- [6] J. Parvizian, A. Duster, and E. Rank, *Topology optimization using the finite cell method*, Optimization and Engineering **13** (2012).

- [7] Y. Wang, Z. Kang, and Q. He, *Adaptive topology optimization with independent error control for separated displacement and density fields*, *Comput. Struct.* **135**, 50 (2014).
- [8] T. H. Nguyen, C. H. Paulino, Le, and J. F. Hajjar, *Topology optimization using the p-version of the finite element method*, *Structural and Multidisciplinary Optimization* **56**, 571 (2017).
- [9] M. Nobel-Jørgensen, N. Aage, A. N. Christiansen, T. Igarashi, J. A. Baerentzen, and O. Sigmund, *3D interactive topology optimization on hand-held devices*, *Structural and Multidisciplinary Optimization* **51**, 1385 (2015).
- [10] A. Takezawa and M. Kitamura, *Geometrical design of thermoelectric generators based on topology optimization*, *International Journal for Numerical Methods in Engineering* **90**, 1363 (2012).
- [11] S. L. Vatanabe and E. C. N. Silva, *Design of Phononic Materials Using Multiresolution Topology Optimization*, in *Proceedings, ASME 2013 International Mechanical Engineering Congress and Exposition* (2013).
- [12] A. Sutradhar, J. Park, D. Carrau, T. H. Nguyen, M. J. Miller, and G. H. Paulino, *Designing patient-specific 3D printed craniofacial implants using a novel topology optimization method*, *Med. Biol. Eng. Comput.* **54**, 1123 (2016).
- [13] J. Guest, J. Prevost, and T. Belytschko, *Achieving minimum length scale in topology optimization using nodal design variables and projection functions*, *International Journal for Numerical Methods in Engineering* **61**, 238 (2004).
- [14] J. P. Groen, M. Langelaar, O. Sigmund, and M. Ruess, *Higher-order multi-resolution topology optimization using the finite cell method*, *International Journal for Numerical Methods in Engineering* **110**, 903 (2017).
- [15] D. K. Gupta, M. Langelaar, and F. van Keulen, *Combined mesh and penalization adaptivity based topology optimization*, in *Proc. 57th AIAA/ASCE/AHS/ASC Structures, Structural Dynamics, and Materials Conference*, (AIAA SciTech Forum, (AIAA 2016-0943), 2016).
- [16] C. S. Jog and R. B. Haber, *Stability of finite element models for distributed-parameter optimization and topology design*, *Comput. Method. Appl. M.* **130**, 203 (1996).
- [17] M. Jouliaian and A. Düster, *Local enrichment of the finite cell method for problems with material interfaces*, *Comput. Mech.* **52**, 741 (2013).
- [18] M. Jouliaian and A. Düster, *The hp-d version of the finite cell method with local enrichment for multiscale problems*, *Proc. Appl. Math. Mech.* **13**, 259 (2013).
- [19] S. Kollmannsberger, A. Özcan, J. Baiges, M. Ruess, E. Rank, and A. Reali, *Parameter-free, weak imposition of Dirichlet boundary conditions and coupling of trimmed and non-conforming patches*, *Int. J. Numer. Meth. Eng.* **101**, 670 (2015).

- [20] N. Zander, T. Bog, S. Kollmannsberger, D. Schillinger, and E. Rank, *Multi-level hp-adaptivity: high-order mesh adaptivity without the difficulties of constraining hanging nodes*, *Comput. Mech.* **55**, 499 (2015).
- [21] N. Moës, J. Dolbow, and T. Belytschko, *A finite element method for crack growth without remeshing*, *Int. J. Numer. Meth. Eng.* **46**, 131 (1999).
- [22] T. E. Bruns and D. A. Tortorelli, *Topology optimization of nonlinear elastic structures and compliant mechanisms*, *Comput. Method. Appl. M.* **190**, 3443 (2001).
- [23] M. P. Bendsøe, *Optimal shape design as a material distribution problem*, *Structural Optimization* **1**, 193 (1989).
- [24] A. Díaz and O. Sigmund, *Checkerboard patterns in layout optimization*, *Struct. O.* **10**, 40 (1995).
- [25] O. Sigmund, *On the design of compliant mechanisms using topology optimization*. *Mech. Struct. Mach.* **25**, 493 (1997).
- [26] O. Sigmund, *Morphology-based black and white filters for topology optimization*. *Structural and Multidisciplinary Optimization* **33**, 401 (2007).
- [27] T. Strouboulis, K. Copps, and I. Babuska, *The generalized finite element method*, *Computer Methods in Applied Mechanics and Engineering* **190**, 4081 (2001).
- [28] S. Kreissl and K. Maute, *Levelset based fluid topology optimization using the extended finite element method*, *Struct. Multidiscip. O.* **46**, 311 (2012).

# 8

## DESIGN AND ANALYSIS ADAPTIVITY IN MTO

*Multiresolution topology optimization (MTO) methods involve decoupling of the design and analysis discretizations, such that a high-resolution design can be obtained at relatively low analysis costs. Recent studies have shown that the MTO method can be approximately 3 and 30 times faster than the traditional topology optimization method for 2D and 3D problems, respectively.*

*To further exploit the potential of decoupling analysis and design, we propose a  $dp$ -adaptive MTO method, which involves locally increasing/decreasing the shape function orders ( $p$ ) and design resolution ( $d$ ). The adaptive refinement/coarsening is performed using a composite refinement indicator which includes criteria based on analysis error, presence of intermediate densities as well as the occurrence of design artefacts referred to as QR-patterns. While standard MTO must rely on filtering to suppress QR-patterns, the proposed adaptive method ensures efficiently that these artefacts are suppressed in the final design, without sacrificing the design resolution. The applicability of the  $dp$ -adaptive MTO method is demonstrated on several 2D mechanical design problems. For all the cases, significant speed-ups in computational time are obtained. In particular for design problems involving low material volume fractions, speed-ups of up to a factor of 10 can be obtained over the conventional MTO method.*

### 8.1. INTRODUCTION

Topology optimization (TO) can be described as an approach that optimally distributes material in a specified domain under a set of constraints, such that the performance function of the structure achieves a maximum [2]. In the past two decades, TO has widely been used in various academic and industrial disciplines. For a survey on the

---

This chapter is based on an article submitted for consideration in International Journal for Numerical Methods in Engineering [1].

latest developments in TO as well as its recent applications, see the review papers by Sigmund and Maute [3], van Dijk *et al.* [4], and Deaton and Grandhi [5].

Typically, in popular density-based TO, the domain is discretized into a finite set of elements and a density value is associated with every finite element [2]. The density of an element indicates the volume fraction of that element filled with a certain amount of material, and can vary from 0 (void) to 1 (solid). These density values are optimized during the course of optimization. Since in traditional approaches, density is assumed to be constant inside an element, a large number of finite elements as well as associated design variables are needed to obtain a well defined design with the desired structural features and boundary resolution, especially for three-dimensional (3D) problems [6]. The computational costs associated with TO are mainly determined by the used finite element analysis (FEA) and associated sensitivity analysis, which limits the number of elements and consequently the design resolution.

With the growing popularity of TO, a clear need exists for improved methods that can deliver high quality results at the lowest computational cost. Various approaches have been proposed in the past to reduce the computational costs associated with solving large-scale TO problems [7–13]. These focused mainly on improving the efficiency of solving the FEA systems of equations. Another possibility that has been explored in the existing literature is to modify the way the FEA system is defined in the first place through the use of adaptive FEA formulations. Popular adaptive FEA approaches are *h*-refinement and *p*-refinement [14]. However, the standard formulations for these methods use FEA based error criteria for adaptation of the mesh. These by themselves are not well suited for TO, as they do not take the need for refinement based on design considerations into account [15]. In the final designs obtained from TO, it is desirable that the material distribution is clearly defined. Thus, the refinement criterion used in TO should depend on the material distribution as well.

Maute and Ramm [16] proposed an adaptive mesh refinement (AMR) approach which involved optimizing the topology of the design followed by approximating the boundaries using cubic or Bézier splines. After every cycle of TO, shape optimization was performed followed by remeshing of the solid domain. The whole process was repeated over a series of cycles and the new mesh generated at the end of each cycle was used as the domain for the TO problem of the next cycle. van Keulen and Hinton [17] for the first time combined the TO with an FEA error based refinement strategy. The recovery of material, in their approach, was controlled by the stress level in the adjacent elements and mesh densities were determined using (a) the standard Zienkiewicz-Zhu error estimator and (b) the shortest distance to the material-void boundary. Both these approaches involved remeshing the whole domain at the end of each cycle, which was computationally expensive.

Costa and Alves [18] presented an AMR strategy which involved refining only the solid material region. For TO problems, intermediate densities are found to be prevalent near the boundaries. On the assumption that refinement of these regions can reduce the intermediate densities, Stainko [19] proposed to refine the region only around the material-void boundary. Bruggi and Verani [15] progressed in the direction of the work proposed by [17], and proposed a goal-based AMR strategy that properly guides the progression of refinement and coarsening in TO. For refinement or coarsening, a dual-

weighted residual based FEA indicator as well as a heuristic density-gradient based indicator were used. While most of these methods helped to achieve the required  $h$ -adaptivity in TO, the fixed choice of density values for refinement at every cycle of TO led to excessive numbers of elements getting refined, thereby leading to undesired increase in computational costs. Gupta *et al.* [20] proposed a heuristic scheme to control the refinement or coarsening bounds at every cycle of TO. The proposed scheme was combined with  $h$ -refinement and very clear material descriptions with low gray regions were obtained. Other adaptive formulations involving  $h$ -refinement or a similar approach include adaptive refinement of polygonal elements [21, 22], combining a continuous density field representation with adaptive mesh refinement [23] and efficient TO based on adaptive quadtree structures [24].

Another possible way to reduce FEA costs is the adaptive  $p$ -refinement, as stated earlier, where the mesh topology remains the same. Additionally, for smooth problems, the accuracy of  $p$ -refinement is dramatically higher than that of  $h$ -refinement for the same computational costs [14]. Increasing the polynomial order of the shape functions gives an exponential rate of convergence. Other advantages of  $p$ -refinement are its robustness against locking effects and high aspect ratios [25]. However, due to the fact that the conventional TO approaches assume an elementwise-constant density distribution, using higher-order shape functions inside a finite element is not an efficient approach. Although it reduces the FEA error to some extent, it cannot improve the material definition within the element.

The recently proposed Finite Cell Method (FCM) offers new perspectives to overcome this limitation [26]. FCM is an FE-based modeling approach where the analysis mesh is decoupled from the material distribution domain and higher order shape functions are used [25]. This approach can handle a material-void boundary within an element through the use of appropriate integration schemes. Recently, a similar approach was proposed by Nguyen *et al.* [27] for TO, termed as multiresolution topology optimization (MTO), where the analysis and design meshes are decoupled. Here, design mesh denotes the distribution of the design points which are used to generate the material distribution. The density values associated with these points serve as optimization parameters for TO. In MTO, a coarse analysis mesh was used and inside every finite element, a large number of design points were positioned. This allowed a high resolution density distribution inside every finite element, unlike an elementwise-constant density distribution as in standard TO approaches. In spite of using low order shape functions and coarse elements, the method is still capable of generating high resolution structures, albeit with reduced analysis accuracy. To increase this accuracy, recently a  $p$ -version of MTO has been proposed, where the potential of higher order polynomial shape functions has been investigated in the context of MTO [28]. Other approaches based on a similar concept were further presented in [29, 30]. Note that in [27] and other research papers thereafter, the term ‘multi-resolution’ refers to allowing the possibility for multiple different design resolutions for the same choice of analysis resolution. In line with these works, we also refer to our formulation as an MTO approach.

It is important to note that although the design and analysis meshes can be decoupled, the iterative updates of the design variables in TO are based on the analysis results. In a recent study, we showed that for a given finite element mesh and polynomial order

of FE shape functions, there exists an upper bound on the number of design variables that can be used in TO [31]. A density resolution beyond this threshold cannot be fully captured by the FEA and can lead to issues such as nonuniqueness. For certain cases, it can also lead to poorly performing designs. Thus, when using large numbers of design points inside an element, both for analysis accuracy as well as well-posedness of the TO problem, higher order shape functions and corresponding numerical integration schemes need to be chosen.

Parvizian *et al.* [26] proposed a TO strategy based on FCM where a coarse analysis mesh with high order shape functions as well as a high order numerical integration scheme is used. Although expected to give more reliable results, FCM-based TO may not necessarily satisfy the bounds proposed in [31], which implies it might still be prone to numerical issues. Groen *et al.* [32] presented results related to rigorous numerical investigations of FCM-based TO. Their observations show close resemblance with those in [31]. Also, the authors showed that using FCM-based TO, remarkable speed-ups of more than 3- and 60-folds for 2D and 3D problems, respectively, could be obtained over the traditional TO approach. However, for certain configurations of FCM-based TO, it is possible that the design consists of ‘QR-patterns’, comprising disconnected or loosely connected material parts which cannot be correctly modeled by the employed modeling scheme [33]. Use of density filtering with a sufficient filter radius was found to suppress the QR-pattern artifacts [28, 31, 32], but has the undesired consequence of reducing the design resolution. Applying  $p$ -refinement was also found to reduce the issue, but rapidly raises the computational cost.

Hereafter, we use the term MTO to refer to all the TO approaches (including FCM-based TO) where the design and analysis discretizations are decoupled. The goal of MTO approaches is to obtain high resolution, high quality designs at low analysis costs. Possible ways to increase resolution versus cost could include using a finely discretized density mesh, reducing the filter size, using shape functions of low polynomial order to describe the state field, *etc.* However, each of these approaches has certain limitations which can adversely affect the analysis accuracy. Using too many density cells and low polynomial order shape functions can lead to nonuniqueness in the design field and result in numerical instability [31]. Reducing the filter size can lead to the formation of QR-patterns, which are numerical artefacts and can affect the model accuracy [32, 33]. Using higher order shape functions can circumvent these problems, however, the analysis related costs are significantly increased. Due to this, the advantage of MTO over the traditional TO approach could be lost. In an MTO setting, this requires considering adaptivity both of the analysis and the design, which thus far has not been explored.

In this chapter, we present an adaptive MTO approach that enables a better balance between resolution and computational costs. Local adaptation is applied to both the analysis and the design description, which allows computational effort to be concentrated in regions of interest. Moreover, the adaptivity allows rigorous prevention of QR-pattern artefacts. We coin the term ‘ $dp$ -adaptivity’, an adaptive multiresolution TO scheme where both the design resolution  $d$  and FE polynomial order  $p$  can be locally adapted based on certain refinement/coarsening criteria. Here, the symbol ‘ $d$ ’ should not be confused with the one in  $hp$ - $d$  adaptivity, where it refers to domain decomposition and mesh overlaying [34]. It is assumed that computational costs are the limit-

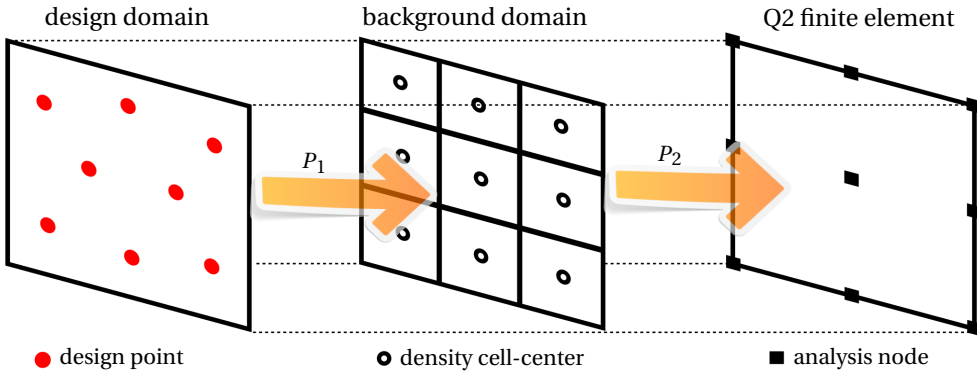


Figure 8.1: Schematic representation of a Q2/d8 MTO element comprising 3 linked overlapping domains. These domains represent a design domain with 8 design points (left) and a Q2 finite element (right), with a background distribution of  $3 \times 3$  density cells (middle). Here,  $P_1$  and  $P_2$  denote the projections from the design to background domain and from background domain to the finite element, respectively. The design points are distributed in the domain using a variant of the  $k$ -means clustering approach (Appendix 8.A).

ing factor, and that the manufacturing-imposed length scale is at or below the smallest lengthscale that can be reached by the adaptive TO process. Our approach can obtain high resolution representations of the material field at significantly lower computational costs compared to non-adaptive MTO approaches. At the same time, by jointly adapting design and FE discretization, we ensure that the bounds proposed in [31] are satisfied and instability issues are avoided. For refinement/coarsening after every TO cycle, analysis error, correctness of the design as well as the error associated with QR-patterns are used. For this purpose, we also propose a novel indicator. Various numerical tests are conducted to analyze the capabilities of the method as well as its robustness. The scope of this chapter is restricted to linear elastostatic problems and the material is assumed to be isotropic, however, the method is expected to be applicable to a wider range of problems.

In the following section, theory of multiresolution TO is presented followed by discussions related to choice of design distribution, polynomial orders and numerical integration schemes. Section 8.3 subsequently presents the theory and formulation for the proposed  $dp$ -adaptivity approach. The applicability of this method is presented on a set of numerical examples (Section 8.4), and discussion and related conclusions are stated in Section 8.5 and 8.6, respectively.

## 8.2. MULTIREOLUTION TOPOLOGY OPTIMIZATION

### 8.2.1. DOMAIN AND VARIABLE DEFINITIONS

In this chapter, we propose an adaptive MTO formulation based on selective refinement and coarsening of the design as well as analysis domains. First a conceptual description is provided, whereas the mathematical formulation follows in Section 8.2.2. The proposed approach uses three meshes: design mesh, background mesh (comprising density cells) and analysis mesh. The analysis mesh is used to determine the solution of the

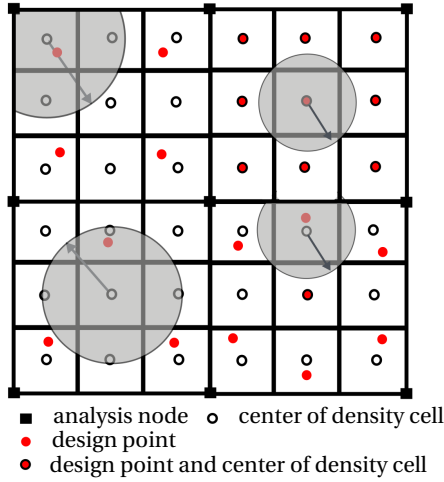


Figure 8.2: Schematic representation of projection  $P_1$  illustrating the projection of density values from the design points in the design mesh to the centers of density cells of the background domain. Four projection regions are indicated in gray. Note that these projections are localized and operate on the design points and the density cell-centers of the same element. Here, the four MTO elements from top-left to bottom-right consist of 4, 9, 3 and 7 design points, respectively. The densities at the centers of the gray projection domains (denoted by  $\circ$ ) shown in each MTO element are computed from contributions of all design points (denoted by  $\bullet$ ) of the same MTO element within its projection domain.

8

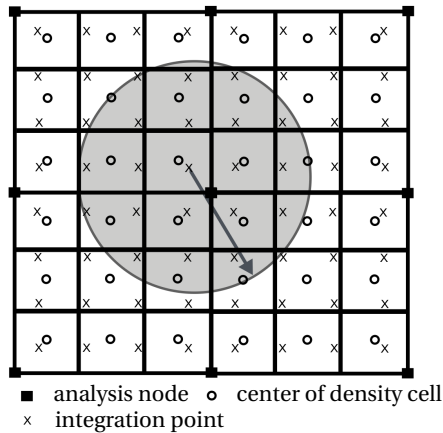


Figure 8.3: Schematic representation of projection  $P_2$  which projects density values from the background mesh to the integration points of the analysis cell. The problem domain is discretized using  $2 \times 2$  MTO elements composed of Q1 finite elements and  $3 \times 3$  density cells per element. For numerical integration, a  $4 \times 4$  Gaussian quadrature rule is used. The density at the integration point at the center of the gray projection domain (denoted by  $\times$ ) is computed from contributions of all background density cell center points (denoted by  $\circ$ ) within its projection domain.

physics at hand (*e.g.* displacement field) and the design mesh represents the distribution of design points in the domain. For simplicity, we use a structured mesh setting, as often used in topology optimization. In an adaptive setting, the analysis resolution and distribution of design points in the domain can be non-uniform. The background mesh is added to provide a convenient link between the analysis and design meshes. More details related to the role of the background mesh follow later in this section.

For practical implementation, we introduce the notion of MTO elements. An MTO element comprises a finite element, a set of design points and an overlapping background element comprising a regular grid of density cells. They all occupy the same spatial domain, and this ordered arrangement is chosen to simplify implementation in an existing FE framework. For example, Fig. 8.1 shows the schematic representation of a Q2/d8 MTO element using a Q2 (bilinear quadrilateral) finite element and consisting of 8 design points distributed non-uniformly in the domain. The overlapping background element comprises  $3 \times 3$  density cells. A density design variable is associated with each design point. During optimization, these density variables are updated at every iteration based on the response functions and the corresponding design sensitivities.

To generate suitably uniform distributions of design points within an element for any number of design variables, a variant of the  $k$ -means clustering method is used [35, 36]. This approach divides the design domain into  $k$  segments (clusters) with roughly equal areas. The design points are assumed to be located at the centroids of these clusters. For self-containment, the details of the method are discussed in Appendix 8.A. We use this approach to obtain an approximately uniform distribution of any given number of design points in the MTO element domain. The achievable resolution limit of the design depends on the spacing between the design points. For a given number of design points and without a priori knowledge of the optimal design, a uniform distribution allows the best possible resolution. Note here that the proposed adaptive MTO approach is independent of the choice of methodology for the distribution of design points, and any other method to distribute points in a domain can be applied, including a set of predefined patterns.

The aligned background mesh consists of a uniform grid of equally-sized density cells in the whole domain, such that a certain number of these cells overlap with every finite element. For these density cells, the respective finite element is referred as the parent analysis cell. For example, in Fig. 8.1,  $3 \times 3$  density cells overlap with the parent Q2 finite element (analysis cell). The density is defined at the centroid of every density cell and is assumed to be constant inside it. This density is obtained from the design mesh through a localized projection operation.

The density inside any density cell of the background mesh is calculated using projection  $P_1$  (as shown in Fig. 8.1, defined in detail in Section 8.2.2), and only those design points are used which lie within the same MTO element. The role of the localized projection is to define density values in all the density cells of the respective MTO element. The projection is restricted to the considered MTO element for two reasons: (i) to minimize the associated loss in design resolution of MTO elements adjacent to other MTO elements with fewer design points and (ii) to enable element-level implementation. While choosing the local projection radius  $P_1$ , it needs to be ensured that the density inside each density cell can be defined. The mathematical details related to choosing this pro-

jection radius are provided in Section 8.2.2. An example is presented in Fig. 8.2, which shows a domain of  $2 \times 2$  MTO elements, each comprising a Q1 finite element and  $3 \times 3$  density cells. As can be seen, the distribution of design points can be non-uniform. The four MTO elements from top-left to bottom-right consist of 4, 9, 3, and 7 design points, respectively. In the bottom-right MTO element shown in Fig. 8.2, a partial projection circle can be seen, which is due to the fact that the projection is restricted to within this MTO element. Mathematical details related to projection  $P_2$  are provided in Section 8.2.2.

The stiffness matrix for every MTO element is obtained by numerical integration using a Gaussian quadrature scheme. For this purpose, the stiffness matrix contribution at the integration point needs to be known, which in turn requires knowing the density value at that point. This density value, referred further as ‘projected density’, is obtained through a projection on the background mesh, denoted by  $P_2$  (Fig. 8.1). Fig. 8.3 illustrates how these density values are computed. It shows a mesh of  $2 \times 2$  MTO elements, comprising Q1 finite elements and the corresponding background domain with  $3 \times 3$  density cells per element. Here, ‘Q1’ refers to quadrilateral finite elements with shape functions of polynomial order 1. Similar to the approach described in [27, 28, 32], the projected densities are computed using a distance-weighted projection of design densities found in the neighborhood of a certain radius  $R$  over the background mesh. In this work, density filtering is used for the projection [37].

The use of the background mesh facilitates  $d$ -adaptivity, *i.e.* the use of different numbers of design points in adjacent elements. In the absence of the background mesh, the non-uniform design field when directly projected on the analysis mesh, can lead to irregular boundary features which are not desired. The design variables are not directly linked to the density cells of the background mesh, because it would not allow an adaptive formulation anymore. Moreover, such a formulation would significantly increase the number of design variables and would lead to nonuniqueness related issues [31]. The background mesh provides the flexibility of having a reference discretization independent of the number of design variables. Moreover, it simplifies the numerical integration required for the stiffness matrix.

### 8.2.2. MATHEMATICAL FORMULATION

In this chapter, the applicability of a  $dp$ -adaptive MTO approach is demonstrated on mechanical problems of two different types: minimum compliance and compliant mechanism.

For the chosen problems, the problem statement for TO can be expressed as

$$\begin{aligned}
 \min_{\boldsymbol{\rho}} \mathcal{J}(\mathbf{u}, \boldsymbol{\rho}) &= \mathbf{z}^\top \mathbf{u}, \\
 \text{s.t. } \mathbf{K}\mathbf{u} &= \mathbf{f}, \\
 V(\boldsymbol{\rho}) &\leq V_0, \\
 \mathbf{0} &\leq \boldsymbol{\rho} \leq \mathbf{1},
 \end{aligned} \tag{8.1}$$

where,  $\mathcal{J}(\cdot)$  denotes the objective functional, and  $\mathbf{K}$ ,  $\mathbf{u}$  and  $\mathbf{f}$  denote the global stiffness matrix, displacement vector and load vector, respectively. The vector  $\mathbf{z}$  is chosen based on the type of problem and will be discussed in Section 8.4.1. The volume constraint

restricts the total volume fraction of the given material to be less than certain predefined volume  $V_0$ .

Next, the details related to various steps associated with the proposed multiresolution modeling approach are described. The matrix  $\mathbf{K}$  in Eq. 8.1 is obtained from the global assembly of the element stiffness matrices  $\mathbf{K}_e$ , which can be expressed as

$$\mathbf{K}_e = \int_{\Omega_e} \mathbf{B}^\top \mathbf{D} \mathbf{B} d\Omega = \sum_{i=1}^{N_g} \mathbf{B}_i^\top \mathbf{D}_i \mathbf{B}_i w_i, \quad (8.2)$$

where  $\mathbf{B}$  and  $\mathbf{D}$  denote the strain-displacement matrix and constitutive matrix, respectively, and  $N_g$  is the number of integration points. More details related to the choice of numerical integration are discussed in Appendix 8.B. The subscript  $i$  refers to the  $i^{\text{th}}$  integration point and  $w_i$  denotes the respective integration weight. The construction of the  $\mathbf{D}$  matrix depends on the choice of the material interpolation model as well as the material itself. In this work, solid isotropic material interpolation (SIMP) model [2] is used such that

$$\mathbf{D}_i = (E_{\min} + \tilde{\rho}_i^q (E_0 - E_{\min})) \mathbf{D}_0, \quad (8.3)$$

where  $E_0$  is the Young's modulus of the solid material and  $E_{\min}$  is a very small value (typically  $10^{-9} E_0$ ) used to avoid singularity of the system stiffness matrix. Also,  $\tilde{\rho}_i$  denotes the density calculated at the  $i^{\text{th}}$  integration point,  $q$  is the penalization power and  $\mathbf{D}_0$  denotes constitutive matrix normalized by the Young's modulus.

The densities at the integration points are calculated by projecting density values from the density cells in the background mesh (Fig 8.3). For this purpose, we employ a linear projection approach for  $P_2$  based on the density filtering method which is widely used in TO [37]. Mathematically, it can be stated as

$$\tilde{\rho}_i = \frac{1}{\sum_{j=1}^{n_{\hat{\rho}}} H_{ij}} \sum_{j=1}^{n_{\hat{\rho}}} H_{ij} \hat{\rho}_j, \quad (8.4)$$

where  $\hat{\rho}$  refers to density values for the cells contained in the background mesh with their centers lying within a distance  $R$  from the corresponding integration point (Fig. 8.3), and their number is denoted by  $n_{\hat{\rho}}$ . Here, terms  $H_{ij}$  reduce linearly with distance from the integration point, *i.e.*,

$$H_{ij} = R - \text{dist}(i, j), \quad (8.5)$$

where  $\text{dist}(\cdot)$  denotes the Euclidean distance operator.

As stated in Section 8.2.1, the background mesh densities are calculated using the  $P_2$  projection from the design mesh to the background mesh. For the  $p^{\text{th}}$  MTO element, the density of the  $q^{\text{th}}$  density cell is given as

$$\hat{\rho}_q^{(p)} = \frac{1}{\sum_{s=1}^{n_p} h_{qs}} \sum_{s=1}^{n_p} h_{qs} \rho_s, \quad (8.6)$$

where,  $\rho_s$  refers to the density value associated with the  $s^{\text{th}}$  design point in the design domain contained within the  $p^{\text{th}}$  MTO element, and lying within a distance  $r_p$  from the

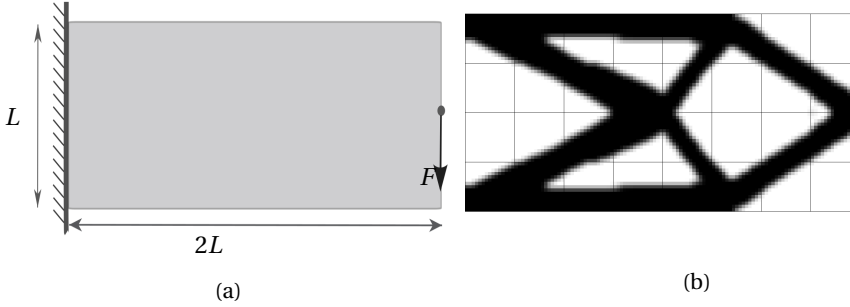


Figure 8.4: (a) Example of a cantilever beam subjected to a point load, and (b) the optimized design obtained using MTO for compliance minimization using  $8 \times 4$  Q10/d225 elements and  $R = 0.13h$ . Here, Q10/d225 refers to a quadrilateral finite element with shape functions of polynomial order 10 and 225 design points.

centroid of its  $q^{\text{th}}$  density cell. The number of such design points is denoted by  $n_p$ , and  $r_p$  is the radius of the projection for the  $p^{\text{th}}$  element (Fig. 8.2). Here,  $h_{qs}$  is defined as

$$h_{qs} = r_p - \text{dist}(q, s). \quad (8.7)$$

As stated earlier, the projection radius  $r_p$  needs to be chosen such that it is as small as possible, however, large enough to define densities for all the density cells that correspond to the respective element. Here, we define it as

$$r_p = 1.04(dim)^{0.5} \frac{L_p}{\lceil d^{1/dim} \rceil}, \quad (8.8)$$

where  $dim$  denotes problem dimension, and  $L_p$  is the edge-length of the  $p^{\text{th}}$  MTO element. The operator  $\lceil \cdot \rceil$  denotes ceiling function which rounds the contained floating-point number to the nearest greater integer value. The term  $\frac{L_p}{\lceil d^{1/dim} \rceil}$  refers to edge-length of the density cells. Next, to obtain a projection length slightly larger than the diagonal, we multiply by  $1.04(dim)^{0.5}$ . Note that Eq. 8.8 has been obtained empirically through observations based on various design distributions obtained using the  $k$ -means clustering approach. For other approaches of choosing the locations of design points, where for any value of  $d$ , the distance between the design points can be provided mathematically, it is possible that even lower values of  $r_p$  work. Lower values of  $r_p$  can help to further reduce the loss in design resolution caused due to the choice of localized projection  $P_1$ , and this could be a potential direction for future research.

Fig. 8.4a shows an example of a cantilever beam subjected to a point load, which we will use to illustrate the MTO concept. The domain is discretized using  $8 \times 4$  finite elements. For each MTO element, 225 design points, distributed in a square grid of  $15 \times 15$ , are used to represent the design field. The polynomial order of the shape functions is chosen to be 10. The choice of shape functions is made in a way that the element-level uniqueness bounds defined in [31] are not violated. As per the uniqueness bound, the number of design points influencing any finite element cannot be greater than the number of deformation modes of that element. With  $p$  equal to 10, the number of deformation modes is 239, which is greater than 225. With  $p$  and  $d$  equal to 10 and 225, respectively, the MTO elements are referred as Q10/d225 type elements. For this example, the

projection radius  $R$  is set to 0.13 times the element-length, which is equivalent to the size of 2 density cells.

Fig. 8.4b shows the optimized design obtained using the outlined MTO configuration. Clearly, the employed MTO approach allows the definition of higher resolution material features on relatively coarser MTO elements. However, in Fig. 8.4b, there are parts of the domain where even lower-order elements and lower design resolution are sufficient. For example, there are totally void MTO elements, where even linear shape functions with only one design point can be used. Clearly, the computational time of the MTO approach can be reduced by exploiting this fact in an efficient way, and in the next section, we propose an approach to do this.

## 8.3. *dp*-ADAPTIVITY

### 8.3.1. GENERAL DESCRIPTION OF THE METHOD

We present here a *dp*-adaptive version of the MTO method which is capable of enhancing further the ratio between the design resolution and analysis cost compared to non-adaptive MTO. The proposed MTO method efficiently distributes the design variables and locally adapts (increases/decreases) the polynomial order of the shape functions. A three-part refinement criterion is defined to select the cells to be refined/coarsened. Note that although the term ‘refinement’ is more commonly used throughout this chapter, we implicitly refer to coarsening (reducing the values of  $p$  and  $d$ ) as well. Here, ‘refined’ cells are those where additional design points are inserted, or the polynomial order of the shape functions is increased, or both. Similarly, ‘coarsened’ cells are the ones where the design resolution (number of design points) is reduced, or the analysis resolution (shape function order) is reduced, or both. With an adaptive formulation, fewer design variables as well as analysis nodes are used, which provides a computational advantage over the conventional MTO method.

At the start of *dp*-adaptive MTO, a cycle of TO is performed, using a certain initial uniform design- and FE-discretization. A ‘TO cycle’ refers to the entire process from starting with an initial design and optimizing it over a number of iterations (or up to a certain stopping threshold) to reaching an improved design. During a TO cycle, the shape function order and design points of all elements remain fixed. In the optimized design, refinement and coarsening zones are subsequently identified based on an integrated criterion comprising an analysis error-based indicator, a density-based indicator, and a QR-based indicator. Here, QR-error refers to the error due to the incapability of the chosen shape function in modeling the displacement field arising from a high-resolution density representation allowed within that element [33]. More details related to these indicators are discussed in Section 8.3.2.

All steps from analyzing the design for refinement to updating the  $d$  and  $p$  values for the whole domain, constitute one cycle of *dp*-adaptivity. The general structure of a *dp*-adaptive MTO cycle is as follows:

1. Perform optimization of an MTO problem with fixed  $p$  and  $d$  values.
2. Adapt  $p$  values based on analysis error indicator.
3. Adapt  $p$  and  $d$  values based on density-based criterion.

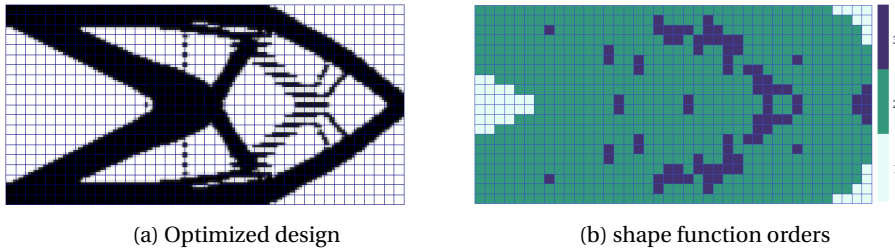


Figure 8.5: Optimized design (left), and the distribution of shape function orders (right) obtained from adaptive refinement controlled by only analysis-based refinement indicator for a cantilever subjected to point load, as shown in Fig. 8.4a. The optimized design clearly shows typical artefacts (QR-patterns) of disconnected structural features. The initial mesh comprises  $40 \times 20$  Q2 finite elements with 16 design points and  $4 \times 4$  density cells per element. Based on the ranking of analysis-based refinement indicator values, top 10% and bottom 5% of the MTO elements have been chosen for refinement and coarsening, respectively.

4. Update  $p$  values to reduce QR-errors in every element.

With the new  $dp$ -adapted mesh, the next cycle of TO is performed. Section 8.3.3 below describes each of the above steps in detail.

### 8.3.2. REFINEMENT CRITERIA

In this section, the details related to the three indicators used in our refinement criterion are provided. As stated earlier, although the term ‘refinement’ is frequently used, we implicitly refer to ‘coarsening’ as well in our adaptive approach. Note that although here certain choices have been made for the refinement indicators, the  $dp$ -adaptive scheme in itself is not dependent on the choice of refinement indicator, and can be coupled with other appropriate indicators as well.

#### ANALYSIS-BASED REFINEMENT INDICATOR

For the purpose of analyzing the modeling related error, the Kelly error estimator has been used [38]. This error indicator analyzes the jump in the gradient of the solution  $\mathbf{u}$  across any face (edge in 2D) of adjacent elements. The error for any element is calculated in a relative sense by integrating the error in the gradient jump across all faces of the respective element. Based on the relative error estimate, only a certain fraction of the MTO elements is selected for updating the orders of the polynomials ( $p$ ). This error estimator can also be understood as a gradient recovery estimator, for details on this aspect, see [39].

There are two reasons to choose the Kelly error estimator instead of more sophisticated recent approaches, e.g., goal-oriented error estimators [15, 40]. The analysis error comprises primarily of two components: *element residual* and *edge residual* [40]. Element residual refers to the error in approximating the gradient field within the element, and edge residual denotes the jumps in gradient across the element edges. The element residual is being taken into account through the QR-error analysis. Thus, the analysis indicator needs to only look at the edge residual term. Moreover, our approach requires only a relative error estimate and not the exact error itself. The use of Kelly error estimator suffices both these requirements. Also, this error estimator is simple to implement

and the associated computational costs are negligible.

For the purpose of ranking the elements for  $p$ -adaptivity based on the Kelly error estimator, the analysis residual error vector  $\Gamma^a$  needs to be defined. For the  $i^{\text{th}}$  MTO element,  $\Gamma_i^a$  can be computed as:

$$\Gamma_i^a = \sum_{F \in \partial i} c_F \int_{\partial i_F} \left[ \frac{\partial \mathbf{u}}{\partial \mathbf{n}} \right]^2 d\mathbf{s}, \quad (8.9)$$

where,  $F$  refers to a face (edge in 2D) of the element and operator  $[\cdot]$  denotes the jump in the argument across face  $F$ . Also,  $\partial i$  denotes the set of all faces of the element. The constant term  $c_F$  is set to  $\frac{h_F}{2p_F}$ , where  $h_F$  is the element diagonal and  $p_F$  denotes the maximum among the polynomial degrees of the adjacent elements [41]. The residual errors  $\Gamma^a$  are ranked, and the top 10% and bottom 5% of the elements are selected for increasing and decreasing the  $p$  values, respectively.

For illustration purposes, we perform a partial adaptive MTO run on the problem shown in Fig. 8.4a. Fig. 8.5a shows the optimized cantilever beam design obtained for this problem after one TO cycle. The design has been obtained on a mesh of  $40 \times 20$  Q2 finite elements with  $4 \times 4$  design points per element. The optimized design clearly shows typical artefacts (QR-patterns) of disconnected structural features. Fig. 8.5b shows the distribution of polynomial shape function orders obtained from  $p$ -adaptivity controlled by only the analysis-based refinement indicator. It is observed that coarsening (reduction in  $p$ ) has mainly occurred in the void cells which are far from material-void boundaries. This is because the jumps in displacement gradients across the edges for these elements are zero. For refinement (increase in  $p$ ), the elements at the boundary have been preferred.

#### DENSITY-BASED REFINEMENT INDICATOR

The density-based refinement indicator aims at adaptively choosing MTO elements for refinement or coarsening in way that over a number of cycles, the intermediate densities are reduced, and a crisp and high-resolution boundary representation is obtained. For this purpose, the refinement indicator proposed in [20] is adapted for our problem and discussed here. This indicator chooses a certain element for refinement/coarsening based on the density value inside that element. For every cycle of adaptivity, refinement (coarsening) density intervals are defined and associated elements are flagged. We adopt this indicator to regulate the number of design points in each MTO element, based on spatial design information specified by the density values of the voxels of the background mesh. The way this indicator affects the number of design variables is discussed in Section 8.3.3, here we focus on the definition of the indicator itself.

Fig. 8.6 shows the refinement ( $r_l \leq \rho \leq r_u$ ) and coarsening ( $\rho < c_l$  or  $\rho > c_u$ ) intervals as a function of adaptive cycle. Unlike the other refinement indicators, here the refinement (coarsening) bounds are chosen not to remain constant. Rather, following [20], the range of density values to be chosen for every adaptive cycle increases. Based on the chosen stopping criterion used for every cycle of TO, it is possible that significant parts of the designs obtained during initial cycles consist of intermediate density values. In such scenarios, selecting all gray (intermediate density) elements for refinement can lead to excessive refinement during the initial cycles, which in turn leads to undesired increase

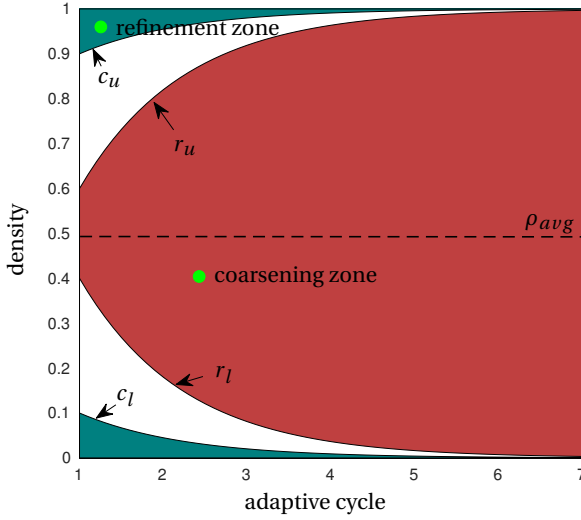


Figure 8.6: Bounds for the design refinement indicator as a function of the adaptive cycle [20].

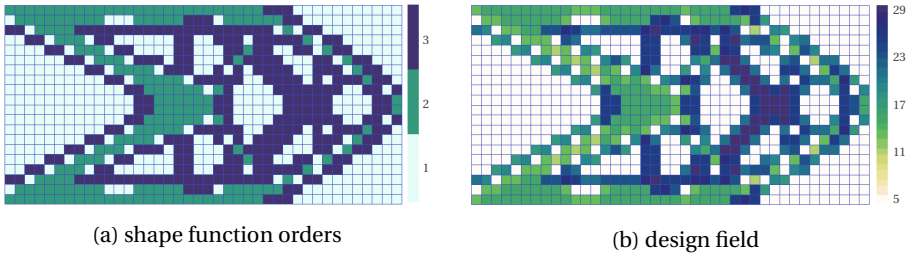


Figure 8.7: Distribution of polynomial orders of the shape functions (left) and the design field (right), showing the number of design points per MTO element, obtained from adaptive refinement (cycle 1) controlled by only density-based refinement indicator for a cantilever subjected to point load, as shown in Fig. 8.4a. The initial mesh comprises  $40 \times 20$  Q2 finite elements with 16 design points and  $4 \times 4$  density cells per element. The optimized design used for adaptive refinement is shown in Fig. 8.5.

in computational burden. Due to the adaptive nature of the refinement indicator proposed in [20], such problems can be avoided.

To start, the density-based refinement indicator  $\Gamma_k^d$  for the  $k^{\text{th}}$  MTO element is set to 0. To update  $\Gamma_k^d$ , we iterate over all the density cells of the  $k^{\text{th}}$  MTO element and consider the sum of individual refinement or coarsening contributions of these cells. Let  $n_{d,k}$  denote the number of density cells contained within the background mesh associated with the  $k^{\text{th}}$  MTO element. Then  $\Gamma_k^d$  is updated as follows:

- Iterate over  $j$  from 1 to  $n_{d,k}$ :
  1. Let the density of the  $j^{\text{th}}$  voxel be denoted by  $\rho_{kj}$ .

2. if  $r_l \leq \rho_{kj} \leq \rho_{avg}$ ,  
set  $\Gamma_k^d = \Gamma_k^d + \frac{1}{n_{d,k}}(\rho_{kj} - r_l)$ .
3. if  $r_{avg} < \rho_{kj} \leq \rho_u$ ,  
set  $\Gamma_k^d = \Gamma_k^d + \frac{1}{n_{d,k}}(r_u - \rho_{kj})$ .
4. if  $\rho_{kj} \leq c_l$ ,  
set  $\Gamma_k^d = \Gamma_k^d - \frac{1}{n_{d,k}}(c_l - \rho_{kj})$ .
5. if  $\rho_{kj} \geq c_u$ ,  
set  $\Gamma_k^d = \Gamma_k^d - \frac{1}{n_{d,k}}(\rho_{kj} - c_u)$ .

Here, the average density  $\rho_{avg}$  is defined using the expression  $\rho_{avg} = (\rho_{max} + \rho_{min})/2$ . The variables  $r_l$ ,  $r_u$ ,  $c_l$  and  $c_u$  are the bounds used to characterize the refinement and coarsening zones as shown in Fig. 8.6, and are defined as follows:

$$r_l = \rho_{min} + (1 - \alpha)\rho_{avg}e^{-\beta(\bar{k}-1)}, \quad (8.10)$$

$$r_u = \rho_{max} - (1 - \alpha)\rho_{avg}e^{-\beta(\bar{k}-1)}, \quad (8.11)$$

$$c_l = \rho_{min} + \alpha\rho_{avg}e^{-\beta(\bar{k}-1)}, \quad (8.12)$$

$$c_u = \rho_{max} - \alpha\rho_{avg}e^{-\beta(\bar{k}-1)}. \quad (8.13)$$

Here,  $\bar{k}$  denotes the adaptive cycle index, and  $\alpha$  and  $\beta$  are tuning parameters chosen here to be 0.2 and 0.8, respectively.

The tuning parameters  $\alpha$  and  $\beta$  are independent of the index of the adaptive cycle. However,  $\beta$  is sensitive to the rate at which the design converges. As stated earlier, our method assumes that the design has sufficiently converged at the end of every TO cycle. For different problems as well as different mesh resolutions, the amount of gray region may vary at this point. For problems where the designs of initial cycles of the *dp*-adaptive MTO process are significantly gray, lower values of  $\beta$  are recommended. This allows the density range for refinement to expand slowly over a span of cycles. Similarly, for rapidly converging designs, a larger value of  $\beta$  is more efficient. Automated adjustment of these parameters could be considered, however, it has not been used in this study.

Fig. 8.7 shows the shape function field and the design field obtained for the optimized cantilever beam design shown in Fig. 8.4a. The shape function field (Fig. 8.7a) denotes the polynomial order of the shape functions used in every finite element. The design field (Fig. 8.7b) denotes the number of design points used in every analysis element. These distributions have been obtained based on adaptive refinement and coarsening controlled by only the density-based refinement indicator. From Fig. 8.7, it is seen that the material-void boundaries where the intermediate densities are prominent, have primarily been refined. Coarsening occurs in void parts of the domain.

#### QR-ERROR INDICATOR

In an MTO scheme, it is possible that the employed shape functions cannot accurately model the displacement field arising due to the allowed high order density representations. As stated earlier, this error arising in an MTO setting due to inappropriate mod-

eling is referred to as QR-error. A closed-form condition to predict this QR-error is currently not known. Groen *et al.* [32] proposed a method to estimate the average error for the whole domain by determining a reference solution using a refined uniform mesh, and evaluating the obtained MTO solution against it. In the context of  $dp$ -adaptivity, QR-errors must be quantified at element level. We have proposed a method in [33], where an approximation to the QR-error can be obtained for any element through a comparison with a reference solution obtained by local  $p$ -refinement. In this work, we use this cost-effective local QR-error indicator proposed in [33]. Once a sufficiently converged design has been obtained from a TO cycle, the QR-error is determined by evaluating the effect of local  $p$ -refinement, as follows.

Let  $\mathbf{K}_k^{(p)}$ ,  $\mathbf{u}_k^{(p)}$  and  $\mathbf{f}_k^{(p)}$  denote the element stiffness matrix, displacement solution and internal load vector for the  $k^{\text{th}}$  MTO element. Here,  $p$  denotes the polynomial degree of the shape functions used in this element. Let  $\mathbf{u}_k^{(p+1)}$  denote the displacement solution obtained for the  $k^{\text{th}}$  element using shape functions of polynomial order  $p+1$ . Note that  $\mathbf{u}_k^{(p+1)}$  will be obtained by solving the element-level system  $\mathbf{K}_k^{(p+1)} \mathbf{u}_k^{(p+1)} = \mathbf{f}_k^{(p+1)}$ . Here, nodal load  $\mathbf{f}_k^{(p+1)}$  is formed by integrating the product of the interpolated original load field  $\mathbf{f}_k^{(p)}$  and the refined shape functions.

To obtain a unique solution for  $\mathbf{u}_k^{(p+1)}$ , sufficient boundary conditions need to be imposed. Thus, degrees of freedom (DOFs) equal to the number of rigid body modes (3 for 2D) need to be fixed. For this purpose, the displacement solution at 3 DOFs of  $\mathbf{u}_k^{(p+1)}$  is copied directly from  $\mathbf{u}_k^{(p)}$  for the DOFs which overlap, and the solution at the rest of the DOFs is obtained through solving the finite element system. Once  $\mathbf{u}_k^{(p+1)}$  has been obtained, the QR-error  $\epsilon_k^{QR}$  can be computed as

$$\epsilon_k^{QR} = 1 - \frac{\mathcal{J}_k^{(p)}}{\mathcal{J}_k^{(p+1)}}, \quad (8.14)$$

where  $\mathcal{J}_k^p$  refers to element-level strain energy for the  $k^{\text{th}}$  finite element using shape functions of order  $p$ . Thus,  $\mathcal{J}_k^{(p+1)} = \frac{1}{2} \mathbf{u}_k^{(p+1)\top} \mathbf{K}_k^{(p+1)} \mathbf{u}_k^{(p+1)}$  and  $\mathcal{J}_k^{(p)} = \frac{1}{2} \mathbf{u}_k^{(p)\top} \mathbf{K}_k^{(p)} \mathbf{u}_k^{(p)}$  have been used. This strain-energy-based criterion (Eq. 8.14) has been found to work well for the cases shown in this chapter.

Fig. 8.8a and 8.8b show an optimized design obtained after first cycle of MTO run, and the corresponding error distribution obtained using the QR-error indicator for the problem shown in Fig. 8.4a. Since the element-level test for QR-error is very conservative, it predicts higher error values compared to the actual full-scale TO problem [33]. Thus, to avoid undesired excessive increase in the values of  $p$ , we restrict the increment of  $p$  by only 1 per adaptive cycle based on the QR-error test. Also, to avoid excessive spatial refinement per adaptive cycle, only the cells with error value larger than 0.9 are adaptively refined. The elements flagged for refinement are shown in Fig. 8.8c. It is observed that the regions where the QR-patterns exist, have been flagged for refinement. Moreover, elements at the material boundaries, which are partially void or solid, also show high value of QR-error and are flagged.

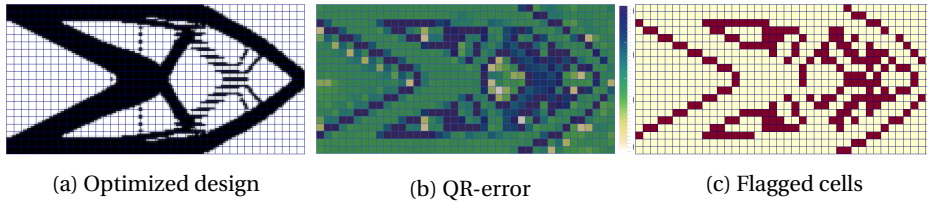


Figure 8.8: (a) Optimized design obtained after first cycle of  $dp$ -adaptive MTO run for a cantilever subjected to point load (Fig. 8.4a), (b) corresponding QR-error distribution plot obtained during the first adaptive cycle, and (c) domain showing the elements flagged for refinement using the QR-indicator. To avoid excessive refinement, only cells with error value larger than 0.9 have been flagged for refinement. The initial mesh comprises  $40 \times 20$  Q2 finite elements with 16 design points and  $4 \times 4$  density cells per element.

An interesting observation in Fig. 8.8b is that the elements which are completely void or solid also show QR-error values in the range 0.3-0.5. Although significant, the QR-error values in this range are relatively smaller than other parts of the domain and these elements do not get flagged for refinement. The reason for substantial QR-error values in these regions is the use of low order shape functions. For low values of  $p$ , the displacement solution for even a uniform density field may not be accurately modeled. When solving element-level FE problems with low shape function orders  $p$  and  $p + 1$ , it is observed that the modeling accuracy significantly improves when  $p$  is increased. Due to this, nonzero large values of  $\epsilon_k^Q$  are recorded in solid and void parts as well.

### 8.3.3. $dp$ -ADAPTIVITY ALGORITHM

The different steps of  $dp$ -adaptivity have briefly been introduced in Section 8.3.1. After treating the three indicators involved, here we discuss each of these steps in more details. Once a TO cycle has been completed, the optimized design is analyzed using the composite refinement criterion, and the following steps are carried out.

1. Once a cycle of TO run is completed, get the optimized design for  $dp$ -adaptivity.
2. Perform  $p$ -adaptivity based on analysis error criterion.
  - (a) Update  $\Gamma^a = \{\Gamma_1^a, \Gamma_2^a, \dots, \Gamma_{n_{el}}^a\}$  values for the whole analysis mesh (discussed in Section 8.3.2), where  $\Gamma_i^a$  is the analysis error indicator value for the  $i^{\text{th}}$  MTO element.
  - (b) Sort  $\Gamma^a$  in ascending order such that a corresponding ordered set  $\tilde{\Gamma}^a$  is obtained.
  - (c) Set the refine/coarsen flag of the  $k^{\text{th}}$  element  $\Theta_k$  to -1 for the first  $\alpha_c^d$  fraction of the MTO elements in  $\tilde{\Gamma}^a$ , and  $\Theta_k = 1$ , for the last  $\alpha_r^a$  fraction of the elements. Here, -1 and 1 denote that the cell has been flagged for coarsening (decrease in  $p$  value) and refinement (increase in  $p$  value), respectively. For no refinement/coarsening,  $\Theta_k$  is set to 0.
  - (d) Increase/decrease  $p$ -values based on flag  $\Theta$ .
3. Refine/coarsen  $p$  and  $d$  values based on density-based refinement criterion.

- (a) Update  $\Gamma^d = \{\Gamma_1^d, \Gamma_2^d, \dots, \Gamma_{n_{el}}^d\}$  values for the whole domain (discussed in Section 8.3.2), where  $\Gamma_i^d$  is the density-based refinement indicator value for the  $i^{\text{th}}$  MTO element.
  - (b) Sort  $\Gamma^d$  in ascending order such that a corresponding ordered set  $\tilde{\Gamma}^d$  is obtained.
  - (c) Update  $p$ -values by iterating over  $k$  from 1 to  $n_{el}$ :
    - i. For the first  $\alpha_c^d$  fraction of the elements in  $\tilde{\Gamma}^d$ , do:
      - A. if  $p_k = 1$ , set  $\Theta_k = -2$ . This helps to identify that the current element has been checked for coarsening. Since  $p_k$  cannot be lower than 1, no coarsening is performed.
      - B. if  $p_k > 1$  and  $\Theta_k = 0$ , set  $p_k = p_k - 1$ .
    - ii. For the last  $\alpha_r^d$  fraction of the elements in  $\tilde{\Gamma}^d$ , do:
      - A. if  $\Theta_k = 0$  or  $\Theta_k = -1$ , set  $p_k = p_k + 1$ . This means that if the element has been coarsened or left untreated based on the analysis indicator above, then refine it.
  - (d) Reduce the difference of  $p$ -values between adjacent elements to a maximum of 2 at this point. This is achieved by iterating through the whole domain ( $p_{\max} - p_{\min} - 2$ ) times, where  $p_{\max}$  and  $p_{\min}$  are the maximum and minimum values of  $p$  in the domain. At every check, the correction is done by raising the lower value of  $p$ .
  - (e) Update the design-field ( $d$  values) by iterating over  $k$  from 1 to  $n_{el}$ :
    - i. if  $\Theta_k = -2$ , set  $d_k = 1$ . This situation occurs when  $p_k = 1$ , and the density-based indicator flags the cell for further coarsening.
    - ii. if  $\Theta_k \neq -2$ , set  $d_k$  equal to the element-level upper bound for the  $k^{\text{th}}$  element (based on [31]). Thus,  $d_k = \text{DOFs} - r_b$ , where  $r_b$  denotes the number of rigid body modes for that element.
  - (f) Update the background mesh
    - i. Find maximum number of design variables per MTO element ( $\max(d_{el})$ ).
    - ii. Find first perfect square (cube in 3D) number ( $\bar{\bar{d}}$ ) greater than  $\max(d_{el})$ .
    - iii. Set the number of density cells per MTO element equal to  $\bar{\bar{d}}$ .
    - iv. Update projection radius  $r$  for every MTO element (Eq. 8.7).
4. Update  $p$  values to reduce the QR-error in every MTO element.
- (a) Iterate over  $k$  from 1 to  $n_{el}$ , do:
    - i. Calculate the QR-error for the  $k^{\text{th}}$  cell (discussed in Section 8.3.2).
    - ii. Update  $p_k = p_k + 1$  for the  $k^{\text{th}}$  element, if QR-error is greater than a certain error tolerance  $\alpha_{QR}$ .

The  $dp$ -adaptive MTO cycle is complete once the domain has been adaptively refined based on the three indicators. With the new  $dp$ -refined mesh, the next cycle of TO is performed.

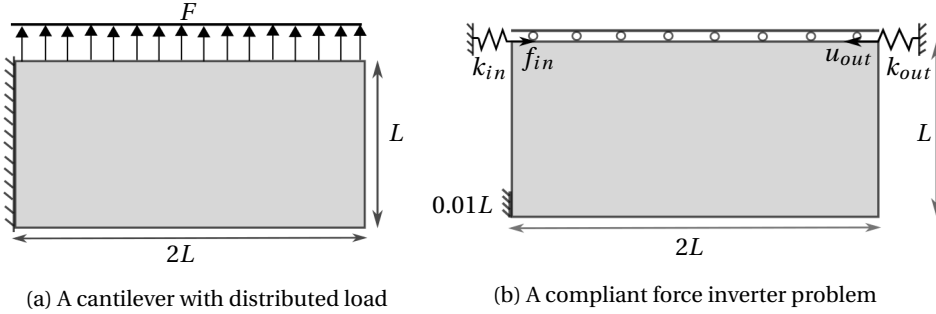


Figure 8.9: Problem domains and boundary conditions for a cantilever beam subjected to distributed load (left) and a force inverter (right). Here,  $L = 1$  m,  $F = \frac{0.5N}{L}$ ,  $k_{in} = 1 \text{ Nm}^{-1}$ ,  $k_{out} = 0.001 \text{ Nm}^{-1}$  and  $f_{in} = 1$  N.

## 8.4. NUMERICAL TESTS

### 8.4.1. DEFINITION OF TEST PROBLEMS

To demonstrate the applicability and effectiveness of  $dp$ -adaptivity, two test problems of minimum compliance and one compliant mechanism problem are considered [32]. In this chapter, only 2D problems are studied, whereas an extension to a 3D setting is a part of future work. Young's modulus  $E_0$  is set to  $1 \text{ Nm}^{-2}$ ,  $\nu = 0.3$ , and the SIMP penalization factor  $q$  is set to 3. The domain in each case is discretized using an initial mesh of  $40 \times 20$  MTO elements, comprising quadrilateral finite elements with shape functions of polynomial order 2 and  $4 \times 4$  design points per element. The radius  $R$  is set to  $0.3h$ , where  $h$  is the edge-length of any MTO element in the mesh. As a stopping criterion for all the test cases used in this chapter, the optimization process for the  $\tilde{k}^{\text{th}}$  cycle is terminated when the change in objective value between two consecutive iterations is less than  $\Delta J_1 \times \gamma^{(\tilde{k}-1)}$ . Here,  $\Delta J_1$  denotes the minimum required change in objective value between two consecutive iterations of the first MTO cycle, below which the optimization process terminates. For the subsequent cycles, the minimum required change in objective value is reduced by a factor of  $\gamma$  at every MTO cycle. The adaptive stopping criterion used here allows to control the extent of design convergence per cycle. For the numerical examples used in this chapter,  $\Delta J_1$  and  $\gamma$  are set to 0.04 and 0.6, respectively, and these values have been found to work well. Based on this, the first ( $\tilde{k} = 1$ ) and second ( $\tilde{k} = 2$ ) optimization cycles are terminated if the minimum changes in objective value are less than 0.04 and 0.024, respectively.

To validate the accuracy of the MTO modeling of the design, we use the method proposed in [32], where the obtained design is compared with a reference solution. For the reference solution, we discretize the domain using a high-resolution traditional TO mesh with elementwise constant densities. In this chapter, the reference mesh comprises  $320 \times 160$  finite elements and the polynomial order  $p$  of the involved shape functions is set to 3. With this mesh configuration, the resolution of the reference domain is equal to the highest density resolution that has been used in the MTO problem.

For the first test problem, compliance needs to be minimized for a Michell beam cantilever subjected to a point load  $F$  (Fig. 8.4a). For this case,  $F = 1$  N and  $L = 1$  m.

Three variants of this problem are used with maximum allowed material volume fractions set to 0.45, 0.2 and 0.1, to study the capability of the method in low volume fraction problems on coarse meshes. For the other problems used in this chapter, only one volume constraint of 0.45 is considered. The second test problem is that of compliance minimization for a cantilever beam subjected to a distributed load (Fig. 8.9a), and it is ensured that the load is consistently distributed over the various cycles of adaptivity. Here,  $F = \frac{0.5N}{L}$  and  $L = 1$  m. The distributed load tends to generate a lot of fine structures locally, and the resultant design was earlier found to be prone to QR artefacts [32], which makes it an interesting problem. For both these problems, the objective functional of Eq. 8.1 with  $\mathbf{z} = \mathbf{f}$ . The third case is a compliant mechanism problem where a force inverter needs to be designed, such that for a point load  $f_{in}$  at one end, the displacement  $u_{out}$  at the other end is maximized (Fig. 8.9b). Here, spring stiffnesses  $k_{in}$  and  $k_{out}$  are set to  $1 \text{ Nm}^{-1}$  and  $0.001 \text{ Nm}^{-1}$ , respectively. For the force inverter,  $\mathbf{z}$  in Eq. 8.1 is a vector of zeros with 1 contained at the DOF where  $u_{out}$  needs to be maximized. Thus,  $\mathbf{z} = [0 \dots 0 \ 1 \ 0 \dots 0]^T$ . The flexure hinges that are formed in this compliant mechanism problem will have sub-element resolution, and this aspect makes also this problem an interesting test for our method.

#### 8.4.2. RESULTS

Here, we discuss the results obtained for the three test problems using a  $dp$ -adaptive MTO scheme. To provide an understanding of the computational advantage of the proposed method, a comparison of CPU times is performed for the designs obtained using the proposed method as well as those obtained using the conventional MTO scheme discussed in [32]. Groen *et al.* [32] have shown that by using the MTO approach, the computational time can already be reduced by factors of up to 2.9 and 32 for 2D and 3D problems, respectively, compared to the traditional TO approach. In this chapter, we demonstrate the potential of  $dp$ -adaptive MTO schemes for 2D problems, and for this purpose, we will compare its performance with the non-adaptive MTO scheme, implemented in the same framework and evaluated on the same computing hardware.

##### COMPLIANCE MINIMIZATION FOR POINT LOAD

Fig 8.10 shows two optimized cantilever designs obtained for the problem shown in Fig. 8.4a. The first design (Fig. 8.10a) has been obtained using the traditional non-adaptive MTO scheme, and the other (Fig. 8.10b) by our  $dp$ -adaptive approach. For the two cases, the maximum allowed material volume fraction  $V_0$  is set to 0.45. Visually, the designs differ only slightly. Table 8.1 provides the details on various parameters related to MTO cases for the two optimized designs. The first remarkable observation regarding the  $dp$ -adaptive MTO result is the reduced computational cost. Adding the  $dp$ -adaptive framework to the existing MTO allows a reduction in computational cost by a factor of 4.5. This reduction in cost is mainly due to the reduced number of design variables  $N_d$  and free DOFs used in the  $dp$ -adaptive MTO case. While the uniformly refined mesh used in MTO comprises 51200 design points and 40400 free DOFs, only 22935 design points and 17262 free DOFs are used in the final (4<sup>th</sup>) cycle of the  $dp$ -adaptive MTO run, *i.e.* a

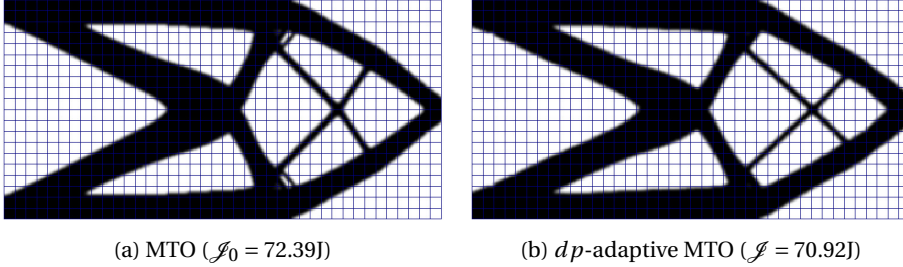


Figure 8.10: Optimized cantilever designs for the point load case shown in Fig. 8.4a, obtained using (a) a uniform MTO mesh and (b)  $dp$ -adaptive MTO approach. The maximum permissible material volume fraction is set to 0.45. A 4.5-fold speed-up as well as a superior objective value are obtained using  $dp$ -adaptivity. Additional information related to this test case is listed in Table 8.1.

Table 8.1: Numerical findings of several  $dp$ -adaptive MTO cases. For all the cases, the domain has been discretized using  $40 \times 20$  MTO elements, and the initial polynomial order of the shape functions is set to 2 for every element. Each MTO element initially consists of 16 design points and the projection radius  $R$  is set to  $0.3h$ , where  $h$  denotes element size. The maximum permissible values for shape function order  $p_{\max}$  and number of design points  $d_{\max}$  are set to 5 and 64, respectively. For the reference solution, a globally uniform mesh comprising  $320 \times 160$  finite elements with  $p = 3$  is used. Below,  $V_0$  denotes maximum allowed volume fraction of material,  $\mathcal{J}$  and  $\mathcal{J}_0$  are the objective values for  $dp$ -adaptive MTO run and the non-adaptive MTO run, and  $\mathcal{J}^*$  denotes the reference solution. The  $N_d$  and DOFs denote number of design points and free degrees of freedom employed in the last cycle of  $dp$ -adaptive MTO run.

Problem	Definition	$V_0$	Speed-up	$\mathcal{J}/\mathcal{J}_0$	$\mathcal{J}/\mathcal{J}^*$	$N_d$	DOFs
Minimum compliance	point load	0.45	4.5	0.98	0.98	22935	17262
		0.20	8.3	0.93	0.98	20056	15096
		0.10	10.0	1.03	0.96	19590	15186
	distributed load	0.45	4.6	0.98	1.0	22636	16932
Compliant mechanism	-	0.45	6.2	1.01 <sup>†</sup>	1.0	23375	17516

<sup>†</sup>This case refers to a maximization problem, where a value higher than 1 denotes that the  $dp$ -adaptive MTO approach performed better over the non-adaptive MTO scheme.

Table 8.2: Parameters related to  $dp$ -adaptive MTO run for the point load cantilever design problem shown in Fig. 8.4a. The material volume fraction  $V_0$  has been set to 0.45 for this case.

Cycle	DOFs	$N_d$	Iterations	$\mathcal{J} / \mathcal{J}^*$
1	6560	12800	67	0.86
2	7204	10646	34	0.97
3	12818	16256	17	0.98
4	17262	22935	18	0.98

reduction by over 50%. The free DOFs and number of design variables used in the earlier cycles are even lower (Table 8.2).

Another reason that accounts for the speed-up is the reduced number of iterations required in the final cycle of the  $dp$ -adaptive method under the same stopping criterion as used for the non-adaptive MTO method. The convergence of the TO process is significantly affected by the choice of the initial design [42]. In our approach, each preceding cycle, after refinement/coarsening, provides a high quality initial design for the next one. Since the design converges significantly in the first 3 cycles itself using less refined meshes, only 18 iterations are needed in the final cycle, while the non-adaptive MTO scheme uses a total of 56 iterations. Table 8.2 provides the details related to the  $dp$ -adaptive MTO run for this case. It is observed that Cycles 1 and 2 use a higher number of iterations. However, since the number of design variables and free DOFs are lower during these cycles, the associated computational cost is not very high.

In terms of performance, the cantilever design obtained from the  $dp$ -adaptive approach slightly outperforms the design obtained using non-adaptive MTO. The obtained performance ratio  $\mathcal{J} / \mathcal{J}_0$  is equal to 0.98, where  $\mathcal{J}$  and  $\mathcal{J}_0$  denote the compliance objective values obtained using the proposed method and non-adaptive MTO, respectively. From Table 8.2, it is observed that the global solution accuracy  $\mathcal{J} / \mathcal{J}^* = 0.98$ , where  $\mathcal{J}$  and  $\mathcal{J}^*$  refer to the objective values reported using adaptive MTO and that evaluated using the reference mesh, respectively. Since solution accuracy is close to 1, it is implied that the final optimized design is correct and free from artefacts. Moreover, we see that with every cycle of refinement, the global solution accuracy has improved. Thus, the  $dp$ -adaptive MTO method allows to obtain designs with a desired analysis accuracy.

Fig. 8.11 shows the distributions of shape function order and design points as well as the optimized designs for 4 cycles of the  $dp$ -adaptive MTO run of this case. It can be seen that refinement mainly occurs near the edges of the structure, and coarsening occurs as desired in solid and void parts. The optimized design in Cycle 1 consists of disconnected features, which are primarily the QR-patterns arising from the limitations of low order polynomial shape functions in those parts of the design [33]. Over the next cycles,  $p$ -refinement occurs in those regions and the QR-patterns are eliminated. Since the design points are distributed in the domain using  $k$ -means clustering without symmetry constraints, the distribution of design points itself can be asymmetrical, which in Cycle 2 leads to an asymmetrical design. An example of such asymmetry can be observed in the optimized design of Cycle 2, which gradually disappears over the next cycle.

In general, TO problems involving lower volume fractions of material are more difficult in terms of convergence. Moreover, for problems involving low volume fractions of

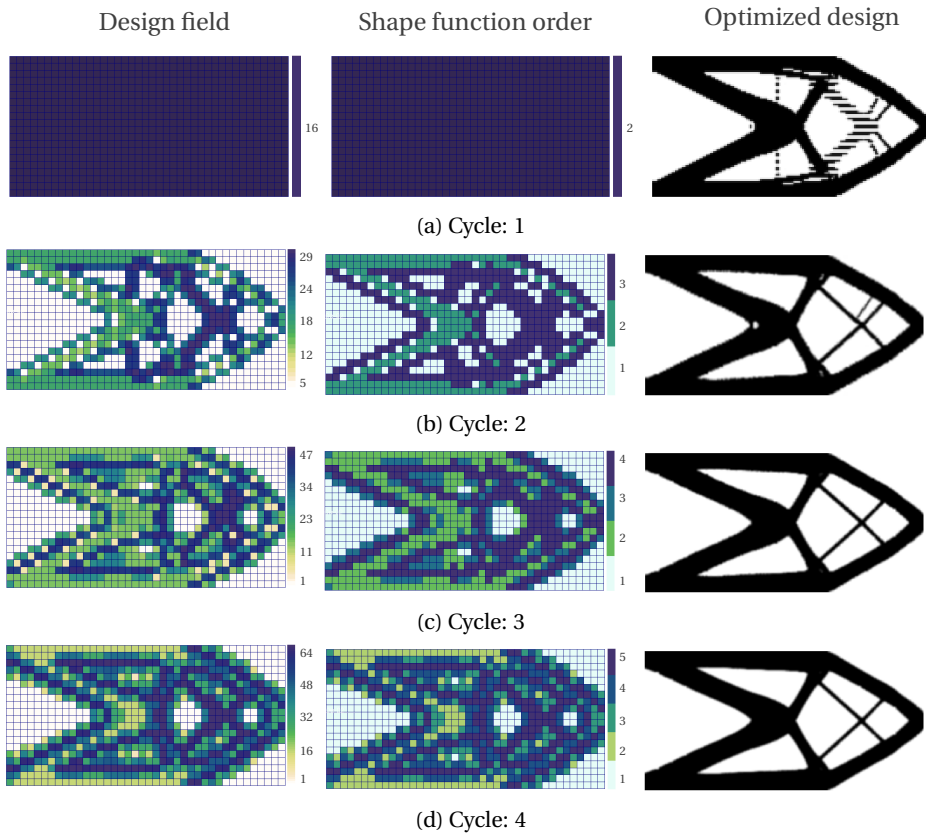


Figure 8.11: Optimized designs (right), and the respective shape function orders (middle) and design field (left) obtained for 4 cycles of  $dp$ -adaptive MTO run for a cantilever beam subjected to point load (Fig. 8.4a). The initial mesh is uniform and each element has shape functions of polynomial order 2 and 16 design points per element. The maximum allowed shape function order and number of design points are restricted to 5 and 64 per element, respectively.

material, a significant part of the domain comprises voids, and in turn does not require a fine mesh resolution. Clearly, for such scenarios,  $dp$ -adaptivity could be potentially beneficial. To investigate this, we study two additional cases of the point load cantilever beam involving lower values of  $V_0$ .

Fig. 8.12 shows the optimized designs for  $V_0 = 0.20$  using conventional MTO (Fig. 8.12a) and  $dp$ -adaptive method (Fig. 8.12b), respectively. For  $V_0 = 0.20$ , the computational time advantage has increased to a factor of 8.3. Also, it is seen that the design obtained using the non-adaptive MTO method differs significantly from the result of  $dp$ -adaptivity. Moreover, in terms of performance, the design obtained using  $dp$ -adaptivity is relatively less compliant. The ratio  $\mathcal{J}/\mathcal{J}_0$  is equal to 0.93. The compliance accuracy of the design obtained using the proposed method is found to be 0.98.

As another test case for lower volume fractions, the point load cantilever problem is

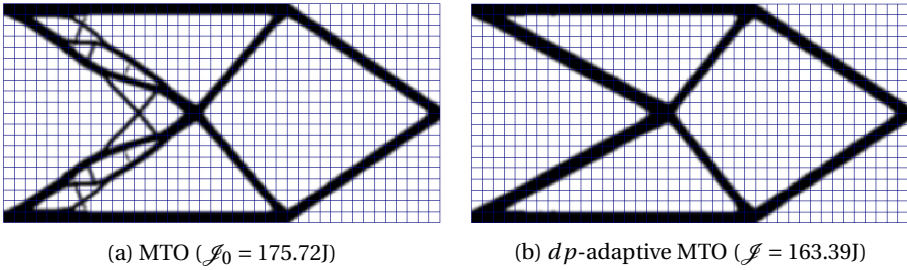


Figure 8.12: Optimized cantilever designs for the point load case shown in Fig. 8.4a, obtained using a uniform MTO mesh (left) and  $dp$ -adaptive MTO approach (right). The maximum permissible material volume fraction is set to 0.20. A speed-up of 8.3 times is obtained using  $dp$ -adaptivity. Additional information related to this test case is listed in Table 8.1.

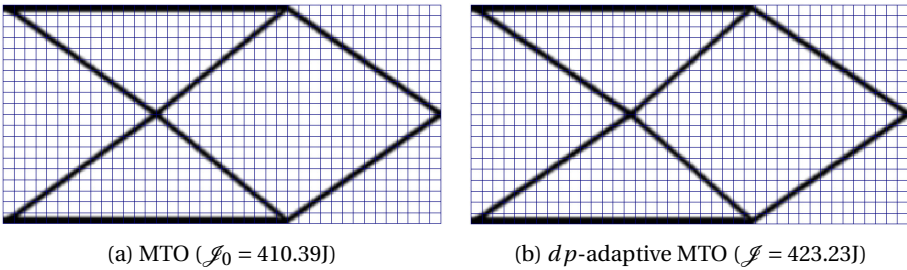


Figure 8.13: Optimized cantilever designs for the point load case shown in Fig. 8.4a, obtained using a uniform MTO mesh (left) and  $dp$ -adaptive MTO approach (right). The maximum permissible material volume fraction is set to 0.10. A 10-fold speed-up is obtained using  $dp$ -adaptivity. Additional information related to this test case is listed in Table 8.1.

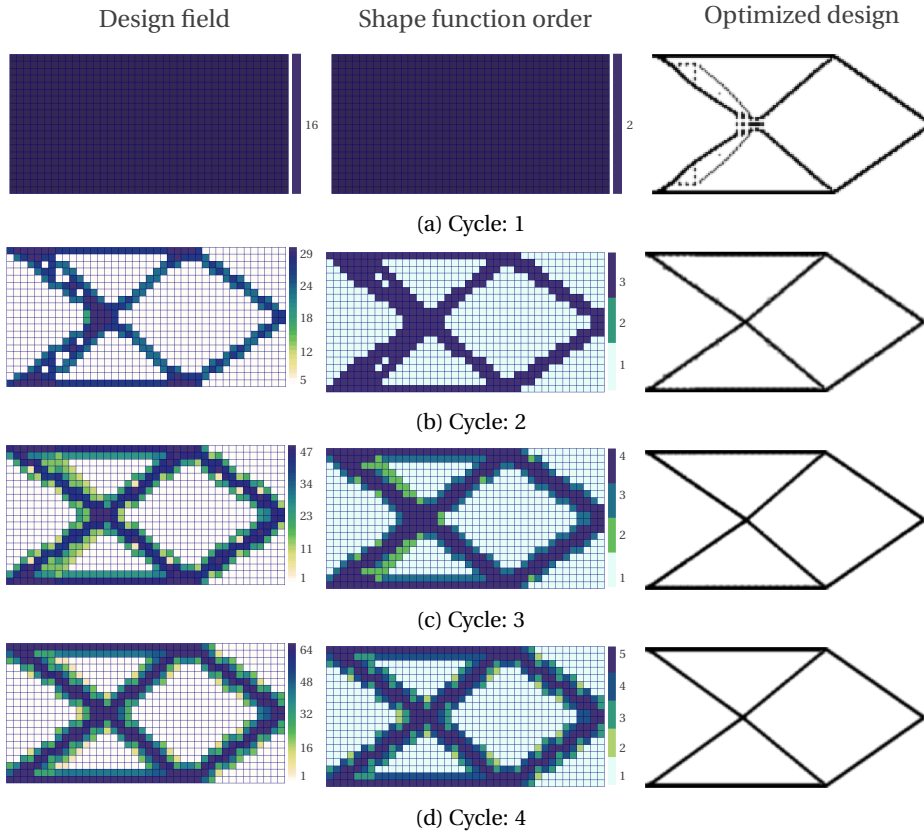


Figure 8.14: Optimized designs (right) and the respective shape function orders (middle) and design field (left) obtained for 4 cycles of  $dp$ -adaptive MTO run for a cantilever beam subjected to point load (Fig. 8.4a). The initial mesh is uniform and each element has shape functions of polynomial order 2 and 16 design points per element. The maximum allowed shape function order and number of design points are restricted to 5 and 64 per element, respectively.

examined with  $V_0 = 0.10$ . Fig. 8.13 shows the optimized designs for this volume fraction obtained using the conventional MTO method and  $dp$ -adaptive MTO, respectively. It is observed that for this volume fraction, the relative reduction in computational cost is even higher. Compared to the conventional MTO, a speed-up of 10 times is observed. The increase in speed-up is mainly due to the reduced number of free DOFs and design points, and the lower number of iterations required for convergence compared to the non-adaptive MTO. For this case, it is observed that  $\mathcal{I}/\mathcal{I}_0$  is 1.03, which implies that the design obtained using  $dp$ -adaptivity is slightly inferior to that obtained using the non-adaptive version. The analysis accuracy is also slightly lower than in the previous cases, with  $\mathcal{I}/\mathcal{I}^* = 0.96$ .

An understanding on the convergence of the  $dp$ -adaptive MTO process for  $V_0 = 0.10$  can be obtained from Fig. 8.14. In the first cycle, the design distribution and shape function orders are uniform for the whole mesh. Similar to the case of  $V_0 = 0.45$ , it is

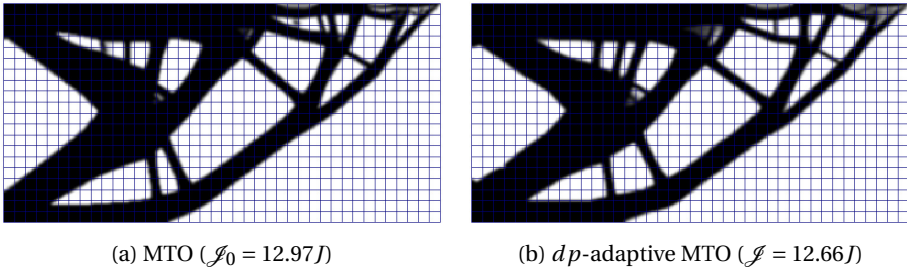


Figure 8.15: Optimized cantilever designs for the distributed-load case shown in Fig.8.9a, obtained using a uniform MTO mesh (left) and  $dp$ -adaptive MTO approach (right). A 4.6-fold speed-up is obtained using  $dp$ -adaptivity.

observed that QR-patterns are formed here as well, which are removed by refinement in later cycles. Compared to Fig. 8.11, it is observed that only a small part of the domain gets refined. Because of the low volume fraction of material used, a significant part of the domain comprises mainly of void regions, which do not require refinement. For the non-adaptive as well as the  $dp$ -adaptive versions of MTO, it is observed that the convergence of the optimization problem slows down significantly when very low material volume fractions are used. For example, for the same error tolerance, the number of iterations required in the final cycle of  $dp$ -adaptive method for  $V_0 = 0.45$  and  $0.10$  are 18 and 82, respectively. Our observations on the effect of material volume fraction on the convergence of TO process align with the results reported in [43], where similar results have been obtained over a set of numerical experiments.

#### COMPLIANCE MINIMIZATION FOR DISTRIBUTED LOAD

## 8

For the cantilever beam subjected to a distributed load (Fig. 8.9a),  $V_0$  is set to 0.45. Fig. 8.15 shows the optimized designs obtained using a uniform MTO mesh (Fig. 8.15a) and the  $dp$ -adaptive approach (Fig. 8.15b). The information on the two runs is listed in Table 8.1. As in the case of the point load cantilever, the designs obtained using the non-adaptive and adaptive variants of MTO are very similar. In terms of performance, a speed-up of 4.6 times is observed, and the accuracy of the obtained solution is close to 1. The obtained  $\mathcal{J}/\mathcal{J}_0$  value is 0.98, which implies that the  $dp$ -adaptive MTO found a slightly stiffer design.

For both the designs, there exists a small region near the top right boundary which comprises intermediate densities and is not improved even with refinement. With  $dp$ -adaptive MTO, this region is more prominent. Among the possible reasons, one explanation could be that the distributed load applied on the upper boundary of the domain requires support material in those parts. In the absence of material near the upper boundary, the load point can get disconnected, which leads to a high overall compliance value for the structure. We observe that the optimizer is not inclined towards adding much solid material in these parts of the domain. Due to this, gray regions are formed, representing fine structural features beyond the design resolution. These intermediate densities can be suppressed by the use of methods such as modified Heaviside projection as

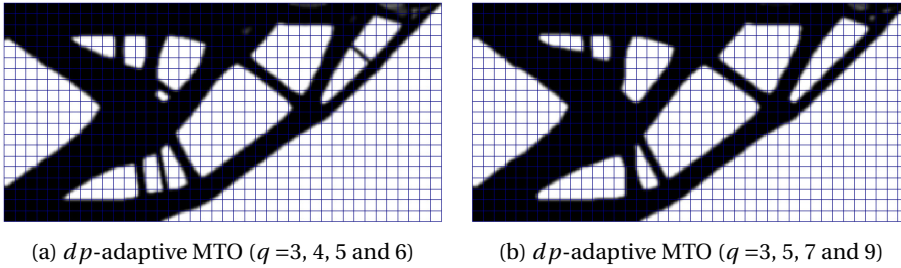


Figure 8.16: Optimized cantilever designs for the distributed-load case shown in Fig.8.9a, obtained using  $dp$ -adaptive MTO approach. For both the cases, adaptive penalization has been used. For the 4 cycles of the  $dp$ -adaptive MTO run, the values of  $q$  used have been reported in the sub-captions.

has been demonstrated in [32], or simply by adding a solid non-design region at the top surface.

Using a stronger penalization on the intermediate densities at the later cycles of MTO has also been found to help in reducing the gray areas. Fig. 8.16 shows two optimized designs for this cantilever problem obtained using adaptive penalization schemes. For the first case (Fig. 8.16a), the initial value of  $q$  is 3 and it is increased by 1 at every cycle. For the second case (Fig. 8.16b), the increment is by 2 at every cycle. It is observed that with stronger penalization on the intermediate densities, the gray regions are significantly reduced.

To obtain an understanding on how the design evolves over 4 cycles of  $dp$ -adaptive refinement, see Fig. 8.17. Due to the low order of the shape function used in Cycle 1, QR-patterns are observed here. Similar to the previous cases, adaptive refinement in the affected regions helps to remove these artefacts. For Cycle 4, only 16 iterations are needed when using the  $dp$ -adaptive method, while the conventional MTO method uses 54 iterations in total. Also, the number of design points and DOFs used in the last cycle of the  $dp$ -adaptive MTO are lower than in the conventional MTO method. Together, these two factors make the  $dp$ -adaptive MTO method 4.6 times faster in this case.

#### FORCE INVERTER COMPLIANT MECHANISM

To demonstrate the applicability of  $dp$ -adaptivity on topology optimization of compliant mechanisms, it is applied to the force inverter problem shown in Fig. 8.9b. The allowed volume fraction  $V_0$  is set to 0.45 and the goal of the problem is to distribute the material in a way that the displacement  $u_{out}$  is maximized. Fig. 8.18 shows the optimized designs obtained using conventional MTO (Fig. 8.18a) and the  $dp$ -adaptive method (Fig. 8.18b). As in the previous cases, the two designs are very similar. Details related to the MTO runs are reported in Table 8.1. It is observed that the objective ratio  $\mathcal{J}/\mathcal{J}_0$  is 1.01. Since this is a maximization problem, a value of  $\mathcal{J}/\mathcal{J}_0$  higher than 1 denotes that the design obtained using  $dp$ -adaptive MTO performs better.  $\mathcal{J}/\mathcal{J}^*$  is equal to 1.0, which means that the solution is as accurate as the reference solution.

Fig. 8.19 shows the distribution of design points and shape function orders, as well as the optimized designs for each cycle of  $dp$ -adaptivity. Similar to the other cases dis-

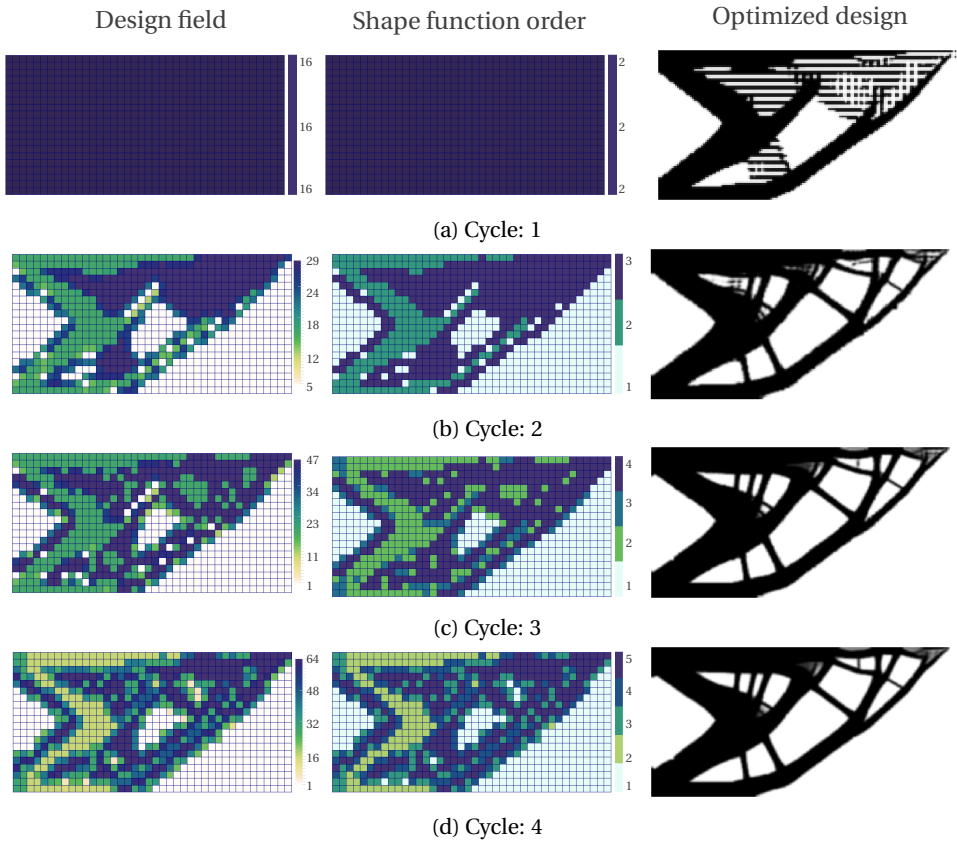


Figure 8.17: Optimized designs (right), and the respective shape function orders (middle) and design field (left) obtained for 4 cycles of  $dp$ -adaptive MTO run for a cantilever beam subjected to distributed load (Fig. 8.9a). The domain has been discretized using  $40 \times 20$  quadrilateral finite elements ( $r = 0.3h$ ). The initial mesh is uniform and each element comprises shape functions of polynomial order 2 and 16 design points per element. The maximum allowed shape function order and number of design points are restricted to 5 and 64 per element, respectively.

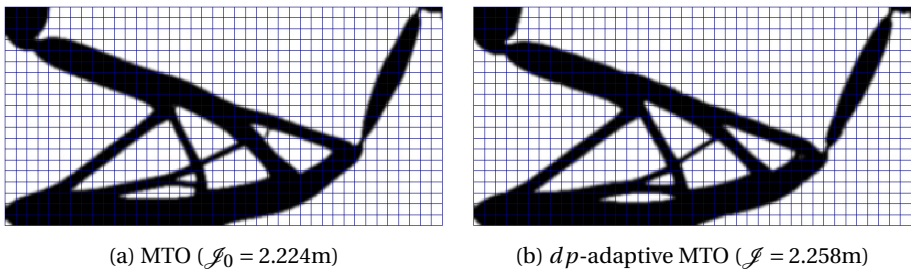


Figure 8.18: Optimized cantilever designs for the force inverter problem shown in Fig.8.9b, obtained using a uniform MTO mesh (left) and  $dp$ -adaptive MTO approach (right). A speed-up of 6.2 folds is obtained using  $dp$ -adaptivity.

cussed in this chapter, QR-patterns are observed in the results of the first cycle. Nevertheless, the overall material distribution after Cycle 1 already corresponds to the final solution. The QR-patterns eventually disappear in the subsequent cycles due to adaptive refinement of the domain. Refinement primarily occurs in regions where intermediate densities are prominent, and coarsening mainly occurs in the void and solid parts of the domain.

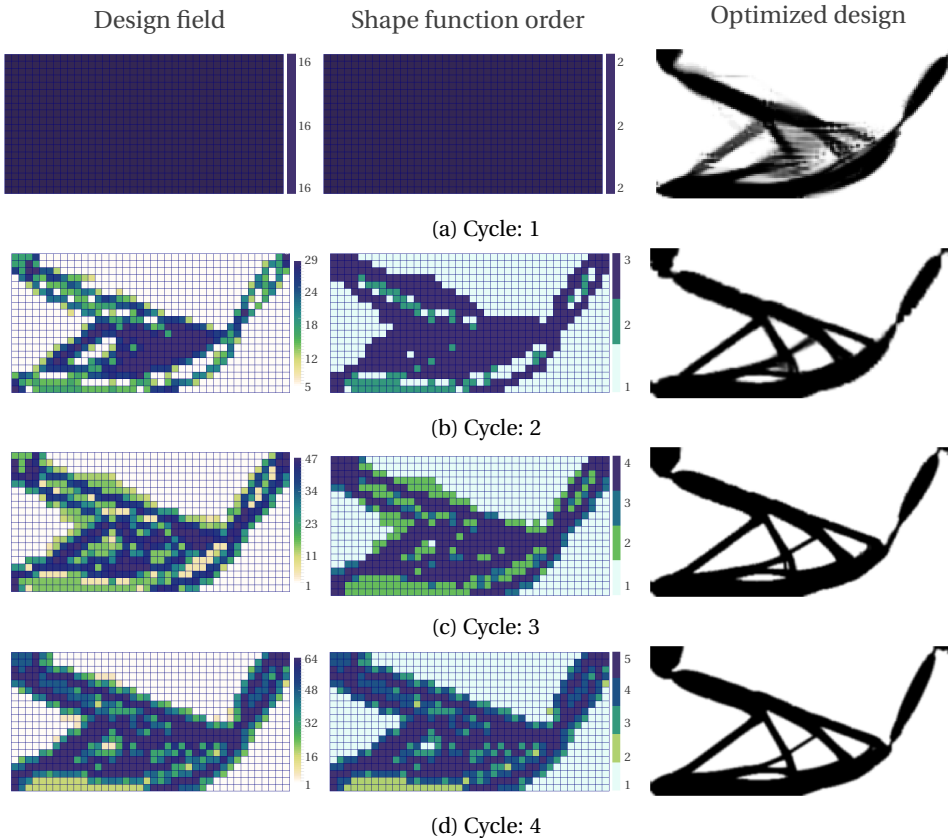


Figure 8.19: Optimized designs (right), and the respective shape function orders (middle) and design field (left) obtained for 4 cycles of a  $dp$ -adaptive MTO run for the force inverter problem shown in Fig. 8.9b. The initial mesh is uniform and each element comprises shape functions of polynomial order 2 and 16 design points per element. The maximum allowed order of the shape functions and number of design points are restricted to 5 and 64 per element, respectively.

## 8.5. DISCUSSIONS

The primary goal of using an MTO scheme is to obtain a high-resolution design at a relatively low computational cost. MTO decouples the design and analysis meshes in way that even for the choice of a coarse analysis mesh, a high-resolution density field can be obtained. The potential of MTO has already been demonstrated in [28, 32]. However,

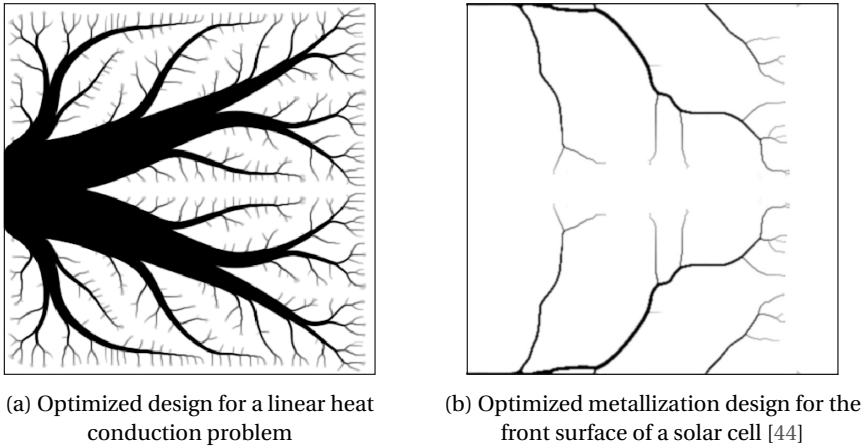


Figure 8.20: Optimized designs obtained using the traditional TO approach on a mesh of  $400 \times 400$  finite elements, with  $R$  set to 1.5 elements. The two cases refer to (a) linear heat conduction problem with  $V_0$  set to 0.3, and (b) nonlinear electrical conduction problem [44].

there are a few aspects of MTO (*e.g.* computational cost, QR-patterns) where scope of improvement existed. The  $dp$ -adaptive approach presented in this chapter addresses these aspects and further enhances the capability of the MTO method.

This chapter has mainly been focused on presenting the rationale and detailed formulation of the method. To demonstrate the applicability of  $dp$ -adaptive MTO, 2D mechanical test problems have been considered in this study. Intended future work includes exploring the application of the proposed method on problems involving other physics as well as in 3D settings. In [32], it has been shown that MTO can bring a speed-up of up to 32 folds over the traditional TO scheme. The improvement in 3D is significantly higher than that observed in 2D. As  $dp$ -adaptive MTO reduces the DOFs compared to the conventional MTO method, it is certainly expected to pay off even more in 3D. To really understand the value of the  $dp$ -adaptive approach for 3D problems, this hypothesis needs to be tested, and this is a part of our future work.

A preliminary investigation related to the application of  $dp$ -adaptive MTO on linear conduction (thermal/electrical) problems with loads distributed throughout the domain, revealed that this approach could bring only limited improvements in speed (less than twofolds) for this problem class. The primary reason is that for this type of problems, the optimized design comprises fine features, dendritic in nature, which spread all across the domain. For example, Fig. 8.20a shows an optimized design obtained for a linear thermal conduction problem using the traditional TO approach. A mesh of  $400 \times 400$  elements was used and  $R$  was set to 1.5 times the length of the element. The material volume fraction was set to 0.3. Details related to the definition of the problem can be found in [45]. It is seen that the optimized design has very few extended void areas, and most of the domain consists of fine material branches. Due to this, the majority of the domain gets refined at every adaptive cycle, which eventually reduces the relative advantage of  $dp$ -adaptive MTO method over its non-adaptive variant.

Fig. 8.20b shows an optimized solar cell front metallization design obtained using the traditional TO approach on a mesh of  $400 \times 400$  finite elements and  $R$  set to 1.5 times the element edge length [44]. This design has been obtained by solving a nonlinear electrical conduction problem, and only 4-5% of the domain is filled with material. For this case, it is seen that significant parts of the domain consists of void regions, which can be easily modeled with low values of  $d$  and  $p$ . Clearly, for such cases, the  $dp$ -adaptive approach can be used to significantly reduce the associated computational costs. From the two examples of conduction problems discussed here, it is clear that  $dp$ -adaptivity could certainly have a potential value for problems where designs feature extended void regions.

To demonstrate the concept of  $dp$ -adaptivity, a composite indicator has been formulated in this chapter. This indicator consists of an analysis error indicator, a density-based indicator and a QR-indicator. Although certain choices have been made for these indicators, the presented methodology itself is independent of these choices. Either of these indicators can be replaced with other alternatives that exist in the literature. For example, the Kelly estimator used as an analysis indicator in this work can be replaced with other analysis-based refinement indicators, *e.g.*, goal-oriented error indicator [46]. Such choices can provide a better control over the absolute error, accordingly helping to make a better choice of mesh resolution and solution accuracy. However, it is important that the tuning parameters associated with the chosen indicators are properly set so that issues related to excessive refinement are avoided. An addition to consider is a limit on, *e.g.*, the increase in DOFs and/or design variables at a given adaptive cycle.

For the analysis indicator discussed in this chapter, the top 10% and bottom 5% of the elements corresponding to  $\Gamma^a$  are chosen for refinement and coarsening, respectively. There is no particular motivation to choose these cut-offs. For problems where the design domain has prominent regions with large jump across the element edges, it is recommended to allow more cells to be refined, so as to reduce the error in fewer cycles. For the density-based indicator, both  $\alpha_r^d$  and  $\alpha_c^d$  are set to 1.0 for the current study. This ensures that all the elements with  $\Gamma^d > 0$  are refined and all elements with  $\Gamma^d < 0$  are coarsened. The reason to set these parameters to 1.0 is that the stopping criterion chosen in this chapter allows the design to converge sufficiently at every MTO cycle. Due to this, the intermediate densities are reduced. However, if fewer iterations are permitted per MTO cycle, it is advisable to set  $\alpha_r^d$  and  $\alpha_c^d$  to values less than 1, in order to avoid excessive refinement and coarsening. The tuning of all these meta-parameters forms an optimization problem in itself, and as adaptive design approaches become more sophisticated, setting such parameters can become highly nontrivial and time-consuming. For the present study, no extensive parameter tuning was performed, yet already significant performance gains are observed. We see opportunities for future research in further adaptive and intelligent tuning strategies of meta-parameters during the adaptive optimization itself, to take this burden away from the user.

For the MTO method,  $dp$ -adaptivity serves as an add-on where the design distribution and shape function orders are adapted at every cycle of refinement based on a pre-defined criterion. However, there are additional aspects of MTO which can be adapted to gain further improvements in accuracy and associated computational cost. Among others, appropriately adapting the filter radius  $R$  could lead to further improvements.

In the context of adaptive  $h$ -refinement, the impact of adaptive filter radius has been explored in [20]. For MTO, this aspect has briefly been discussed in [29]. However, the advantage of using an adaptive filter radius in an MTO setting remains an open question and needs to be explored. Also, based on our numerical tests, here we chose to use an adaptive stopping criterion, such that the cutoff value for minimum change in objective value between successive iterations is relaxed by a factor of 0.6 at every adaptive cycle. However, further investigations are needed to decide how this aspect can be adapted in the most efficient way.

Additional directions associated with  $dp$ -adaptivity exist that could be investigated for further improvement of the methodology. For example, currently the number of design variables is set to the maximum allowed value based on the element-level upper bound described in [31]. However, it is still an open question whether this is the most appropriate way to refine the design field. Moreover, for the problems presented in this chapter, we observed that for the chosen setting, violating the system-level bounds (also derived in [31]) did not have any detrimental impacts. Hence, we decided to not incorporate the system-level bounds in the method. However, for more complex problems, where the objective is very sensitive to small design changes, the system-level bounds might have to be enforced.

To wrap up the discussions, there are several research aspects that can be explored in the context of adaptive MTO. This work lays the foundation for an adaptive MTO scheme that is mathematically reliable as well as computationally efficient. It is hoped that with further research along the directions outlined above, the proposed approach can be improved further.

## 8.6. CONCLUSIONS

Multiresolution topology optimization (MTO) methods decouple the analysis and design discretizations, such that high resolution design representations are permitted on relatively coarse analysis meshes. In this chapter, the first adaptive variant of the MTO scheme, namely  $dp$ -adaptive MTO, has been presented. Through several 2D numerical examples, it has been demonstrated that the proposed method can obtain highly optimized designs at significantly lower computational cost than in conventional MTO, and high analysis accuracy. Moreover, undesired features such as intermediate densities and QR-patterns can be significantly reduced in the resulting designs, and a desired analysis accuracy can be enforced. A particularly interesting application of this  $dp$ -adaptive MTO method is for TO problems involving low material volume fractions. The speed-up over conventional MTO was found to increase with decreasing material volume fraction. It has been shown that for test cases with a 10% maximum relative volume, 10-fold speed-up can be obtained over the conventional MTO scheme in 2D, when the  $dp$ -adaptive MTO method is used. For 3D problems, even higher speed-ups are expected.

Clearly, the proposed adaptive approach improves on the conventional MTO method by tackling some of the issues associated with it. For future work, we aim at exploring the application of  $dp$ -adaptive approach for problems involving different physics and three-dimensional problems. However, based on the results presented in this study, it can already be argued that the proposed approach could serve as an important methodology to obtain high resolution designs at an attractive computational cost.

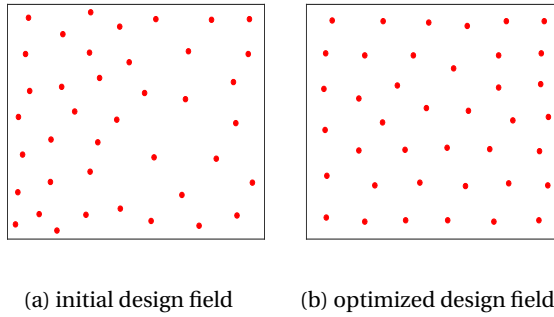


Figure 8.21: Distribution of 40 design points in a Q-type finite element obtained using  $k$ -means clustering.

## 8.A. $k$ -MEANS CLUSTERING

$k$ -means clustering is a cluster analysis technique popularly used in data mining [35]. It aims to partition  $\psi$  observations into  $k$  clusters such that the observations in each cluster tend to be close to each other. Note that although the problem is computationally difficult, there are various heuristic techniques that can quickly obtain a locally optimal solution.

This technique can be used to choose locations of design points within a finite element (FE) and one of the primary advantages of this method is that it is easily applicable to various finite elements differing in geometry. Synonymous to the observations required in  $k$ -means clustering, a large number of uniformly distributed random points  $\psi$  are chosen within the FE using Mersenne twister pseudorandom number generator [47]. Given that  $k$  design points' locations need be to chosen in the FE, we choose  $\psi = 1000k$ . Next, an initial set of  $k$  points is chosen in the FE using  $k$ -means++ cluster center initialization algorithm [36]. These points serve as the initial  $k$  means for the  $\psi$  observations.

Let  $m_1^{(1)}, m_1^{(2)}, \dots, m_1^{(k)}$  denote the initial locations of  $k$  design points, then the following two steps are iteratively performed to optimize these locations:

1. **Assignment step:** Each observation  $x_p$  is assigned to exactly one out of  $k$  clusters based on the shortest Euclidean distance. Thus, during the  $t^{\text{th}}$  iteration,  $x_p$  is assigned to the  $i^{\text{th}}$  cluster, if

$$\|x_p - m_i^{(t)}\|^2 \leq \|x_p - m_j^{(t)}\|^2 \quad \forall 1 \leq j \leq k. \quad (8.15)$$

2. **Update step:** The new centroids of each of the  $k$  clusters then become the new locations of the design points. The centroids are calculated as follows:

$$m_i^{(t+1)} = \frac{1}{c_i} \sum_{p=1}^{c_i} x_p. \quad (8.16)$$

The two steps are repeated until locally optimal cluster-means are obtained. Note that for every number of design points, these distributions are generated once, and stored for use during optimization.

Fig. 8.21 shows the initial and optimized distributions of 40 design points in a Q-type FE. The optimized design distribution has been obtained using the  $k$ -means clustering algorithm. Clearly, in the optimized design field, the design points are more uniformly distributed and away from the boundaries of the element.

## 8.B. NUMERICAL INTEGRATION SCHEME

The element stiffness matrix  $\mathbf{K}_e$  needs to be accurately integrated for every finite element. For the traditional TO using Q1 elements with elementwise constant densities, a  $2 \times 2$  Gauss quadrature rule is sufficient. However, for more complex density fields and higher order shape functions, more advanced ways of integration are needed to obtain correct  $\mathbf{K}_e$ . One of the possibilities is to use higher order integration schemes. A drawback of this approach is that a solid-void boundary may not be correctly modeled. However, the associated error is very small, and with higher order integration schemes, numerically correct designs are obtained using MTO.

The density inside every voxel in the background mesh is constant. Thus, a composite integration scheme can also be used, where the voxel-contributions to the stiffness matrix are evaluated first, and these are then summed together to obtain the element stiffness matrix [32]. Since density is assumed to be constant inside each voxel, the choice of integration scheme depends on the polynomial order of the shape functions only. The advantage of this scheme is that the solid-void boundaries are aligned with the edges of the voxels, due to which the stiffness matrix can be accurately integrated.

The composite integration, in general, is superior over the traditional integration scheme which is based on higher order Gauss quadrature rule. However, since in TO the design changes during the course of optimization, significant amount of information related to the stiffness matrices needs to be precomputed to use it in an adaptive MTO formulation. To avoid this excessive storage issue and to reduce the additional computational costs related to assembling the stiffness matrix at each iteration of MTO, we prefer to use the traditional Gauss quadrature rule with higher number of integration points.

Table 8.3: Choice of integration scheme for different combinations of design fields and polynomial shape functions for Q-type finite elements. Here,  $d$  and  $p$  denote the number of design points and polynomial order of the shape functions, respectively,  $n_{\text{sup}}$  refers to the number of support points, and  $\overline{\mathcal{P}}(d)$  and  $\overline{\mathcal{P}}(\mathbf{K})$  denote the maximum possible polynomial order of the design field and stiffness matrix, respectively.

$d$	$\overline{\mathcal{P}}(d)$	$p$	$n_{\text{sup}}$	$\overline{\mathcal{P}}(\mathbf{K})$	Gauss quadrature rule
1	0	1	4	2	$2 \times 2$
4	2	1	4	4	$3 \times 3$
9	3	2	9	7	$4 \times 4$
16	5	3	16	11	$6 \times 6$
25	6	3	16	12	$7 \times 7$
36	7	4	25	15	$8 \times 8$
49	9	5	36	19	$10 \times 10$
64	10	5	36	20	$11 \times 11$

Table 8.3 lists the minimum Gauss quadrature rule needed to accurately integrate the

element stiffness matrix for several different density fields and polynomial shape functions. Here, only quadrilateral finite elements are considered. Based on the number of design points, a polynomial design field is constructed, and based on the shape functions, the order of element stiffness matrix is determined.

## REFERENCES

- [1] D. K. Gupta, F. van Keulen, and M. Langelaar, *A dp-adaptive multiresolution topology optimization approach (submitted)*, International Journal for Numerical Methods in Engineering (2019).
- [2] M. P. Bendsøe, *Optimal shape design as a material distribution problem*, Structural Optimization **1**, 193 (1989).
- [3] O. Sigmund and K. Maute, *Topology optimization approaches: a comparative review*, Structural and Multidisciplinary Optimization **48**, 1031 (2013).
- [4] N. P. van Dijk, K. Maute, M. Langelaar, and F. van Keulen, *Level-set methods for structural topology optimization: a review*, Structural and Multidisciplinary Optimization **48**, 437 (2013).
- [5] J. Deaton and R. Grandhi, *A survey of structural and multidisciplinary continuum topology optimization post 2000*, Structural and Multidisciplinary Optimization **49**, 1 (2014).
- [6] N. Aage and B. S. Lazarov, *Parallel framework for topology optimization using the methods of moving asymptotes*, Struct. Multidiscip. O. **47**, 493 (2013).
- [7] S. Wang, E. Sturler, and G. H. Paulino, *Large-scale topology optimization using preconditioned Krylov subspace methods with recycling*, International Journal for Numerical Methods in Engineering **69**, 2441 (2007).
- [8] K. Suresh, *Efficient generation of large-scale pareto-optimal topologies*, Struct. Multidiscip. O. **47**, 49 (2013).
- [9] O. Amir, N. Aage, and B. S. Lazarov, *On multigrid-CG for efficient topology optimization*, Struct. Multidiscip. O. **49**, 815 (2014).
- [10] Z. Xia, Y. Wang, Q. Wang, and C. Mei, *GPU parallel strategy for parameterized LSM-based topology optimization using isogeometric analysis*, Struct. Multidiscip. O. **56**, 413 (2017).
- [11] O. Amir, M. P. Bendsøe, and O. Sigmund, *Approximate reanalysis in topology optimization*, International Journal for Numerical Methods in Engineering **78**, 1474 (2009).
- [12] O. Amir, *Revisiting approximate reanalysis in topology optimization: on the advantages of recycled preconditioning in a minimum weight procedure*, Struct. Multidiscip. O. **51**, 41 (2015).

- [13] J. Martinez-Frutos and D. Herrero-Perez, *Efficient matrix-free GPU implementation of Fixed Grid Finite Element Analysis*, *Finite Elem. Anal. Des.* **104**, 61 (2015).
- [14] I. Babuška and B. Q. Guo, *The  $h$ ,  $p$  and  $h$ - $p$  version of the finite element method: basis theory and applications*, *Adv. Eng. Softw.* **15**, 159 (1992).
- [15] M. Bruggi and M. Verani, *A fully adaptive topology optimization algorithm with goal-oriented error control*, *Computers and Structures* **89**, 1481 (2011).
- [16] K. Maute and E. Ramm, *Adaptive topology optimization*, *Structural Optimization* **10**, 100 (1995).
- [17] F. van Keulen and E. Hinton, *Topology design of plate and shell structures using the hard kill method*, in *Advances in structural Engineering Optimization*, edited by B. Topping (Civil Comp. Press, Edinburgh, 1996) pp. 177–188, presented at the Third International Conference in Computational Structural Technology in Budapest, 21–23 August, 1996.
- [18] J. C. Costa and M. K. Alves, *Layout optimization with  $h$ -adaptivity of structures*, *International Journal for Numerical Methods in Engineering* **58**, 83 (2003).
- [19] R. Stainko, *An adaptive multilevel approach to the minimal compliance problem in topology optimization*, *Communications in Numerical Methods in Engineering* **22**, 109 (2006).
- [20] D. K. Gupta, M. Langelaar, M. Barink, and F. van Keulen, *Optimizing front metalization patterns: Efficiency with aesthetics in free-form solar cells*, *Renewable Energy* **86**, 1332 (2016).
- [21] H. Nguyen-Xuan, *A polytree-based adaptive polynomial finite element method for topology optimization*, *Int. J. Numer. Meth. Engg.* **110**, 972 (2017).
- [22] T. Y. S. Hoshina, I. F. M. Menezes, and A. Periera, *A simple adaptive mesh refinement scheme for topology optimization using polygonal meshes*, *J. Braz. Soc. Mech. Sci. & Eng.* **40**, 1 (2018).
- [23] A. B. Lambe and A. Czekanski, *Topology optimization using a continuous density field and adaptive mesh refinement*, *Int. J. Numer. Meth. Eng.* **113**, 357 (2018).
- [24] J. Wu, *Continuous optimization of adaptive quadtree structures*, *Comput. Aided Des.* **102**, 72 (2018).
- [25] J. Parvizian, A. Duster, and E. Rank, *Finite cell method:  $h$ - and  $p$ -extension for embedded domain problems in solid mechanics*, *Comput. Mech.* **41**, 121 (2007).
- [26] J. Parvizian, A. Duster, and E. Rank, *Topology optimization using the finite cell method*, *Optimization and Engineering* **13** (2012).
- [27] T. H. Nguyen, G. H. Paulino, J. Song, and C. H. Le, *A computational paradigm for multiresolution topology optimization (MTOPT)*, *Structural and Multidisciplinary Optimization* **41**, 525 (2010).

- [28] T. H. Nguyen, C. H. Paulino, Le, and J. F. Hajjar, *Topology optimization using the p-version of the finite element method*, Structural and Multidisciplinary Optimization **56**, 571 (2017).
- [29] T. H. Nguyen, G. H. Paulino, J. Song, and C. H. Le, *Improving multiresolution topology optimization via multiple discretizations*, International Journal for Numerical Methods in Engineering **92**, 507 (2012).
- [30] Y. Wang, J. He, and Z. Kang, *An adaptive refinement approach for topology optimization based on separated density field description*, Computers and Structures **117**, 10 (2013).
- [31] D. K. Gupta, G. J. van der Veen, A. M. Aragón, M. Langelaar, and F. van Keulen, *Bounds for decoupled design and analysis discretizations in topology optimization*, International Journal for Numerical Methods in Engineering **111**, 88 (2017).
- [32] J. P. Groen, M. Langelaar, O. Sigmund, and M. Ruess, *Higher-order multi-resolution topology optimization using the finite cell method*, International Journal for Numerical Methods in Engineering **110**, 903 (2017).
- [33] D. K. Gupta, M. Barink, and M. Langelaar, *CPV solar cell modeling and metallization optimization*, Solar Energy **159**, 868 (2018).
- [34] E. Rank, *Adaptive remeshing and h-p domain decomposition*, Comput. Method. Appl. M. **101**, 299 (1992).
- [35] D. Mackay, *Information Theory, Inference and Learning Algorithms* (Cambridge University Press, 2003).
- [36] D. Arthur and S. Vassilvitskii, *K-means++: The Advantages of Careful Seedings*, in *SODA '07: Procc 18th Annual ACM-SIAM Symp, Discrete Algorithms* (2007) pp. 1027–1035.
- [37] T. E. Bruns and D. A. Tortorelli, *Topology optimization of nonlinear elastic structures and compliant mechanisms*, Comput. Method. Appl. M. **190**, 3443 (2001).
- [38] D. W. Kelly, J. R. Gago, O. C. Zienkiewicz, and I. Babuska, *A posteriori error analysis and adaptive proceses in the finite element method. Part I - Error analysis*, Int. J. Numer. Meth. Eng. **19**, 1593 (1983).
- [39] M. Ainsworth and J. T. Oden, *A Posteriori Error Estimation in Finite Element Analysis* (John Wiley & Sons, Inc., USA, 2000).
- [40] T. Grätsch and K. Bathe, *A posteriori error estimation techniques in practical finite element analysis*, Comput. and Struct. **83**, 235 (2005).
- [41] O. C. Zienkiewicz, D. W. Kelly, J. Gago, and I. Babuska, *Hierarchical finite element approaches error estimates and adaptive refinement*, .

- [42] J. van Schoubroeck, D. K. Gupta, and M. Langelaar, *An investigation of the effect of initial design choices in density-based topology optimization (submitted)*, Struct. Multidiscip. O. (2018).
- [43] S. Rojas-Labanda and M. Stolpe, *Benchmarking optimization solvers for structural topology optimization*, Struct. Multidiscip. O. **52**, 527 (2015).
- [44] D. K. Gupta, M. Langelaar, M. Barink, and F. van Keulen, *Topology optimization of front metallization patterns for solar cells*, Structural and Multidisciplinary Optimization **51**, 941 (2015).
- [45] M. P. Bendsøe and O. Sigmund, *Topology Optimization: Theory, methods and applications* (Springer, 2003).
- [46] J. T. Oden and S. Prudhomme, *Goal-oriented error estimation and adaptivity for the finite element method*, Comput Math Appl **41**, 735 (2001).
- [47] M. Matsumoto and T. Nishimura, *Mersenne twister: A 623-dimensionally equidistributed uniform pseudo-random number generator*, ACM Trans. Model. Comput. Simul. **8**, 3 (1998).

# III

## CONCLUSIONS AND FUTURE WORK



# 9

## CONCLUSIONS AND RECOMMENDATIONS

This chapter provides overall conclusions of the research presented in the preceding chapters in Parts I and II. Several recommendations including directions for future research are discussed regarding the optimization-based design of highly-efficient solar cells as well as the optimization of high resolution structural designs in general.

### 9.1. CONCLUSIONS

The conclusions presented in this chapter have been organized into two parts based on the two related research questions that were formulated at the beginning of this thesis. These two parts are (1) optimizing metallization patterns in solar cells, and (2) designing high-resolution efficient structural designs using topology optimization (TO). Further, overall conclusions of this research work are stated at the end of this section.

#### 9.1.1. OPTIMIZING METALLIZATION PATTERNS IN SOLAR CELLS

In this thesis, one of the two research questions was how TO could be used to optimize the metallization patterns in solar cells. This question has been answered in Chapters 2, 3 and 4, where TO frameworks have been presented for various types of solar cells and different conditions. In Chapter 2, rectangular solar cells of thin c-Si type have been modeled, and a uniform illumination condition with a single light intensity has been considered. In Chapter 3, the application of TO has been demonstrated on freeform solar cells, and the metallization pattern has been simultaneously optimized on the front and rear sides. Chapter 4 extends the application of TO to concentrating solar cells under nonuniform illumination and temperature conditions.

Based on the various cases considered in this thesis, it can be concluded that TO definitely is capable of obtaining well performing designs. Designs obtained by TO perform better or at least equal to the traditionally used counterparts. TO has a particular benefit in situations where the geometry of the solar cell and/or the load patterns are irregular.

Moreover, TO has also been found to work well with irregular temperature profiles and nonuniform illumination conditions. This has been shown through the application of TO on freeform geometries and concentrating solar cells, where remarkable improvements of more than 50% and 26%, respectively, are obtained in the power output. For rectangular solar cells, it has been found that the conventional H-pattern performs very well, and it is very difficult to achieve a similar performance or converge to its geometry using TO.

Apart from the improvement in solar cell performance obtained using TO, the metallization design problem would be of interest to the TO community from an optimization point of view. The material volume fraction for this problem is generally close to 4-6%, and identifying this exact number is also a part of the optimization problem. Due to the very low material fraction, this problem is very prone to local minima and has a slow convergence. Also, there is a high degree of nonlinearity in the physics of the problem. These features make this optimization problem unique and of interest from a mathematical perspective.

### 9.1.2. DESIGN OF HIGH-RESOLUTION STRUCTURES USING TO

The solar cell metallization requires designing high-resolution fine features. With the traditional TO, where the domain is uniformly discretized using finite elements with elementwise constant densities, high resolution implies high computational costs. Thus, part of this research thesis was also directed towards developing TO variants to efficiently obtain high-resolution structural designs. Since these results could be of interest to the community outside photovoltaics as well, the discussion and results in this part of the thesis were kept general and common TO test problems (*e.g.* cantilever design, force inverter) were used to investigate the concepts.

In Chapter 5, an adaptive  $h$ -refinement scheme was presented. The adaptive refinement approach presented in this work helps to avoid excessive refinement at early stages of design evolution, and reduces the associated computational cost to a certain extent. Also, from the experiments involving filter radius adaptation as well as adaptive penalization of densities, it can be concluded that these aspects play an important role in controlling the cost and convergence of TO. Thus, these aspects need to be taken into account to efficiently obtain high-resolution designs.

Among the various possibilities, the multiresolution topology optimization (MTO) approach was chosen for further study due to its potential to express high-resolution design representations at relatively low analysis costs. It was found that for a certain choice of analysis resolution in MTO, there is always an upper limit on the design resolution that can be uniquely bound. The theoretical investigations and numerical results presented in Chapter 6 support this claim. Thus to avoid any issues related to nonuniqueness (*e.g.* undesired convergence) it is advisable to keep the design resolution always below the threshold described in Chapter 6.

Further, QR-patterns, numerical artefacts arising in MTO formulations, were studied in detail. Based on the results presented in Chapter 7, it can be concluded that QR-patterns can lead to misleading results, and it is important that the MTO results are free from these artefacts. Solutions such as increasing the polynomial order of the shape functions, increasing the filter radius, *etc.* have been found to be of help for several in-

stances. However, we have shown that these remedies can also fail and cannot always be relied upon to obtain high-resolution designs at low computational cost.

In Chapter 8, an adaptive variant of MTO, namely *dp*-adaptive MTO, has been proposed, that builds on the insights gained in the previous chapters. This approach possesses the properties of the traditional MTO approach. Moreover, it ensures that the design bounds proposed in Chapter 6 are not violated, and the design is free from QR-patterns. Due to the adaptive nature, *dp*-adaptive MTO can obtain a speed-up of upto 10 times over the non-adaptive MTO scheme. As known from a recent work by Groen *et al.* [1], the non-adaptive version of MTO has proved to be more than 3 times faster than the traditional TO approach for 2D problems. Thus, in a relative sense, it can be argued our method can produce comparable results 30 times faster than the traditional method for 2D problems. The potential of *dp*-adaptive MTO for 3D problems needs to be still investigated.

### 9.1.3. OVERALL CONCLUSIONS

Based on various numerical examples and comparison with experimental results, it can be concluded that TO has enormous potential in improving the performance of solar cells. In particular, it is of interest to use TO for designing metallization patterns in freeform solar cells as well as concentrating solar cells under nonuniform illumination, where significant improvements in performance can be obtained over the conventional patterns. With the presented modeling and optimization methodology for solar cells, the cost per unit of solar power can be reduced further. Also, an important conclusion is that the traditional *H*-pattern is already a quite efficient metallization design for rectangular solar cells. In general, the research output of this thesis is expected to be another step towards making renewable energy affordable and making this world greener.

Furthermore, the decoupled analysis and design based TO methods that have been presented in this thesis significantly increase the usable TO design resolution at a given computational cost. This shows promise not only for solar cell design, but for the wide array of applications of TO in general. The numerical investigations related to high-resolution TO and the *dp*-adaptive MTO scheme show hope of designing high-resolution structures that can deliver increased power output.

## 9.2. RECOMMENDATIONS

In Part I and II of this thesis, the research questions that were posed at the beginning have been answered. However, during the course of research, several new research directions have been identified. While some of these aspects have been investigated in this thesis, there are several questions that require follow-up research to be answered. In this section, we present recommendations for future work along ten important research directions.

1. Although the thesis ends with the development of an adaptive MTO approach which can generate high resolution designs at relatively low computational costs, its applicability for solar cell metallization design is unexplored due to time restrictions. Since the majority of the solar cell front surface comprises void areas, it is

- expected that  $dp$ -adaptive MTO could lead to a substantial reduction in computational costs.
2. Significant effort was put in obtaining metallization patterns for rectangular solar cells which could be superior over the traditional H-patterns. However, from numerous numerical experiments, it was observed that the dendritic designs obtained using TO were not able to outperform it. As per a recent study [2], although most of the TO approaches converge to tree-like designs, these tree-like structures are not optimal for thermal volume-to-point problems, and the true optima for such cases comprise lamellar, needle-like structures. Based on several numerical tests, we also concluded that the H-pattern is already close to an optimal design, however, it would be interesting to reach similar conclusions through analytical methods. Results related to this aspect could possibly provide novel insights for other design problems (*e.g.* electrical conduction problems or thermal management problems), where similar dendritic designs obtained using TO are currently accepted as quite superior and well performing designs.
  3. There are several parameters that affect the convergence of the TO process, and it is of interest to understand their impact on the final design. The metallization designs obtained using TO are found to be very sensitive to the choice of initial designs. Thus, choosing the right starting point for the design process is something that needs further investigation. Recently, van Schoubroeck *et al.* [3] explored the effect of initial designs in TO, and it would be a nice direction to perform a similar study focused on solar cell metallization design.
  4. For the solar cell metallization, the choice of boundary conditions can also affect the overall performance of the solar cell. While the busbar voltage  $V_b$  has been included as a design variable in the optimization process, the choice of busbar location and the number of busbar points has been mostly intuitive or driven by the conventional metallization patterns. However, the choices made in this thesis may not necessarily be optimal, and optimizing these parameters could also help in further improving the solar cell performance.
  5. For freeform geometries, 2D solar cell surfaces have been assumed in this study. However, in reality, the freeform solar cells can also comprise curved surfaces spanning in 3D, and the application of TO on such cases needs to be explored. Further, freeform geometries can generally be very large in size, and manufacturing large solar cells is not viable. Thus, a suitable direction would be to split the large freeform domain into several smaller solar cells. In such scenarios, the metallization design needs to be optimized on a solar panel level to ensure that the power output is maximized. The applicability of TO on a panel level has not been touched upon in this study and would be an interesting research question.
  6. From the manufacturing point of view, the aspects of sensitivity, fouling and robustness need to be included in the TO formulation for solar cell metallization design. Also, further experimental validations are required to confirm that the designs obtained from TO perform well. An additional factor to consider is the optimization of metallization designs for multiple illumination intensities. Over the

- period of a day, the illumination intensity changes. Thus, the metallization designs can be optimized in a way that the total power output for the whole day is maximized.
7. In Part II of the thesis, significant research has been dedicated towards developing efficient methods to obtain high resolution designs using TO. However, these studies have been restricted to 2D cases and global objectives. To further explore the potential of the adaptive  $h$ -refinement based TO and the  $dp$ -adaptive MTO method proposed in this study, 3D numerical examples need to be studied.
  8. The refinement indicators used in this work for adaptive refinement of the mesh comprise several tuning parameters which need to be properly chosen to obtain desired results. To avoid manual tuning of these parameters, an approach would be to include them as meta-variables in the optimization process. Alternatively, it should be possible to get rid of some of these parameters by extracting additional information from the optimization process. This could potentially increase the robustness of this method.
  9. In Chapter 6, we have proposed upper bounds on the number of design variables that can be chosen for a certain choice of analysis resolution. Also, in Chapter 7, QR-patterns and their impact have been studied. These studies have been tailored to structural problems, and in particular linear elastostatic problems. Future work could include investigation on problems involving harmonic excitations, eigenvalue problems, *etc.*
  10. Advanced modeling techniques such as XFEM/GFEM use enrichment functions to accurately model nonsmooth and discontinuous displacement fields [4, 5]. XFEM has also been used in the context of TO [6]. However, the significantly high complexity of this method restricts its attractiveness and how to combine XFEM with MTO is still an open research question. Moreover, it would be of interest to explore if the  $dp$ -adaptive scheme can be combined with such extended finite element methods.

## REFERENCES

- [1] J. P. Groen, M. Langelaar, O. Sigmund, and M. Ruess, *Higher-order multi-resolution topology optimization using the finite cell method*, International Journal for Numerical Methods in Engineering **110**, 903 (2017).
- [2] S. Yan, F. Wang, and O. Sigmund, *On the non-optimality of tree structures for heat conduction*, Structural and Multidisciplinary Optimization **122**, 660.
- [3] J. K. van Schoubroeck, D. K. Gupta, and M. Langelaar, *An investigation of the effect of initial design choices in density-based topology optimization (submitted)*, Structural and Multidisciplinary Optimization , 1.
- [4] N. Moës, J. Dolbow, and T. Belytschko, *A finite element method for crack growth without remeshing*, Int. J. Numer. Meth. Eng. **46**, 131 (1999).

- [5] T. Strouboulis, K. Copps, and I. Babuska, *The generalized finite element method*, Computer Methods in Applied Mechanics and Engineering **190**, 4081 (2001).
- [6] S. Kreissl and K. Maute, *Levelset based fluid topology optimization using the extended finite element method*, Struct. Multidiscip. O. **46**, 311 (2012).

# ACKNOWLEDGEMENTS

This thesis might show only me as an author, but there are several people whose efforts have been very important and deserve appreciation. I could have never thought of pursuing research if it had not been for my late mother who inspired me during my childhood. It was more of her dream that I become a scientist, and when she left me at 10, it became my dream. I thank my mother from the depth of my heart. Thanks also to my wife Debjani who has always believed in me and been a source of motivation. I am very grateful to my father, my brother Jai and other family members for the support that they have offered during this period.

I would like to thank my supervisors Dr. Matthijs Langelaar and Prof. Fred van Keulen for the hard-work and commitment that they have shown in moulding me into a researcher. When I started my PhD, I had very limited knowledge of the subject, but the belief that my supervisors put in me is what makes me write this book today. It is remarkably unbelievable that a PhD advisor can dedicate so much time for a PhD student; at least it contradicts the theories that I had heard from others. I have to say that the regular chats with Fred and Matthijs have offered me a fine blend of philosophy and science during the four years. Dr. Marco Barink, my co-supervisor from TNO has also helped me a lot with my research and I am very thankful to him.

I also had the opportunity to collaborate with a few people, and this has had significant impact on the research results presented in this thesis. I am thankful to Dr. Alejandro Aragón and Dr. Gijs van der Veen for the critical remarks and exciting discussions. I also appreciate the help that I received from Dr. Yulia Galagan from Solliance. Without her support, I would not have been able to validate my computational models against experimental results. I would also like to thank Prof. Arthur Weeber and Dr. René van Swaij for sharing their knowledge and providing feedbacks.

Many would agree with me that the workplace environment plays an important role in an individual's performance. Although I cannot judge my own performance, I can say that I had an awesome work environment with some of the best colleagues to work with. For all the good time that I had and the memories that we shared, I would like to thank Alex, Anil, Banafsheh, Birgit, Can, Eleenoor, Emiel, Evert, Gaby, Hans, Kai, Laura, Long, Marco, Marianne, Marli, Max, Murali, Qi, Rob, Roy, Samee, Sanne, Yabin, Yi, Yong and Yueting. I also had an opportunity to supervise Jimmy and Marco for their M.Sc. theses. I have to say that I had a great time doing this and I am thankful to both of you for it. Worth mentioning are the football matches that we played (unofficially between India and China) and the Indo-Chinese dinners, attempting to settle the geopolitical tensions. These have been very enjoyable and refreshing for me.

There is a life outside the workplace, and for me, most of it was along playing cricket, football, computer games, cooking and eating awesome Indian dinner, exploring Europe as well sitting with friends doing nothing. For all these moments, I would like to thank Aayush, Anurag, Aritra, Ashish, Darwin, Devashish, Gaurav, Rajeev, Rajit, Rakesh, Ram,

Sanjeev, Shaafi, Silky, Varun and Vijayragavan. I have spent significant part of this period with Rakesh at the Gym, playing badminton, cycling, running, swimming, cooking, discussing research and much more, and I am very thankful to him for his time and company. I am also thankful to Aaditya, Akash, Akshat, Anshul, Ashutosh, Rama and Saurish for the good times that we shared at Shell in India. The push I received from you guys has been fruitful in completing the book.

Pursuing research requires money, and in my case it came from Shell and NWO. I would like to thank both the organizations for funding this research project. I am very grateful to TU Delft for hosting me as a researcher and offering the needed resources. I would like to acknowledge Prof. Krister Svanberg for the 'Method of Moving Asymptotes' and Prof. Wolfgang Bangerth for the 'deal.II' software. Lastly, my thanks to everyone else not mentioned here, who have made this period even more enjoyable and inspiring.

*Deepak Gupta*  
*Tilburg, February 2019*

# LIST OF PUBLICATIONS

Publications in refereed journals and conference proceedings related to this thesis are listed below.

## JOURNAL PAPERS

1. **D. K. Gupta**, F. van Keulen, and M. Langelaar, *Design and analysis adaptivity in multi-resolution topology optimization*, arXiv:1811.09821 (2018) (submitted to International Journal for Numerical Methods in Engineering).
2. **D. K. Gupta**, M. Langelaar, and F. van Keulen, *QR-patterns: artefacts in multi-resolution topology optimization*, Structural and Multidisciplinary Optimization, **58**, 1335-1550 (2018).
3. **D. K. Gupta**, M. Barink, and M. Langelaar, *CPV solar cell modeling and metalization optimization*, Solar Energy, **159**, 868-881 (2018).
4. **D. K. Gupta**, G. J. van der Veen, A. M. Aragón, M. Langelaar, and F. van Keulen, *Bounds for decoupled design and analysis discretizations in topology optimization*, International Journal for Numerical Methods in Engineering, **111**, 88-100 (2017).
5. **D. K. Gupta**, M. Barink, Y. Galagan, M. Langelaar, and F. van Keulen, *Integrated front-rear-grid optimization of free-form solar cells*, IEEE Journal of Photovoltaics, **7**, 294-302 (2017).
6. **D. K. Gupta**, M. Langelaar, M. Barink, and F. van Keulen, *Optimizing front metallization patterns: Efficiency with aesthetics in free-form solar cells*, Renewable Energy, **86**, 1332-1339 (2016).
7. **D. K. Gupta**, M. Langelaar, M. Barink, and F. van Keulen, *Topology optimization of front metallization patterns for solar cells*, Structural and Multidisciplinary Optimization, **51**, 941-955 (2015).

## CONFERENCE PAPERS

1. **D. K. Gupta**, M. Langelaar, and F. van. Keulen, *Combined mesh and penalization adaptivity based topology optimization*, Proceedings of AIAA SciTech Forum: 57<sup>th</sup> AIAA/ASCE/AHS/ASC Structures, Structural Dynamics, and Materials Conference, San Diego, CA, USA (2016).
2. **D. K. Gupta**, M. Langelaar, M. Barink, and F. van Keulen, *Topology optimization: An effective method for designing front metallization patterns of solar cells*, Proceedings of 2014 IEEE 40<sup>th</sup> Photovoltaic Specialists Conference (PVSC), Denver, CO, USA (2014).

3. **D. K. Gupta**, M. Langelaar, F. van Keulen, and M. Barink, *Topology optimization for improving the performance of solar cells*, Proceedings of the 4<sup>th</sup> International Conference on Engineering Optimization, EngOpt2014, Lison, Portugal (2014).

## CONFERENCE ABSTRACTS

1. **D. K. Gupta**, M. Langelaar, and F. van Keulen, *Numerical artefacts in topology optimization approaches involving decoupled analysis and design discretizations*, Proceedings of the 12<sup>th</sup> World Congress on Structural and Multidisciplinary Optimization WCSMO12, Braunschweig (2017).

# CURRICULUM VITÆ

## Deepak K. GUPTA

28-06-1990      Born in Basti, U.P., India.

### EDUCATION

- 2013-2017      PhD. candidate at Structural Optimization and Mechanics Group of  
Dept. Precision & Microsystems Engineering,  
Delft University of Technology, The Netherlands  
*Thesis:*      Topology optimization for high-resolution designs,  
application in solar cell metallization  
*Promotors:*   Prof. dr. ir. F. van Keulen and Dr. ir. M. Langelaar
- 2008-2013      Master of Science & Technology (5 yr. course) in Applied Geophysics  
Indian Institute of Technology, ISM, Dhanbad, India  
*Thesis:*      Soft computing for intelligent interpretation of  
petroleum data and characterization of reservoirs  
*Supervisor:*   Dr. Rima Chatterjee  
Graduated with a distinction and received Director's Gold Medal for  
securing first position in the batch.
- 2006-2008      Senior Secondary Education (CBSE)  
Sir Padampat Singhania Education Centre, Kanpur, U.P., India
- 2004-2006      Secondary Education (ICSE Board)  
St. Basil's School, Basti, U.P., India

## WORK EXPERIENCE

- 2019-Present      Postdoctoral Researcher at QUVA Lab  
Informatics Institute, University of Amsterdam, The Netherlands  
Working with deep learning and computer vision for efficient  
object tracking in long-term videos.
- 2017-2019      Research Scientist in Advanced Imaging/Seismic Analytics Team  
Shell Technology Center, Bengaluru, India  
Worked on automating seismic processing steps using machine  
learning and computer vision techniques.
- 12/2012-01/2013      Visiting researcher, EarthByte Group, School of Earth Sciences,  
University of Sydney, Australia
- 05/2012-06/2012      Student intern at Schlumberger Information Solutions,  
Gurugram, India.

## AWARDS

- 2018      Shell Special Recognition Award
- 2014      SIAM Gene Golub Summer Fellowship
- 2013      Shell-NWO Computational Science for Energy Research Fellowship
- 2013      SEG-Eni Scholarship
- 2012      SEG Foundation Grant
- 2013      Director's Gold Medal, Indian Institute of Technology, ISM, Dhanbad
- 2008-13      SHE-INSPIRE scholarship, Dept. Science & Technology, Govt. of India